Gold nanomaterials-based optical biosensors for rapid and cost-efficient diagnostics

Liming Hu

Universitat Autònoma de Barcelona

Gold nanomaterials-based optical biosensors for rapid and cost-efficient diagnostics

Liming Hu

PhD Thesis

PhD in Biotechnology

Directors:

ICREA Prof. Arben Merkoçi

Dr. Andrea Idili

Dr. Marianna Rossetti

2023

The present work entitled “Gold nanomaterials-based optical biosensors for rapid and cost-efficient diagnostics”, presented by Liming Hu to obtain the degree of doctor by the Universitat Autònoma de Barcelona, was performed at the Nanobioelectronics and Biosensors Group at the Institut Català de Nanociencia i Nanotecnología (ICN2), under the supervision of Prof. Arben Merkoçi, ICREA Professor and Group Leader, Dr. Andrea Idili and Dr. Marianna Rossetti.

Bellaterra, October 2023

The supervisors

Prof. Arben Merkoçi Hyka Dr. Andrea Idili Dr. Rossetti Marianna

The present Thesis was performed also under the doctoral program studies “Doctorado en Biotecnología” at the Faculty of Chemical Engineering, Universitat Autònoma de Barcelona, under the tutorship of Professor Francesc Godia.

The University tutor

Prof. Francesc Gòdia Casablancas

"A ship is always safe at the shore, but that is not what it is built for."

— **Albert Einstein**

The research conducted has resulted in several publications and manuscripts that were submitted to international peer-reviewed scientific journals.

The state-of-the art studies conducted resulted in one published chapter and one unpublished review.

Hu, L., Idili, A., Parolo, C., Álvarez-Diduk, R., Calucho, E., & Merkoçi, A. (2022). Optical smartphone-based sensing: diagnostic of biomarkers. In *The Detection of Biomarkers* (pp. 277-302). Academic Press.

Hu, L., Rossetti, M., Idili A. & Merkoçi, A. Gold nanomaterials-based optical biosensors for point of care diagnosis. *In preparation* (2023).

The experimental work carried out resulted in two publications and one article not yet published.

Hu, L., Calucho, E., Fuentes-Chust, C., Parolo, C., Idili, A., Álvarez-Diduk, R., Rivas, L. & Merkoçi, A. (2022). Selection and characterisation of bioreceptors to develop nanoparticle-based lateral-flow immunoassays in the context of the SARS-CoV-2 outbreak. *Lab on a Chip*, 22(16), 2938-2943. – work related to Chapter 3.

Rivas, L., **Hu, L.**, Parolo, C., Idili, A., & Merkoçi, A. (2023). Rational Approach to Tailor Au–IrO2 Nanoflowers as Colorimetric Labels for Lateral Flow Assays. *ACS Applied Nano Materials*, 6(6), 4151-4161. – work related to Chapter 4.

Hu, L., Rossetti M., Bergua, J. F., Parolo, C., Álvarez-Diduk, R., Rivas, L., Idili, A., & Merkoçi, A. Harnessing Bioluminescent Bacteria to Develop an Enzymatic-Free ELISA for the detection of Clinically Relevant Biomarkers. *To be sumitted to ACS Nano* (2023). – work related to Chapter 5.

A research paper that is not included in the dissertation being prepared.

Hu, L., Rossetti M., Álvarez-Diduk, R., Capolungo C., Maroli G. & Merkoçi A. Paper-based fluorescent aptasensor for real-time sensing of NGAL and miRNA for monitoring of acute kidney injury. (*In preparation*)

Additionally, the collaborations performed with the Ph.D. thesis resulted in several other publications unrelated to this thesis:

Zhao, L., Rosati, G., Piper, A., de Carvalho Castro e Silva, C., **Hu, L.**, Yang, Q., ... & Merkoçi, A. (2023). Laser Reduced Graphene Oxide Electrode for Pathogenic Escherichia coli Detection. *ACS Applied Materials & Interfaces*, 15(7), 9024-9033.

Bergua, J. F., Alvarez-Diduk, R., Idili, A., Parolo, C., Maymó, M., **Hu, L.**, & Merkoçi, A. (2022). Low-cost, user-friendly, all-integrated smartphone-based microplate reader for optical-based biological and chemical analyses. *Analytical chemistry*, 94(2), 1271-1285.

Rosati, G., Idili, A., Parolo, C., Fuentes-Chust, C., Calucho, E., **Hu, L.**, ... & Merkoçi, A. (2021). Nanodiagnostics to face SARS-CoV-2 and future pandemics: From an idea to the market and beyond. *ACS nano*, 15(11), 17137-17149.

Bergua, J. F., Alvarez-Diduk, R., **Hu, L.**, Hassan, A. H., & Merkoci, A. (2021). Improved Aliivibrio fischeri based-toxicity assay: Graphene-oxide as a sensitivity booster with a mobile-phone application. Journal of Hazardous Materials, 406, 124434.

Bergua, J. F., **Hu, L.**, Fuentes-Chust, C., Álvarez-Diduk, R., Hassan, A. H., Parolo, C., & Merkoçi, A. (2021). Lateral flow device for water fecal pollution assessment: from troubleshooting of its microfluidics using bioluminescence to colorimetric monitoring of generic Escherichia coli. *Lab on a Chip*, 21(12), 2417-2426.

Parolo, C., Sena-Torralba, A., Bergua, J. F., Calucho, E., Fuentes-Chust, C., **Hu, L.**, ... & Merkoçi, A. (2020). Tutorial: design and fabrication of nanoparticle-based lateral-flow immunoassays. *Nature protocols*, 15(12), 3788-3816.

Sena-Torralba, A., Ngo, D. B., Parolo, C., **Hu, L.**, Álvarez-Diduk, R., Bergua, J. F., ... & Merkoçi, A. (2020). Lateral flow assay modified with time-delay wax barriers as a sensitivity and signal enhancement strategy. *Biosensors and Bioelectronics*, 168, 112559.

When I start to write this part, I am really grateful for everybody I encountered during my PhD studies. Firstly, I am sincerely thankful for my supervisor and tutor, professor Arben Merkoçi, the soul of our team. You are so kind, considerable, spiritual and professional. Thanks for providing so free and relaxed academic environment and at same time giving me so many opportunities to experience and enjoy international and diverse cultures. Thanks to the team, I can still maintain a healthy body and mind, especially still rich hair, when I almost finished my PhD. In academic terms, you always quickly gave me positive and quite helpful suggestions in the key process of my projects. In terms of life, you organize as many activities as possible to let everyone relax and communicate. Next, I want to thank another soul figure in our group, Anna Puig. Everything in the research group can proceed smoothly because of you. Thank you so much for your great patience in processing my countless emails. Thanks to Rosa Maria Fuentes Gracia, the administrator of chemical, biological and environmental engineering department, Flora Fuentes Garcia, the interim manager of cell biology, physiology and immunology department, and the coordinator of Prof. Francesc Gòdia Casablancas for the patient and nice help for my thesis defense.

I am grateful for the members of our postdocs group. During my PhD, so many postdocs helped me a lot. Dr. Andrea Idili, you joined the team when first independent project of my PhD is bottlenecked. You not only guide me in academic issues, but also gave me a lot of suggestions on time management, academic career planning etc. You are so kind and sincere, and are willing to listen my confusion and complaints and propose effective solutions. You are always quick-thinking, energetic and strong execution. It is really a pity that we only stayed together for less than two years. Dr. Marianna Rossetti, you are so logical, executive and responsible. Many times our ideas are so compatible. I really enjoyed the time of discussion about the projects. I feel honored to be working with you in the final phase of my PhD. Dr Claudio Parolo, you are so quick in thinking and strong in execution. I feel very lucky that you are involved in every project of my PhD. Every time I get confused in scientific research, I can always get your help. Thank you for your prompt and very constructive feedback and revisions to each manuscript. Dr. Ruslan Álvarez, you are so smart and creative. You can always come up with some really cool and meaningful ideas combined with actual needs. You always tend to design and build some auxiliary equipment for experimental research. When most people buy a lot of things directly in order to produce results quickly, they just miss the opportunity to think and research like this. I'm grateful that almost every project during my PhD stemmed from the foundation you laid before. Your behavioral traits have a subtle influence on me. Even though we don't communicate very often, some of your feedback is always so to the point. Dr. Giulio Rosati, a really excellent engineering-researcher, you are so rigorous and organized. Since your joining, our team's laboratory management has become more orderly. I am also more than happy to enter the lab 2015. It can be said that the laboratory is the first important work place for us. Thank you very much for your dedication for these trivial things. Dr. Daniel Quesada, a very very nice guy, you are so kind, so enthusiastic, so good at management and organization. Unfortunately, when I arrived our group, you just finished your PhD and I didn't have the opportunity of working with you. And fortunately, you came back

our group. Although I left so soon, I still felt the improvement of our working environment. Dr. Andrew Piper, a very clever, strict (jaaa..) guy, thanks to your great efforts for our research work and our group management. Dr. Sinan Uzunçar, you are so humorous, chatty and enthusiastic. Every time I chat with you, I can feel your kindness and care. I am so encouraged by your affirmations and compliments. Chatting with you makes me feel so enjoy and relax.

I'm thankful for the PhD team, José Fran, Amadeo, Qiuyue, Lei, Celia, Enric, José Marrugo, Ana Rubio, Massimo, Vernalyn and Nerea. José Fran, the first person I worked with and worked together for two years. He was so kind, patient, intelligent, and dynamic. He has always insisted on making weekly plans, daily plans and writing experimental outlines and procedures. I really saw how this good habit of planning and organization can make work so efficient. He has such a wide range of interests, especially in Spanish and Chinese we learned from each other. Now he can write short essays and diaries in Chinese, while I just say greetings in Spanish. Every time I see him, I can feel how he is a person who loves life. I really enjoy the happy time of working, playing, traveling and gathering with him. Amadeo, I really envy his fluent English. Whenever I talk to him about experiments, I am amazed at his memory of the details of the experiments. Thanks to him for his timely and meticulous advice and guidance whenever I asked some research questions after his graduation. In the early days of the PhD, when everyone was saying you could easily get through this time, he was the only one who said you had to take each stage of the PhD seriously and not let yourself go. Sincerely thank him for the reminder. Let me show my sincere gratitude to Celia and Enric. You are really kind and dedicated. I can say that every member of the team has been helped by you. I would like to say that a good team can lack one or two excellent but selfish staff in scientific research, but you must be indispensable. José Marrugo, he was always so gentle and polite. It was a pleasure for me to watch and listen to his oral presentations. Gabriel, I'd love to call him an excellent engineer-researcher. Since he joined our research group, some old equipment has been reactivated, especially the 3D printer. He always humbly says that his English is not good enough. But every question and answer is always so concise and to the point. Massimo, such a bright, research-minded and positive guy, every seminar presentation is so creative and inspiring. Vernalyn, such a soft and artistic girl. Since her joining, our group's social media content has become more colorful, and she has become our group's professional photographer and media communicator. I really like her layout of the Hall of Fame module in our 2097 office. Nerea, a new PhD student but an old member of our group, she is so thoughtful and expressive. I believe that with the addition of these fresh blood, our team will become better and better.

I would like to give special thanks to Zhao Lei and Qiuyue. During my application for a PhD in Arben's research group, Lei gave me a lot of advice and help. Especially when the deadline for the doctorate was approaching and I still did not receive the admission certificate from UAB. When I had no way to communicate, Lei helped me to contact Anna Puig. Only then did I know that there was a communication problem between different departments of UAB. The problem was quickly resolved. Many thanks to Lei for his kind help in a situation we didn't even know. When I first joined our research group, I was afraid to communicate with members of the group due to my

poor English. Their encouragement and help made me integrate quickly. Thanks to them for giving me guidance and advice on research and for patiently listening to some of my confusions. I really enjoy discussing research projects with Qiuyue from time to time, she is so patient and smart, always giving me some constructive advice. I also hope that in the collision of ideas, she also gains something.

I'm thankful for Manuela Dietrich, the senior laboratory officer of the Biolab Facility. I am fortunate to be working in our own biolab at ICN2. A big thank you to Manuela for organizing the biolab and keeping everything in order. I feel very convenient and happy working here. Thank you for your patient guidance and help in bacterial culture. I would like to thank the Electron Microscopy Unit in ICN2, Belén and Marcos for their support and patience during these years. Also thanks to Javiez Saiz, Raúl Pérez, and Antonio Pablo Pérez, from ICN2 Instrumental Core Research Facilities, and to Martí de Cabo Jaume and Alejandro Sánchez Chardi from UAB Microscopy Service.

I would also like to thank the ICN2 reception team. Marta, Luis, Rosalía, Joan, Albert, Oriol, Raquel, Ramio and Malika etc. You are the people I say 'hola' every day. I'm sorry I didn't have time to say goodbye when some people left. Thank you for your tireless sending emails to notify me to pick up the package, and thank you for your patient reception every time I pick up office items. I would like to thank the team of IT department. Thanks to your efforts, I can use the computer to conduct literature research, data analysis, paper writing and document printing conveniently, quickly and safely. I want to especially thank the maintenance and service team. You are everywhere at ICN2. Your work is reflected in every corner of ICN2. In particular, I would like to thank the cleaning ladies who are also the ones I say 'hola y gracias' the most every day. They are smiling and doing their due diligence every day. Every day when I enter ICN2, I see neat countertops and floors in offices, laboratories, dining rooms and toilets. I feel so blessed and lucky to be able to work and study here.

I must thank my master supervisor, professor Lai. He is my guide on the road to scientific research. Despite being out of the country for all these years, I can still receive his care and attention. When I encounter difficulties, I can always think of my master team (619 big family), which has become my backing and motivation. He personally demonstrated that while focusing on scientific research, he also maintains the habit of exercising for hobbies and health. From then on, I also fell in love with playing badminton and kept exercising over the years. This sport has benefited me a lot. How lucky I am to meet my current doctoral supervisor, professor Arben, during my Ph.D. They are so rigorous and dedicated to scientific research, and are so patient, tolerant and thoughtful towards students, creating a free and professional academic atmosphere. It is because of their dedication that I have been able to study and research with great pleasure throughout the several years of postgraduate study.

Thanks to my friends Huang Juan, Minghua, Congcong, Yunwei, Jiahui, Junjie, Yunhui, and Jinhui etc. We've had a lot of fun traveling, dining and chatting together at various stages over the past

four years. I would also like to thank my friends in China. Xiaobin, my most special friend, you are always there, and every time I can receive your most timely reply, concern, support and encouragement. Liu Miao, my master classmate and good friend, always chats for hours on scientific research topics (Jaaaaaa...it's because we don't chat very often). You and Yonggang are the couple I admire the most. You have shown the most beautiful appearance of perseverance and support in love. Please accept my best and most sincere wishes. Jiaojiao, I always receive your care and attention when some important events happen. Sorry for the delayed response, sometimes. I am grateful to those friends, classmates, colleagues and teachers who have given me care and blessings for the limited life status displayed on WeChat.

I want to thank every one of my flatmates, Tan Yu, Kaijun, Wenchao, Jinghai, Yanyan, Yufei, Xiaobao and Xueliang. I would like to call the house we live in home, where we cook, eat, chat and rest. This is a different experience from the dormitory that I have lived in at different stages before. Everyone's organization, coordination, tolerance and dedication create a good, tidy and harmonious living environment. That's why the bedroom has become one of the two most important places in my doctoral career, where I spend nearly half of my time sleeping, entertaining, and working. Thank you for every gathering, which has become an opportunity for our Chinese students in UAB to exchange feelings and have fun and relax. Thanks for the care from my flat mates when I am sick or in a bad mood making me feel the affection of family and friend.

I would like to thank every member of the badminton team. In the past four years, we have spent a lot of happy evenings together with sweat and sweat. The badminton court of SAF has become my most important leisure and entertainment field. Thank you for your sincere cooperation and generous advice. My hitting skills have improved, and I've been able to release stress while building my body.

Last but not least I have to thank my family and my homeland. My family has always given me the greatest support and encouragement in every choice of my life. A big thank you to my older sisters, my older brothers-in-law and younger brother for their company and care for my parents during my absence. Thank you to my little nephew for the joy and laughter for this extended family. I miss you so much. I have to thank my country. It is your thriving and booming economy that allows me to receive funding from CSC and be focus on studying abroad without discrimination.


ICN2
Institut Català
de Nanociència
i Nanotecnologia
EXCELENCIA
SEVERO
OCHOA


NANO
Bioelectronics
& Biosensors Group


UAB
Universitat Autònoma
de Barcelona


Generalitat
de Catalunya


GOBIERNO
DE ESPAÑA
MINISTERIO
DE CIENCIA
E INNOVACIÓN


MICROB-PREDICT


CHINA SCHOLARSHIP COUNCIL

A. fischeri	*Allivibrio fischeri*
a.u.	arbitrary units
AFP	aloha-fetoprotein
AgNPs	silver nanoparticles
AI	artificial intelligence
ALP	alkaline phosphatase
ASOs	antisense oligonucleotides
Au NBPs	gold nanobipyramids
Au-IrO_2 NFs	gold and iridium oxide nanoflowers
AuNCs	gold nanoclusters
AuNMs	gold nanomaterials
AuNPs	gold nanoparticles
AuNRs	gold nanorods
AuNSs	gold nanospheres / gold nanostars
AuNTs	gold nanotriangles
BB	borate buffer
BBLISA	bioluminescent bacteria-linked immunosorbent assay
BL	bioluminescence
BSA	bovine serum albumin
CBS	carbonate-bicarbonate buffer
CDs	carbon dots
CEA	carcinoembryonic antigen
cfDNA	circulating cell-free DNA
ChOx	cholesterol oxidase
CL	control line
COVID-19	coronavirus disease 2019
CQDs	carbon quantum dots
CRISPR	clustered regularly interspaced short palindromic repeats
CRP	c-reaction protein
Cryo-TEM	cryogenic transmission electron microscopy

CTCs	circulating tumor cells
CV	coefficient variation
Cys-AuNPs	cysteamine-capped gold nanoparticles
DLS	dynamic light scattering
E coli	*Escherichia coli*
EC50	half maximal effective concentration
EDX	energy dispersive X-ray
ELISA	enzyme-linked immunosorbent assay
et al.	*et alia* (and others)
EXPAR	exponential amplification reaction
FRET	Förster resonance energy transfer
GO	graphene oxide
GOQDs	graphene oxide quantum dots
GOx	glucose oxidase
GSH	glutathione
HCR	hybridization chain reaction
HIgG	human immunoglobulin
HIV	human immunodeficiency virus
HRP	horseradish peroxidase
IAVs	influenza A virused
IC_{50}	half-maximal inhibitory concentration
ICP-OES	inductively coupled plasma optical emission spectroscopy
IFE	inner filter effect
IgG	immunoglobulin
IrO_2	Iridium oxide
LAMP	loop-mediated isothermal amplification
LFA	lateral flow assay
LFIA	lateral flow immunoassay
LFS	lateral flow strip
LOD	limit of detection

LOQ	limit of quantification
LOx	lactate oxidase
LSPR	localized surface plasmon resonance
mAbs	monoclonal antibodies
MBs	magnetic beads
MEF	metal-enhanced fluorescence
miRNA	microRNAs
ML	machine learning
NA	nucleic acid
N-CDs	nitrogen-doped carbon dots
NIR	near-infrared fluorescence
NP	nucleocapsid protein
OD	optical density
pAbs	polyclonal antibodies
PBS	phosphate buffered saline
PBST	phosphate buffered saline with Tween-20
PCR	polymerase chain reaction
PDI	polydispersity index
p-ELISA	plasmonic ELISA
PNA	peptide nucleic acid
POC	point-of-care
POCT	point-of-care testing
PSA	prostate-specific antigen
QDs	quantum dots
RBD	receptor-binding domain
RBP4	retinol-binding protein 4
RPA	recombinase polymerase amplification
RT	room temperature
RT-LAMP	reverse transcription loop-mediated isothermal amplification
RT-RPA	reverse transcription recombinase polymerase amplification

SARS-CoV-2	severe acute respiratory syndrome coronavirus 2
SD	standard deviation
SELEX	systematic evolution of ligands by exponential enrichment
SEM	scanning electron microscope
SERs	surface-enhanced Raman scattering
SPR	surface plasmon resonance
T2DM	type 2 diabetes
TE	tyndall effect
TEM	transmission electron microscopy
TL	test line
TMB	3,3′,5,5′-tetramethylbenzidine
UCNPs	upconversion nanoparticles
USD	Unites States dollar
WHO	World Health Organization
XPS	X-ray photoelectron spectroscopy
ε	extinction coefficient

Page

THESIS OVERVIEW **1**

CHAPTER 1 ..... **7**

Introduction **7**

1.1. Biomarkers and point-of-care diagnostics 9

1.1.1. What is a biomarker? 9

1.1.2. Diagnostic biomarkers detection 9

1.1.3. Point-of-care diagnostics 10

1.2. Gold nanomaterials-based optical biosensors for POC diagnostics 12

1.2.1. AuNPs aggregation-based assays 14

1.2.2. AuNMs etching/growth-based optical biosensors for POC diagnostics 22

1.2.2.1. H_2O_2 and TMB^{2+}-mediated etching of AuNMs 22

1.2.2.2. H_2O_2 and iodide ions-mediated etching of AuNMs 25

1.2.2.4. In situ formation of AuNMs 28

1.2.3. AuNMs and IFE/MEF/FRET-based optical biosensors for POC diagnostics 30

1.2.3.1. Inner filter effect (IFE) between AuNPs and fluorophores 30

1.2.3.2 Metal-enhanced fluorescence (MEF) between AuNPs and fluorophores 34

1.2.3.3 Förster resonance energy transfer (FRET) between AuNPs and fluorophores ... 40

1.2.4. AuNPs-based LFAs for SARS-COV-2 diagnosis 45

1.2.4.1. Modification of physical structure for delayed flow of LFAs 46

1.2.4.2. Gold nanocomposites-based LFAs 48

1.2.4.3. AuNPs clusters or in situ growth of AuNPs-based LFAs 50

1.2.4.4. Integration with CRISPR-Cas system with AuNPs-based LFAs 51

1.3. Conclusions 53

1.4. References 54

CHAPTER 2 ..... **71**

Thesis objectives **71**

CHAPTER 3 ..... **75**

AuNPs as colorimetric labels in LFAs for detection of SARS-CoV-2 nucleoprotein **75**

3.1. Introduction 77

3.2. Materials and methods 78
3.2.1. Reagents and devices 78
3.2.2. ELISA assay for selection of antibodies 79
3.2.3. Gold nanoparticle synthesis 80
3.2.4. Conjugation of AuNPs with anti-nucleoprotein antibodies (M5) 81
3.2.5. Fabrication of the half-stick lateral flow strips (Dot test) 81
3.2.6. Calibration curves of nucleoprotein detection based on half-stick LFA 82
3.2.7. Data analysis 82
3.3. Results and discussions 82
3.3.1. ELISA tests for screening antibody combinations 82
3.3.2. Half-stick dot test for screening out antibody combinations 87
3.3.3. Calibration curve of nucleoprotein detection based on half-stick LFA 89
3.4. Conclusions 93
3.5. References 93
CHAPTER 4. 99
Au-IrO_2 NFs as novel colorimetric labels in LFAs 99
4.1. Introduction 101
4.2. Materials and methods 104
4.2.1. Reagents and apparatuses 104
4.2.2. Preparation of AuNPs and Au–IrO_2 NFs 105
4.2.2.1. Synthesis of AuNPs 105
4.2.2.2. Synthesis of Au–IrO_2 NFs 105
4.2.3. Characterization of Au–IrO_2 NFs 106
4.2.4. Extinction coefficient calculations 106
4.2.5. Conjugation of antibodies to AuNPs and Au–IrO_2 NFs 107
4.2.6. Lateral flow immunoassays: Preparation of the strips and procedure 107
4.2.6.1. Preparation and assembly of strips 107
4.2.6.2. Lateral flow immunoassay procedure 108
4.2.6.3. Calibration curves of HIgG detection based on Au–IrO2 NFs LFAs 108
4.2.6.4. Specificity tests for Au–IrO_2 NFs LFAs 108

4.2.6.5. Recovery tests for Au–IrO_2 NFs LFAs 108

4.2.6.6. Stability tests for Au–IrO_2 NFs LFAs 109

4.2.7. Data Analysis 109

4.3. Results and discussions 109

4.3.1. Synthesis of Au-IrO_2 nanoflowers 109

4.3.2. Au–IrO_2 nanoflower characterization 112

4.3.3. Bioconjugation of the Au–IrO_2 nanoflowers 115

4.3.4. Lateral flow immunoassay 116

4.3.4.1. Calibration Curves of Au–IrO_2 NFs LFAs for detecting HIgG in PBS buffer and spiked human serum 116

4.3.4.2. Specificity and selectivity of Au-IrO_2 NFs-based LFAs 122

4.3.4.3. Recovery of Au-IrO_2 NFs-based LFAs for detection of HIgG 123

4.3.4.4. Stability of Au-IrO_2 NFs-based LFAs for detection of HIgG 123

4.4. Conclusions 124

4.5. References 125

CHAPTER 5 133

AuNPs and Au-IrO_2 NFs as bioluminescence absorbers in bioanalytical platform based on inner filter effect 133

5.1. Introduction 135

5.2. Materials and methods 138

5.2.1. Reagents and buffers preparation 138

5.2.1.1 Chemicals and biomaterials 138

5.2.1.2. Preparation of marine broth medium 138

5.2.1.3. Preparation of various buffers for BBLISA and ELISA 138

5.2.2. Production of bioluminescent bacteria 139

5.2.3. Synthesis of metallic nanoparticles 139

5.2.4. Optical characterization of *A. fischeri* and metallic nanoparticles 140

5.2.5. Bioluminescence of bacteria in the presence of metallic nanoparticles 140

5.2.6. Growth curves of *A. fischeri* in presence of AuNPs or Au-IrO_2 NFs 141

5.2.7. Characterization of *A. fischeri* and metallic nanoparticles 141

5.2.8. Conjugation of metallic nanoparticles with antibodies 142

5.2.9. Detection of human IgG and SARS-CoV-2 nucleoprotein based on colorimetric ELISA 143

5.2.10. Detection of human IgG or nucleoprotein based on BBLISA 143

5.2.11. Data analysis 144

5.3. Results and discussions 145

5.3.1. BBLISA design and inner filter effect characterization 145

5.3.2. BBLISA based on AuNPs 150

5.3.3. BBLISA based on Au-IrO_2 NFs 155

5.4. Conclusions 161

5.5. References 162

GENERAL CONCLUSIONS 169

ANNEXES 173

THESIS OVERVIEW

This thesis is organized in five chapters. The first chapter is a general overview on the gold nanomaterials-based optical biosensors for point-of-care diagnosis. The experimental work conducted throughout this PhD project is described in the next four chapters of the thesis. Each chapter is presented as a scientific paper and consists of different sections, including a general introduction, a description of the relevant experimental details, a presentation of the results, discussions and conclusions and the references. A brief explanation of each chapter is given below:

Chapter 1. Introduction. This chapter begins with a general introduction to the concepts of biomarkers and point-of-care diagnostics. Next, examples (from 2020 to 2023) of various optical biosensors based on gold nanomaterials (AuNMs) for point-of-care (POC) diagnostics are presented and classified according to different signal transduction mechanisms, including aggregation of AuNMs, etching/growth of AuNMs, and inner filter effect (IFE)/metal-enhanced fluorescence effect (MEF)/ fluorescence resonance energy transfer (FRET) between fluorophores and AuNMs. In particular, different signal enhancement strategies proposed to enhance the sensitivity of gold nanoparticles-based LFAs for SARS-CoV-2 diagnosis, are reported.

Chapter 2. Objectives of the thesis. This chapter briefly describes the objectives that motivated and conducted this work.

Chapter 3. AuNPs as colorimetric labels in LFAs for detection of SARS-CoV-2 nucleoprotein. Gold nanoparticles are commonly used in lateral flow assays for point-of-care diagnosis due to unique optical properties, ease of synthesis, functionalization, conjuation and labelling with bioreceptors, rapid signal generation, and cost-effective production. In this chapter, I first screened over 80 antibody pairs to find those providing the highest sensitivity and specificity using ELISA. Then I used the 5 best couples in a half-stick format, to select those providing the best analytical performance in a lateral flow assay. Of the 3 antibody couples that worked better in the lateral flow assay format (Figure 0.1). Although I achieved to develop a working lateral flow assay, in the chapter I want to emphasize that the antibody selection process that could and should be a relatively straightforward and quick procedure, it required over 10 months and 24,422.6 €. This is unacceptable if I want to develop effective diagnostics technologies in a short period of time such as during the current COVID-19 pandemic. This chapter aims to focus the

attention of the scientific community on the need for **better characterized bioreceptors** for faster development of point-of-care diagnostic devices, e.g. antibodies with **fast binding kinetics** for a LFA.

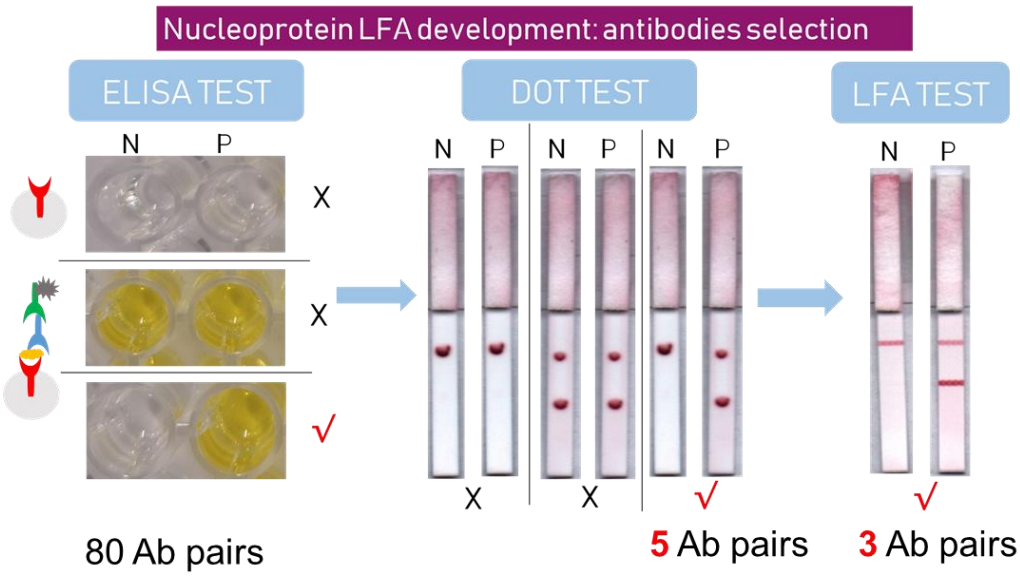

Figure 0.1. The screening process to select antibody couples to use in lateral flow assay for detecting nucleoprotein of SARS-CoV-2. Adapted with permission from Hu, L. *et al.* Selection and characterisation of bioreceptors to develop nanoparticle-based lateral-flow immunoassays in the context of the SARS-CoV-2 outbreak. *Lab Chip* **22**, 2938–2943 (2022).

Chapter 4. Au-IrO_2 NFs as novel colorimetric labels in LFAs. I introduced the use of gold and iridium oxide nanoflowers (Au–IrO_2 NFs) as colorimetric labels in LFAs to **improve the analytical performance of the platform**. The idea is to exploit their dark color to create a higher contrast with the white background of the lateral flow strips, and therefore to improve the sensitivity of nanoparticle-based LFAs. These Au–IrO_2 NFs display strong optical properties, but due to their size (over 100 nm), not ideal for LFAs. Specifically, they would be more prone to precipitation and aggregation once dried on the LFA, limiting their flow through the membrane. Therefore, I rationally adapted their synthesis to decrease the size of Au–IrO_2 NFs without compromising their stability. In particular, I achieved it by changing the reaction time and the reducing agent (citrate) concentration while keeping their optical properties. As a test bed, I successfully used the Au–

IrO_2 NFs in a LFA for the detection of human immunoglobulin G (HIgG). Due to their unique optical and redox properties, their bioconjugation capabilities and the synergistic combination of the individual components, Au–IrO_2 NFs therefore appear to be potential candidates for the next generation of optical LFAs (Figure 0.2).

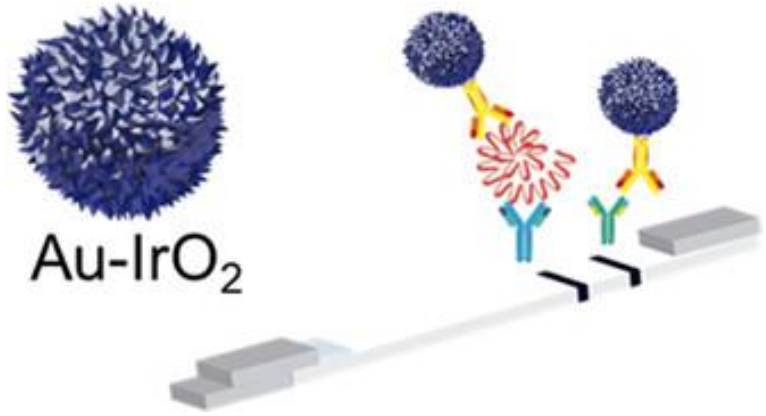

Figure 0.2. Use of Au–IrO_2 NFs as potential candidates for the next generation of optical LFAs. Adapted with permission from Rivas, L., Hu, L., Parolo, C., Idili, A. & Merkoçi, A. Rational Approach to Tailor Au–IrO2 Nanoflowers as Colorimetric Labels for Lateral Flow Assays. *ACS Appl. Nano Mater.* **6**, 4151–4161 (2023).

Chapter 5. AuNPs and Au-IrO_2 NFs as bioluminescence absorbers in bioanalytical platform based on inner filter effect. In this chapter a new bioanalytical platform, Bioluminescent Bacteria-Linked Immunosorbent Assay (BBLISA), is presented. BBLISA is an enzyme-free assay that utilizes the **inner filter effect (IFE)** between the bioluminescent bacteria *Allivibrio fischeri* and a molecular absorber, specifically metallic nanoparticles (i.e., AuNPs and Au-IrO_2 NFs). The nanoparticles can be easily functionalized with antibodies that allow their absorption in the well in the presence of the molecular target, by forming of the classical immune sandwich. Thanks to their ability to adsorb the light emitted by the bacteria, the nanoparticles can suppress the bioluminescence signal, and thus allow rapid quantification of the target (Figure 0.3). Taking advantage of the modularity and versatility of the BBLISA, two clinically relevant biomarkers (human IgG and nucleoprotein of SARS-CoV-2) are detected in serum with the same or even better sensitivity and precision as a conventional ELISA. The IFE between natural bioluminescent bacteria and established nanomaterials is exploited for the first time, and the results show that the BBLISA is faster, safer, cheaper, and more user-friendly than the current ELISA platform.

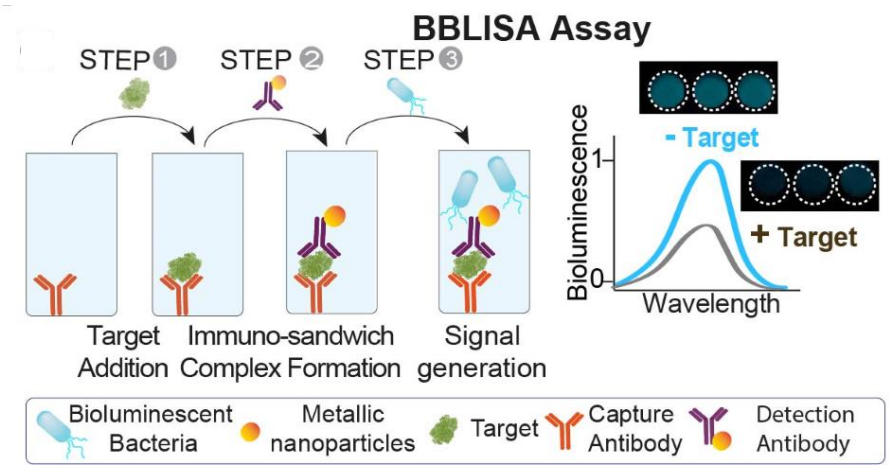

Figure 0.3. Schematic illustration of Bioluminescent Bacteria-Linked Immunosorbent Assay (BBLISA).

General conclusions. In this chapter, a summary of the objectives achieved, concluding remarks, future perspectives and ongoing work are reported.

CHAPTER 1

Introduction

1.1. Biomarkers and point-of-care diagnostics

1.1.1. What is a biomarker?

A biomarker, short for biological marker, is a measurable and quantifiable characteristic or substance that serves as an indicator of a biological process, condition or disease state[1]. Biomarkers can be found in various biological samples, such as blood, urine, tissues, or even breath. They play a crucial role in medical research, diagnostics and clinical practice by providing valuable information about the health status of an individual or the progression of a disease. There are several types of biomarkers, including diagnostic biomarkers, which are used to identify the presence or absence of a disease[2], prognostic biomarkers, which help predict the likelihood of disease progression or outcome[3], predictive biomarkers, which indicate the response to a particular treatment[4], and pharmacodynamic biomarkers, which measure the biological effects of a drug[5].

1.1.2. Diagnostic biomarkers detection

In recent decades, high-throughput sequencing[6] and mass spectrometry techniques[7] have accelerated the discovery of novel biomarkers. Among them, nucleic acid-based biomarkers have gained considerable importance in the field of diagnostics. These biomarkers provide valuable information on the presence, progression, and characteristics of various diseases[8–10]. In particular, liquid biopsy, which detect various biomarkers, such as circulating cell-free DNA (cfDNA)[11], circulating tumor cells (CTCs)[12], extracellular vesicles[13] and microRNAs (miRNAs)[14], in bodily fluids such as blood, urine or saliva, is an alternative to invasive traditional biopsy, providing valuable information on genetic mutations, gene expression profiles, and epigenetic changes associated with cancer, thus enabling early cancer detection and personalized treatment approaches. Currently, polymerase chain reaction (PCR) is a widely used technique for amplification and detection of specific DNA/RNA sequences[15,16]. Recently, isothermal amplification methods, such as loop-mediated isothermal amplification (LAMP)[17] and recombinase polymerase amplification (RPA),[18,19] have gained attention due to their simplicity and rapidity. Additionally, tests based on CRISPR (Clustered Regularly Interspaced Short Palindromic Repeats) could detect specific genetic sequences and offer potential advantages in

terms of simplicity, cost-effectiveness, and speed, which are being explored for rapid and portable testing[20–22].

Proteins play a crucial role in various diseases, and their detection can provide valuable diagnostic information. Advances in genomics[23], proteomics[24], and metabolomics[25] have enabled researchers to identify a wide range of potential biomarkers associated with various diseases[26]. Enzyme-linked immunosorbent assays (ELISAs)[27–29] are commonly used to detect specific proteins in patient samples. However, newer technologies such as multiplex immunoassays[30] and microarray-based assays[31] enable the simultaneous analysis of multiple proteins in a single test, providing more comprehensive diagnostic information. Additionally, advancements in microfluidics[32] and lab-on-a-chip technologies[33] have led to the development of portable and cost-effective protein detection platforms.

1.1.3. Point-of-care diagnostics

Point-of-care (POC) diagnostics refers to medical tests, assessments, and diagnoses performed at or near the site where the patient is being treated, rather than sending samples to a centralized laboratory for analysis. This approach offers several important benefits that make it a crucial aspect of modern healthcare. These include rapid results (within minutes to hours)[34], early detection and timely treatment decisions (i.e. for cancers[35]), public health benefits (i.e. for infectious diseases of COVID-19[15,36], HIV[37]), better accessibility (i.e. particularly valuable in remote and resource-limited areas[38]), improved patient management (i.e. regular testing and monitoring for chronic diseases[39]), cost-effectiveness, personalized medicine, and minimized patient stress and anxiety.

Currently, POC diagnostics are widely used in infectious disease testing[40] (such as influenza[41], COVID-19[42], HIV[43], tuberculosis[2], hepatitis[44] and sexually transmitted infections[45]), in emergency medicine (e.g., rapid determination of cardiac markers such as troponin, diagnosis of heart attacks,[46] blood gas analysis to assess the patient's oxygen supply and acid-base status[47]), in the monitoring and treatment of chronic disease (such as diabetes[48], cardiovascular disease through the monitoring of cholesterol[49] and C-reactive protein (CRP) levels[50]), in cancer screening (detecting specific tumor markers)[34], in hematology (e.g., blood counts and coagulation tests to

assess blood disorders[51]), in allergy[52] and immunology (e.g., skin prick test and immunoglobulin levels measurement for the diagnosis and management of autoimmune and immunodeficiency disorders), and in home testing and monitoring[53] (such as pregnancy testing, blood pressure and blood sugar monitoring) **(Figure 1.1)**[54].

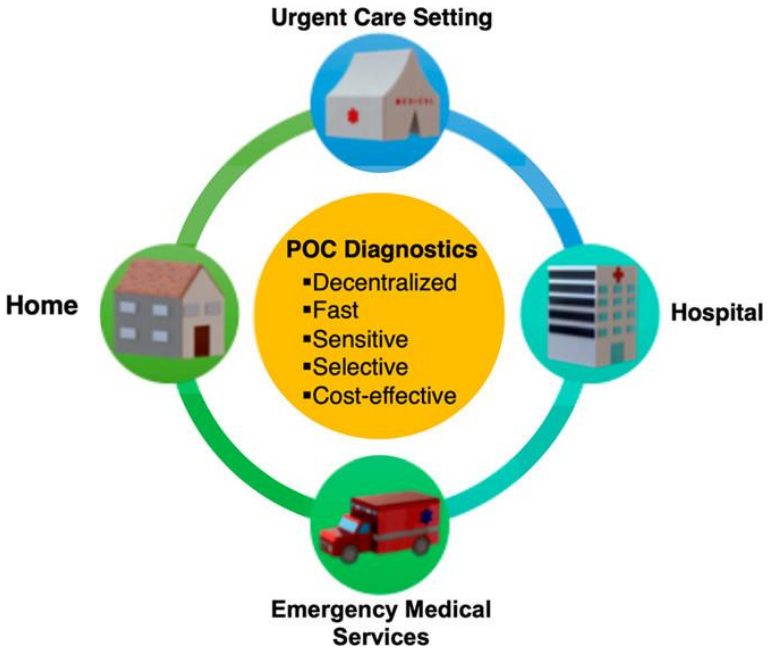

Figure 1.1. Schematic illustration of the applications of point-of-care diagnostics. Adapted with permission from ref. 54 and copyright 2021 American Chemical Society.

POC devices are designed to provide rapid and accurate diagnostic information at the point of care, allowing healthcare professionals to make quick decisions for patient management. Commercialized POC devices play a crucial role in various healthcare settings, including hospitals, clinics, and even home care. There are several representative and commercialized POC devices across various medical fields, including glucose meters (e.g., OneTouch, Accu-Chek, and FreeStyle), pregnancy tests (e.g., Clearblue and First Response), cardiac markers diagnostics (e.g., i-STAT for Troponin tests), hematology analyzers (e.g., HemoCue Hb 201+ and i-STAT), infectious disease tests (e.g., ID NOW Influenza, OraQuick HIV test and BinaxNOW COVID-19 Antigen Test), coagulation monitors (e.g., CoaguChek), hemoglobin A1c analyzers (e.g., DCA Vantage), cholesterol monitors (e.g., CardioChek), urinalysis strips (e.g., Siemens Multistix and ACON Urinalysis Reagent Strips), digital thermometers (e.g., Braun and Omron), and blood gas analyzer (e.g., GEM Premier and ABL90 FLEX).

Although POC diagnostics offers several advantages in terms of speed, accessibility, and early intervention, it also presents challenges in terms of accuracy, quality control, and regulatory considerations. Nanomaterials[55], lateral flow assays[56], microfluidics[57], miniaturized molecular testing devices[58], lab-on-a-chip systems[40] and smartphone[59], are currently being developed to enhance POC diagnostics. Advances in nanotechnology have led to the development of various nanomaterials[60], such as nanoparticles[61], nanowires[62], and nanotubes[63], which can be used in biosensors for sensitive and rapid detection. These nanomaterials can enhance signal generation, improve sensitivity, and enable multiplexed detection, contributing to cost-efficient diagnostic tests[64].

Furthermore, rather than relying on a single biomarker, diagnostic tests able to detect a panels of multiple biomarkers, can improve sensitivity and specificity[65], enhancing the accuracy of disease diagnosis and risk assessment[66]. Artificial Intelligence (AI)[67,68] and Machine Learning (ML) algorithms[69,70] can be helpful to analyze complex datasets from biomarker studies. These algorithms can identify patterns, classify disease states, and predict treatment outcomes based on biomarker profiles. Integrating AI and ML into diagnostic tests can further enhance accuracy, speed, and cost-effectiveness, enabling more efficient and reliable diagnostics[71]. Currently, AI-based diagnostic tools are being developed for a wide range of diseases, including cancer[72], neurological disorders[73], and infectious diseases[74].

Overall, the discovery of novel diagnostic biomarkers, coupled with technological innovations, holds great promise for the development of rapid and cost-efficient diagnostic tests. These advancements have the potential to revolutionize healthcare by enabling early detection, personalized treatment selection, and improved patient outcomes.

1.2. Gold nanomaterials-based optical biosensors for POC diagnostics

Gold nanomaterials (AuNMs) refer to structures or particles made of gold that have at least one dimension in the nanoscale range, typically ranging from 1 to 100 nanometers. These materials exhibit unique physical, chemical, and optical properties due to their small size and high surface-to-volume ratio. AuNMs are widely employed in optical biosensors for POC diagnostics[75] due to several key advantages, including surface plasmon resonance (SPR) properties, good

biocompatibility and stability, ease of synthesis, functionalization, conjugation and labelling, tunability of size and shape, rapid signal generation, ease of miniaturization and integration with optical device, and cost-efficient production. AuNMs can be categorized based on their shapes, structures, and dimensions. Here are some common types of gold nanomaterials used in medicine and diagnostics.

Spherical gold nanoparticles (AuNPs)[76,77] are among the most widely studied and utilized nanomaterials. They can range in size from a few to hundreds of nanometers in diameter. Their optical properties, particularly surface plasmon resonance, make them useful in various applications, including diagnostics, imaging, and drug delivery **(Figure 1.2A)**. Gold nanorods (AuNRs)[78], elongated nanoparticles with a rod-like shape, exhibits unique optical properties, and their absorption and scattering characteristics can be tuned by adjusting their aspect ratio. This tunability is widely exploited in applications such as biosensing **(Figure 1.2B)**. Gold nanobipyramids (Au NBPs) have two distinct pyramid-shaped ends connected by a central axis, exhibiting anisotropic properties due to their distinctive bipyramidal shape. This anisotropy can result in enhanced electromagnetic fields at the tips of the bipyramids, which is advantageous for certain applications, such as surface-enhanced Raman scattering (SERs)[79] **(Figure 1.2C)**. The plasmonic properties of Au NBPs can be tuned based on their size and aspect ratio, making them useful for applications in sensing, imaging, and photothermal therapy[80]. Gold nanostars (AuNSs)[81] have multiple branches radiating from a central core, resembling a star. The branches of gold nanostars contribute to enhanced surface plasmon resonance **(Figure 1.2D)**. Gold nanoflowers (AuNFs)[82] with a flower-like morphology at the nanoscale, are characterized by multiple branches or petals radiating from a central core. The branched structure of AuNFs results in a high surface area, contribute to enhanced plasmonic properties, and provides numerous sites for functionalization with various molecules, such as targeting ligands or biomolecules, making them suitable for applications in drug delivery[83] and diagnostics[82] **(Figure 1.2E)**. In addition, the high surface area and unique morphology of AuNFs make them promising candidates for catalytic applications. Gold nanoclusters (AuNCs) are ultra-small assemblies of a few to several gold atoms. Due to their discrete electronic states, AuNCs exhibit unique properties. They are employed in catalysis, imaging, and sensing applications[84] **(Figure 1.2F)**.

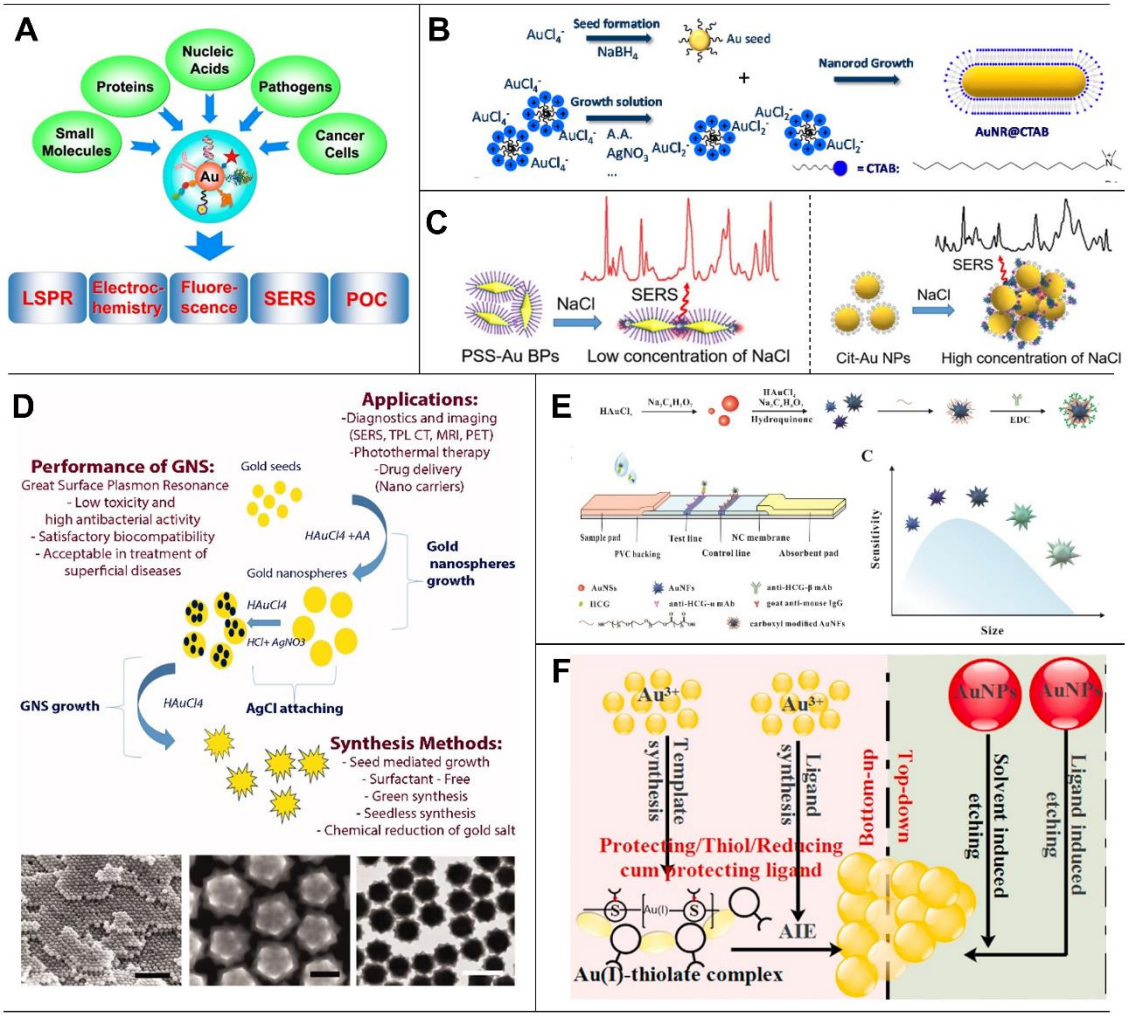

Figure 1.2. Schematic illustration of the synthesis or applications of different types of AuNMs. (A) Schematic presentation of AuNPs-based assays for various targets detection for the IVDs application. (B) Synthesis of AuNRs from crystal seed using the seed-mediated growth method. (C) Schematic illustration of the solution-based SERS detection protocol and the influence of NaCl as aggregating agent on SERS enhancement due to different aggregation states of (left) PSS-Au NBPs and (right) Cit-AuNPs. (D) Synthesis methods, properties and applications of AuNSs. (E) Schematic of lateral flow strips based on AuNFs with different sizes for human chorionic gonadotropin detection. (F) Synthesis of AuNCs according to Bottom-up and Top-dow methods. Adapted with permission from ref. 76 (A), 78 (B), 79 (C), 81 (D), 82 (E) and 84 (F). Copyright 2015 American Chemical Society (A), 2020 MDPI (B), 2022 American Chemical Society (C), 2020 Taylor & Francis Online (D), 2019 Elsevier (E) and 2023 Elsevier (F).

1.2.1. AuNPs aggregation-based assays

Gold nanoparticles aggregation refers to the phenomenon where individual AuNP come together

to form larger clusters or aggregates. The color of the dispersed AuNPs is due to their SPR, which is typically red. When nanoparticles aggregate, the SPR shifts, leading to changes in color (e.g., from red to blue). This aggregation can be induced by electrostatic interaction (e.g., changes of pH or the presence of ions), ligand-receptor binding (e.g., antibody-antigen and aptamer-target specific binding), enzyme-substrate interaction (enzymatic reaction producing a product or byproduct that induces AuNP aggregation), and changes of temperature and environment. Aggregation-based biosensors that utilize AuNPs have gained significant attention due to their sensitivity, simplicity, and versatility in various bioanalytical applications. The mechanisms of AuNPs aggregation-based biosensors involve the controlled assembly or disassembly of AuNPs in response to specific target molecules[85]. In the AuNPs aggregation-based assays, AuNPs could be functionalized or non-functionalized with a recognition element (i.e., antibodies, aptamers, DNAs, RNAs, PNAs, etc.).

Antibodies were mostly used to conjugate with AuNPs for specific recognition of target molecules. Ventura B. et al.[86] developed a reliable, fast and cheap colorimetric biosensor based on AuNPs interaction with SARS-CoV-2 cell for detecting viral particles in nasal and throat swabs. The AuNPs were functionalized with three antibodies targeting spike, envelope and membrane protein of SARS-CoV-2, respectively. The spectrum of AuNPs-antibody conjugates is red-shifted in presence of SARS-CoV-2 viral particles and the optical density at 560 nm was measured for quantitative detection. This approach could be particularly useful in microbiology for detecting the bacteria particles **(Figure 1.3A)**. Park Y. et al.[87] reported an ultrasensitive (sub-fM), rapid and simple “mix-and-read” plasmonic colorimetric assay for the detection of large-size (~180 KDa) proteins using an ultralow-noise multilayer molybdenum disulfide (MoS_2) photoconducting channel. The multilayer MoS_2 operated under near-infrared illumination, enables the detection of a subtle plasmonic extinction shift caused by by antigen-induced nanoprobe aggregation. After mixing a biofluid sample (such as whole blood, urine, and saliva) with antibody-modified AuNPs, analyte-induced AuNP aggregation leads to the formation of an antibody-protein-nanoparticle complex. The authors showed the quantitative detection of carcinoembryonic antigen (CEA) in unprocessed whole blood with a dynamic range of 10^6 in 10 mins and a LOD of 0.1-3 pg/mL, ~100-fold more sensitive than the clinical-standard ELISA **(Figure 1.3B)**.

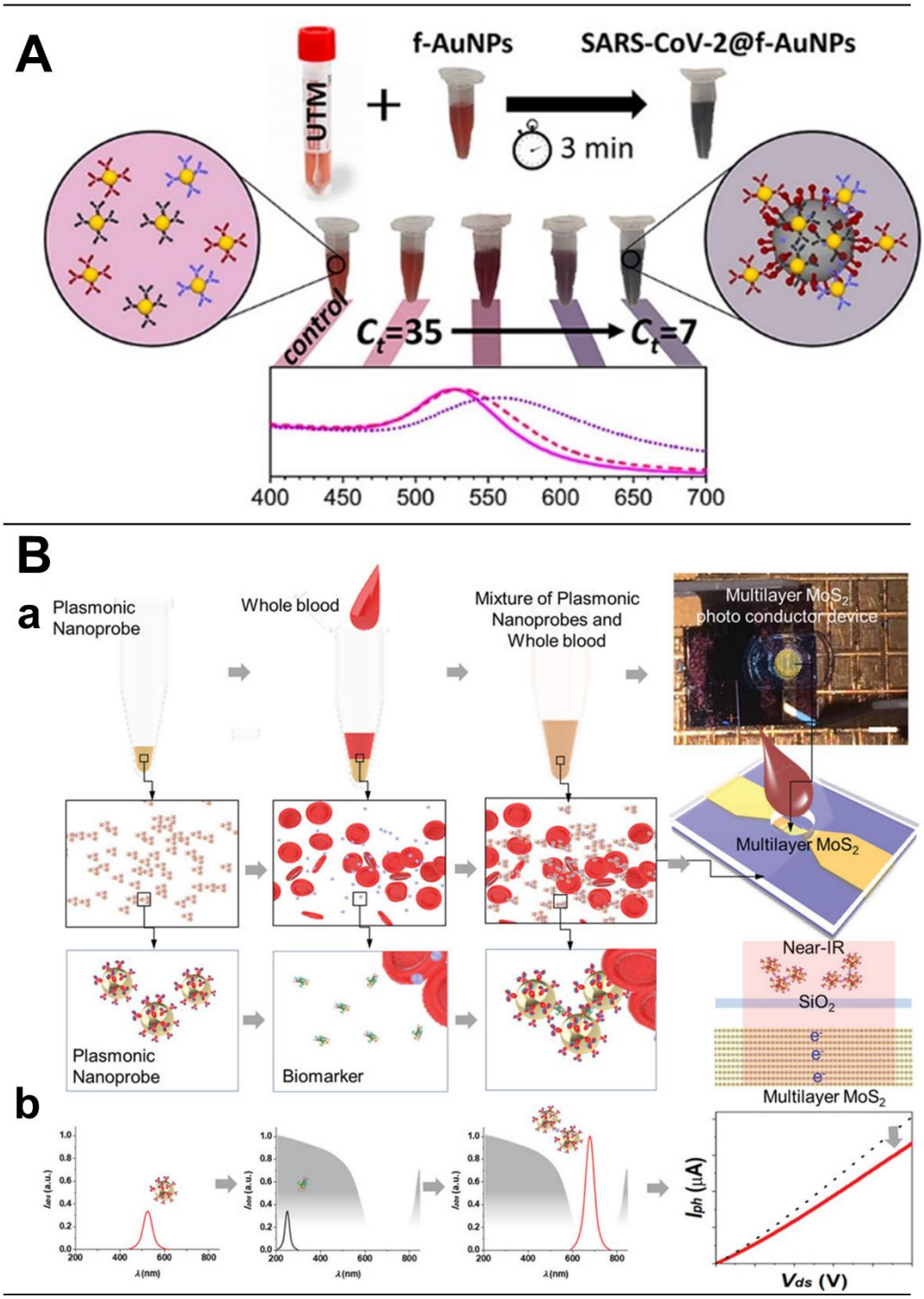

Figure 1.3. AuNPs (labeled with antibodies) aggregation-based assay for POC diagnostics. (A) Schematic illustration of the reliable, fast and cheap colorimetric biosensor based on antibodies conjugated AuNPs interaction with SARS-CoV-2 cell for detecting viral particles in nasal and throat swabs. (B) Concept of multilayer MoS_2 photoconductivity-enabled NIR "mix-and-read" plasmonic colorimetric assay for cancer biomarker detection. (a) Mixing of antibody-conjugated AuNPs (AuNPs-Ab) and whole blood (WB). (b)

Extinction spectrum of AuNPs-Ab (left), blood constituents (center), and aggregated/assembled AuNPs-Ab (right). Adapted with permission from ref. 86 (A) and 87 (B). Copyright 2020 American Chemical Society (A) and 2021 John Wiley & Sons (B).

Aptamers have been widely employed as recognition element to develop sensor for a wide range of target[88–90]. Aptamers are short, single-stranded nucleic acid sequences (DNA or RNA) that can be chemically synthesized with high reproducibility and purity by using the systematic evolution of ligands by exponential enrichment (SELEX) assay and that can specifically bind to target molecules with high affinity and selectivity. Aptamers offer several advantages over antibodies, including ease of synthesis and modification, small size and excellent stability, low batch-to-batch variability, low cost, and reduced immunogenicity.

Aptamers can be adsorbed on the AuNPs surface, protecting AuNPs from aggregation in high-salt solution. In the presence of the target, aptamers bind with target and as results they are detached from the surface of AuNPs, inducing aggregation of AuNPs with a visible color change from red to purple/blue andthis color change can be exploited for the target detection. As example, Moabelo K. et al.[91] developed a rapid AuNPs-based aptasensor for the detection of retinol-binding protein 4 (RBP4), a potential biomarker for early diagnosis of Type 2 diabetes (T2DM). The assay was finished within 5 min with a LOD of 90.76 ± 2.81 nM **(Figure 1.4A)**. Wen L. et al.[92], instead, developed a rapid and visible colorimetric aptasensor based on sodium chloride-induced aggregation of AuNPs for detection of clusterin, a potential biomarker for multiple disease. The biosensor showed a linear range of 0.02-2 ng/mL with a LOD of 5.37 pg/mL. The detection results of clusterin in spiked human serum showed an acceptable recovery.

Peptide nucleic acids (PNAs) is another class of recognition elements that can be used to develop AuNPs aggregation-based assays. Specifically, PNA for its distinct backbone properties (such as neutrality, high rigidity and peptide composition) induce AuNPs aggregation. Kumar N. et al.[93].used PNA as a bioreceptor and unmodified AuNPs as a reporter to develop a label-free visual assay for detection and quantification of Influenza A Viruses (IAVs). The author shows that in the presence of IAVs RNA target that is complementary to the PNA probe, the formation of a PNA-RNA complex leads to change in color from blue/purple to red. Random sequences, instead, do not have effect on the AuNPs aggregation. The assay could detect IAVs RNA with a limit of

detection of 2.3 ng and the quantification of RNA was achieved by a simple spectrophotometer. Additionally, the assay was validated on 419 avian clinical samples and showed high specificity of 96.46% and sensitivity of 82.41%, comparable with the performance of RT-qPCR. This simple, rapid and universal assay shows the potential for point-of-care diagnostic of viral infections and biomolecules in resource-limited settings **(Figure 1.4B)**.

Other recognition elements could be used. For example, Landa G. et al.[94] reported the use of sialic acid for the detection of pathogenic bacteria. A rapid optical biosensor based on sialic acid-functionalized gold nanoparticles was developed for selective screening of Gram-positive and Gram-negative bacteria in wound bed tissue of chronically infected local wounds, obtaining results consistent with culture methods the result of **(Figure 1.4C)**.

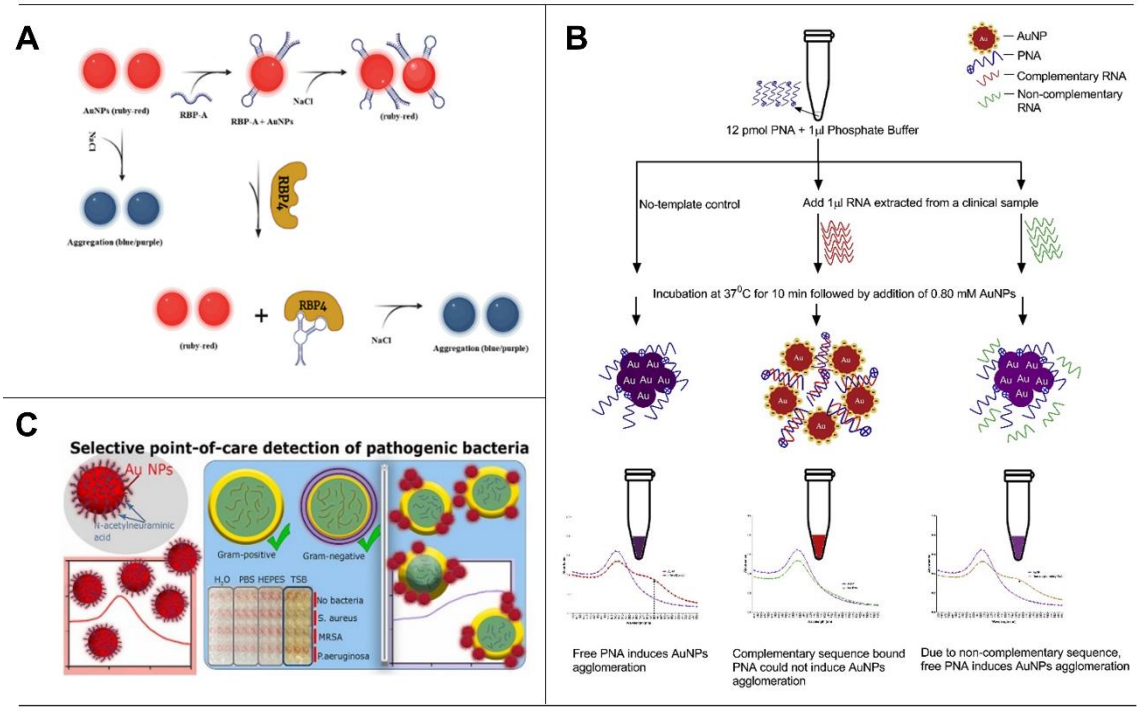

Figure 1.4. AuNPs (labelled with other bioreceptors) aggregation-based assays for POC diagnostics. (A) Schematic illustration of the colorimetric aptasensor for the detection of RBP4. (B) Schematic presentation of the design of the label-free visual assay showing agglomerative behavior of AuNPs in the presence and absence of complementary RNA sequence to peptide nucleic acid (PNA). (C) Schematic presentation of the rapid optical biosensor based on sialic acid functionalized AuNPs for selective screening of Gram-positive and Gram-negative bacteria by choosing the appropriate dispersing media. Adapted with permission from ref. 91 (A), 93 (B), and 94 (C). Copyright 2022 MDPI (A), 2020 Elsevier (B) and 2021

Elsevier (C).

The aggregation of AuNPs as a means of detecting specific targets can also be achieved by using mechanisms that are independent of specific biological receptors such as aptamers, DNA, RNA, PNA, and antibodies. Bastami T. et al.[95] developed an optical nanosensor based on hyrids of AuNPs and phosphomolybdic acid (AuNPs@ PMo_{12}) for accurate and rapid detection of the drug acetaminophen (AP) for clinical POC diagnostics. They used low-frequency sonication (20 kHz) and reducing reagent and stabilizer of PMo_{12} to synthesis spherical AuNPs. The aggregation of AuNPs@ PMo_{12} caused by the AP resulted in a red-shift in spectrum of AuNPs@ PMo_{12}. The color change from red to purple was visible to the naked eye. The A_{600}/A_{540nm} values of AuNP@PMo_{12} nanosensor showed a concentration range of AP (1-30 mg/L) and a LOD of 0.42 mg/L. In addition, the results were also recorded using the smartphone and the images were analyzed using eyedropper in Microsoft PowerPoint or RGB model of Image to quantitatively determine the AP concentrations (**Figure 1.5A**). Mo X. et al.[96] reported a new colorimetric nanosensor based on unmodified AuNPs and TMB to detect Fe^{3+} ions using the Tyndall effect (TE). In the presence of Fe^{3+} ions, the TMB was oxidized to positively charged TMB_{ox}, which triggered the aggregation of the negatively charged AuNPs by electrostatic interaction and led to a significant enhancement of the TE. The assay can be completed in 15 mins using only a laser pointer (as a hand-held light source) and a smartphone (as a TE reader). The results show that the platform was able to linearly detect the Fe^{3+} ions in a range from 0.5 to 64 μM with a LOD of ~370 nM, and to detect Fe^{3+} in tap water, commercial drinking water, and human serum with recoveries ranging from 85.96 to 115.52% (**Figure 1.5B**).

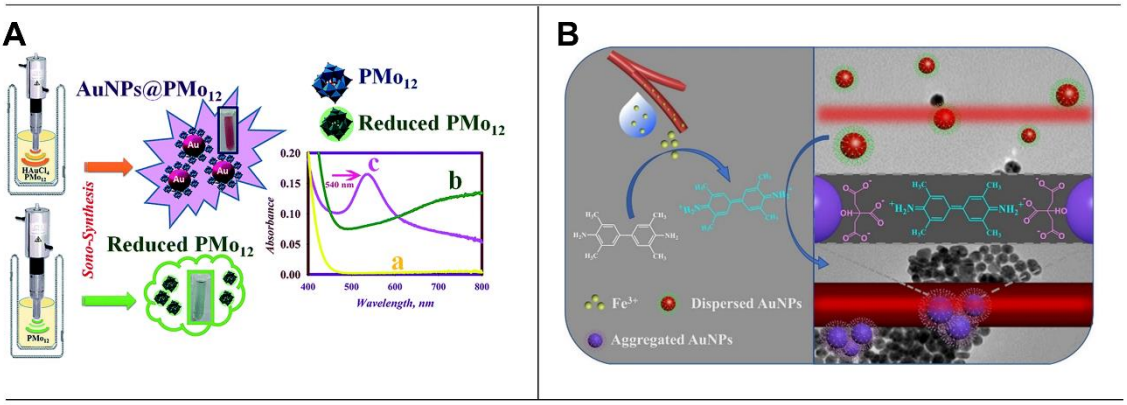

Figure 1.5. AuNPs (non-labeleled with bioreceptors)-based aggregation assay for POC diagnostics. (A) Schematic illustration of the synthetic strategy for AuNPs@PMo_{12} showing the preparation and reduction of PMo_{12} under ultrasonic irradiation ((a) $PMo_{12}O_{40}^{3-}$ solution, (b) reduced $PMo_{12}O_{40}^{4-}$, (c) AuNP@PMo_{12}). (B) Schematic representation of the working principle of the proposed AuNP-based sensor for visual Fe^{3+} detection via TE signaling (red light path). Adapted with permission from ref. 95 (A) and 96 (B). Copyright 2020 Royal Society of Science (A) and Elsevier 2022 (B).

A limitation of these AuNPs aggregation-based assays could be the low sensitivity[97]. However, Signal amplification strategies can be integrated in AuNPs-based colorimetric assay for enhance the sensitivity. With this aim, Wang L. et al.[98] developed a simple colorimetric assay for the detection of miRNA-155 in real serum samples without complex sample pretreatment by combining unmodified AuNPs and magnetic 3D DNA walker, reaching a a LOD of 16.7 fM ,. In the proposed platform, hundreds of substrate strands (DNA tracks) and dozens of DNAzyme strands initially locked by a complementary locking DNA (blocked walking strands) were attached on an Au-Fe_3O_4 nanocomposite, which serves as a 3D magnetic DNA walker. The target was able to activate this DNA walker to liberater the walking strands, which moved along the track via the DNAzyme-induced cleavage reaction, resulting in the release of the leavage fragments (displaced ssDNA). After magnetic separation, the resulting displaced ssDNA in supernatant was incubated with AuNPs to protect the unmodified nanoparticles from aggregation in high-salt solutions. **(Figure 1.6A)**. Lópex-Valls M. et al.[99] presented a CRISPR/CAS-based Colorimetric nucleic Acid DEtection (CASCADE) system based on Cas13a and AuNPs for fast and specific naked-eye detection of SARS-CoV-2 RNA. In this system, the collateral nuclease activity of Cas13a triggered by the presence of target viral RNA lead to the cleavage of ssRNA oligonucleotides conjugated to AuNPs, causing the AuNPs aggregation. CASCADE can detect the SARS-CoV-2 RNA at pM level and it was tested also in clinical samples from nasopharyngeal swabs level. If coupled to RPA or NASBA isothermal nucleic acid amplification the system can reach a sensitivity of 3 fM and 40 aM, respectively. **(Figure 1.6B)**. Alafeef M. et al.[100] reported a RNA-extraction-free nano-amplified colorimetric biosensor, which integrates nucleic acid amplification and plasmonic sensing for visual and POC diagnostics of SARS-CoV-2 within 1 h. In this biosensor, AuNPs are modified with antisense oligonucleotides (ASOs), specific for the SARS-CoV-2 N-gene, and the

binding of the ASO to the target nucleic acid causes the aggregation of AuNPs, leading to a change in the plasmonic response of the AuNPs. When tested in clinical smaples, the accuracy, sensitivity and specificity of the biosensor were >98.4%, >96.6% and 100%, respectively, with a LOD of 10 copies/μL. This biosensor has great versatility and can be easily adapted to diagnose other viral infectious disease with a simple modification of specific ASOs and primer sequences. **(Figure 1.6C)**. Wei S. et al.[101] reported a miRNA detection method based on exponential amplification reaction (EXPAR) and triplex DNA mediated aggregation of AuNPs. Specifically, the system includes two classed of AuNPs, one class of AuNPs functionalized with EXPAR probe with a complementary sequence of the target miRNA, and one conjugated with a single DNA probe. The EXPAR reaction is triggered and duplex DNA is formed on the surface of AuNPs in presence of target miRNA. Then these two classes of AuNPs forms triplex DNA and aggregates, and changes of spectrum could be quantified by UV-vis. The method with highly selectivity achieves a LOD of 0.23 fM. All of reagent could be pre-add to a tube and the whole detection process could be finished within 30 min **(Figure 1.6D)**.

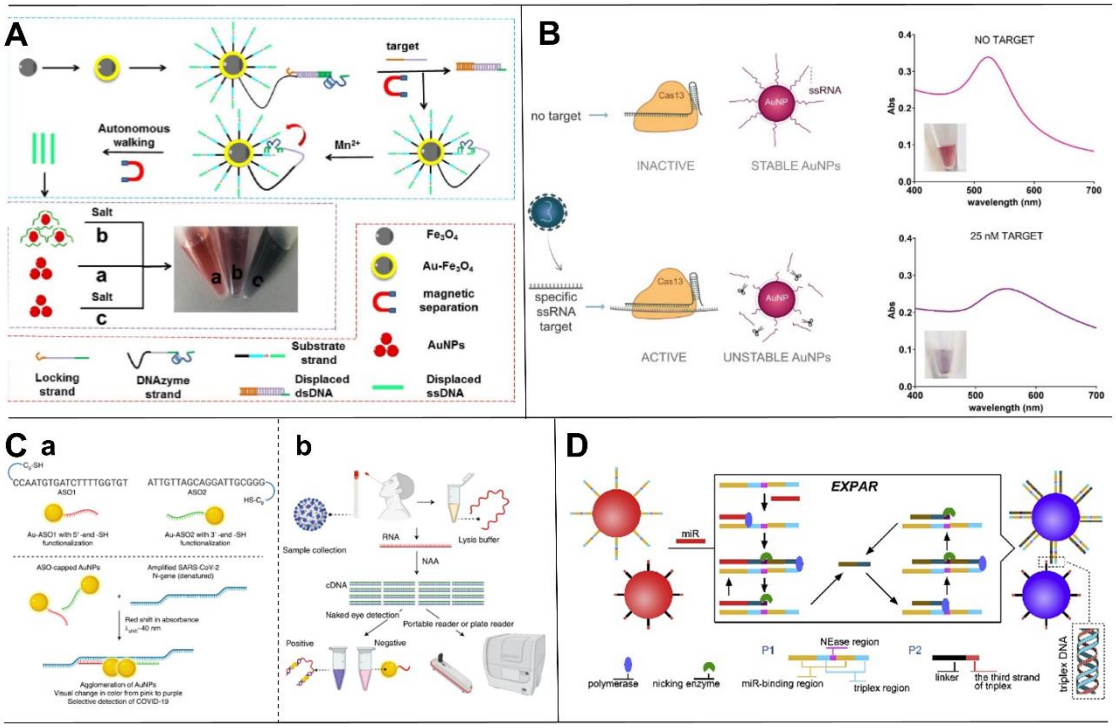

Figure 1.6. Signal amplification strategies of AuNPs aggregation-based assays for POC diagnostics. (A) Schematic illustration of the simple colorimetric assay by combining unmodified AuNPs

and magnetic 3D DNA walker for miRNA-155 detection: (up) magnetic 3D DNA walker amplification and magnetic separation; (middle) AuNPs-based detection by naked-eyes; (below) Materials used in the colorimetric assay. (B) Schematic representation of CRISPR/CAS-based Colorimetric nucleic Acid DEtection (CASCADE) sensing system. (C) Schematic illustration of the RNA-extraction-free nano-amplified colorimetric test (NACT) for POC diagnostics of COVID-19: (a) Schematic representation of the hybridization process of the ASO-capped AuNPs to the complementary target gene sequence to enable colorimetric, naked-eye detection of SARS-CoV-2; (b) The workflow of NACT. (D) Schematic illustration of the miRNA detection method based on exponential amplification reaction (EXPAR) and triplex DNA mediated aggregation of AuNPs. Adapted with permission from ref. 98 (A), 99 (B), 100 (C) and 101 (D). Copyright 2021 Elsevier (A), 2022 Elsevier (B), 2021 Springer Nature (C) and 2020 Elsevier (D).

1.2.2. AuNMs etching/growth-based optical biosensors for POC diagnostics

1.2.2.1. H_2O_2 and TMB^{2+}-mediated etching of AuNMs

The HRP, H_2O_2 and TMB system is widely employed to develop etching AuNPs-based optical biosensors for POC diagnostics. In the system, the enzyme HRP hydrolyses TMB into TMB^{+}, which is oxidized into TMB^{2+} in acid environment. TMB^{2+} acts as an etchant for the AuNPs and leads to their size and shape transformation, resulting in a shift in their plasmonic spectrum and a change in color. Gold nanorods (AuNRs) have gained significant attention in etching-based assays for POC diagnostics. This etching process involves controlled chemical reduction to tailor the nanorods' shape and size, which adjusts the nanorods' aspect ratio and alters the localized surface plasmon resonance (LSPR) peak wavelength, making it suitable for specific detection purposes. Yadav S. et al[102] developed an AuNRs competitive p-ELISA for the detection of human IgG, which showed an ultra-low visual LOD of 1 fg/mL (~6.54 aM), without complex or large equipment, using a strategy that can be easily adopted for biomarkers diagnosis of various diseases **(Figure 1.7A)**. In particular, they showed that AuNRs produced a higher change in spectral shift and absorbance intensity compared to other shapes (i.e., nanotriangles (AuNTs) and nanospheres (AuSs)).

Liu D. et al.[103] have integrated a AuNRs-etching based HRP-linked immunoassay in a single microfluidic chip to develop a multicolor immunosensor for sensitive and reliable semi-quantitative

analysis of HIV-1 p24. In the HRP-linked immunoassay, the magnetic beads coated with capture antibody was used for capturing, separation and enrichment of target from the different aqueous solution containing various immunoassay reagents. HRP-catalyzed TMB^{2+} is used to induce AuNRs etching to producing visible multicolor changes. The fully integrated immunosensor with sample-to-answer capability allows sensitive and reliable semi-quantitative detection of HIV-1 p24 within 1h by naked eye. **(Figure 1.7B)**. Similarly, Ma L. et al.[104] developed an AuNRs etching-based p-ELISA integrated with a paper/poymer hybrid microfluidic devices for POC diagnostics of hepatitis C virus core antigen (HCV antigen), a biomarker of hepatitis C. The integrated system provided fast assays in 50 min, with a LOD of 9.1 ng/μL of HCV antigen.

Other enzymes and nanoparticles that mimic HRP activity can also be used in etching-based assays. Li D. et al.[105] reported a multicolor visual biosensor for POCT of prostate –specific antigen (PSA) using target-induced tripedal G-quadruplex DNAzyme (TGD) and electrospun nanofibrous films decorated with AuNRs. The TGD, including recycling amplification cascades of target-triggered catalytic hairpin assembly (CHA), mimick the enzymatic activity of HRP, in presence of H_2O_2 to oxide TMB into TMB^{+}, which is then converted into TMB^{2+} under acidic condition, triggering the etching of AuNRs for the blue shift of longitudinal LSPR. The strategy showed naked-eye visible multicolor changes of green, cyan, violet and red allowing the semi-quantitative detection with cutoff values near 4.0 and 10.0 ng/mL in human blood and serum. in addition, this strategy could be integrated with a portable and lable-free TDG device to improve the sensitivity of PSA protein to 61.1 fg/mL, indicating great versatility and potential for early disease diagnosis **(Figure 1.7C)**. The peroxidase-like property of AuNRs has been exploited by Wang F. et al.[106] to distinguish native from thermally denatured protein, providing a new chance for studying the conformational information of protein, and also can efficiently differentiate the pure protein from binary protein mixtures in urine samples.

In order to enhance the sensitivity of the etching-based assay, many strategies can be adapted. As example, Zhou J. et al.[107] exploited enzyme-nanozyme cascade reaction to trigger the etching of AuNRs for the ultrafast and ultrasensitive detection of β-galactosidase (β-gal). The proposed platform consists of two main parts, one part of MnO_2 nanosheets as a mimicked oxidase to catalyze the oxidation of TMB to TMB^{2+} in acidic condition, and one part of β-gal to

hydrolyze p-aminophenyl β-d-galactopyranoside (PAPG) to p-aminophenol (PAP), which mediates the reduction of MnO_2 nanosheets, destroying their oxidase-mimicking activity, thus decreasing the amount of TMB^{2+} generated. The whole assay can be completed in 37 min with great rapidity and efficiency. Zhao X. et al[108], instead, exploited hybridization chain reaction (HCR), magnetic beads (MBs), and oxidized TMB (TMB^{2+})- for detection of Dengue nucleic acid. In this approach, the HCR was applied for amplifying the nucleic acid signal and MBs for separation and enrichment of target from the reaction solution. With this approach, the authors were able to detect Dengue sequence in 40 min with a LOD of 1.25 nM and excellent selectivity for distinguishing single-base mutation **(Figure 1.7D)**.

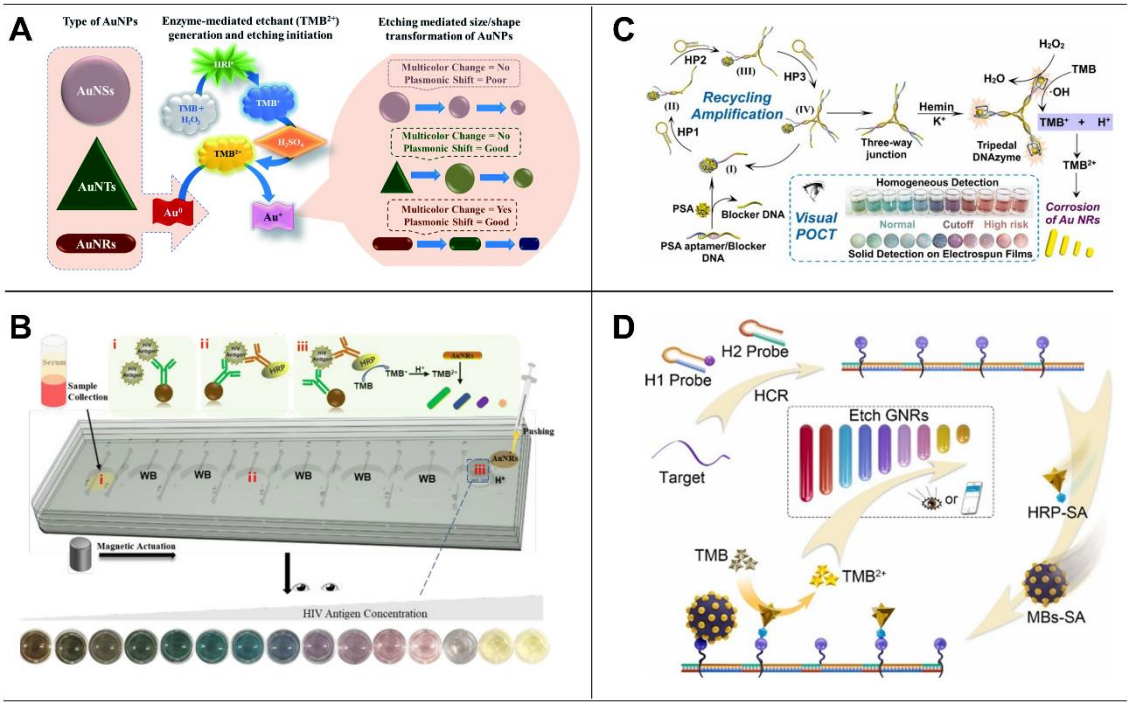

Figure 1.7. H_2O_2 and TMB^{2+}-mediated etching of AuNPs. (A) Schematic illustration of etching-based plasmonic ELISA (p-ELISA) strategy developed by employing gold nanospheres (AuNSs), gold nanorods (AuNRs), and gold nanotriangles (AuNTs). (B) Working principle of the microfluidic-integrated multicolor immunosensor for POCT of HIV-1 p24 antigen by the naked eye using HRP-linked immunoassay assisted by magnetic actuation and TMB^{2+}-mediated etching of AuNRs. (C) Schematic illustration of the target-triggered tripedal G-quadruplex DNAzyme (TGD) for the visually point-of-care testing of PSA biomarker by using Au NRs-decorated electrospun nanofibrous films. (D) Schematic illustration of smartphone-assisted POCT of nucleic acids based on hybridization chain reaction (HCR), magnetic beads (MBs), and TMB^{2+}-

mediated etching of gold nanorods. Adapted with permission from ref. 102 (A), 103 (B), 105 (C) and 108 (D). Copyright 2022 Royal Society of Chemistry (A), 2020 American Chemical Society (B), 2021 Elsevier (C) and 2023 Elsevier (D).

In addition of AuNRs, gold nanobipyramids (Au NBPs)[109,110] are nanostructures made of gold and have a bipyramid shape, meaning they have two pyramid-like ends. The unique structure and shape of the Au NBPs provides an enhanced LSPR effect compared to traditional spherical AuNPs, which makes them promising candidates for POC diagnostics. Yu L. et al.[111] fabricated a multicolored visible immunosensor for POCT neurotrophic tropomyosin receptor kinase (NTRK) gene fusion, a biomarker of tumor and multiple cancers. The HRP-TMB immunobiosensor combined with Au NBPs, which were etched by TMB^{2+}, produced multicolor in different concentration of NTRK gene, achieving qualitative and semi-quantitative analysis within 20 min by naked eye, with a relevant linear range from 7.7 pg/mL to 240 pg/mL **(Figure 1.8)**.

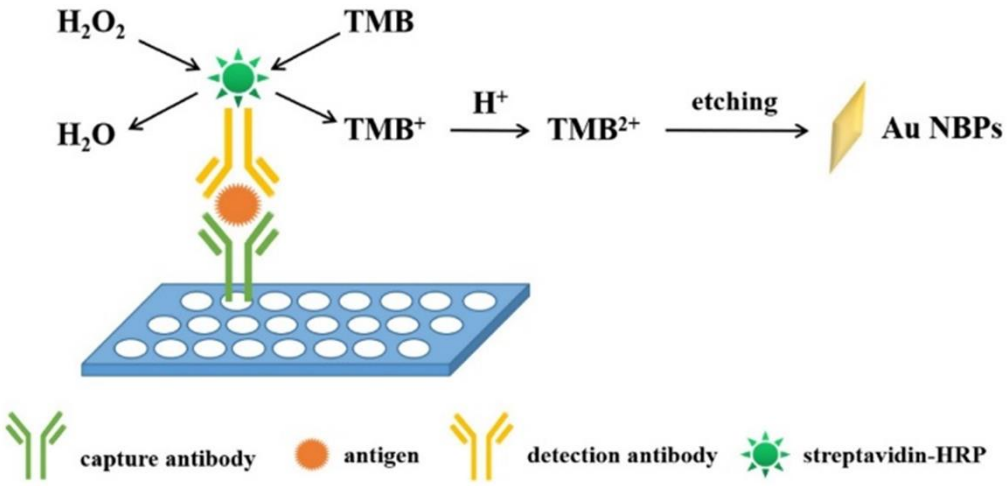

Figure 1.8. Schematic illustration of the principle of the multicolor immunosensor for point-of-care testing NTRK1 gene fusion using HRP-linked immunoassay and TMB^{2+}-mediated etching of gold nanobipyramids (Au NBPs). Adapted with permission from ref. 111 and copyright 2021 Elsevier.

1.2.2.2. H_2O_2 and iodide ions-mediated etching of AuNMs

Recently, various etching assays mediated by iodine ions[112,113] have been proposed, as iodine ions as etchant have several advantages over TMB^{2+}, including milder etching conditions (e.g. no need for HRP enzyme), faster etching kinetics, better stability and lower toxicity. Zhang X. et al.[112]

reported a simple, convenient, highly sensitive and noninvasive colorimetric assay based on gold bipyramids (GBPs) for detection of glucose in urine samples. In this approach, glucose oxidase is used to catalyze the glucose to generate H_2O_2, with the help of iodide ions to etch GBPs, resulting in the shift of the absorption peak of GBPs for quantitative detection of glucose. This colorimetric assay with optimal optimized condition shows a dynamic range of 0.5-250 μM and a LOD of 3.4 μM in artificial urine samples. The high sensitivity is attributed to the unique sharp tips morphology and the etching from tips of GBPs. Moreover, the multicolor changes of GBPs can be easily distinguished by naked eyes for semi-quantitative analysis of glucose. Furthermore, in this assay, the iodide ion was used as mimicked HRP to reduce H_2O_2 and as etchant of GBPs, without HRP enzymes, simplifying the reaction and reducing costs **(Figure 1.9A)**.

The iodine mediated-etching assays have also been integrated with paper-based devices for rapid, real-time and on-site POC diagnostics[114–116]. For example, Pomili T. et al.[114] developed a fully integrated paper-based multiplexed colorimetric device for the simple, convenient and non-invasive detection of three prognostic biomarkers in saliva samples. The device includes a central sample zone and three individual arms, each containing a pre-treatment and a test zone, all cut with a CO_2 laser with remarkable parallelization and speed. The device uses cholesterol oxidase (ChOx), glucose oxidase (GOx) and lactate oxidase (LOx) to catalyze the corresponding target and to generate H_2O_2. The iodide ions, acting as catalyst, trigger the target-induced reshaping of the plasmonic multi-branched AuNPs to produce a color change from blue to pink and a significant spectral shift which can be detected by the naked eye and smartphone. The entire test can be completed within 10 min. Moreover, a prototype kit for POCT was developed, showing the great robustness and ease of use of this test **(Figure1.9B)**.

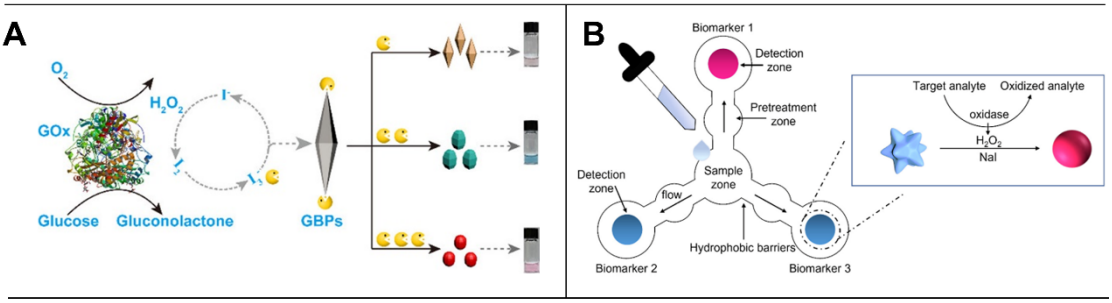

Figure 1.9. H_2O_2 and iodide ions-mediated etching of AuNMs. (A) Schematic illustration of the

colorimetric assay for sensitive visual readout of the glucose content based on GOx catalytic activity and the iodide-promoted etching of gold bipyramids (GBPs). ((B) Schematic illustration of the monolithic paper-based device for the simultaneous detection of three salivary biomarkers. Adapted with permission from ref. 112 (A) and 114 (B). Copyright 2020 American Chemical Society (A) and 2021 MDPI (B).

1.2.2.3. Other ions-mediated etching of AuNMs

In addition to the commonly used etchants, such as TMB^{2+} and iodine ions, some other chemical reagents (e.g. ascorbic acid, superoxide radicals and $HAuCl_4$)[116–118] are also employed as etchants for developing AuNPs etching-based assays for POC diagnostics. Zhang Y. et al.[117] proposed a highly sensitive plasmonic colorimetric biosensor for the quantification of exosomes using an exosome-triggered competitive assay and ascorbic acid (AA)-mediated etching of gold nanobipyramid@MnO_2 nanosheet nanostructures (Au NBP@MnO_2 NSs). In the competitive reaction, the hybridization complex of a sort of ubiquitous tetraspanins enriched on the surface of exosomes of CD63 aptamer, placeholder chain 1 and 2 labeled with ALP (P1-ALP and P2-ALP) were conjugated onto magnetic beads. In presence of CD63 exosome, the combination of CD63 and CD63 aptamer leads to the release of P1-ALP, and P2-ALP, both of which catalyzed the dephosphorylation of AAP to produce AA. The produced AA reduced the MnO_2 nanosheets to generate Mn^{2+}, resulting in a morphological change of Au NBP@MnO_2 NSs and a blue-shift of the LSPR band of Au NBPs, leading to a color change of Au NBPs. Due to the ALP-triggered signal amplification and superior plasmonic properties of Au NBPs, this assay shows high sensitivity to exosomes from 8.5×10^2 to 8.5×10^4 particles /μL, along with a LOD of 1.35×10^2 particles/μL, which is more sensitive than previously reported colorimetric methods. Moreover, a sensitive visual multicolor detection was realized by adjusting the aspect ratio of the Au NBPs **(Figure 1.10A)**.

Yi J. et al.[116] used core-shell Au@Ag nanostars (Au@Ag NSs) to develop an agarose-based plasmonic test strip for the detection of antioxidants based on $HAuCl^{4-}$ induced etching and the antioxidant anti-etching of the Ag shell of Au@Ag NSs. In this sensor, the antioxidants are able to react with HAuCl4, which prevents $HAuCl_4$-induced etching of the Ag shell of Au@Ag NSs. The anti-etching effect of the antioxidants modulate the Ag shell of Au@Ag NSs, inducing a significant change in the SPR spectrum (quantified by smartphone) and the color of the solution (visible to

naked-eye). The sensor detects antioxidants such as cysteine and gallic acid with a linear range of 0.1-10 μM. The Au@Ag NSs can be immobilized in agarose gels to produce plasmonic test strip in 10 min, which can display multicolor changes in a range of 0-1000 μM in the presence of $HAuCl_4$ **(Figure 1.10B)**.

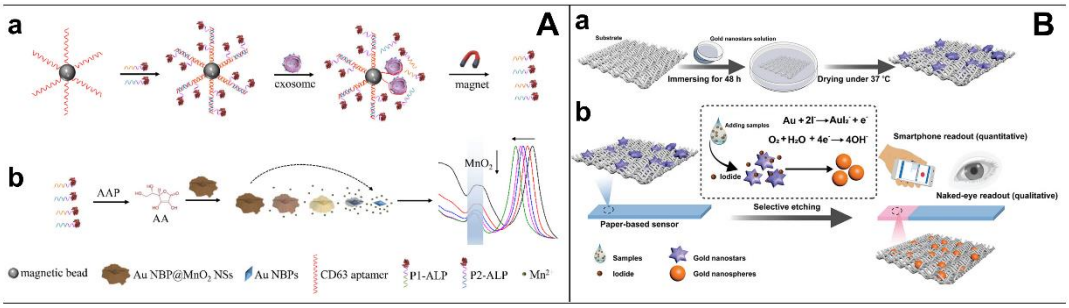

Figure 1.10. Other ions-mediated etching of AuNMs. (A) Schematic illustration of the plasmonic colorimetric for exosome detection via competitive reaction (a) and ascorbic acid mediated-etching of Au NBP@MnO_2 NSs (b). (B) Illustration of the fabrication and detection principle of this paper-based sensor: (a) Gold nanostars are loaded on paper substrate by simply immersing in AuNSs solution. (b) Detection principle and signal readout of the POC paper-based sensor. Adapted with permission from ref. 117 (A) and 116 (B). Copyright 2020 American Chemical Society (A) and 2023 American Chemical Society (B).

1.2.2.4. In situ formation of AuNMs

The *in situ* formation of gold nanomaterials involves the synthesis or creation of AuNMs directly within a system or environment of interest, without pre-synthesizing and subsequently introducing the nanoparticles. Some common methods for the *in situ* formation of AuNMs are used, including chemical reduction, biological synthesis (green synthesis), photochemical reduction, electrochemical synthesis, and thermal reduction. The choice of method depends on the specific requirements of the application, such as the desired size, shape, and stability of AuNMs. *In situ* formation offers advantages in terms of simplicity, control over the reaction conditions, and the ability to integrate nanoparticle synthesis directly into various systems and environments. The *in situ* formation of AuNPs has attracted considerable attention for POC diagnostics in recent years[119–122]. The ability to synthesize AuNPs directly at the site of analysis offers several advantages, including simplified assay procedures, enhanced sensitivity, and reduced risk of contamination. Zhou J. et al.[119] reported a colorimetric assay based on multiple hybridization chain

reactions (HCR) on AuNPs for signal amplification and alkaline phosphatase (ALP)-mediated *in situ* growth of Au NBPs for the ultrasensitive detection of the *mecA gene of Staphylococcus aureus*. In this assay, the target DNA is hybridized with biotin-labeled hairpin DNA modified on magnetic beads (MB) and then amplified on AuNPs by multiple HCRs. The biotin and streptavidin-based reaction together with the large specific surface area of AuNP leads to a large amount of ALP on AuNP. The ALP-mediated in situ growth of AuNBPs results in a series of rainbow-like colors related to the different concentrations of target DNA. The results of this assay show a LOD of 2.71 pM of target DNA with high specificity. Moreover, the authors were able to successfully detect the *mecA gene* extracted from *S. aureus*, indicating the potential of this method for clinical diagnosis **(Figure 1.11A)**.

Sivakumar R. et al.[122] presented the ultraviolet-induced *in situ* formation of AuNPs coupled with loop-mediated isothermal amplification (LAMP) for POC diagnostics of two infectious agents, such as SARS-CoV-2. Au^{3+} ions were reduced by the reducing agent trisodium citrate and red-colored AuNPs were produced upon UV illumination in the presence of LAMP amplicons. The nitrogenous bases of the target DNA serve as a physical carrier for the capture of Au^{3+} ions. The high affinity of Au with the nitrogenous bases enabled rapid detection within 10 mins with a LOD of SARS-CoV-2 plasmid of 42 fg/µL. Furthermore, the assay was integrated into a portable device containing reagent chambers (dried colorimetric reagents such as $HAuCl_4$ and Na_3Ct) and detection champers (presented LAMP amplicons), allowing convenient sample delivery and multiplexing detection. This fabricated portable device could serve as a kit for instantaneous POCT of infectious disease **(Figure 1.11B)**.

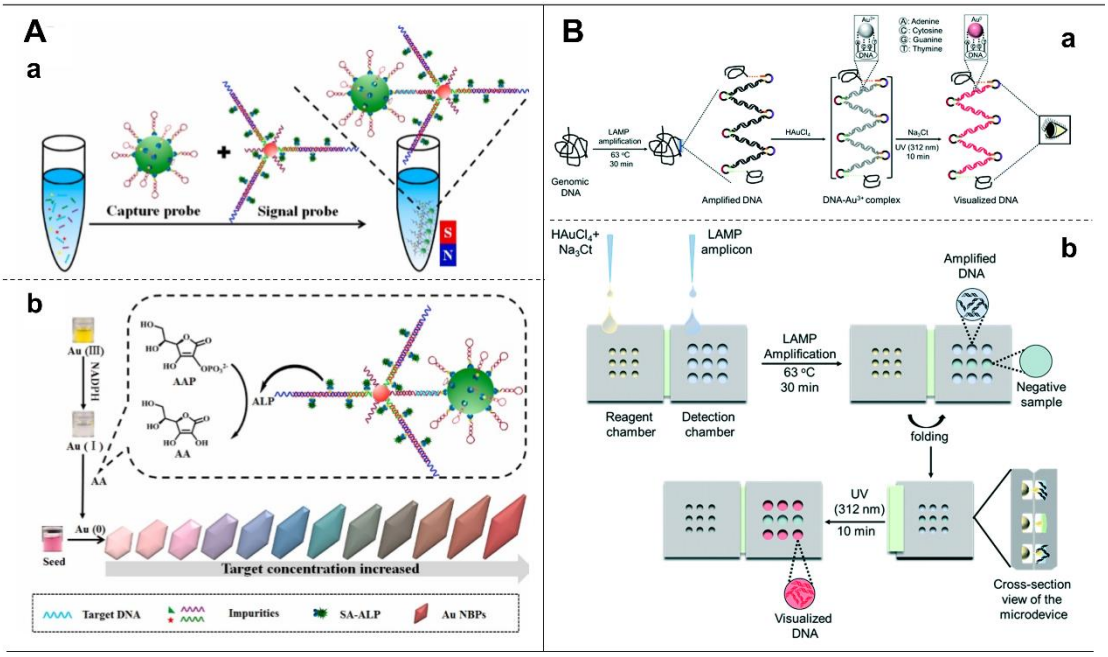

Figure 1.11. *In situ* formation of AuNMs. (A) Schematic illustration of the principle of the multicolor colorimetric DNA biosensor for visual determination of target DNA: (a) the hybridization process of capture probe, target DNA and signal probe; (b) the signal producing process by using NADPH-assisted ALP-mediated in situ growth of Au NBPs. (B) Schematic presentation of the ultraviolet-induced in situ formation of AuNPs coupled with loop-mediated isothermal amplification (LAMP) for POC diagnostic of infectious pathogens: (a) Scheme of DNA detection process using in situ formation of AuNPs and LAMP; (b) Scheme of the procedure of the portable device for visual detection of LAMP amplicons. Adapted with permission from ref. 119 (A) and 122 (B). Copyright 2021 Elsevier (A) and 2021 Royal Society of Science (B).

1.2.3. AuNMs and IFE/MEF/FRET-based optical biosensors for POC diagnostics

1.2.3.1. Inner filter effect (IFE) between AuNPs and fluorophores

Inner filter effect (IFE) was normally considered a negative effect that should be avoided in fluorescent measurements[123]. Recently, however, IFE between absorber and fluorescent emitter has been widely used to develop biosensors. To use this optical effect, the absorption spectrum of the absorber must overlap with the emission spectrum of the fluorophore[123]. Compared to the most used FRET, IFE is quite easy and does not require a complex design. Most IFE-based fluorescent biosensors rely on target-induced aggregation or dispersion of AuNPs, which leads to the significant reduction or increase of IFE between AuNPs and fluorescent dyes. There are

several commonly used fluorophores in the IFE-based fluorescent biosensor, including organic dyes, carbon dots (CDs), quantum dots (QDs) and gold nanoclusters (AuNCs).

Organic dyes[124,125] are commonly used as fluorescent labels because they offer several advantages, including strong fluorescence emission (high quantum yield), spectral diversity, low cost, biocompatibility, and compatibility with various assay formats (e.g., lateral flow assays, microarrays, and microfluidic devices). Liu D.[125] et al. proposed a "turn-on" fluorescence system based on IFE between 7-hyfrixycoumarin (emission peak at 458 nm) as fluorescent molecule and Rutin-AuNPs (absorption peak at 528 nm) as absorber and quencher for the detection of the antibiotic etimicin. In this system, rutin-AuNPs can efficiently absorb and quench the fluorescence of 7-hydroxycoumarin in the absence of target. In the presence of the target, instead, due to strong binding of etimicin with AuNPs through electrostatic interaction, 7-hydroxycoumarin is released bringing to the aggregation of AuNPs, resulting in the restoration of fluorescence of 7-hydroxycoumarin. This method showed a LOD of 0.12 μM. The integration of this system into smartphone enables rapid quantitative detection and application for POCT **(Figure 1.12A)**. Despite their advantages, organic dyes also have some limitations including a tendency to photobleach, potential of false negatives or positives due to endogenous fluorophores leading to background interference, a relatively low signal-to-noise ratio compared to inorganic nanomaterials. Among inorganic nanomaterials, carbon dots[126,127] are an attractive choice thanks to their unique combination of strong fluorescence properties, biocompatibility, ease of functionalization, stability, and cost effectiveness. Le T. et al.[127] developed a "turn-on"fluorescent sensor based on IFE between nitrogen and phosphorus co-doped carbon dots (NPCDs) as fluorescent donors and AuNPs as fluorescence absorber to detect GSH, which plays an important role in nutrient metabolism, antioxidant defense and regulation of cellular processes. Interestingly, the formation of AuNPs in this system was directly reduced with $HAuCl_4$ salt by NPCDs without additional reducing agents and stabilizers. The closed binding of NPCDs and AuNPs by the rich negative charge and amine groups of NPCD, enhances the IFE and quenching efficiency of fluorescence, resulting in a very low fluorescence background. GSH molecules with multidentate and steric structure show strong binding ability with AuNPs through the sulfhydryl group, resulting in aggregation of AuNPs, which decreases the FE and restores the fluorescence of NPCD. In

addition, the GSH "turn-on" biosensor showed reduced false positive with high specificity and a good sensitivity (i.e., LOD of 0.1 μM in human serum). In addition to the NPCD, Bao Q. et al.[128] reported an "off-on-off" fluorescent nanosensor based on IFE between nitrogen and sulfur doped carbon dots (N,S-CDs) as fluorescent reporters and AuNPs as fluorescent absorber for the ultrasensitive detection of protamine and trypsin. In this assay, the binding of protamine and AuNPs leads to aggregation of AuNPs by electrostatic interaction and Au-N bonds, resulting in the restoration of absorbed fluorescence of N,S-CDs by dispersed AuNPs. In addition, typsin can specifically hydrolyze the arginine of protamine, leading to the release of protamine from AuNPs and the deaggregation and redispersion of AuNPs, thus absorbing the fluorescence of N,S-CDs. This "off-on-off" nanosensor developed under optimal conditions showed a good linear range of 20-260 ng/mL with a LOD of 4.7 ng/mL for protamine, and a range of 10-140 ng/mL with a LOD of 4.3 ng/mL for trypsin. Moreover, this fluorescent nanosensor was also successfully validated in human serum for the detection of protamine and trypsin **(Figure 1.12B)**.

Quantum dots (QDs)[129,130] are nanometer-sized semiconductor nanocrystals that possess unique optical properties, making them excellent candidates for fluorescent labeling in optical biosensor for POC diagnostics. QDs-based optical biosensor show several advantages, including size-tunable emission, strong fluorescence intensity due to high quantum yield, photostability, high sensitivity due to the large stoke shift, multiplexing capabilities due to the broad excitation and narrow emission spectra. Li M. et al.[130] developed a fluorescent aptasensor based on IFE between graphene oxide QDs (GOQDs) as fluorescencer and AuNPs as absorbers for the detection of kanamycin in food samples and clinical specimens. In the presence of kanamycin, the aptamers bound to kanamycin were released from the surface of the AuNPs, leading to the aggregation of the AuNPs in high-salt solution, and thus restoring the fluorescence of the GOQDs. Under optimal conditions, the aptasensor showed a range of 5-600 nM with a LOD of 3.6 nM. In addition, the aptasensor was successfully used in milk, honey and human serum **(Figure 1.12C)**.

Gold nanoclusters[131,132] consist of a few to several tens of gold atoms and exhibit fluorescence properties that differ from those of bulk gold or conventional fluorophores. These include strong and stable fluorescence with high quantum yield, size-tunable emission and multiplexing capability, low toxicity and biocompatibility, small size that allows easy penetration into tissues

and cells, flexibility in conjugation, and enhanced sensitivity. Pezhhan H. et al.[133] presented a simple fluorescence method based on IFE between histidine-capped gold nanoclusters (His-AuNCs) as fluorescencer and H_2O_2-induced magnification of AuNPs as absorbers to detect glucose and H_2O_2. In this system, AuNPs as mimicked glucose oxidase (GOx) catalyze glucose to produce H_2O_2, which reduces $HAuCl_4$ to Au^0 to deposit on the AuNPs core, resulting in enlargement of AuNPs and a change in the absorption spectrum of AuNPs. As the concentration of glucose and H_2O_2 increass, the fluorescence of His-AuNCs by IFE decrease because the absorption spectrum of the enlarged AuNPs and the emission spectrum of His-AuNCs overlap. The assay exhibited a linear range of 5–135 μM with a LOD of 3.6 μM for H_2O_2, and a range of 5–125 μM with a LOD of 3.4 μM for glucose. The method was successfully applied in human urine samples from diabetic patients to detect glucose **(Figure 1.12D)**.

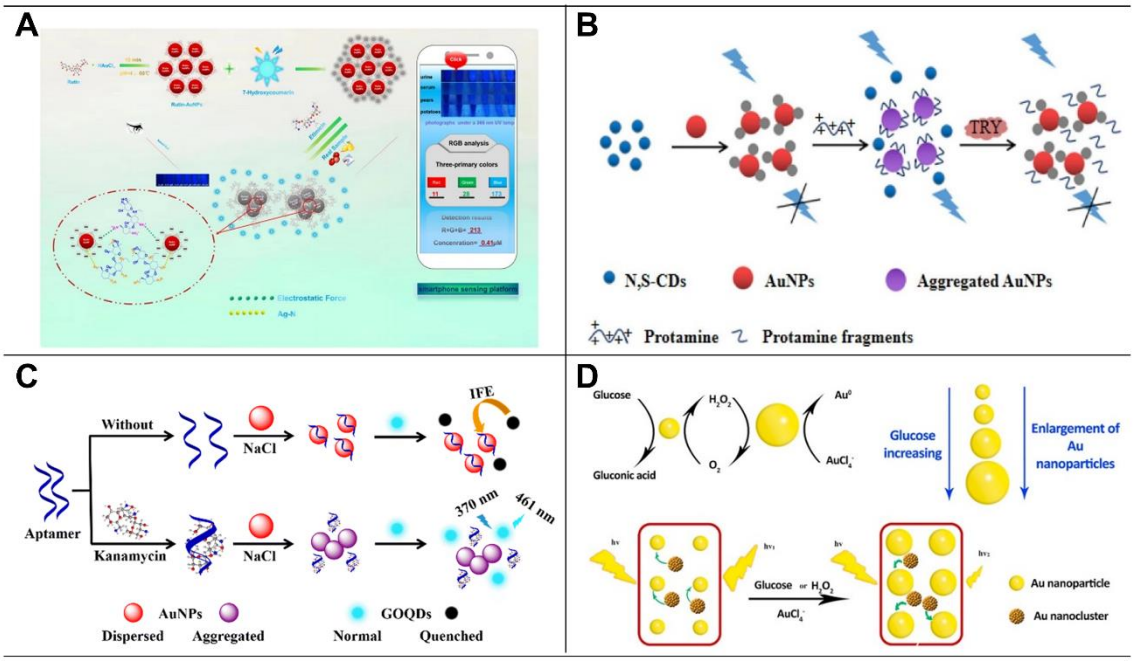

Figure 1.12. Fluorescent biosensors based on IFE between AuNPs and fluorophores for POC diagnostics. (A) Scheme of the fluorescent system based on 7-hyfrixycoumarin fluorophores and rutin-functionalized AuNPs for sensitive detection of emiticin in food and human samples via smartphone. (B) Scheme of the "off-on-off" fluorescent nanosensor using sulphur doped carbon dots (N,S-CDs) and AuNPs for the detection of protamine and trypsin. (C) Schematic illustration of the IFE-based fluorescent aptasensor using graphene quantum dots and AuNPs for kanamycin detection. (D) Scheme of the fluorescent glucose biosensor based on the IFE between His-gold nanoclusters (fluorescencer) and the self-catalyzed

enlargement of AuNPs (absorber). Adapted with permission from ref. 125 (A), 128 (B), 130 (C) and 130 (D). Copyright 2022 Elsevier (A), 2021 Elsevier (B), 2022 Royal Society of Chemistry (C) and 2020 Elsevier (D).

1.2.3.2 Metal-enhanced fluorescence (MEF) between AuNPs and fluorophores

Metal-enhanced fluorescence (MEF) is a phenomenon that occurs when the fluorescence of a fluorophore is significantly enhanced in the presence of metal nanostructures, such as gold nanoparticles (AuNPs). When fluorophores are in close proximity to AuNPs (usually at a distance of a few nanometers), they experience an enhanced local electromagnetic field. This enhanced electromagnetic field in turn leads to an increased excitation rate of the fluorophores, resulting in higher fluorescence emission. The MEF effect is strongly dependent on the distance between the fluorophores and the AuNPs, with optimal enhancement occurring at specific nanoscale distances. The size, shape, and surface properties of the AuNPs also play a crucial role in determining the degree of enhancement. In the context of POC diagnostics, the use of MEF in optical biosensors can enable more sensitive and faster detection of specific biomarkers or analytes. This enhanced sensitivity can improve the accuracy of disease diagnosis, especially when dealing with low-concentration samples. Various MEF-based assays have been proposed to increase the sensitivity in POC diagnostics by using AuNPs and fluorophores[134–136] and integrating with the CRISPR/Cas12 system[137], paper-based devices[136,138], and microneedle patches[139,140], especially for multiplexed sensing[141,142].

Liu J. et al.[134] proposed a fluorescence method based on binding-induced DNA assembly and fluorescence signal enhancement by AuNPs for direct nucleocapsid protein (N protein) analysis in saliva samples. In this method, aptamer 1 (Apt-1) labelled with FAM, a fluorescent dye, was functionalized with 13 nm AuNPs and then hybridized with a portion of Apt-2 to form a stable stem duplex. In the absence of N protein, the fluorescence is minimal due to the distance between FAM and AuNPs. In the presence of N protein, the formation of a closed-loop conformation due to the specific recognition of two aptamers on N protein results in two aptamers approaching the AuNPs, leading to a metal-enhanced effect, and thus an enhancement of fluorescence. The assay shows a LOD of 150 fg/mL, which is 1-2 orders of magnitude lower than existing commercial antigen ELISA kits and comparable or better than PCR. Moreover, the whole diagnosis is completed in about 3 min, much faster than existing nucleic acid tests **(Figure 1.13A)**.

Choi J. et al.[137] used the MEF between AuNPs and fluorophores to develop a CRISPR/Cas12-based fluorescent and colorimetric dual-mode DNA sensor for the detection of cell-free DNA (cfDNA), a biomarker for cancers. There are two types of AuNPs in this system. The smaller AuNPs are functionalized with ssDNA labeled with fluorophores, and the larger AuNPs are linked to the smaller AuNPs by the complementary strand of the fluorophore-labeled ssDNA, and are located near the fluorophores, resulting in quenching of the fluorescence of the fluorophores. Once, Cas12 was activated by target cfDNA, the complementary strand is cleaved resulting in the release of AuNPs functionalized with DNA-fluorophores. The fluorescence of the fluorophores increases due to dequenching of the large AuNPs and MEF from the small AuNPs, and the color changes from purple to red-purple. The authors have used this system for the detection of breast cancer gene-1 (BRCA-1). The detection is highly sensitive and completed in 30 min without conventional nucleic acid amplification. **(Figure 1.13B)**.

Minopoli A. et al.[141] reported a fluorescent apta-immunoassay based on double-resonant AuNPs immobilized onto a glass slide and two types of fluorescent reporters (5-FAM and Cy5) for multiplexing detection. In this system, hexagonal plasmon-coupled AuNPs are arranged along multibranched surface with a resonance in the red region (~675 nm), which overlaps with the excitation/emission peaks of Cy5. The plasmon-uncoupled AuNPs exhibit a narrow resonance at 524 nm, which overlaps with the emission peak of 5-FAM. In order to detect the plasmodium falciparum lactate dehydrogenase (PfLDH), a biomarker of malaria, the authors used double-resonant AuNPs functionalized with anti- PfLDH Abs as the capture layer, and 5-FAM and Cys5 reporters modified with anti-PfLDH aptamers as the detection layer. The results show a linear range of five orders of magnitude with a LOD of 50 pM (1.6 ng/mL) for the 5-FAM probe and 260 fM (8.6 pg./mL) for the Cy5 probe. The high sensitivities are due to the 160-fold amplification of the fluorescence signal of for 5-FAM and 4500-fold for Cys5 by the double-resonant nanostructured AuNPs surface. The application shows great potential for the simultaneous detection of two analytes using different fluorophores and for high-throughput analysis **(Figure 1.13C)**.

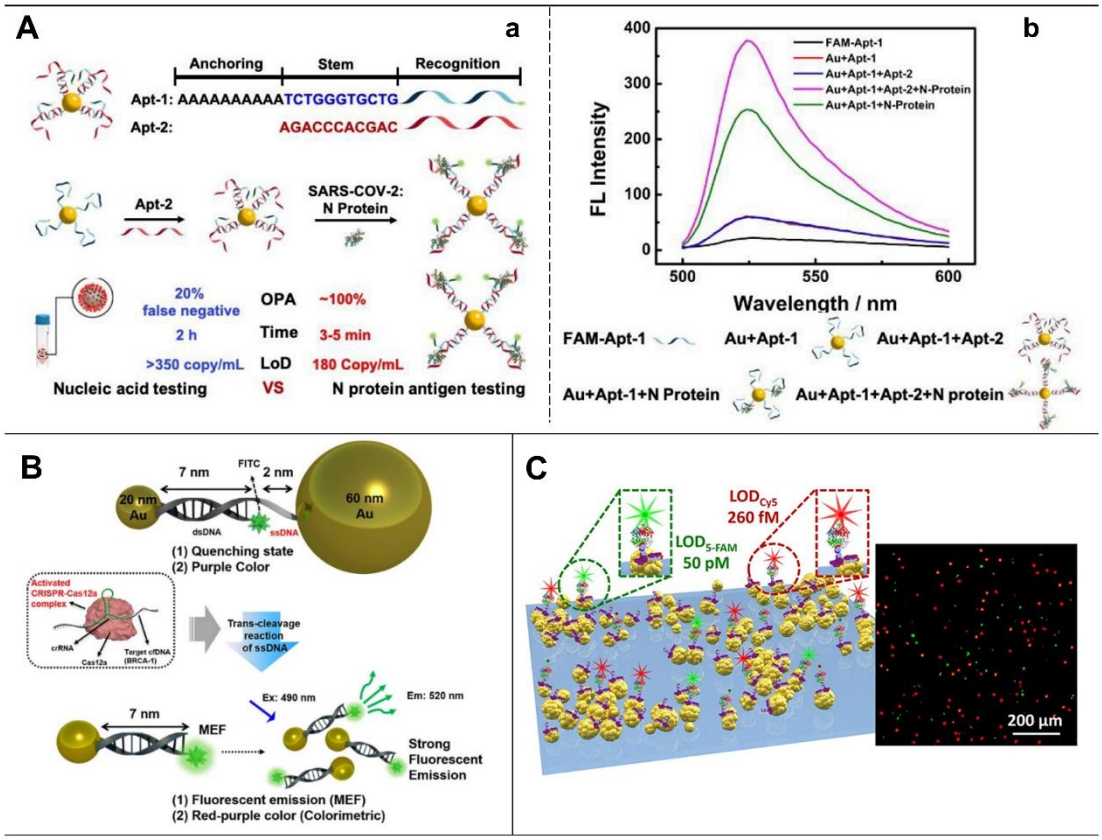

Figure 1.13. (A) Schematic Illustration of fabrication of binding-induced DNA assembly assay for N protein. (a) Conformation of the two aptamers on the surface of AuNP (up). The process of the synchronous recognition of N protein by binding-induced two-aptamer assembly (middle). Performance comparison between the nucleic acid testing and the proposed assay (below). (b) Fluorescence emission spectra (λem = 524 nm) of Apt-1 in the presence of different mixture systems. (B) Schematic diagram of the CRISPR/Cas12a-based fluorescent system using DNA-functionalized AuNPs via colorimetric and MEF for detection of cell-free DNA (cfDNA). (C) Scheme of double-resonant nanostructure consisting of branch hexagonally arranged and sprinkled AuNPs. Adapted with permission from ref. 134 (A), 137 (B) and 141 (C). Copyright 2022 American Chemical Society (A), 2020 American Chemical Society (B) and 2022 American Chemical Society (C).

Luan J. et al.[136] developed a plasmonic construct consisting of a BSA scaffold with approximately 210 IRDye 800CW fluorophores, a polymer-coated AuNR as a plasmonic antenna and a biotin as a high-affinity bioreceptor. The fluorescence intensity of 800CW fluorophores embedded in BSA increases 6700-fold compared to a single 800CW fluorophore. When used in fluorescence-linked immunosorbent assays (FLISA) to detect of urinary biomarkers in patient samples, the construct

improves the LOD of FLISA by up to 4750-fold and can be easily used in multiplexed bead-based immunoassays, immunomicroarrays, flow cytometry and immunocytochemistry assays. In addition, the assay requires less analysis time (about 20 min) and lower sample volumes. Furthermore, the emission peak of the plasmonic construct can be easily tuned across the visible and near-infrared spectral regions by changing the shape, size and composition ratio, indicating great potential for multiplexing analysis. In addition, the same researchers [142] used plasmonic fluor to develop a plasmonically-enhanced competitive fluorescent immunoassay for small molecules detection. They showed the application of the detection of cortisol with a 30-fold lower LOD than the existing commercial ELISA kit. Moreover, they demonstrated a spatially-multiplexed competitive assay for the simultaneous detection of cortisol and fluorescein **(Figure 1.14)**.

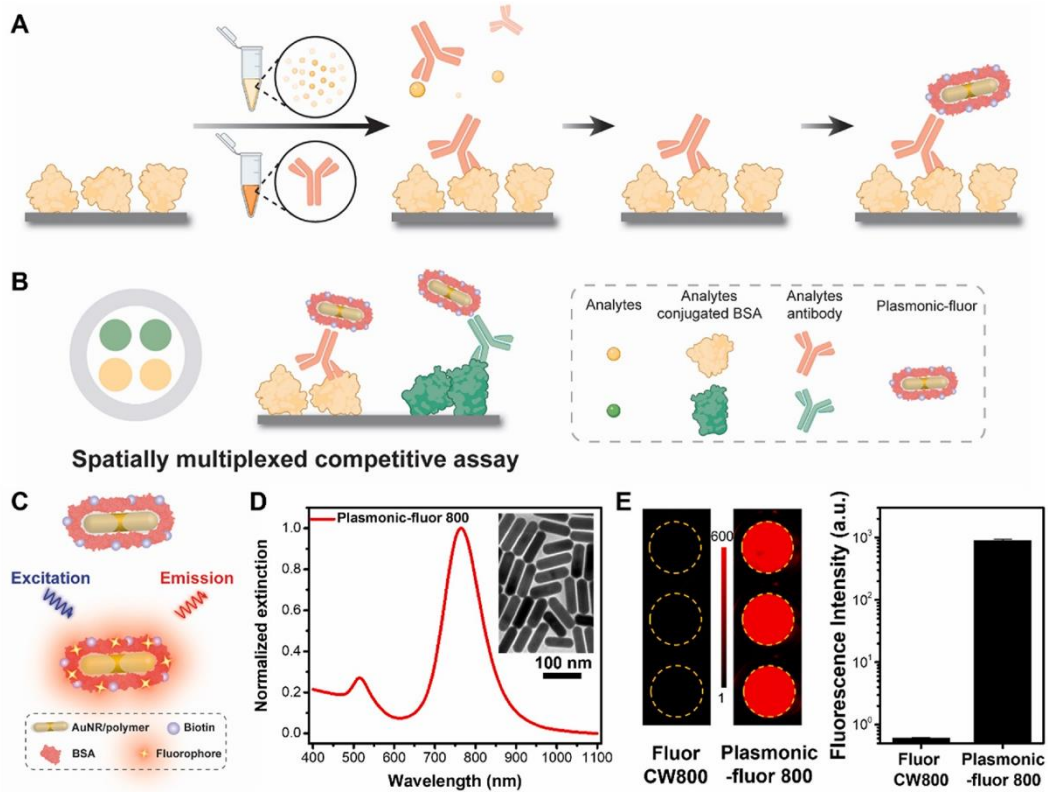

Figure 1.14. Schematic illustration of the plasmonically-enhanced competitive fluorescent immunoassay for (A) single and (B) multiplex analysis. Design and characterization of plasmonic-fluor: (C) Schematic presentation of plasmonic-fluor as an ultrabright nanolabel. (D) Normalized visible–NIR extinction spectra of plasmonic-fluor 800. Inset: TEM images of AuNRs for plasmonic-fluor 800. (E) Fluorescence images and corresponding intensity of streptavidin-CW800 fluorophores and plasmonic-fluor 800. Data are mean ± s.d. Adapted with permission from ref. 142 and copyright 2022 Elsevier.

They[139,140] have also successfully proposed an ultrasensitive method for the detection of protein markers in interstitial fluid (ISF) using microneedle patches for minimally invasive in vivo sampling and on-needle quantification. The same plasmonic fluor, used in the microneedle patch, improved the LOD of various protein biomarkers in ISF by almost 800-fold compared to conventional fluorophores and significantly decreasing the sampling time **(Figure 1.15A)**. Similarly, Miranda B. et al.[140] demonstrated an array of hollow microneedles (HMNs) for the detection of biomarkers in interstitial fluid. The core element of the plasmonic transducer in HMNs, consists of AuNPs embedded in poly (ethylene glycol) diacrylate (PEGDA) hydrogels[143], filled in the inner cavity of the HMNs. The optical properties of the AuNPs before and after embedding in PEGDA change slightly, and the absorption peak of AuNPs embedded in PEGDA overlaps precisely with the excitation peak of Cy3 fluorophores. The authors used this system to detect a model target of biotin, which has a high affinity for streptavidin. In this assay, the Cy3-labeled streptavidin was able to bind specifically to biotin, which initially bound to the cysteamine-modified AuNPs, resulting in fluorescence enhancement of Cy3 via MEF due to the close distance of Cy3 and AuNPs **(Figure 1.15B)**.

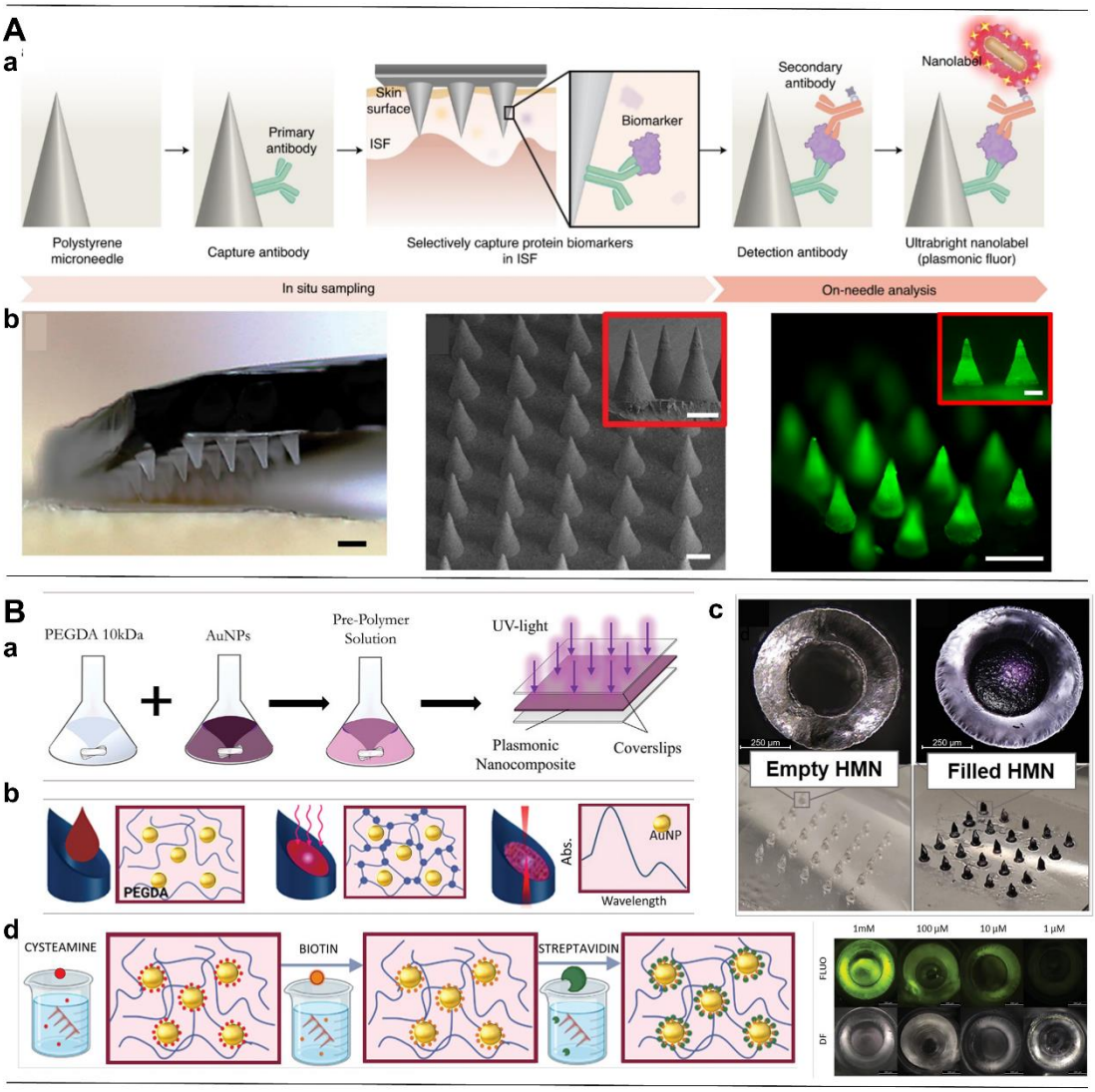

Figure 1.15. (A) (a) Schematic presentation of the workflow of microneedle-based assay involving in situ sampling and on-needle detection of protein biomarkers in ISF. (b) Optical image of a microneedle patch with the magnetic backing layer (black) and pristine polystyrene needles (hazy) (left). SEM image of as-fabricated microneedle patch (middle). Fluorescence microscopy image demonstrating efficient and uniform adsorption of antibodies on polystyrene microneedles. (B) Schematic presentation of Hollow Microneedles (HMNs)-based plasmonic sensor for on patch detection molecules in dermal interstitial fluid. (a) Scheme of the fabrication of PEGDA 10 kDa embedding AuNPs. (b) Schematic illustration of filling, UV polymerization, and LSPR measurement steps performed on a single HMN. (c) Optical images of a single HMN and of an array of empty HMNs (left) and HMNs filled with PEGDA/AuNPs nanocomposites (right). (d) Schematic illustration of the functionalization and sensing protocols in solution consisting of AuNPs capping by cys, covalent immobilization of biotin, and incubation in fluorescent Cy3-labeled streptavidin (left), and

Fluorescence and dark field (DF) images of HMNs bases after interaction with Cy3-streptavidin at for four different biotin concentrations of 1 mM, 100 μM, 10 μM, and 1 μM, respectively) (n ≥ 3) (right). Adapted with permission from ref. 139 (A) and 140 (B). Copyright 2021 Springer Nature (A) and 2023 John Wiley and Sons (B).

1.2.3.3 Förster resonance energy transfer (FRET) between AuNPs and fluorophores

In Förster resonance energy transfer (FRET) the energy of an excited fluorophore is transferred non-radiatively to an acceptor, which lead to the quenching of the fluorophore's emission. AuNPs can be used as energy acceptors. The FRET efficiency strongly depends on the distance between the AuNPs and the fluorophore, with the donor and acceptor molecules having overlapping emission and absorption spectra, respectively. Recently, many fluorophores of organic dyes, upconversion nanoparticles (UCNPs), quantum dots (QDs), carbon dots (CDs), and gold nanoclusters (AuNCs) have been combined with AuNPs to develop FRET-based fluorescent sensors.

Wu Y. et al.[144] reported a dual-color fluorescent aptasensor based on FRET between spherical AuNPs and fluorophores (TAMRA and FAM) for specific quantification of human epidermal growth factor receptor 2 (HER2) and estrogen receptor (ER), and classification of breast cancer. In this approach, HER2 and ER aptamers were functionalized with AuNPs and then hybridized with fluorophore-labeled complementary aptamers to form duplexes that bring the fluorophores in proximity to the AuNPs, resulting in quenching of the fluorescence of TAMRA and FAM. The fluorophore-labeled aptamers were displaced by the binding of HER2 or/and ER protein with their anti-aptamers, leading to the restoration of fluorescence of TAMRA and FAM. The sensor can specifically and simultaneously detect HER2 and ER, enabling the quantitative classification of breast cancer subtypes **(Figure 1.16A)**.

Fu X. et al.[145] developed a novel CRISPR/Cas12a-based fluorescent biosensor in which spherical AuNPs were anchored with a spherical nucleic acid (SNA) reporter to enable stable and sensitive biosensing. The authors showed different trans-cleavage activity of several types of Cas12a systems on the AuNPs surface and reported that the trans-cleavage activity of LbCas12a on AuNPs surface is strongly dependent on the density and length of DNA strands. **(Figure 1.16B)**.

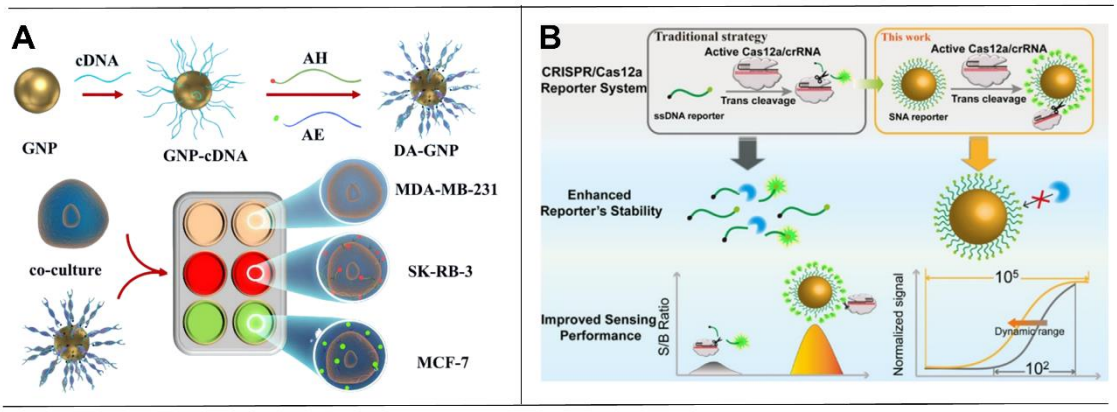

Figure 1.16. Fluorescent biosensors based on FRET between AuNPs and organic dyes for POC diagnostics. (A) Illustration of classification of breast cancer by dual-aptamer functionalized gold nanoprobe (DA-GNP). (B) Schematic Illustration of the CRISPR/Cas12a-based fluorescent biosensor using AuNPs anchored with a spherical nucleic acid (SNA) reporter for stable and sensitive biosensing. Adapted with permission from ref. 144 (A) and 145 (B). Copyright 2022 Elsevier (A) and 2021 American Chemical Society (B).

Upconversion nanoparticles (UCNPs)[146–148] are a unique class of nanomaterials that can convert low-energy photons, typically in the near-infrared (NIR) region, into higher-energy emissions, such as visible light or ultraviolet light. This allows UCNPs to overcome some of the limitations of conventional organic fluorophores used in FRET-based biosensors. These include near-infrared excitation that causes less damage to samples and enables deep tissue penetration suitable for in vivo diagnosis, efficient upconversion emission that ensures a strong and detectable fluorescence signal even at low excitation power, reduced background autofluorescence that lead to improved sensitivity and signal-to-noise ratio, and long lifetime emission that enables time-triggered detection to further improve sensitivity. Liu Z. et al.[146] reported for first time a 'head-to-tail' system using NaYF4:Yb,Er nanoparticles (UCNPs) as donor and nanoquencher of AuNPs as acceptor for the detection of long-chain DNA (i.e., HIV DNA, 52 bp). The 5' end of the capture DNA strand was covalently modified with the carboxylated UCNPs and the reported DNA was functionalized with AuNPs. The AuNPs were brought ito proximity with the UCNPs by forming a 'head-to-tail' sandwich hybridization, resulting in quenching of the upconversion luminescence of the UCNPs. The assay shows several advantages: strong photobleaching and stability, high sensitivity with a nanomolar LOD, and high selectivity **(Figure 1.17A)**. Li L. et al.[147] introduced a

FRET-based upconversion luminescence nanosystem between upconversion nanoparticles (UCNPs) and AuNRs for rapid, ultrasensitive, quantitative and on-site detection of SARS-CoV-2 spike protein (S protein). In this system, the surface of the UCNPs with high positive charge can efficiently capture the free S protien and then be combined with anti-S protein antibody modified onto AuNRs (Au-ab), leading to quenching of upconversion luminescence (UCL) due to the high energy transfer efficiency between UCNPs and AuNRs. Here, the emission peak of the UCNPs is at 800 nm in near-infrared (NIR) region, which avoids autofluorescence and false-positive results. The assay can be performed within minutes with a LOD of 1.06 fg/mL for S protein and with comparable performance for the nucleocapsid protein using a commercial test kit **(Figure 1.17B)**.

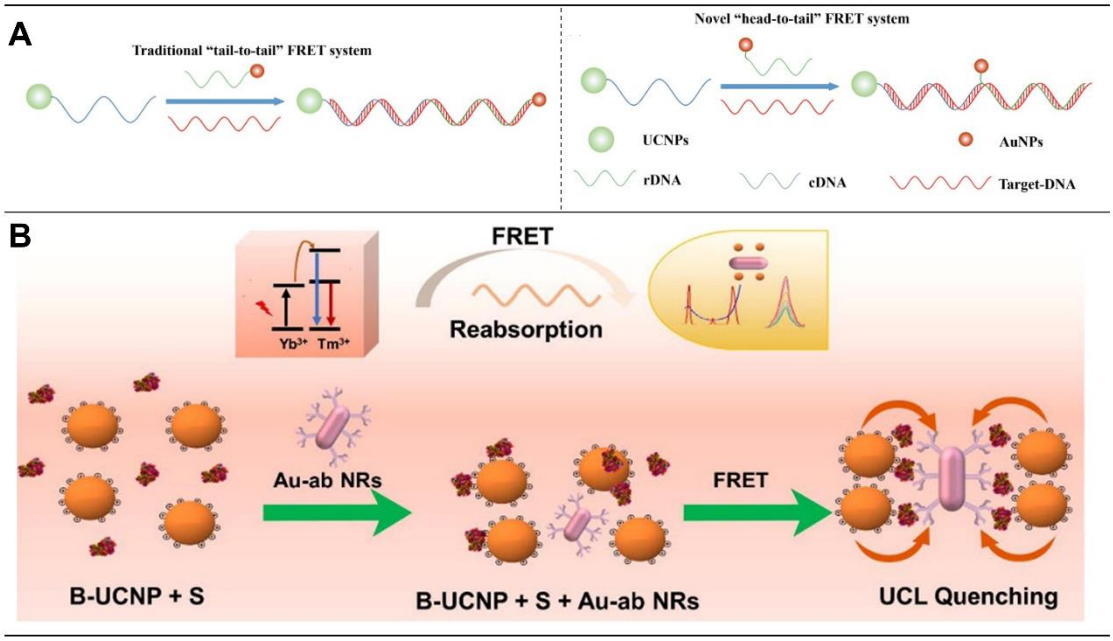

Figure 1.17. Upconversion luminescence biosensor based on FRET between AuNPs and upconversion nanoparticles (UCNPs) for POC diagnostics. (A) Schematics of the traditional "tail-to-tail" FRET system and the novel "head-to-tail" UCNP-based FRET system presented in this work. (B) Schematic illustration of ultra-rapid S protein detection using UCNPs and AuNR system. Adapted with permission from ref. 146 (A) and 147 (B). Copyright 2020 IOP Publishing (A) and 2022 Elsevier (B).

Graphene quantum dots are small, nanoscale carbon-based materials with excellent optical properties. By introducing nitrogen atoms into the graphene structure (doping), their properties can be tuned to enhance fluorescence emission. Nitrogen-doped graphene quantum dots (N-

GQDs) exhibit high quantum yield, good photostability and biocompatibility, making them ideal candidates as fluorescence donors. Chen X. et al.[149] reported a fluorescent aptasensor based on FRET between N-GQDs (donor) and spherical AuNPs (acceptor), both functionalized and linked to aptamers, to detect C-reactive protein (CRP), a biomarker for acute inflammation response and with a level in human serum which is closely associated with the severity of acute myocardial infarction (AMI). When CRP binds to the aptamers, the conformational change of the aptamers bring in close proximity the N-GQDs and the AuNPs, resulting in quenching and decrease of fluorescence of the N-GQDs. The aptasensor shows good rapidity a LOD of 0.2 ng/mL of CRP in PBS, which is much lower than the physiological CRP level in human serum. The sensor has also been validated for the detection of CRP in human serum from patients. In addition, the whole assay is very simple (one-step and easy operation) and can be completed within 40 min, indicating great potential for POCT **(Figure 1.18A)**. CdSe/CdS/ZnS core/shell/core quantum dots are another example of QDs used as FRET donors in optical biosensors. The CdSe core provides high fluorescence quantum yield, while the CdS and ZnS shells improve the QDs' stability, preventing potential toxicity and photobleaching issues. The shells also help tune the emission wavelength by controlling the size and composition of the QDs. Lu X. et al.[150] proposed a dual-color CdSe/CdS/ZnS QDs aptasensor based on FRET between QDs and gold nanorods@polydopamine (AuNRs@PDA) for simultaneous detection of amyloid-β oligomers (AβO) and tau protein, two important biomarkers of Alzheimer's disease (AD). In absence of targets, both types of CdSe/CdS/ZnS core/shell/core QDs labeled with aptamers were modified via π–π stacking and hydrogen bonding to AuNRs@PDA, which triggered quenching of the QDs' fluorescence of. In the presence of targets, the aptamer-labeled QDs were released from the surface of AuNRs@PDA due to the specific binding between targets and aptamers and conformational change of aptamers, which led to the restoration of the fluorescence of QDs. The dual-color aptasensor exhibits a LOD of 50 pM for AβO and 20 pM for the tau protein **(Figure 1.18B)**.

Carbon dots are carbon-based nanomaterials with excellent biocompatibility, low toxicity, and tunable fluorescence emission, making them ideal candidates for biomedical applications. By introducing nitrogen atoms during the synthesis of carbon dots, their optical and chemical

properties can be tuned. Nitrogen doping enhances the fluorescence intensity and stability of carbon dots, making them more suitable for sensing applications. Mahani M. et al.[151] have developed a "turn-on" fluorescent DNA nanosensor based on FRET between N-doped carbon dots (NCDs, donors) and AuNPs (acceptors) for the detection of the transcription factor NF-kB p50. The single-stranded DNA functionalized onAuNPs hybridizes with duplex DNA strands modified with NCDs to form a triplex DNA in the absence of the target, leading to significant quenching of the fluorescence of the NCDs. The AuNPs coated with single-stranded DNA were released from the NCDs as the target sequences were bound very specifically to the duplex DNA in the presence of the target. The results of the triplex-based biosensor showed a linear detection range of 20-150 pM with a LOD of 9 pM of NF-kB p50, highly specific quantification and validated application in synthetic medium **(Figure 1.18C)**.

Gold nanoclusters are ultra-small, luminescent particles consisting of a few to several dozen gold atoms. Their unique properties, such as size-dependent fluorescence emission and biocompatibility, make them excellent candidates as FRET donors in biosensing applications. The emission wavelength of AuNCs can be tuned by controlling their size and surface chemistry, to ensure efficient energy transfer to a suitable acceptor. Gu Y. et al.[152] developed a "turn-on" fluorescent nanoprobe using AuNCs@GSH-cys and AuNRs/end-NH2/side-SiO2 linked by a low molecular weight heparin (LMWH) for ultrasensitive detection of heparanase activity, dysregulation of which promotes cancer metastasis. The longitudinal absorption peak of AuNRs at 825 nm and the emission peak of AuNCs at 824 nm overlap exactly, which increases FRET efficiency and eliminates background autofluorescence, both of which enable highly sensitive detection. The nanoprobe shows a dynamic range of 0.125 ng/μL - 0.01 μg/μL with a LOD of 82.15 pM (0.43 pg/μL) *in vitro*, as well as excellent specificity and simplicity (one-step) **(Figure 1.18D)**.

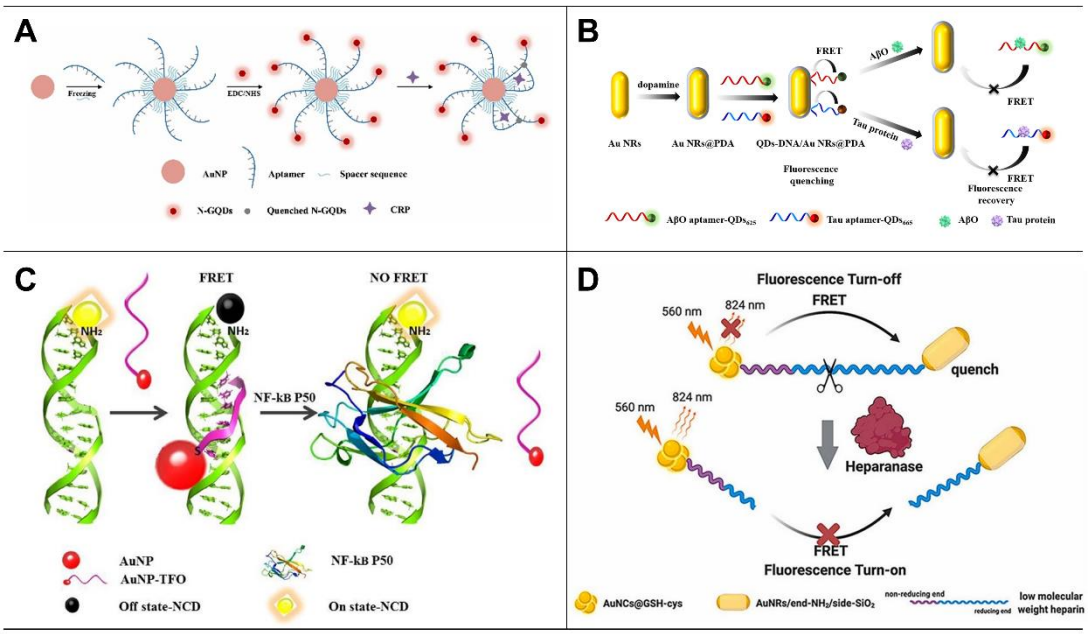

Figure 1.18. Fluorescent aptasensors based on FRET between AuNPs and QDs or CDs or AuNCs for POC diagnostics. (A) Scheme of the fluorescent aptasensor based on the FRET between N-GQDs modified aptamers and AuNPs. (B) Schematic illustration of the simultaneous detection of AβO and tau protein using the QDs and AuNRs-based FRET aptasensor. (C) Scheme of the label-free triplex DNA-based biosensor for detection of transcription factor NF-kB p50 using the FRET between NCD and AuNPs. (D) Schematic illustration of the "turn-off" fluorescent nanoprobe based on FRET between AuNCs@GSH-cys and AuNRs/end-NH2/side-SiO_2 for ultrasensitive detection of heraranase activity. Adapted with permission from ref. 149 (A), 150 (B), 151 (C) and 152 (D). Copyright 2022 Elsevier (A), 2022 MDPI (B), 2021 Elsevier (C) and 2023 Elsevier (D).

1.2.4. AuNPs-based LFAs for SARS-COV-2 diagnosis

Lateral flow assays (LFAs), also known as lateral flow tests or immunochromatographic assays, are simple paper-based devices designed for the rapid detection and quantification of target analytes without the need for specialized equipment. The structure and main components of a typical LFA are shown in **Figure 1. 19**[153]. These assays are widely used in various fields, including medical diagnostics, food safety testing, and environmental monitoring. In particularly, due to their simplicity, rapidity and ease of use, the LFAs are commonly used for point-of-care testing, especially in resource-limited settings. They are applied for detecting various analytes, including proteins, pathogens, virus, antibodies, antigens, nucleic acids, and hormones etc. While LFAs

offer several advantages for POC diagnostics, they also have some limitations, including lower sensitivity compared with laboratory-based tests, qualitative or semi-quantitative results, and interference of sample matrices. Various signal amplification strategies[154–157] and the integration with portable device (i.e. smartphone) were introduced in LFAs for enhancing the sensitivity, quantitative analysis and better display of results, especially in response to the COVID-19 pandemic.

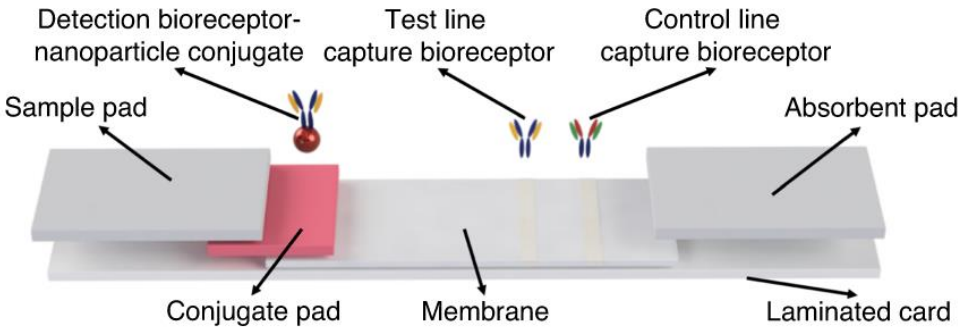

Figure 1.19. Schematic illustration of the structure and main components of a typical LFA. Adapted with permission from ref. 153 and copyright 2020 Springer Nature.

1.2.4.1. Modification of physical structure for delayed flow of LFAs

Adapting and modifying the physical structure of LFA hs been explored and widely used to slightly amplify the signal and increase the sensitivity[158–160]. Srithong P. et al.[154] developed a sensitivity-enhanced competitive LFIA using a delayed hydrophobic barrier fabricated with trimethylsilyl cellulose (TMSC). The platform was used to detect the SARS-CoV-2 spike receptor-binding domain (RBD) antigen as a model analyte to demonstrate feasibility. The novel platform (i.e. delay LFIA, d-LFIA) consisted of two separate layers, an upper layer for analyte or sample flow, where the solution flowed directly into the detection zone to bind with the primary Abs, and a lower layer located below and loaded with the signal reporter of SARS-CoV-2 SP RBD-coated AuNPs conjugates. This layer was fabricated with a TMSC barrier to delay the flow of SARS-CoV-2 SP RBD-AuNPs, allowing the antigen to bind more efficiently to the primaryAbs. Under optimal conditions, the d-LFIA platform showed a LOD of 0.11 ng/mL of SARS-CoV-2 RBD, which is 9.1times lower than conventional LFIA. Moreover, the total assay time of 15 min was still comparable to conventional LFIA (**Figure 1.20A**).

Kim K. et al.[161] demonstrated an ultrafast PCR testing kit comprising a lateral flow paper strip (LFS) with a nichrome-based thin film heater (i.e., Joule heater). In the novel platform, the LFS was used as a container for the PCR-solution, which resulted in a fast thermocycling without a cooler due to the high specific surface area of the paper heated by the Joule heater and also enabled visual detection of PCR amplicons in the detection zone of the LFS with the naked eye. In demonstratingthe detectability of the novel device, the platform was used to detect SARS-CoV-2 viral RNA with a LOD of 1 copy/μL with naked eye, within 30 min after addition of the PCR solution, while conventional PCR and real-time PCR require 130 min and 90 min, respectively. The sensitivity of colorimetric signal detection based on the PCR kit was comparable to fluorescence detection using conventional PCR and real-time PCR devices. In the platform, LFTS not only provides a flow channel, but also represents a promising platform for fast PCR and detection (**Figure 1.20B**).

Boumar I. et al.[162] developed a novel hybrid (vertical-lateral-vertical) flow assay assembled in a finger-stick POC device, similar to an adhesive bandage for the timely detection of IgM and IgG against the S and N proteins of SARS-CoV-2, enabling further screening of SARS-CoV-2 infections.The platform, which consists of a vertically stacked plasma/serum separation membrane, a conjugate pad and a detection zone, uses S and N protein-coated AuNPs as probes and reporters to specifically and efficiently capture the IgM and IgG Abs from a pinprick of ~15 μL of blood in just one step. The platform shows the immune response of no immune IgM−/IgG−, early immune IgM+/IgG−, active immune IgM+/IgG+ or immune IgM−/IgG+ in a few minutes with a LOD of less than 1 ng/mL of IgM and IgG spiked in healthy plasma (**Figure 1.20C**).

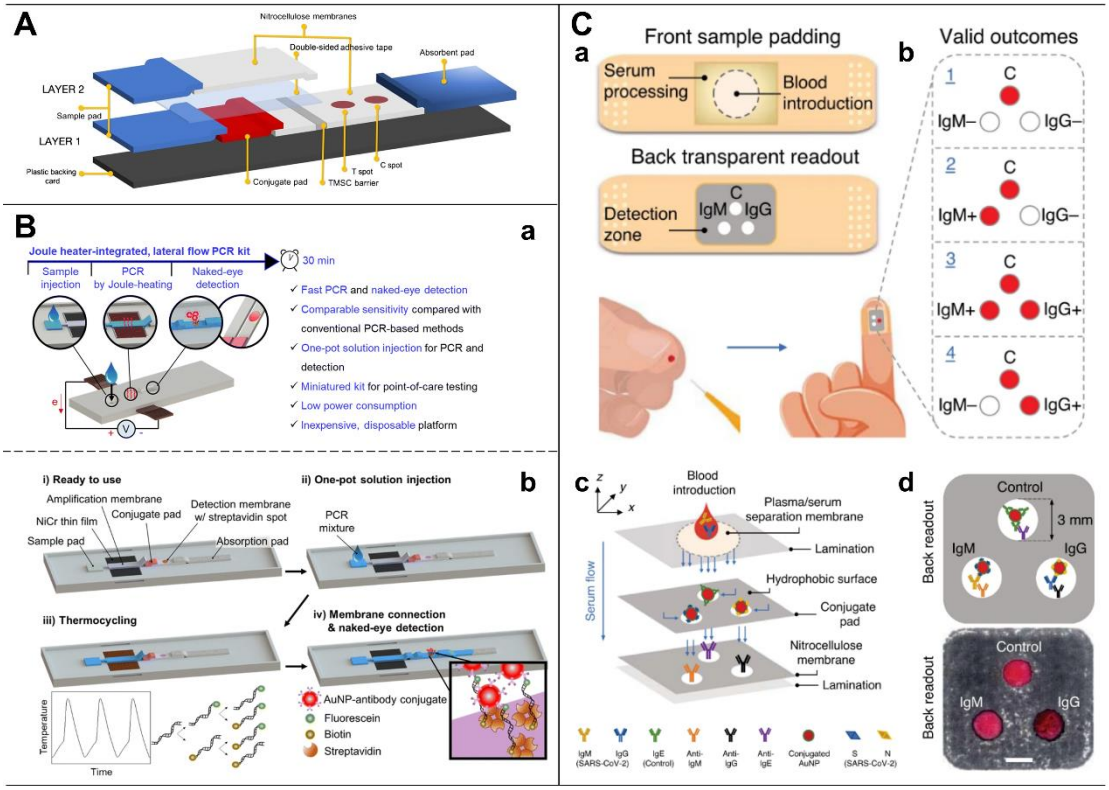

Figure 1.20. Delay flow based on modification of physical structure for enhancing sensitivity of LFA with/without auxiliary device. (A) Schematic illustration of delay-LFIA based on trimethylsilyl cellulose (TMSC) barrier. (B) Schematic illustration of Joule heater-integrated lateral flow PCR kit. (a) advantages of the rapid PCR kit; (b) procedure of the POC PCR kit. (C) Schematic illustration of an adhesive bandage based on hybrid (vertical-lateral-vertical) flow assay (HFA) for detection of SARS-CoV-2 IgM and IgG. (a) schematic of finger-stick adnesive bandage; (b) Valid outcomes: 1) negative (IgM-/IgG-) or 2-4) positive (IgM+/IgG−, IgM+/IgG+, IgM−/IgG+, respectively) for SARS-CoV-2 infection, C represents valid control; (c) Schematic illustration of the HFA's bioactive layers and their working mechanism for AuNPs-based capture and detection of IgM and IgG Abs from a pinprick (~15 µL) of blood; (d) Schematic presentation (up) and photographs (below) showing the back readout of the HFA when a mixture of IgM and IgG Abs was introduced to the conjugate pad. Adapted with permission from ref. 154 (A), 161 (B) and 162 (C). Copyright 2022 Springer Nature (A), 2023 Royal Society of Chemistry (B) and 2023 Springer Nature (C).

1.2.4.2. Gold nanocomposites-based LFAs

Wang C. et al.[155] proposed a colorimetric-fluorescent dual-mode lateral flow immunoassay (LFIA) using spike (S) protein-conjugated SiO_2@Au@QD nanobeads (NBs) as labels for the

simultaneous detection of IgG and IgM antibodies against SARS-CoV-2. The assay can be performed in 15 min, requiring only 1 µL of human serum and the sensitivity is 100 times higher than colloidal gold-based LFIA. The colorimetric mode is used for visual detection and qualitative screening of the patients with suspected SARS-CoV-2 infection. The fluorescent mode is used for sensitive and quantitative analysis of IgM/IgG in human serum using a portable fluorescence device. When validating real samples, the results of the assay show sensitivity of 100% and a specificity of 100% (**Figure 1.21A**).

Hong D. et al.[163] designed a sensitive LFIA using isolated spherical AuNPs-assembled SiO_2 core-satellite NPs (SiO_2@Au CSNPs). The SiO_2@Au CSNPs have significantly enhanced light absorption compared to isolated AuNPs, which increases the sensitivity and lowers the LOD by 2 orders of magnitude compared to conventional colloidal gold. The proposed assay can be completed in 20 min, with a visual and quantitative LOD of 10 pg/mL and 0.24 pg/mL of SARS-CoV-2 nucleocapid (N) protein, respectively. For the detection of heat-inactivated SARS-CoV-2 viral culture fluid, the assay shows a visual and quantitative LOD of $3.8x10^2$ and 4.9 $TCID_{50}$/mL. The simple assay, which only modulates the absorbance of the AuNPs labels, shows great potential to serve as an effective strategy for monitoring the pandemic situation and preventing the spread of the viruses (**Figure 1.21B**).

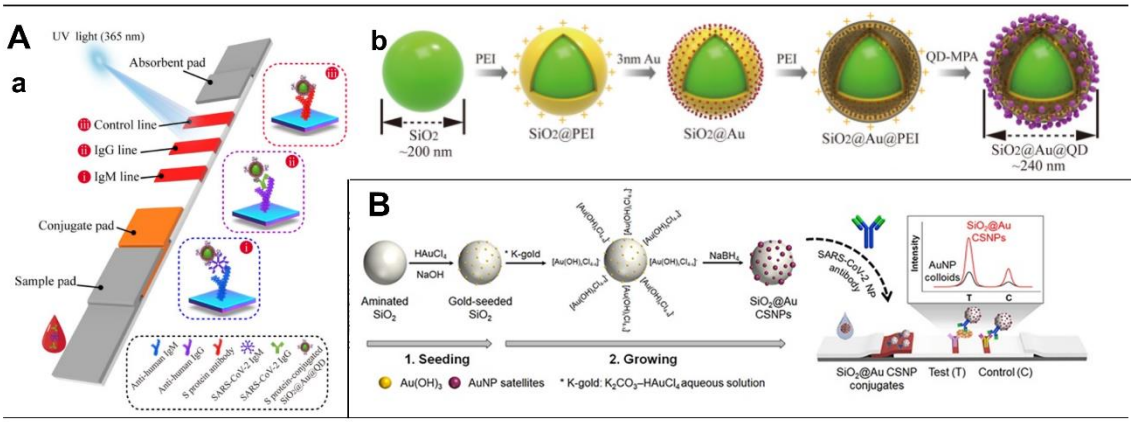

Figure 1.21. Gold nanocomposites-based LFA for COVID-19 diagnosis. (A) Dual-mode QD nanobeads-based LFIA for detection of SARS-CoV-2 IgM/IgG. (a) Schematic illustration of the colorimetric-fluorescent dual-mode LFIA biosensor; (b) fabrication procedure of dual-mode SiO2@Au@QD fluorescent labels. (B) Schematic presentation showing the synthesis of AuNP-assembled SiO_2 core–satellite nanoparticles

(SiO_2@Au CSNPs) and the integration with an LFIA for highly sensitive detection of SARS-CoV-2 N protein. Adapted with permission from ref. 155 (A) and163 (B). Copyright 2020 American Chemical Society (A) and 2022 American Chemical Society (B).

1.2.4.3. AuNPs clusters or in situ growth of AuNPs-based LFAs

OH H. et al.[156] reported a plasmon color-preserved (PLASCOP) AuNPs cluster-based LFIA for highly sensitive detection of SARS-CoV-2 NP. Specifically, the PLASCOP AuNPs cluster consisted of a streptavidin-coated AuNPs core and a biotinylated Abs-coated AuNPs satellite, with the biotinylated Abs-streptavidin forming a gap of more tham 15 nm to avoid the aggregation of AuNPs, thus preserving the plasmonic color while increasing the overall light absorption. Under optimal conditions, the total assay can be completed within 10 min. The LFIA based on the PLASCOP AuNPs-clusters consisiting of 40 nm AuNPs showed good specificity and high sensitivity for the detection of SARS-CoV-2 NP with a LOD of 0.038 ng/mL, which was 23.8-fold and 5.9-fold lower than single 15 nm and 40 nm AuNP conjugates, respectively. In the clinical validation test, the proposed assay showed a LOD of 54 TCID50/mL of SARS-CoV-2 particles spiked in human saliva. Overall, the PLASCOP AuNPs clusters showed great potential as the promising colorimetric reporters with enhanced sensitivity in LFA sensing for broad POC diagnostics (**Figure 1.22A**).

Ruantip S. et al.[164] developed a self-enhanced LFIA that avoids complex multi-step proceduresand the use of enhancers to detect a model analyte of SAR S-CoV-2 antigens as in saliva.The self-enhanced LFIA was composed not only of the conventional conjugate pad and the sample pad, but also of an additional enhanced pad consisting of gold ions and a reducing agent, which was adhered tothe sample pad with a common ashesive tape. The one-step self-enhanced LFIA achieved ten-times higher sensitivity than the conventional visual LFIA, with a visual LOD of 0.5 ng/mL and a quantitative LOD of 1.0 ng/mL in nucleocapsid protein spiked saliva samples. When validating 207 real human saliva samples confirmed by RT-PCR, the assay showed a sensitivity of 96.10% and a specificity of 99.23%, while being large-scale producible and easy to use, showing great potential for POC diagnostics and on-site mass screening (**Figure 1.22B**).

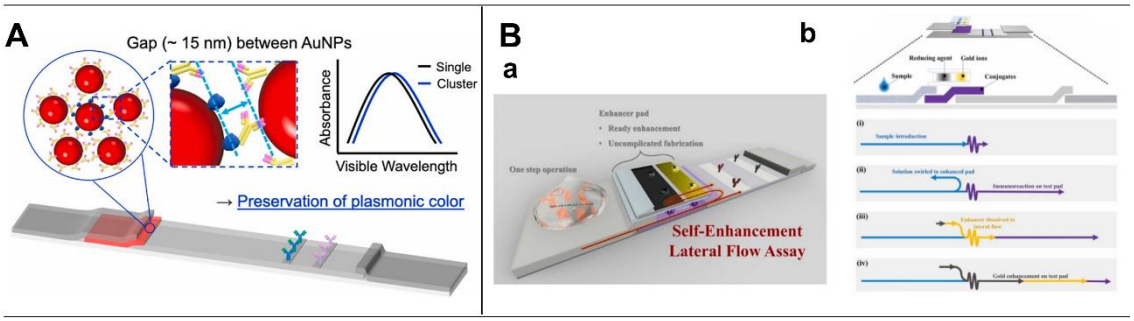

Figure 1.22. AuNPs clusters or *in situ* growth of AuNPs-based LFA for COVID-19 diagnosis. (A) Schematic illustration of plasmon color-preserved AuNPs clusters and their absorption properties when using proteins such as streptavidin and biotinylated antibodies as proposed herein. (B): (a) Schematic illustration of a self-enhancement LFIA for COVID-19 diagnosis; (b) Schematic presentation showing the flow behavior of self-enhancement of enhancing-LFIA. Adapted with permission from ref. 156 (A) and 164 (B). Copyright 2022 Elsevier (A) and 2023 Elsevier (B).

1.2.4.4. Integration with CRISPR-Cas system with AuNPs-based LFAs

CRISPR, which stands for Clustered Regularly Interspaced Short Palindromic Repeats, is a revolutionary technology that allows precise editing of DNA within living organisms. It originated from the natural defense mechanisms of bacteria and archaea (the domain of single-celled microorganisms). CRISPR-based diagnostics (e.g., SHERLOCK and DETECTR) leverage the precision and specificity of the CRISPR-Cas system to detect and identify specific nucleic acid sequences, such as DNA or RNA. In particular, the integration of the CRISPR-Cas system with AuNPs-based LFAs has been explored for COVID-19 diagnosis, offering a rapid and specific approach for detecting the presence of the SARS-CoV-2 virus or its genetic material. This hybrid method combines the precision of CRISPR-mediated nucleic acid detection with the simplicity and visual readout of LFAs.

.Xiong E. et al.[157] developed a CRISPR/Cas9-mediated dual-test line LFA combined with multiplexed RT-RPA for the simultaneous detection of the envelope (E) and open reading frame 1ab (ORF1ab) genes of SARS-CoV-2 in a single strip test. For detection of the E and ORF1ab genes from cell-cultured SARS-CoV-2 and SARS-CoV-2 viral RNA standards, the assay showed a visual LOD of 100 RNA copies/reaction (i.e. 4 copies/μL), and for genes detection from

nasopharyngeal swab samples, the assay showed 97.14% positive predictive agreement (PPA) and 100% negative predictive agreement (NPA). The whole procedure can be complete in 1h, providing a more sensitive, accurate and convenient tool for the diagnosis of COVID-19 or other infectious diseases in resource-limited settings (**Figure 1.23A**).

Li Z. et al.[165] developed an instrument-free, CRISPR/Cas12a-based LFA using a self-contained microfluidic and RT-RPA amplification technique for the simple and cost-efficient detection of SARS-CoV-2 RNA. In the system, a portable hand warmer was used to incubate the microfluidic chip, enabling current-free molecular diagnostics. The self-contained microfluidic system showed a visual sensitivity of 100 RNA copies per test with the naked eye. In the validation application with clinical nasopharyngeal swabs confirmed by real-time RT-PCR, the system demonstrated a sensitivity of 94.1%, specificity of 100% and accuracy of 95.8% for SARS-CoV-2 RNA detection, showing potential for POC diagnostics of COVID-19 disease (**Figure 1.23B**).

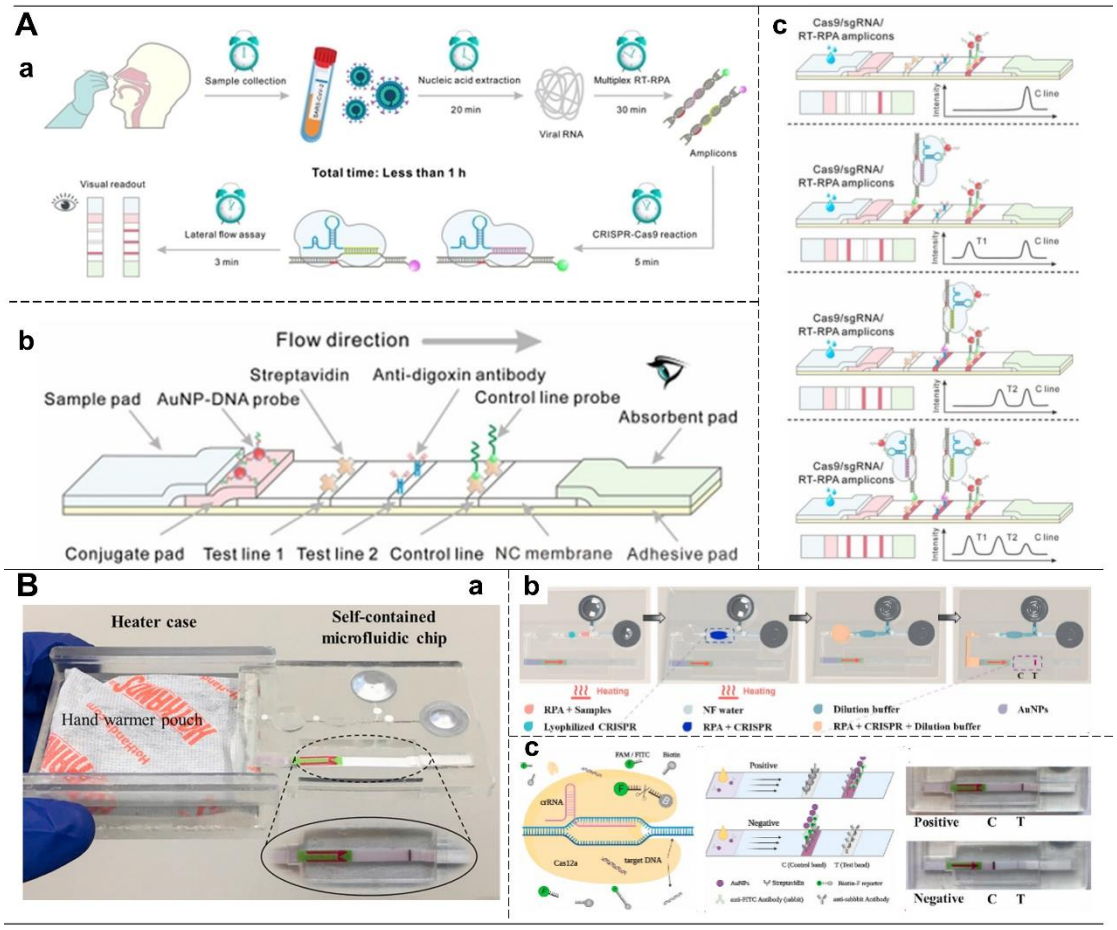

Figure 1.23. Integration with CRISPR-Cas system with AuNPs-based LFAs. (A) Simultaneous dual-gene

diagnosis of SARS-CoV-2 using CRISPR/Cas9-mediated LFA: (a) Workflow and time requirements for clinical diagnosis of SARS-CoV-2 using CRISPR/Cas9-mediated LFA; (b) Design of the tripe-line LFA (TL-LFA); (c) Visual CRISPR/Cas9-mediated TL-LFA readout by naked eye, and four potential test results for TL-LFA including negative test result, E-gene positive, Orf1ab-gene positive, and both E-gene and Orf1ab-gene positive. (B) CRISPR-based LFA integrated with a self-contained microfluidic system for diagnosis of SARS-CoV-2: (a) Photograph of the self-contained microfluidic system, including the self-contained microfluidic chip and hand warmer-powered heater case; (b) Process of operating the self-contained microfluidic system: RT-RPA amplification, CRISPR-Cas12a cleavage, dilution, and LFA; (c) The cleavage of ssDNA-BF probe by CRISPR-Cas12a activated by RPA amplicons (left), schematic of visual detection mechanism of LFA (middle), and photographs of LFA visual detection for positive and negative samples in the self-contained microfluidic chip. Adapted with permission from ref. 157 (A) and 165 (B). Copyright 2021 John Wiley and Sons and 2022 Elsevier (B).

1.3. Conclusions

AuNPs have gained significant attention in the development of optical biosensors for POC due to their unique optical properties, biocompatibility, and ease of functionalization. These sensors offer rapid, sensitive, and specific detection of various biomolecules, making them valuable tools for medical diagnostics. AuNPs are widely used as colorimetric labels for POC diagnostics. This is due to the distinctive optical properties set by the size and shape of the AuNPs (e.g. SPR or LSPR), the easy functionalization with different biorecognition elements (e.g. antibodies, aptamers, or DNA probes), the aggregation or dispersion of AuNPs leading to a shift in the SPR of the AuNPs and casuing a color change visible to the naked eye, the signal amplification by different strategies In this introduction, optical biosensors based on AuNPs aggregation, etching and , growth for POC diagnostics were introduced, reporting works published from 2020 to 2023. Various AuNPs aggregation-based assays can be divided into label-free and recognition element-labeled AuNP. Etching-based optical biosensors have been developed by introducing common etching agents (e.g., TMB^{2+} and iodine ions) or some other chemical reagents (e.g., ascorbic acid, superoxide radicals, and $HAuCl_4$). Optical biosensors based on AuNPs growth or metallization, in which AuNPs are formed *in situ* by enzymes or reducing agents, have been developed, especially in conjunction with portable devices for POC diagnostics.

In addition to AuNPs as colorimetric labels for POC diagnostics, AuNPs have also been widely combined with various fluorophores (e.g., organic dyes, carbon dots, quantum dots and gold nanoclusters, and upconversion nanoparticles), even CRISPR systems and microfluidic platforms to develop fluorescent biosensors to increase sensitivity for POC diagnostics, especially for infectious diseases and cancer diagnosis. The various fluorescent biosensors were constructed based on the inner filter effect (IFE), metal-enhanced fluorescence effect (MEF) and Förster resonance energy transfer (FRET) between AuNPs and various fluorophores, combining sensitivity, specificity, and rapidity in a compact and cost-effective format. Their versatility and ability to detect multiple analytes simultaneously make them valuable tools in healthcare and diagnostics.

In addition, AuNPs-based optical biosensors integrated with smartphone for diagnostic of biomarkers were included in the published chapter, attached in the annexes section

1.4. References

1. Strimbu, K. & Tavel, J. A. What are biomarkers? *Curr. Opin. HIV AIDS* **5**, 463–466 (2010).

2. Hong, J. M. *et al.* Point-of-care diagnostic tests for tuberculosis disease. *Sci. Transl. Med.* **14**, eabj4124 (2023).

3. Wang, X., Tian, L., Lu, J. & Ng, I. O.-L. Exosomes and cancer - Diagnostic and prognostic biomarkers and therapeutic vehicle. *Oncogenesis* **11**, 54 (2022).

4. Byeon, S. K. *et al.* Development of a multiomics model for identification of predictive biomarkers for COVID-19 severity: a retrospective cohort study. *Lancet Digit. Heal.* **4**, e632–e645 (2022).

5. Strauss, D. G., Wang, Y.-M., Florian, J. & Zineh, I. Pharmacodynamic Biomarkers Evidentiary Considerations for Biosimilar Development and Approval. *Clin. Pharmacol. Ther.* **113**, 55–61 (2023).

6. de Masson, A. *et al.* High-throughput sequencing of the T cell receptor β gene identifies aggressive early-stage mycosis fungoides. *Sci. Transl. Med.* **10**, eaar5894 (2018).

7. Bharucha, T. *et al.* Mass spectrometry-based proteomic techniques to identify

cerebrospinal fluid biomarkers for diagnosing suspected central nervous system infections. A systematic review. *J. Infect.* **79**, 407–418 (2019).

8. Hansson, O. Biomarkers for neurodegenerative diseases. *Nat. Med.* **27**, 954–963 (2021).

9. Teunissen, C. E. *et al.* Blood-based biomarkers for Alzheimer's disease: towards clinical implementation. *Lancet Neurol.* **21**, 66–77 (2022).

10. Hermann, P. *et al.* Biomarkers and diagnostic guidelines for sporadic Creutzfeldt-Jakob disease. *Lancet Neurol.* **20**, 235–246 (2021).

11. Marcatti, M. *et al.* Quantification of Circulating Cell Free Mitochondrial DNA in Extracellular Vesicles with PicoGreen™ in Liquid Biopsies: Fast Assessment of Disease/Trauma Severity. *Cells* vol. 10 (2021).

12. Singh, S., Podder, P. S., Russo, M., Henry, C. & Cinti, S. Tailored point-of-care biosensors for liquid biopsy in the field of oncology. *Lab Chip* **23**, 44–61 (2023).

13. Ramirez-Garrastacho, M. *et al.* Extracellular vesicles as a source of prostate cancer biomarkers in liquid biopsies: a decade of research. *Br. J. Cancer* **126**, 331–350 (2022).

14. Petrou, L. & Ladame, S. On-chip miRNA extraction platforms: recent technological advances and implications for next generation point-of-care nucleic acid tests. *Lab Chip* **22**, 463–475 (2022).

15. Zhu, H. *et al.* The vision of point-of-care PCR tests for the COVID-19 pandemic and beyond. *TrAC Trends Anal. Chem.* **130**, 115984 (2020).

16. Xu, L. *et al.* Portable integrated digital PCR system for the point-of-care quantification of BK virus from urine samples. *Biosens. Bioelectron.* **175**, 112908 (2021).

17. Bokelmann, L. *et al.* Point-of-care bulk testing for SARS-CoV-2 by combining hybridization capture with improved colorimetric LAMP. *Nat. Commun.* **12**, 1467 (2021).

18. Liu, D. *et al.* A microfluidic-integrated lateral flow recombinase polymerase amplification (MI-IF-RPA) assay for rapid COVID-19 detection. *Lab Chip* **21**, 2019–2026 (2021).

19. Ji, T., Zhang, J., Gao, Y., Zhao, C. & Gao, X. A rapid and visual detection of Staphylococcus haemolyticus in clinical specimens with RPA-LFS. *Anal. Chim. Acta* **1273**, 341534 (2023).

20. van Dongen, J. E. *et al.* Point-of-care CRISPR/Cas nucleic acid detection: Recent advances, challenges and opportunities. *Biosens. Bioelectron.* **166**, 112445 (2020).

21. Wang, X. *et al.* Dual Methylation-Sensitive Restriction Endonucleases Coupling with an RPA-Assisted CRISPR/Cas13a System (DESCS) for Highly Sensitive Analysis of DNA Methylation and Its Application for Point-of-Care Detection. *ACS Sensors* **6**, 2419–2428 (2021).

22. Chen, H., Zhou, X., Wang, M. & Ren, L. Towards Point of Care CRISPR-Based Diagnostics: From Method to Device. *Journal of Functional Biomaterials* vol. 14 (2023).

23. Macchia, E. *et al.* Organic Field-Effect Transistor Platform for Label-Free, Single-Molecule Detection of Genomic Biomarkers. *ACS Sensors* **5**, 1822–1830 (2020).

24. Messner, C. B. *et al.* Ultra-High-Throughput Clinical Proteomics Reveals Classifiers of COVID-19 Infection. *Cell Syst.* **11**, 11-24.e4 (2020).

25. Ozcelikay, G. *et al.* Sensor-based MIP technologies for targeted metabolomics analysis. *TrAC Trends Anal. Chem.* **146**, 116487 (2022).

26. Kaur, J., Srivastava, R. & Borse, V. Recent advances in point-of-care diagnostics for oral cancer. *Biosens. Bioelectron.* **178**, 112995 (2021).

27. Wang, S. *et al.* Integration of cell phone imaging with microchip ELISA to detect ovarian cancer HE4 biomarker in urine at the point-of-care. *Lab Chip* **11**, 3411–3418 (2011).

28. Berg, B. *et al.* Cellphone-Based Hand-Held Microplate Reader for Point-of-Care Testing of Enzyme-Linked Immunosorbent Assays. *ACS Nano* **9**, 7857–7866 (2015).

29. C.C.G. Carneiro, M., Rodrigues, L. R., Moreira, F. T. C. & Goreti F. Sales, M. Paper-based ELISA for fast CA 15–3 detection in point-of-care. *Microchem. J.* **181**, 107756 (2022).

30. Lin, D. *et al.* A novel polymer-based nitrocellulose platform for implementing a multiplexed

microfluidic paper-based enzyme-linked immunosorbent assay. *Microsystems Nanoeng.* **8**, 53 (2022).

31. Dawson, E. D. *et al.* Multiplexed, microscale, microarray-based serological assay for antibodies against all human-relevant coronaviruses. *J. Virol. Methods* **291**, 114111 (2021).

32. Hu, X., Gao, X., Chen, S., Guo, J. & Zhang, Y. DropLab: an automated magnetic digital microfluidic platform for sample-to-answer point-of-care testing—development and application to quantitative immunodiagnostics. *Microsystems Nanoeng.* **9**, 10 (2023).

33. Lu, C. H. *et al.* Finger-powered agglutination lab chip with CMOS image sensing for rapid point-of-care diagnosis applications. *Lab Chip* **20**, 424–433 (2020).

34. Min, J. *et al.* CytoPAN—Portable cellular analyses for rapid point-of-care cancer diagnosis. *Sci. Transl. Med.* **12**, eaaz9746 (2020).

35. Sharifi, M., Hasan, A., Attar, F., Taghizadeh, A. & Falahati, M. Development of point-of-care nanobiosensors for breast cancers diagnosis. *Talanta* **217**, 121091 (2020).

36. Harpaldas, H. *et al.* Point-of-care diagnostics: recent developments in a pandemic age. *Lab Chip* **21**, 4517–4548 (2021).

37. Luo, R., Fong, Y., Boeras, D., Jani, I. & Vojnov, L. The clinical effect of point-of-care HIV diagnosis in infants: a systematic review and meta-analysis. *Lancet* **400**, 887–895 (2022).

38. Jiang, N. *et al.* Low-Cost Optical Assays for Point-of-Care Diagnosis in Resource-Limited Settings. *ACS Sensors* **6**, 2108–2124 (2021).

39. Shanmugasundaram, A., V Manorama, S., Kim, D.-S., Jeong, Y.-J. & Weon Lee, D. Toward Point-of-Care chronic disease Management: Biomarker detection in exhaled breath using an E-Nose sensor based on rGO/SnO2 superstructures. *Chem. Eng. J.* **448**, 137736 (2022).

40. Wang, C. *et al.* Point-of-care diagnostics for infectious diseases: From methods to devices. *Nano Today* **37**, 101092 (2021).

41. Clark, T. W. *et al.* Clinical impact of a routine, molecular, point-of-care, test-and-treat strategy for influenza in adults admitted to hospital (FluPOC): a multicentre, open-label, randomised controlled trial. *Lancet Respir. Med.* **9**, 419–429 (2021).

42. Yuan, H., Chen, P., Wan, C., Li, Y. & Liu, B.-F. Merging microfluidics with luminescence immunoassays for urgent point-of-care diagnostics of COVID-19. *TrAC Trends Anal. Chem.* **157**, 116814 (2022).

43. Tharakan, S., Faqah, O., Asghar, W. & Ilyas, A. Microfluidic Devices for HIV Diagnosis and Monitoring at Point-of-Care (POC) Settings. *Biosensors* vol. 12 (2022).

44. Xiao, Y., Thompson, A. J. & Howell, J. Point-of-Care Tests for Hepatitis B: An Overview. *Cells* vol. 9 (2020).

45. Gaydos, C. A., Manabe, Y. C. & Melendez, J. H. A Narrative Review of Where We Are With Point-of-Care Sexually Transmitted Infection Testing in the United States. *Sex. Transm. Dis.* **48**, S71–S77 (2021).

46. Cullen, L., Collinson, P. O. & Giannitsis, E. Point-of-care testing with high-sensitivity cardiac troponin assays: the challenges and opportunities. *Emerg. Med. J.* **39**, 861 LP – 866 (2022).

47. Park, H.-D. Current Status of Clinical Application of Point-of-Care Testing. *Arch. Pathol. Lab. Med.* **145**, 168–175 (2020).

48. Liu, Y. *et al.* Review of point-of-care platforms for diabetes: (1) sensing. *Sensors and Actuators Reports* **4**, 100113 (2022).

49. Zhang, M., Cui, X. & Li, N. Smartphone-based mobile biosensors for the point-of-care testing of human metabolites. *Mater. Today Bio* **14**, 100254 (2022).

50. Prajapati, A., Verma, N. & Pandya, A. Highly sensitive vertical flow based point-of-care immunokit for rapid and early detection of human CRP as a cardiovascular risk factor. *Biomed. Microdevices* **22**, 28 (2020).

51. Sahli, S. D. *et al.* Point-of-Care Diagnostics in Coagulation Management. *Sensors* **20**,

(2020).

52. Alving, K. *et al.* Point-of-care biomarkers in asthma management: Time to move forward. *Allergy* (2020).

53. Shrivastava, S., Trung, T. Q. & Lee, N.-E. Recent progress{,} challenges{,} and prospects of fully integrated mobile and wearable point-of-care testing systems for self-testing. *Chem. Soc. Rev.* **49**, 1812–1866 (2020).

54. Valera, E. *et al.* COVID-19 point-of-care diagnostics: present and future. *ACS Nano* **15**, 7899–7906 (2021).

55. Gowri, A., Ashwin Kumar, N. & Suresh Anand, B. S. Recent advances in nanomaterials based biosensors for point of care (PoC) diagnosis of Covid-19 – A minireview. *TrAC Trends Anal. Chem.* **137**, 116205 (2021).

56. Liu, Y., Zhan, L., Qin, Z., Sackrison, J. & Bischof, J. C. Ultrasensitive and Highly Specific Lateral Flow Assays for Point-of-Care Diagnosis. *ACS Nano* **15**, 3593–3611 (2021).

57. Pittman, T. W., Decsi, D. B., Punyadeera, C. & Henry, C. S. Saliva-based microfluidic point-of-care diagnostic. *Theranostics* **13**, 1091 (2023).

58. Lopes, L. C., Santos, A. & Bueno, P. R. An outlook on electrochemical approaches for molecular diagnostics assays and discussions on the limitations of miniaturized technologies for point-of-care devices. *Sensors and Actuators Reports* **4**, 100087 (2022).

59. Hu, L. *et al.* Chapter 11 - Optical smartphone-based sensing: diagnostic of biomarkers. in (eds. Ozkan, S. A., Bakirhan, N. K. & Mollarasouli, F. B. T.-T. D. of B.) 277–302 (Academic Press, 2022). doi:https://doi.org/10.1016/B978-0-12-822859-3.00003-1.

60. Byakodi, M. *et al.* Emerging 0D, 1D, 2D, and 3D nanostructures for efficient point-of-care biosensing. *Biosens. Bioelectron. X* **12**, 100284 (2022).

61. Blumenfeld, N. R. *et al.* Multiplexed reverse-transcriptase quantitative polymerase chain reaction using plasmonic nanoparticles for point-of-care COVID-19 diagnosis. *Nat. Nanotechnol.* **17**, 984–992 (2022).

62. Sahoo, S. R., Huey-Jen Hsu, S., Chou, D.-A., Wang, G.-J. & Chang, C.-C. Surface plasmon-enhanced fluorescence and surface-enhanced Raman scattering dual-readout chip constructed with silver nanowires: Label-free clinical detection of direct-bilirubin. *Biosens. Bioelectron.* **213**, 114440 (2022).

63. Li, S. *et al.* A HiPAD Integrated with rGO/MWCNTs Nano-Circuit Heater for Visual Point-of-Care Testing of SARS-CoV-2. *Adv. Funct. Mater.* **31**, 2100801 (2021).

64. Dave, S., Das, J. & Ghosh, S. *Advanced Nanomaterials for Point of Care Diagnosis and Therapy*. (Elsevier, 2022).

65. Zupančič, U., Jolly, P., Estrela, P., Moschou, D. & Ingber, D. E. Graphene Enabled Low-Noise Surface Chemistry for Multiplexed Sepsis Biomarker Detection in Whole Blood. *Adv. Funct. Mater.* **31**, 2010638 (2021).

66. Harpak, N., Borberg, E., Raz, A. & Patolsky, F. The “Bloodless” Blood Test: Intradermal Prick Nanoelectronics for the Blood Extraction-Free Multiplex Detection of Protein Biomarkers. *ACS Nano* **16**, 13800–13813 (2022).

67. Bachtiger, P. *et al.* Point-of-care screening for heart failure with reduced ejection fraction using artificial intelligence during ECG-enabled stethoscope examination in London, UK: a prospective, observational, multicentre study. *Lancet Digit. Heal.* **4**, e117–e125 (2022).

68. DeCamp, M. & Lindvall, C. Mitigating bias in AI at the point of care. *Science (80-.).* **381**, 150–152 (2023).

69. Qin, J., Guo, J., Tang, G., Li, L. & Yao, S. Q. Multiplex Identification of Post-Translational Modifications at Point-of-Care by Deep Learning-Assisted Hydrogel Sensors. *Angew. Chemie Int. Ed.* **62**, e202218412 (2023).

70. Porras, A. R., Rosenbaum, K., Tor-Diez, C., Summar, M. & Linguraru, M. G. Development and evaluation of a machine learning-based point-of-care screening tool for genetic syndromes in children: a multinational retrospective study. *Lancet Digit. Heal.* **3**, e635–e643 (2021).

71. Angehrn, Z. *et al.* Artificial intelligence and machine learning applied at the point of care.

Front. Pharmacol. **11**, 759 (2020).

72. James, B. L. *et al.* Validation of a Point-of-Care Optical Coherence Tomography Device with Machine Learning Algorithm for Detection of Oral Potentially Malignant and Malignant Lesions. *Cancers* vol. 13 (2021).

73. Frigieri, G., Robba, C., Machado, F. S., Gomes, J. A. & Brasil, S. Application of non-invasive ICP waveform analysis in acute brain injury: Intracranial Compliance Scale. *Intensive Care Med. Exp.* **11**, 5 (2023).

74. Shang, M., Guo, J. & Guo, J. Point-of-Care Testing of Infectious Diseases: Recent Advances. *Sensors & Diagnostics* (2023).

75. Tessaro, L., Aquino, A., de Carvalho, A. P. A. & Conte-Junior, C. A. A systematic review on gold nanoparticles based-optical biosensors for Influenza virus detection. *Sensors and Actuators Reports* **3**, 100060 (2021).

76. Zhou, W., Gao, X., Liu, D. & Chen, X. Gold nanoparticles for in vitro diagnostics. *Chem. Rev.* **115**, 10575–10636 (2015).

77. Cordeiro, M., Ferreira Carlos, F., Pedrosa, P., Lopez, A. & Baptista, P. V. Gold nanoparticles for diagnostics: advances towards points of care. *Diagnostics* **6**, 43 (2016).

78. Pellas, V. *et al.* Gold nanorods for LSPR biosensing: synthesis, coating by silica, and bioanalytical applications. *Biosensors* **10**, 146 (2020).

79. Amin, M. U. & Fang, J. Self-Assembled Gold Nano-Bipyramids for Solution-Based Surface-Enhanced Raman Spectroscopy Detection. *ACS Appl. Nano Mater.* **5**, 10421–10430 (2022).

80. Feng, J. *et al.* Bioconjugation of gold nanobipyramids for SERS detection and targeted photothermal therapy in breast cancer. *ACS Biomater. Sci. Eng.* **3**, 608–618 (2017).

81. Mousavi, S. M. *et al.* Gold nanostars-diagnosis, bioimaging and biomedical applications. *Drug Metab. Rev.* **52**, 299–318 (2020).

82. Zhang, W. *et al.* Effect of different-sized gold nanoflowers on the detection performance

of immunochromatographic assay for human chorionic gonadotropin detection. *Talanta* **194**, 604–610 (2019).

83. Song, C. *et al.* A gold nanoflower-based traceable drug delivery system for intracellular SERS imaging-guided targeted chemo-phototherapy. *J. Mater. Chem. B* **6**, 3030–3039 (2018).

84. Niazi, S. *et al.* Aptamer functionalized gold nanoclusters as an emerging nanoprobe in biosensing, diagnostic, catalysis and bioimaging. *Talanta* 125270 (2023).

85. Geng, H. *et al.* Noble Metal Nanoparticle Biosensors: From Fundamental Studies toward Point-of-Care Diagnostics. *Acc. Chem. Res.* **55**, 593–604 (2022).

86. Ventura, B. Della *et al.* Colorimetric test for fast detection of SARS-COV-2 in nasal and throat swabs. *ACS Sensors* **5**, 3043–3048 (2020).

87. Park, Y., Ryu, B., Ki, S. J., Liang, X. & Kurabayashi, K. Near-Infrared Multilayer MoS2 Photoconductivity-Enabled Ultrasensitive Homogeneous Plasmonic Colorimetric Biosensing. *Adv. Mater. Interfaces* **8**, 1–9 (2021).

88. Song, S., Wang, L., Li, J., Fan, C. & Zhao, J. Aptamer-based biosensors. *TrAC Trends Anal. Chem.* **27**, 108–117 (2008).

89. Kim, Y. S., Raston, N. H. A. & Gu, M. B. Aptamer-based nanobiosensors. *Biosens. Bioelectron.* **76**, 2–19 (2016).

90. Zhao, Y., Yavari, K. & Liu, J. Critical evaluation of aptamer binding for biosensor designs. *TrAC Trends Anal. Chem.* **146**, 116480 (2022).

91. Moabelo, K. L. *et al.* A Label-Free Gold Nanoparticles-Based Optical Aptasensor for the Detection of Retinol Binding Protein 4. *Biosensors* vol. 12 (2022).

92. Wen, L. *et al.* Colorimetric Aptasensor for the Visual and Microplate Determination of Clusterin in Human Urine Based on Aggregation Characteristics of Gold Nanoparticles. *ACS Omega* (2022) doi:10.1021/acsomega.2c08040.

93. Kumar, N. *et al.* Label-free peptide nucleic acid biosensor for visual detection of multiple

strains of influenza A virus suitable for field applications. *Anal. Chim. Acta* **1093**, 123–130 (2020).

94. Landa, G. *et al.* Selective point-of-care detection of pathogenic bacteria using sialic acid functionalized gold nanoparticles. *Talanta* **234**, 122644 (2021).

95. Bastami, T. R., Ghaedi, A., Mitchell, S. G., Javadian-Saraf, A. & Karimi, M. Sonochemical synthesis of polyoxometalate-stabilized gold nanoparticles for point-of-care determination of acetaminophen levels: preclinical study in an animal model. *RSC Adv.* **10**, 16805–16816 (2020).

96. Mo, X. *et al.* Simple, rapid, portable and quantitative sensing of Fe3+ ions via analyte-triggered redox reactions mediating Tyndall effect enhancement of Au nanoparticles. *Microchem. J.* **174**, 107075 (2022).

97. Wang, R., Bowling, I. & Liu, W. Cost effective surface functionalization of gold nanoparticles with a mixed DNA and PEG monolayer for nanotechnology applications. *Rsc Adv.* **7**, 3676–3679 (2017).

98. Wang, L., Liu, Z.-J., Cao, H.-X. & Liang, G.-X. Ultrasensitive colorimetric miRNA detection based on magnetic 3D DNA walker and unmodified AuNPs. *Sensors Actuators B Chem.* **337**, 129813 (2021).

99. López-Valls, M. *et al.* CASCADE: Naked eye-detection of SARS-CoV-2 using Cas13a and gold nanoparticles. *Anal. Chim. Acta* **1205**, 1–11 (2022).

100. Alafeef, M., Moitra, P., Dighe, K. & Pan, D. RNA-extraction-free nano-amplified colorimetric test for point-of-care clinical diagnosis of COVID-19. *Nat. Protoc.* **16**, 3141–3162 (2021).

101. Wei, S. *et al.* Exponential amplification reaction and triplex DNA mediated aggregation of gold nanoparticles for sensitive colorimetric detection of microRNA. *Anal. Chim. Acta* **1095**, 179–184 (2020).

102. Yadav, S. & Satija, J. Shape dependent sensing potential of gold nanoparticles in etching based multicolorimetric plasmonic-ELISA. *Nanoscale Adv.* **4**, 3928–3939 (2022).

103. Liu, D. *et al.* Microfluidic-Integrated Multicolor Immunosensor for Visual Detection of HIV-1 p24 Antigen with the Naked Eye. *Anal. Chem.* **92**, 11826–11833 (2020).

104. Ma, L., Abugalyon, Y. & Li, X. Multicolorimetric ELISA biosensors on a paper/polymer hybrid analytical device for visual point-of-care detection of infection diseases. *Anal. Bioanal. Chem.* **413**, 4655–4663 (2021).

105. Li, D. Y. *et al.* Target-induced tripedal G-quadruplex DNAzyme for multicolor visual point-of-care testing of biomarkers using Au nanorods-decorated electrospun nanofibrous films. *Sensors Actuators B Chem.* **371**, 132510 (2022).

106. Wang, F., Na, N. & Ouyang, J. A catalytic—regulated gold nanorods etching process as a receptor with multiple readouts for protein detection. *Sensors Actuators B Chem.* **318**, 128215 (2020).

107. Zhou, J. *et al.* Enzyme–Nanozyme Cascade Reaction-Mediated Etching of Gold Nanorods for the Detection of Escherichia coli. *ACS Appl. Nano Mater.* **3**, 9016–9025 (2020).

108. Zhao, X. *et al.* Smartphone-assisted point-of-care testing of nucleic acids based on hybridization chain reaction, magnetic beads, and gold nanorods etching. *Sensors Actuators B Chem.* **392**, 134111 (2023).

109. Campu, A., Lerouge, F., Maniu, D., Magyari, K. & Focsan, M. Ultrasensitive SEIRA detection using gold nanobipyramids: Toward efficient multimodal immunosensor. *J. Mol. Struct.* **1246**, 131160 (2021).

110. Campu, A. *et al.* Gold nanobipyramids performing as highly sensitive dual-modal optical immunosensors. *Anal. Chem.* **90**, 8567–8575 (2018).

111. Yu, L. *et al.* A multicolor immunosensor for point-of-care testing NTRK1 gene fusion. *Sensors Actuators B Chem.* **346**, 130473 (2021).

112. Zhang, X., Sucre-Rosales, E., Byram, A., Hernandez, F. E. & Chen, G. Ultrasensitive Visual Detection of Glucose in Urine Based on the Iodide-Promoted Etching of Gold Bipyramids. *ACS Appl. Mater. Interfaces* **12**, 49502–49509 (2020).

113. Zhang, Y.-D., Ma, C. & Shi, Y.-P. Gold bipyramids molecularly imprinted gel colorimetric device for whole blood cholesterol analysis. *Anal. Chim. Acta* **1236**, 340584 (2022).

114. Pomili, T., Donati, P. & Pompa, P. P. Paper-Based Multiplexed Colorimetric Device for the Simultaneous Detection of Salivary Biomarkers. *Biosensors* vol. 11 (2021).

115. Torné-Morató, H., Donati, P. & Pompa, P. P. Nanoplasmonic Strip Test for Salivary Glucose Monitoring. *Nanomaterials* vol. 12 (2022).

116. Yi, J. *et al.* Point-of-Care Detection of Antioxidant in Agarose-Based Test Strip through Antietching of Au@Ag Nanostars. *ACS Appl. Mater. Interfaces* **15**, 29789–29800 (2023).

117. Zhang, Y. *et al.* Plasmonic Colorimetric Biosensor for Sensitive Exosome Detection via Enzyme-Induced Etching of Gold Nanobipyramid@MnO2 Nanosheet Nanostructures. *Anal. Chem.* **92**, 15244–15252 (2020).

118. Khani, H., Abbasi, S., Tavakkoli Yaraki, M. & Gholivand, M. B. Colorimetric detection and determination of glutathione based on superoxide radical-assisted etching approach. *Microchem. J.* **173**, 107006 (2022).

119. Zhou, J. *et al.* Integrating multiple hybridization chain reactions on gold nanoparticle and alkaline phosphatase-mediated in situ growth of gold nanobipyramids: An ultrasensitive and high color resolution colorimetric method to detect the mecA gene of Staphylococcus aure. *J. Hazard. Mater.* **418**, 126223 (2021).

120. Appidi, T., Mudigunda, S. V., Kodandapani, S. & Rengan, A. K. Development of label-free gold nanoparticle based rapid colorimetric assay for clinical/point-of-care screening of cervical cancer. *Nanoscale Adv.* **2**, 5737–5745 (2020).

121. Appidi, T. *et al.* Development of a Point-of-Care Cervico-Vaginal Sampling/Testing Device for the Colorimetric Detection of Cervical Cancer. *Diagnostics* **13**, (2023).

122. Sivakumar, R., Dinh, V. P. & Lee, N. Y. Ultraviolet-induced in situ gold nanoparticles for point-of-care testing of infectious diseases in loop-mediated isothermal amplification. *Lab Chip* **21**, 700–709 (2021).

123. Chen, S., Yu, Y.-L. & Wang, J.-H. Inner filter effect-based fluorescent sensing systems: A review. *Anal. Chim. Acta* **999**, 13–26 (2018).

124. Qin, X., Yuan, C., Chen, Y. & Wang, Y. A fluorescein–gold nanoparticles probe based on inner filter effect and aggregation for sensing of biothiols. *J. Photochem. Photobiol. B Biol.* **210**, 111986 (2020).

125. Liu, D. *et al.* Design of fluorescence system based on rutin functionalized gold nanoparticles: Sensitive detection of etimicin via a smartphone in the food and human samples. *Arab. J. Chem.* **15**, 104325 (2022).

126. Zhang, G.-Q. *et al.* A flow injection fluorescence “turn-on” sensor for the determination of metformin hydrochloride based on the inner filter effect of nitrogen-doped carbon dots/gold nanoparticles double-probe. *Spectrochim. Acta Part A Mol. Biomol. Spectrosc.* **250**, 119384 (2021).

127. Le, T.-H., Kim, J.-H. & Park, S.-J. “Turn on” Fluorescence Sensor of Glutathione Based on Inner Filter Effect of Co-Doped Carbon Dot/Gold Nanoparticle Composites. *International Journal of Molecular Sciences* vol. 23 (2022).

128. Bao, Q. *et al.* Ultrasensitive off-on-off fluorescent nanosensor for protamine and trypsin detection based on inner-filter effect between N,S-CDs and gold nanoparticles. *Microchem. J.* **168**, 106409 (2021).

129. Zhao, Q. *et al.* Fluorometric discrimination of tyrosine isomers based on the inner filter effect of chiral Au nanoparticles on MoS2 quantum dots. *Anal. Methods* **13**, 2290–2296 (2021).

130. Li, M. *et al.* An inner filter effect-based fluorescent aptasensor for sensitive detection of kanamycin in complex samples using gold nanoparticles and graphene oxide quantum dots. *Anal. Methods* **15**, 843–848 (2023).

131. Halawa, M. I., Lai, J. & Xu, G. Gold nanoclusters: synthetic strategies and recent advances in fluorescent sensing. *Mater. Today Nano* **3**, 9–27 (2018).

132. Chen, L.-Y., Wang, C.-W., Yuan, Z. & Chang, H.-T. Fluorescent gold nanoclusters: recent

advances in sensing and imaging. *Anal. Chem.* **87**, 216–229 (2015).

133. Pezhhan, H., Akhond, M. & Shamsipur, M. Histidine capped-gold nanoclusters mediated fluorescence detection of glucose and hydrogen peroxide based on glucose oxidase-mimicking property of gold nanoparticles via an inner filter effect mechanism. *J. Lumin.* **228**, 117604 (2020).

134. Liu, J. *et al.* A Rapid SARS-CoV-2 Nucleocapsid Protein Profiling Assay with High Sensitivity Comparable to Nucleic Acid Detection. *Anal. Chem.* **94**, 14627–14634 (2022).

135. Phuc, L. G. *et al.* Metal-Enhanced Fluorescence for Alpha-Fetoprotein Detection and for SERS Using Hybrid Nanoparticles of Magnetic Cluster Core—Plasmonic Shell Composite. *Chemosensors* vol. 11 (2023).

136. Luan, J. *et al.* Ultrabright fluorescent nanoscale labels for the femtomolar detection of analytes with standard bioassays. *Nat. Biomed. Eng.* **4**, 518–530 (2020).

137. Choi, J.-H., Lim, J., Shin, M., Paek, S.-H. & Choi, J.-W. CRISPR-Cas12a-Based Nucleic Acid Amplification-Free DNA Biosensor via Au Nanoparticle-Assisted Metal-Enhanced Fluorescence and Colorimetric Analysis. *Nano Lett.* **21**, 693–699 (2021).

138. Susu, L., Vulpoi, A., Astilean, S. & Focsan, M. Portable Plasmonic Paper-Based Biosensor for Simple and Rapid Indirect Detection of CEACAM5 Biomarker via Metal-Enhanced Fluorescence. *International Journal of Molecular Sciences* vol. 23 (2022).

139. Wang, Z. *et al.* Microneedle patch for the ultrasensitive quantification of protein biomarkers in interstitial fluid. *Nat. Biomed. Eng.* **5**, 64–76 (2021).

140. Miranda, B. *et al.* Hollow Microneedle-based Plasmonic Sensor for on Patch Detection of Molecules in Dermal Interstitial Fluid. *Adv. Mater. Technol.* **2300037**, 1–15 (2023).

141. Minopoli, A. *et al.* Double-Resonant Nanostructured Gold Surface for Multiplexed Detection. *ACS Appl. Mater. Interfaces* **14**, 6417–6427 (2022).

142. Wang, Z. *et al.* Plasmonically-enhanced competitive assay for ultrasensitive and multiplexed detection of small molecules. *Biosens. Bioelectron.* **200**, 113918 (2022).

143. Miranda, B. *et al.* Plasmonic Hydrogel Nanocomposites with Combined Optical and Mechanical Properties for Biochemical Sensing. *Chemistry Proceedings* vol. 5 (2021).

144. Wu, Y., Feng, Y. & Li, X. Classification of breast cancer by a gold nanoparticle based multicolor fluorescent aptasensor. *J. Colloid Interface Sci.* **611**, 287–293 (2022).

145. Fu, X. *et al.* Exploring the Trans-Cleavage Activity of CRISPR/Cas12a on Gold Nanoparticles for Stable and Sensitive Biosensing. *Anal. Chem.* **93**, 4967–4974 (2021).

146. Liu, Z., Shang, C., Ma, H. & You, M. An upconversion nanoparticle-based photostable FRET system for long-chain DNA sequence detection. *Nanotechnology* **31**, 235501 (2020).

147. Li, L. *et al.* Rapid and ultrasensitive detection of SARS-CoV-2 spike protein based on upconversion luminescence biosensor for COVID-19 point-of-care diagnostics. *Mater. Des.* **223**, 111263 (2022).

148. Li, Y. *et al.* Opal photonic crystal-enhanced upconversion turn-off fluorescent immunoassay for salivary CEA with oral cancer. *Talanta* **258**, 124435 (2023).

149. Chen, X. *et al.* A rapid fluorescent aptasensor for point-of-care detection of C-reactive protein. *Talanta* **249**, 123661 (2022).

150. Lu, X., Hou, X., Tang, H., Yi, X. & Wang, J. A High-Quality CdSe/CdS/ZnS Quantum-Dot-Based FRET Aptasensor for the Simultaneous Detection of Two Different Alzheimer’s Disease Core Biomarkers. *Nanomaterials* vol. 12 (2022).

151. Mahani, M. *et al.* Label-free triplex DNA-based biosensing of transcription factor using fluorescence resonance energy transfer between N-doped carbon dot and gold nanoparticle. *Anal. Chim. Acta* **1181**, 338919 (2021).

152. Gu, Y., Peng, L., Ding, W., Wang, Y. & Zeng, X. An ultrasensitive FRET-based fluorescent low molecular weight heparin nanoprobe for quantifying heparanase activity. *Talanta* **254**, 124207 (2023).

153. Parolo, C. *et al.* Tutorial: design and fabrication of nanoparticle-based lateral-flow immunoassays. *Nat. Protoc.* **15**, 3788–3816 (2020).

154. Srithong, P. *et al.* A novel delayed lateral flow immunoassay for enhanced detection of SARS-CoV-2 spike antigen. *Microchim. Acta* **189**, 386 (2022).

155. Wang, C. *et al.* Sensitive and Simultaneous Detection of SARS-CoV-2-Specific IgM/IgG Using Lateral Flow Immunoassay Based on Dual-Mode Quantum Dot Nanobeads. *Anal. Chem.* **92**, 15542–15549 (2020).

156. Oh, H.-K. *et al.* Plasmon color-preserved gold nanoparticle clusters for high sensitivity detection of SARS-CoV-2 based on lateral flow immunoassay. *Biosens. Bioelectron.* **205**, 114094 (2022).

157. Xiong, E. *et al.* Simultaneous Dual-Gene Diagnosis of SARS-CoV-2 Based on CRISPR/Cas9-Mediated Lateral Flow Assay. *Angew. Chemie Int. Ed.* **60**, 5307–5315 (2021).

158. Parolo, C., Medina-Sánchez, M., de la Escosura-Muñiz, A. & Merkoçi, A. Simple paper architecture modifications lead to enhanced sensitivity in nanoparticle based lateral flow immunoassays. *Lab Chip* **13**, 386–390 (2013).

159. Rivas, L., Medina-Sánchez, M., de la Escosura-Muñiz, A. & Merkoçi, A. Improving sensitivity of gold nanoparticle-based lateral flow assays by using wax-printed pillars as delay barriers of microfluidics. *Lab Chip* **14**, 4406–4414 (2014).

160. Sena-Torralba, A. *et al.* Lateral flow assay modified with time-delay wax barriers as a sensitivity and signal enhancement strategy. *Biosens. Bioelectron.* **168**, 112559 (2020).

161. Kim, K. *et al.* Rapid PCR kit: lateral flow paper strip with Joule heater for SARS-CoV-2 detection. *Mater. Horizons* **10**, 1697–1704 (2023).

162. Boumar, I., Deliorman, M., Sukumar, P. & Qasaimeh, M. A. Spike- and nucleocapsid-based gold colloid assay toward the development of an adhesive bandage for rapid SARS-CoV-2 immune response detection and screening. *Microsystems Nanoeng.* **9**, 82 (2023).

163. Hong, D., Jo, E.-J., Jung, C. & Kim, M.-G. Absorption-Modulated SiO2@Au Core–Satellite Nanoparticles for Highly Sensitive Detection of SARS-CoV-2 Nucleocapsid Protein in Lateral Flow Immunosensors. *ACS Appl. Mater. Interfaces* **14**, 45189–45200 (2022).

164. Ruantip, S. *et al.* Self-enhancement lateral flow immunoassay for COVID-19 diagnosis. *Sensors Actuators B Chem.* **389**, 133898 (2023).

165. Li, Z. *et al.* Instrument-free, CRISPR-based diagnostics of SARS-CoV-2 using self-contained microfluidic system. *Biosens. Bioelectron.* **199**, 113865 (2022).

CHAPTER 2

Thesis objectives

The main aim of this PhD was to investigate and advance the field of optical biosensors based on gold nanomaterials for point-of-care (POC) diagnostics. This included not only the exploration of gold nanomaterials as efficient colorimetric labels in lateral flow assays, but also as superior bioluminescence absorbers within a novel bioanalytical platform for enzyme-free bioluminescent bacteria-linked immunosorbent assays.

Over the course of this research several key projects and milestones have been achieved, all of which have contributed significantly to the overall goal. These are described below:

- Development of LFAs to detect the SARS-CoV-2 nucleoprotein.
    - Rigorous screening and selection of antibody pairs from the extensive range of newly developed commercial antibodies that can be used effectively in LFAs.
    - Evaluation and application of AuNPs-based LFAs in artificial saliva samples.
- Commitment to improving the sensitivity of LFAs, a critical aspect for the effectiveness of POC diagnostic tools
    - Synthesis and characterization of size controllable Au-IrO_2 nanoflowers (NFs).
    - Design and preparation of LFAs using Au-IrO_2 NFs.
    - A detailed comparison and evaluation of the performance of AuNPs-based and Au-IrO2 NFs-based LFAs, highlighting the advantages of the latter.
- Use of AuNPs and Au-IrO_2 NFs as bioluminescence absorber for bioluminescence based ELISA (BBLISA), a faster, safer, cheaper and more user-friendly alternative to conventional ELISA.
    - Study of the inner filter effect (IFE) between bioluminescent bacteria *Allivibrio fischeri* and metallic nanoparticles (AuNPs and Au-IrO_2 NFs).
    - The thoughtful design and development of BBLISA using AuNPs and Au-IrO_2 NFs, demonstrating their versatility.
    - Evaluation and comparison of the performance of BBLISA and traditional ELISA for the detection of two clinically relevant biomarkers (i.e., human IgG and nucleoprotein of SARS-CoV-2)

CHAPTER 3

AuNPs as colorimetric labels in LFAs for detection of SARS-CoV-2 nucleoprotein

3.1. Introduction

The COVID-19 pandemic[1–3] has shown the importance of developing reliable yet easy-to-use, cheap, fast, and portable diagnostic devices to support mass testing[4–10]. Diagnostic testing is fundamental for a rapid screening of the population, to identify and track positive cases (i.e. both symptomatic and asymptomatic individuals), and immunity assessment[11,12]. As suggested by World Health Organization (WHO), in order to meet such a high demand of testing, countries have been relying on Lateral Flow Assays (LFAs)[13]. Indeed, such molecular sensing platforms allow to achieve the rapid (< 30 min), low-cost (5 USD), and single-step detection of the SARS-CoV-2 biomarkers[14]. Moreover, LFAs are an evolving platform with constantly improving sensitivity[15–17]. Our group recently provided a protocol describing the fabrication of a LFA to detect human IgG[18]. This is a generalisable protocol that can be easily adapted to other targets, such as SARS-CoV-2 virus, only by changing the bioreceptors (e.g. antibodies or aptamers). However, the selection of suitable bioreceptors for the detection of SARS-CoV-2 unveiled several experimental hurdles, which I want to share with the community. More specifically, I want to raise the attention towards the importance of a comprehensive characterisation of bioreceptors (in this case, antibodies) before their implementation into LFAs. Many studies compare the performance of commercial SARS-CoV-2 diagnostic kits[19–26], but to the best of our knowledge, only one recent work focuses on the technical challenges behind the bioreceptor selection[27].

The COVID-19 pandemic represents a unique situation due to the scarcity of antibodies against SARS-CoV-2 antigens at the beginning of the outbreak (from December 2019 to May 2020). During this period, the research community made an important effort in the characterisation process to select the proper antibodies to rapidly face the fast spread of the virus. The main goal of this characterisation is to understand if the selected antibodies exhibit the required binding properties to work in a LFA platform. Specifically, antibodies have to display: (1) stability, in order to work at variable environmental conditions (temperature, humidity, pressure) and support long-term storage; (2) fast binding kinetics, due to the short time window for the bioreceptor analyte interaction in LFA assay (in the range of seconds to few minutes); (3) strong binding affinity, as I

want the signal to remain stable while and after the assay takes place.[18] Unfortunately, besides already identified technical problems associated with antibodies such as batch to batch differences[28–31], suppliers do not provide enough characterisation of important binding parameters (e.g. binding and kinetic constants), and they test antibodies using only standard laboratory procedures (e.g., ELISA, Western Blot). A parallel approach could be the estimation of these parameters through thermodynamics, binding, and kinetics studies, but this requires resources, time, and facilities that private companies may not be willing to implement[18]. This lack of experimental data does not allow developers to pursue a rational selection of the antibodies forcing them into a trial-and-error approach. Since this can hide many technical challenges, here I present a study which describes how to proceed in such circumstances with experimental tools that are more available and can be performed by any laboratory, always keeping in mind that the final goal is the development of a colorimetric LFA to be implemented in COVID-19 diagnostics, and considering that similar scenarios can occur in the future.

3.2. Materials and methods

3.2.1. Reagents and devices

17 commercial anti-SARS-CoV-2 nucleoprotein antibodies are listed in Table 3.1. For further information, contact the authors. Artificial saliva for medical and dental research (part number 1700-0305) was purchased from LCTech GmbH (Obertaufkirchen, Germany) and it was used as received. Tetrachloroauric acid trihydrate 99%, sodium citrate, phosphate buffer saline (PBS) tablets, disodium hydrogen phosphate heptahydrate, monosodium phosphate, sodium bicarbonate, sodium carbonate anhydrous, boric acid, sodium tetraborate decahydrate, hydrochloric acid, sodium hydroxide, bovine serum albumin (BSA), Tween-20, 3,3′,5,5′-Tetramethylbenzidine (TMB, cat no. T0440), and sulfuric acid were purchased from Sigma-Aldrich (Spain). Secondary antibodies labelled with horse radish peroxidase (HRP) chicken anti-rabbit IgG (ab6829) and chicken anti-mouse IgG (ab6814) was purchased from Abcam (Cambridge, United Kingdom). SARS-CoV-2 nucleoprotein-his recombinant protein (40588-V08B) was purchased from Sino Biological. Transparent immuno nonsterile 96-well microplates (10777621) was purchased from Thermo Fisher (Spain). Nitrocellulose membrane CN150 was purchased from Sartorius Stediem (Göttingen, Germany). Cellulose membrane (CFSP001700) and glass

fibre were purchased from Merck Millipore (Billerica, MA, USA). Supporting adhesive cards were purchased from Kenosha (Amstelveen, The Netherlands). TEM grids (Ted Pella carbon film 300 MESH Copper grids CF300-CU 01843-F) were purchased from Monocomp Instrumentación (Spain).

AuNPs were synthesised on an IKA® RCT basic IKAMAG™ hot plate magnetic stirrer (Merck Millipore, USA). The conjugates of AuNPs with antibodies was performed in a PCMT ThermoShaker (Grant Instruments, UK). Nanoparticles were centrifuged in an Allegra 64 R centrifuge from Beckman Coulter (USA). A lateral flow reagent dispenser was used to deposit the antibodies on the nitrocellulose membrane (IsoFlow Bioreagent, Imagene Technology, Germany). The SkanMulti reader was provided by Skannex (Oslo, Norway). Colorimetric signal from ELISA assays was acquired by the spectrophotometer SpectraMax iD3 from Molecular Devices (San José, CA, USA). TEM analysis was performed using HR TEM Tecnic G2-F20 from FEI (Hillsboro, OR, USA). DLS and Z-potential measurements were performed using ZetaSizer Nano ZS (Malvern, United Kingdom).

3.2.2. ELISA assay for selection of antibodies

A solution of anti-nucleoprotein monoclonal antibodies (anti-nucleoprotein mAbs, capture antibodies M1, M2, M3, M4, M5, H1, and H2) was prepared in carbonate-bicarbonate buffer (CBS, 0.05M, pH 9.6) at a concentration of 5 µg/mL, and 100 µL was used to coat the ELISA wells overnight at 4 °C. Then, the antibodies solution was removed and the wells were washed three times using 250 µL of washing buffer PBST (0.01M PBS, 0.1% Tween-20, pH 7.4). Next, 200 µL of a solution of 3% BSA in PBS (0.01 M, pH 7.4) were added in the wells for blocking free sites for 1 h at 37 °C and the BSA solution was removed and the wells were washed just like previous washing steps. The solutions of nucleoprotein were prepared in PBS at concentrations of 0 ng/mL (blank/negative) and 100 ng/mL (positive), and 100 µL of the solutions were added into the wells and incubated for 1h at 25 °C. Then 100 µL of 0.5 µg/mL anti-nucleoprotein Abs (detection antibodies R1, R2, R3, R4, R5, R6, R7, R8, R9, R10 or M1-M5) were added into the wells and incubated for 1h at 25 °C. Next, 100 µL of secondary antibody modified with HRP (0.1 µg/mL) were added into the wells and incubated for another 1h at 25 °C. After every incubation process (incubation with nucleoprotein, detection antibodies, and secondary antibodies), three to five

washing steps were followed. 100 µL of TMB (substrate solution) were added into the wells and incubated for 30 min at 25 °C and 50 µL of 1M H_2SO_4 (stop solution) were mixed in the wells. The plates immediately were measured by a spectrophotometer at 450 nm and 620 nm.

Similarly, in order to select the best antibody pairs, we also performed three nucleoprotein calibration curves based on three different pairs of anti-nucleoprotein antibodies. For the experimental work, we followed sandwich ELISA protocol reported in the previous paragraph. In particular, we coated the wells with the rabbit anti-nucleoprotein pAb antibody (R8). Then, we used a series of nucleoprotein standard solutions (0, 1, 3, 10, 30, 100, 300 and 1000 ng/mL in PBS), and 0.5 µg/mL in PBS of M2, M4, and M5 antibody solutions (used as detection antibodies). Next, 100 µL of an HRP-modified anti-mouse pAb (0.1 µg/mL) were added. Finally, the enzymatic reaction took place as described in the previous paragraph.

3.2.3. Gold nanoparticle synthesis

Following the Turkevich method[18,32] AuNPs of approximately 20 nm diameter were synthesised by citrate reduction of tetrachloroauric acid ($HAuCl_4$). Specifically, 200 mL of a 0.01 % (w/v) solution of $HAuCl_4$ prepared in Milli-Q water was taken to boiling point. Then, 5 mL of 1 % (w/v) sodium citrate solution was added under continuous vigorous stirring with 600 rpm. The solution was kept boiling for 10 more minutes and then allowed to cool down to room temperature taking about 2 hours. And the AuNPs solution was stored at 4 °C away from light for further usage. The characterization of morphology and size distribution of synthesized AuNPs was shown in Figure 3.1.

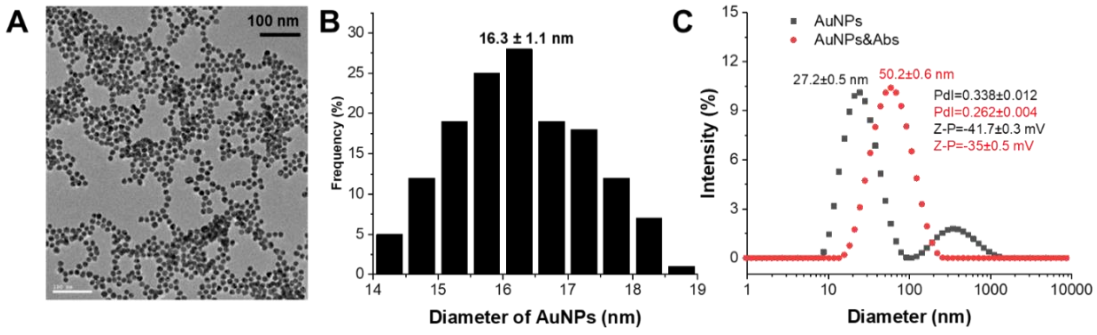

Figure 3.1. Characterization of AuNPs before and after conjugation with anti-nucleoprotein Abs. All the characterisation results support the successful conjugation of the antibodies to the AuNPs and the

stability of the conjugate particles. (A) TEM images of AuNPs with uniform shape distribution; (B) Histogram of AuNPs (Average size of AuNPs: 16.3 ± 1.1 nm, 150 particles); (C) The change of average hydrodynamic diameters from 27.2 ± 0.5 nm (naked AuNPs) to 50.2 ± 0.6 nm (AuNPs-Abs conjugate) proved AuNPs were covered after conjugation and hence successfully conjugated to anti-nucleoprotein Abs. The change in zeta potential values (-41.7±0.3 mV before and -35±0.5 mV after conjugation) further demonstrated a change on the AuNPs surface attributed to the conjugation. The obtained values indicate that the conjugates remained stable in colloidal solution (absolute Zeta potential value between 30 and 60 mV) [2]. Besides, particle dispersion is better after (polydispersity index (PdI) = 0.262±0.004) than before conjugation with antibodies (PdI = 0.338±0.012).

3.2.4. Conjugation of AuNPs with anti-nucleoprotein antibodies (M5)

The conjugates AuNPs&anti-nucleoprotein Abs were prepared by following our protocol[18]. The optimal pH and optimised amount of anti-nucleoprotein antibodies were pH 7.0 and 5 µg/mL (Abs amount/ AuNPs voulme) according to gold aggregation test (not shown). In the final step, the pellet of AuNPs&anti-nucleoprotein conjugates was resuspended in 150 µL of 1% BSA solution in PBS (0.01 M, pH 7.4) instead of 500 µL of the conjugated pad buffer. The characterization of AuNPs before and after conjugation with anti-nucleoprotein Abs was shown in Figure 3.1C.

3.2.5. Fabrication of the half-stick lateral flow strips (Dot test)

CN150 nitrocellulose membrane was adhered to a laminated card. Absorbent pad (cellulose membrane) was also assembled on the laminated card overlapping 2 mm with the membrane. Then the card was cut into 3 mm-wide lateral flow strips. Anti-nucleoprotein Abs of R1, R7, R8, and R9 were manually dropped (0.3 µL) onto nitrocellulose half-sticks as test dots (T-dot). Additionally, anti-mouse secondary antibodies were as well dropped (0.3 µL) in the same fashion to obtain the control dots (C-dots). The half-stick strips were dried for 1 h at 37 °C. The AuNPs conjugates were first incubated with PBS buffer in presence of nucleoprotein (100 ng/mL) and absence of nucleoprotein (0 ng/mL) for 10 minutes at room temperature (RT). Then, the half-stick dotted strips were immersed vertically in 20 µL of pre-incubated AuNPs conjugates solutions (2 µL of 10X concentrated AuNPs + 18 µL of sample). After 10 mins of flowing, the half-stick dotted strips were scanned with a SkanMulti reader and the images analysed with ImageJ.

3.2.6. Calibration curves of nucleoprotein detection based on half-stick LFA

In the Dot test, several pairs of antibodies showed similar performance. In order to decide which one was the best performing couple, preliminary calibration curves were obtained based on half-stick LFA. Here anti-nucleoprotein antibodies R1 or R8 were used as test line and anti-nucleoprotein antibodies M4 or M5 were conjugated with AuNPs, obtaining the following combinations: R1/M5, R8/M4 and R8/M5. A series of concentrations of nucleoprotein (0, 3, 10, 30, 100, 300, 1000 and 3000 ng/mL) were prepared in PBS. The process of preparation of nitrocellulose membrane, deposition of antibody Test and Control dots, AuNPs conjugation and detection of nucleoprotein was as described in the previous section.

For the final calibration curve, Test and Control lines were prepared using an automatic reagent dispenser. 1 mg/mL of anti-nucleoprotein Abs (R8) and 0.75 mg/mL of anti-mouse secondary antibodies were dispensed onto CN150 membrane as test line and control line, respectively. The anti-nucleoprotein mAbs (M5) were conjugated with AuNPs. A series of concentrations of nucleoprotein (0, 1, 3, 6, 10, 20, 30, 60, 100, 200, 300, 600, 1000, 2000, 3000, 6000 and 10000 ng/mL) were spiked in artificial saliva and incubated with AuNPs conjugates for 10 min at RT. Afterwards, half-stick test strips were immersed vertically in 20 µL of pre-incubated AuNPs conjugates solutions (2 µL of 10X concentrated AuNPs + 18 µL of sample). After 10 min of flowing, the half-stick LFA strips were scanned with a SkanMulti reader and the images of LFA strips analysed with ImageJ, correcting the dot area with an equally sized background area[18].

3.2.7. Data analysis

Fiji ImageJ software was used to analyse all the images from SkanMulti reader. Origin 2018 software was used for drawing all the bar charts and fitting four-parameters logistics curves[18].

3.3. Results and discussions

3.3.1. ELISA tests for screening antibody combinations

Following our fabrication protocol for LFA[18], I characterized antibodies for their adaptation as bioreceptors in an AuNPs-based LFA as they were released in the market. Specifically, among the antigens of SARS-CoV-2, I decided to target the nucleoprotein since it is highly abundant in

the virion[32,33]. From April 2020 to February 2021, I purchased 17 commercial anti-nucleoprotein antibodies from different companies (see Table 3.1).

Table 3.1. Information of all commercial anti-nucleoprotein antibodies.

Code	Host	Antibody Type	Company	Price	Isotype	Proven application
R1	Rabbit	Polyclonal	A	310€/100μg	IgG	WB, ELISA
R2	Rabbit	Polyclonal	B	258€/100μg	IgG	WB, ELISA
R3	Rabbit	Polyclonal	B	331€/100μg	IgG	WB, Simple Western, ELISA, ICC, IF, IHC, IHC-P, Dual RNAscope ISH-IHC
R4	Rabbit	Monoclonal	A	310€/100μg	IgG	WB, ELISA , IHC-P
R5	Rabbit	Polyclonal	C	585€/50μg	IgG	WB
R6	Rabbit	Monoclonal	D	345€/100μg	IgG	WB, ELISA, FC, IHC-P, IP
R7	Rabbit	Monoclonal	A	540€/100μg	IgG	WB, ELISA, IHC-P
R8	Rabbit	Polyclonal	A	310€/100μg	IgG	ELISA
R9	Rabbit	Monoclonal	A	310€/100μg	IgG	WB,ELISA, IHC-P, ICC/IF
R10	Rabbit	Monoclonal	E	303€/100μg	IgG	WB, ELISA, FC, IHC, IF, IP
M1	Mouse	Monoclonal	D	391€/100μg	IgG	WB, ELISA, IHC
M2	Mouse	Monoclonal	D	390€/100μg	IgG	WB, ELISA, ICC, IHC, IF, IP
M3	Mouse	Monoclonal	C	715€/100μg	IgG1	WB,ELISA
M4	Mouse	Monoclonal	A	250€/100μg	IgG1	WB, ELISA, IHC-P, FCM

M5	Mouse	Monoclonal	A	430€/100µg	IgG1	WB, ELISA, IHC-P, FCM
H1	Human	Monoclonal	D	371€/100µg	IgG1, kappa	WB, ELISA
H2	Human	Monoclonal	D	590€/100µg	IgG	WB, ELISA

The criteria for the selection were: (1) cost, (2) antibody concentration (over 1 mg/mL), (3) delivery time, and (4) animal host used for its production. Since the recognition event in LFAs is based on the formation of the classic immune-sandwich complex (Figure 3.2), I screened antibodies through two phases: (1) ELISA, to quickly check antibody binding performance (Figure 1); and (2) half-stick format, to check their compatibility with the conditions encountered in a LFA (i.e., under a constant flow in a nitrocellulose membrane) (Figure 3.5A).

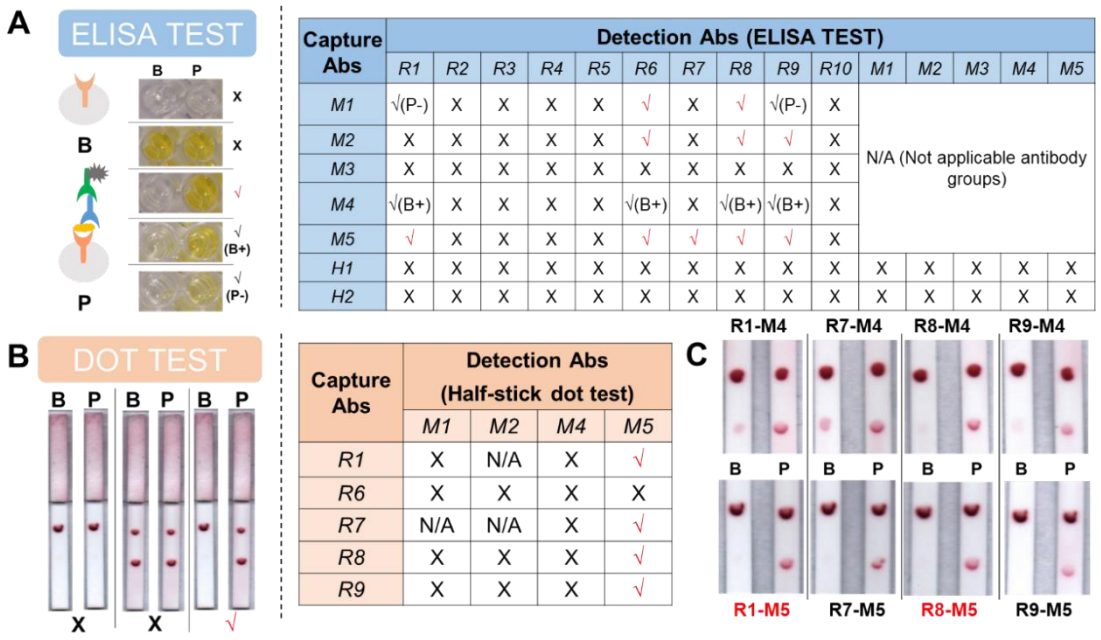

Capture Abs	Detection Abs (ELISA TEST)														
	R1	*R2*	*R3*	*R4*	*R5*	*R6*	*R7*	*R8*	*R9*	*R10*	*M1*	*M2*	*M3*	*M4*	*M5*
M1	√(P-)	X	X	X	X	√	X	√	√(P-)	X	N/A (Not applicable antibody groups)				
M2	X	X	X	X	X	√	X	√	√	X					
M3	X	X	X	X	X	X	X	X	X	X					
M4	√(B+)	X	X	X	X	√(B+)	X	√(B+)	√(B+)	X					
M5	√	X	X	X	X	√	√	√	√	X					
H1	X	X	X	X	X	X	X	X	X	X	X	X	X	X	X
H2	X	X	X	X	X	X	X	X	X	X	X	X	X	X	X

Capture Abs	Detection Abs (Half-stick dot test)			
	M1	*M2*	*M4*	*M5*
R1	X	N/A	X	√
R6	X	X	X	X
R7	N/A	N/A	X	√
R8	X	X	X	√
R9	X	X	X	√

Figure 3.2. Results of ELISA test and half-stick dot test. (A) Schematic representation of possible ELISA outcomes (left) and all the results of antibody combinations in the table (right); (B) Images of possible outcomes of half-stick dot test (left) and all the results of half-stick dot test (right); (C) Images of half-stick dot test (R1/M5 and R8/M5 are the best two combinations by naked eye). *'X' indicates a negative outcome (lacking in specificity and/or sensitivity). '√' indicates satisfactory outcome* $OD_{Blank} < 0.2$ *and* $OD_{Positive} > 1.0$*), '√(P-)' and '√(B+)' indicates less satisfactory results* ($OD_{Positive}$ *less than a little bit 1.0 and* OD_{Blank} *more than 0.2, respectively) (Figure S3A-left), and 'N/A' means not applicable antibodies groups; B and P indicate blank*

(0 ng/mL of nucleoprotein) and positive (100 ng/mL of nucleoprotein).

Firstly, I performed ELISA tests to identify the antibody combinations with the best binding performance (Figure 3.3A). In order to carry out these measurements I followed a previously reported ELISA protocol[34,35]. The experimental criteria to identify such antibodies were similar to the standard for evaluating antibody titre by the chessboard titration method, which allows to assess two variables simultaneously: antibody couple and presence/absence of nucleoprotein. Specifically, in the absence of target (i.e. blank) the background signal has to display a value lower of 0.2 a.u. (OD Blank), while in the presence of a saturating concentration of nucleoprotein (100 ng/mL) the produced signal should be higher than 1.0 a.u. (OD Positive). Surprisingly, I found that out of 80 tested combinations only 10 met these two criteria (Figure 3.3B). Such low success rate (12.5 %) is a consequence of the high cross-reactivity between antibodies (in most cases, a blank signal as high as the positive can be observed (Figure 3.3C)) and their low affinity for the target or slow kinetics (for antibody couples whose positive signals were lower than 1.0 a.u.) (Figure 3.3D and 3.3E). And ELISA test results of all possible antibody groups for detection of nucleoprotein were shown in Figure 3.3. It should be noted that all but one antibodies were publicized to be working in ELISA and that none of them were part of a pre-validated matched pair.

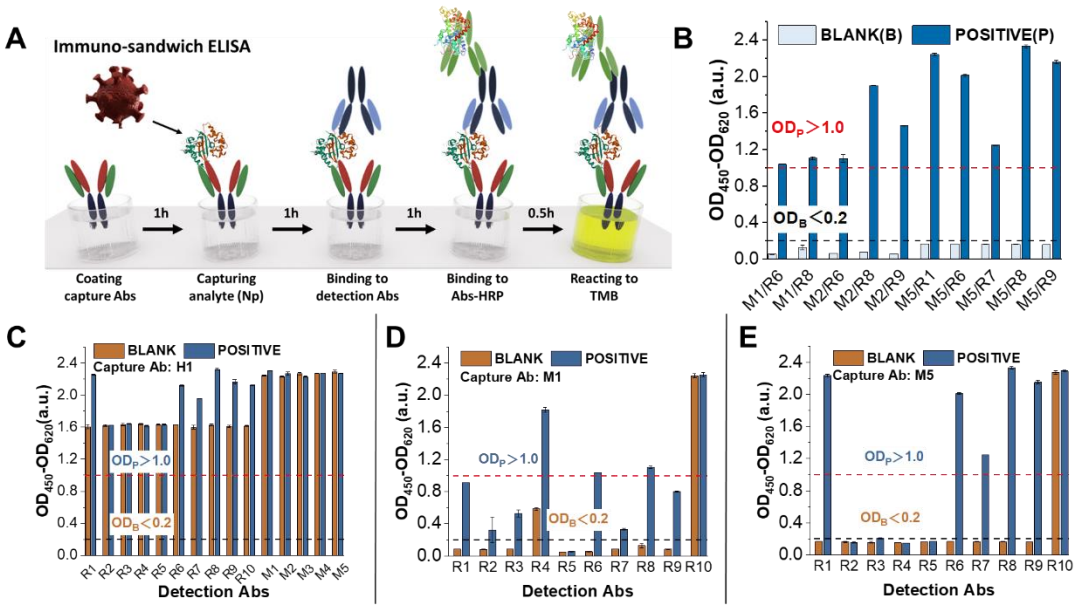

Figure 3.3. ELISA tests were performed to screen antibody combinations with the best binding performance against the nucleoprotein N protein of the SARS-CoV-2. (A) Schematic representation of

the immunosandwich ELISA. (B) Antibody combinations with best ELISA performance. The nucleoprotein concentrations of blank and positive solution are 0 ng/mL and 100 ng/mL, respectively. The antibody combination that meets the performance requirements should have the following conditions: the OD value of blank nucleoprotein solution is less than 0.2 a.u. and the OD value of positive nucleoprotein solution is greater than 1.0 a.u.[27] (C-E) Each individual graph shows the ELISA test results of same capture antibodies (coated on ELISA plate wells) combined with multiple detection antibodies. (C) Capture Abs H1 and detection Abs R1-R10 and M1/M5. None of the antibody combinations qualified because the OD value of the blanks was much greater than 0.2, which means high cross-reactivity and poor specificity; (D) Capture Abs M1 and detection Abs R1-R1. Only M1/R6 and M1/R8 were qualified with OD Blank < 0.2 and OD Positive > 1.0 while the rest were not qualified due to OD Blank > 0.2 or OD Positive < 1.0; and (E) Capture Abs M5 and detection Abs R1/R10. Couples M5/R1, M5/R6, M5/R7, M5/R8 and M5/R9 were satisfactory, especially M5/R1 and M5/R8, and others were not qualified due to OD Blank > 0.2 (M5/R10) or OD Positive < 1.0.

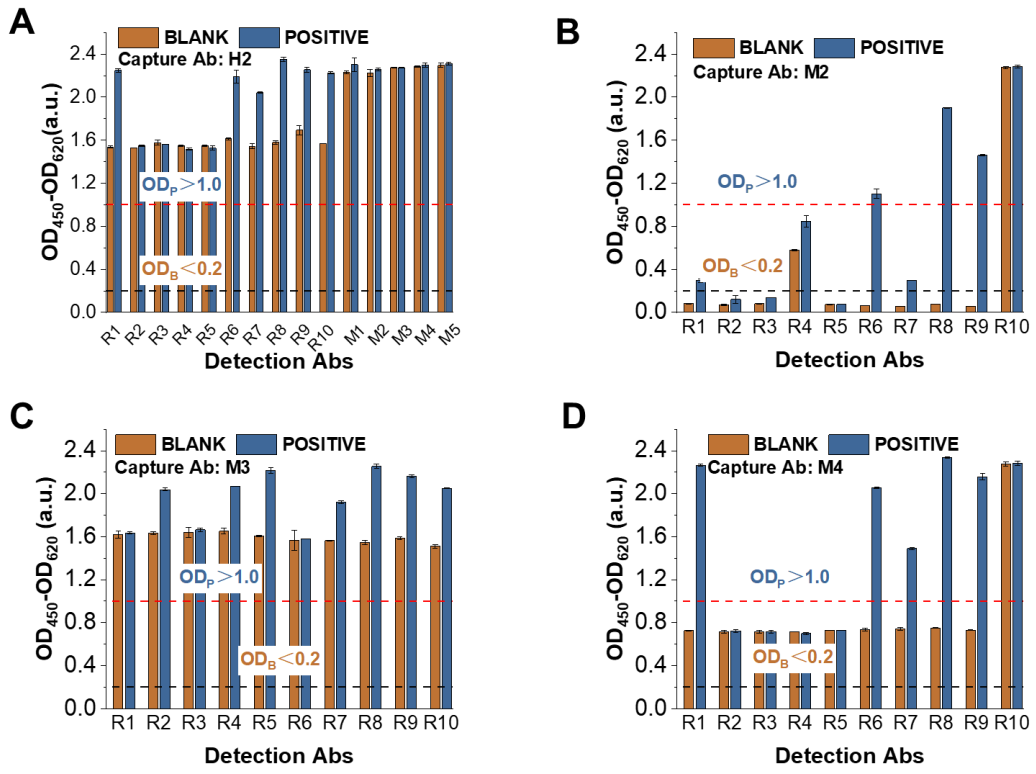

Figure 3.4. ELISA test results of all possible antibody groups for detection of nucleoprotein. Each individual panel shows the ELISA test results of same capture antibody (coated on ELISA plate wells) combined with various detection antibodies. The antibody combination that meets the performance

requirements should have the following conditions: the OD value of blank nucleoprotein solution is less than 0.2 a.u. and the OD value of positive nucleoprotein solution is greater than 1.0 a.u. (A) ELISA results using H2 as capture Ab with different detection Abs (R1-R10 and M1-M5). The results show that there is cross-reactivity between all of the antibody couples, as the OD values of blank samples are far greater than 0.2 a.u. and the blank signal is comparable to that of positive samples. (B) ELISA results using M2 as capture Ab with different detection Abs (R1-R10). The results show that there is high specificity and high affinity towards target between antibody couples of M2/R6, M2/R8 and M2/R9, as the blank signal is less than 0.2 a.u. and the positive signal is more than 1.0 a.u. Antibody couples M2/R4 and M2/R10 show cross-reactivity, as seen by the blank OD values greater than 0.2 a.u. The OD values of positive samples are comparable to that of the blank samples, thus indicating that there is low affinity towards the target between antibody couples M2/R1, M2/R2, M2/R3, M2/R5 and M2/R7. (C) ELISA results using M3 as capture Ab with different detection Abs (R1-R10). The results show that there is cross-reactivity between all of the antibody couples, as the OD values of blank samples are far greater than 0.2 a.u. and the blank signal is comparable to that of positive samples. (D) ELISA results using M4 as capture Ab with different detection Abs (R1-R10). The results show that there is cross-reactivity between all of the antibody couples, as the OD values of blank are greater than 0.2 a.u..

3.3.2. Half-stick dot test for screening out antibody combinations

Among the 10 working antibody combinations, I selected the 5 combinations of capture and detection antibodies (M2/R8, M5/R1, M5/R6, M5/R8 and M5/R9) with the best performance in order to move on with the half-stick characterization. To do this, I used dotted half-sticks rather than full LFA strips because they are faster to prepare (taking into account the number of antibody combinations) and smaller reagent amounts are required[18,36]. In order to identify the antibodies with the best binding performance in the nitrocellulose membrane, I established that the blank's signal should be < 5.0 a.u. and the positive sample's signal > 30.0 a.u. These values approximately correspond with the dynamic range obtained in the provided protocol for human IgG detection[18]. With these criteria, only 6 couples of antibodies showed a suitable binding performance in the half-stick format (Figure 3.5B). I hypothesise that the shorter time of incubation/recognition and the absence of washing steps in half-stick dot tests compared to ELISAs are the causes of the decrease in the number of antibody couples compatible with a

paper-based platform.

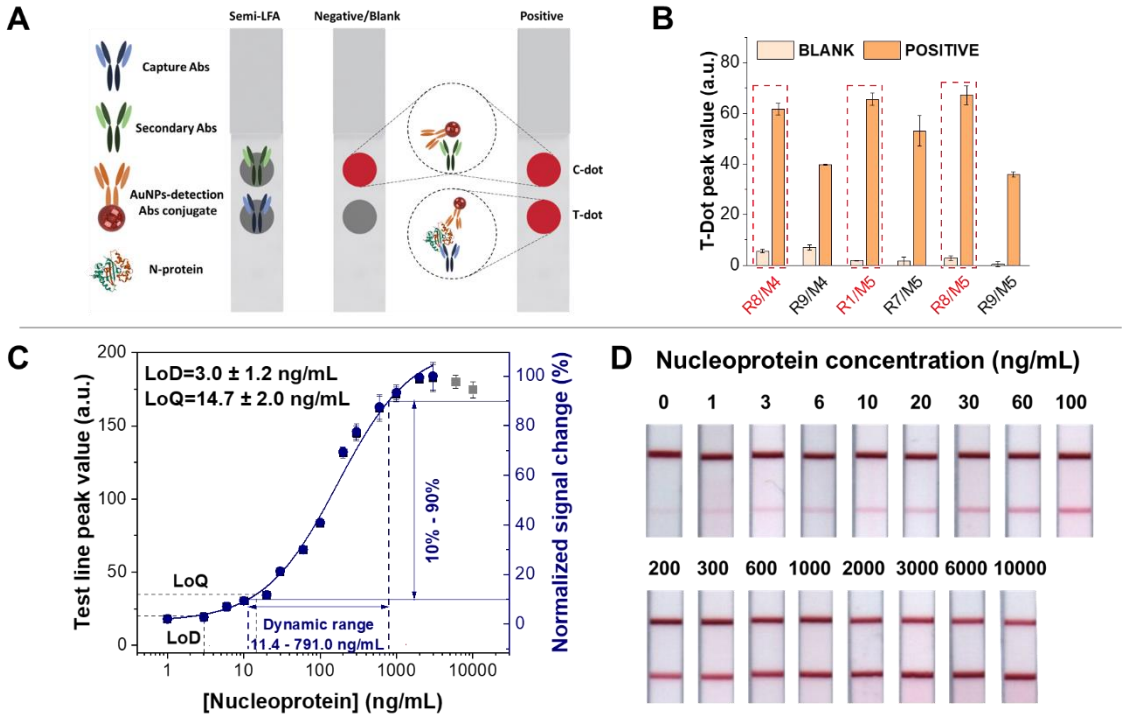

Figure 3.5. Dot test for screening out antibody combinations and calibration curve of detection of nucleoprotein spiked in artificial saliva based on half-stick LFA. (A) Schematic representation of the dot test on half-stick LFA: anti-nucleoprotein Abs (capture Abs) and secondary Abs were manually dropped on the nitrocellulose membrane as test dot and control dot, respectively. When the half-stick is tested with a blank sample, only the control dot (or line) is visible, demonstrating that the assay functioned properly. If the sample contains nucleoprotein, both control and test dots (or lines) are visible, and the intensity of the latter will depend on the analyte concentration. (B) All antibody combinations with good performance in the dot test (easy to distinguish between blank and positive samples with the naked eye). R1/M5, R8/M4 and R8/M5 elicit the best response. (C) Calibration curve of the half-stick LFA with R8/M5 antibodies. The data was fitted to a four-parameter logistic curve (blue line). The fitted curve (obtained using Origin 2018 32-bit and presented as value ± standard error) corresponds to the following equation: y = start + (end – start) × x^n / (k^n + x^n), with start = 1.04 ± 1.09, end = 112.12 ± 10.21, k = 169.28 ± 44.06 and n = 0.90 ± 0.12. The reduced $\chi 2$ = 2.58, R2 = 1.00 and the adjusted R2 = 0.99 Grey points were beyond the curve range due to the saturation of bioreceptors binding sites. The dynamic range of the half-sticks is from 11.4 ng/mL to 791.0 ng/mL, calculated by signal change from 10 % to 90 %), and the graph were obtained by analysing at least three (n = 3) independent LFAs for each target concentration. Fitting curve, LoD, LoQ, and dynamic range

fully were acquired by the protocol from Parolo *et al*.[18] (D) Half-stick LFA for detection of nucleoprotein, responding to increasing concentrations of nucleoprotein.

3.3.3. Calibration curve of nucleoprotein detection based on half-stick LFA

To demonstrate the feasibility of the half-stick assay for further experimentation with clinical samples, I tested it using artificial saliva, taking into account that COVID-19 diagnosis is possible using such kind of sample[4,37]. The dot test results showed that three antibody couples (R1/M5, R8/M4 and R8/M5) had similar test line peak values for detection of 100 ng/mL of nucleoprotein (Figure 3.5B). Then, preliminary calibration curves of R1/M5, R8/M4 and R8/M5 were obtained after testing the sensors with increasing concentrations of nucleoprotein (0, 3, 10, 30, 100, 300, 1000, and 3000 ng/mL) (Figure 3.6). Fitting the curves with a four-logistic parameter equation, I calculated the EC50, that is, the half maximal concentration of nucleoprotein that elicits a response halfway between the baseline and saturation signal. Given the immune-sandwich nature of the system, EC50 is a good indicator of affinity. The R8/M5 couple displays the lowest EC50 value (134.7 ng/mL), while EC50 values for R8/M4 and R1/M5 are 197.9 ng/mL and 337.1 ng/mL respectively (Figure 3.6 and Table 3.2). Moreover, R8/M5 showed the best sensitivity for nucleoprotein detection, as observed by the steeper slope in the calibration curves (Figure 3.6A and B). Consequently, antibody couple R8/M5 was selected for the further development of nucleoprotein LFA sensor. The half-stick was prepared by dispensing the R8 antibody on the test line (TL), the secondary antibodies (anti-mouse IgG) on the control line (CL), while the antibody nucleoprotein M5 was conjugated to AuNPs. In order to characterise the sensor response, I challenged it using nucleoprotein-spiked artificial saliva samples covering a nucleoprotein concentration range between 1 ng/mL (21.2 pM) and 10 µg/mL (0.2 µM) (Figure 3.5C). Through the analysis of the obtained half-sticks, I calculated a limit of detection (LoD) of 3.0 ± 1.2 ng/mL, limit of quantification (LoQ) of 14.7 ± 2.0 ng/mL, a useful dynamic range of 11.4 – 791.0 ng/mL (Figure 3.5C). The test line signals obtained using nucleoprotein concentrations higher than 10 ng/mL were clearly seen by the naked eye (Figure 3.5D). In addition, recovery of nucleoprotein samples ranged from 83.0 ± 2.0% to 116.7 ± 16.7% demonstrating the accuracy of the test (Table

3.3). The analytical performance of the described half-sticks is comparable to a full SARS-CoV-2 nucleoprotein LFA recently published for the detection of the nucleoprotein[38]. To further support our results, I found another recently published study by Cate *et al*., in which 1021 anti-nucleoprotein antibodies were tested in LFA, taking advantage of an automatized, high-throughput robotic system[27] and the couple of antibody I independently selected has been found among the top performing couples.

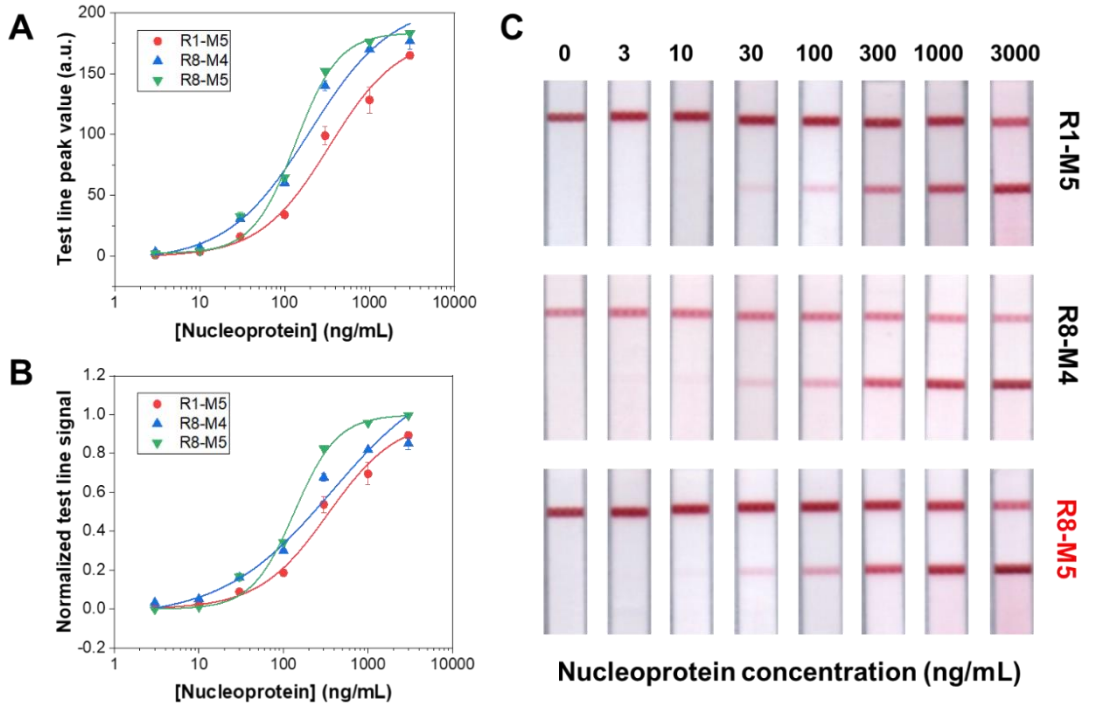

Figure 3.6. Preliminary calibration curve for screening out the best antibody for detection of nucleoprotein based on half-stick LFA. Preliminary half-stick LFA calibration curves with R1/M5, R8/M4 and R8/M5 antibody couples for nucleoprotein (0, 3, 10, 30, 100, 300, 1000 and 3000 ng/mL): (A) Calibration curves fitted by using the original test line peak value and (B) Calibration curves fitted by using normalised test line signal. The fitted curve (obtained using Origin 2018 32-bit and presented as value ± standard error corresponds to a four parameter logistic equation (sigmoidal curve): y = start + (end – start) × x^n / (k^n + x^n). And the normalised signal was calculated by the equation of (test line peak value – start) / (end - start) and the normalised calibration curve was fitted by the same mode. All parameters of calibration curve equation are shown in Table 3.2.

Table 3.2. The equation parameters of half-stick LFA calibration curves (original OD a.u.) for detection of nucleoprotein based on three different pairs of antibodies (R1, R8 as the capture

antibody, and M4 and M5 as detection antibodies).

	R1-M5	R8-M4	R8-M5
START	0.5 ± 2.1	-3.6 ± 10.8	2.3 ± 1.5
END	181.3 ± 11.4	208.3 ± 43.6	183.8 ± 1.6
k	337.1 ± 92.5	197.9 ± 116.0	134.7 ± 11.4
n	1.1 ± 0.2	0.9 ± 0.3	1.7 ± 0.2
RSS	2.4	57.4	11
Adj. R2	0.999	0.9841	0.9994

Table 3.3. Recovery of nucleoprotein detection based on half-stick LFA.

Spiked (ng/mL)	Calculated (ng/mL)	Recovery (%)[a]
6	7.0 ± 1.0	116.7 ± 16.7
20	16.6 ± 0.4	83.0 ± 2.0
60	51.6 ± 3.0	86.0 ± 5.0
200	214.3 ± 9.1	107.2 ± 4.6
600	557.3 ± 4.7	92.9 ± 0.8

[a] Recovery (%) = (concentration of calculated nucleoprotein / concentration of spiked nucleoprotein) *100%

Finally, to make stronger our message that knowing beforehand the binding behaviour of bioreceptors would speed up the development of diagnostic tests, I studied the binding constant of three couples of antibodies selected according to their performance in the preliminary steps, which goes as follows. One of them had worked in ELISA but did not in half-stick (R8/M2), while the other two couples did work in both types of assay (R8/M4 and R8/M5). R8/M2 showed an EC50 at least 72% higher than the other two couples (R8/M4 and R8/M5) and also a higher working range, thus indicating a lower affinity, which is not suitable for LFAs (Table 3.4 and Figure 3.7).

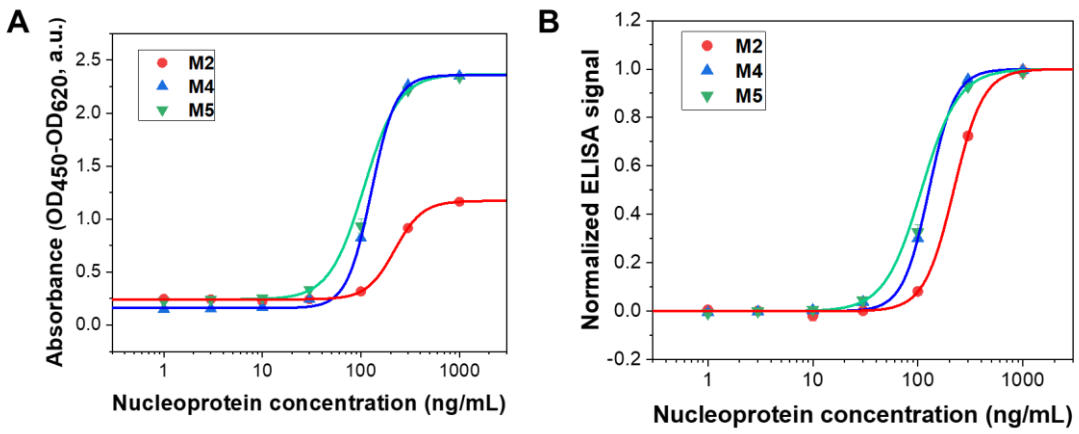

Figure 3.7. ELISA calibration curves of three antibody pairs for detection of nucleoprotein. ELISA calibration curve using R8 as capture Ab with different detection Abs (M2, M4 and M5). R8/M2 had previously worked in ELISA but not in half-stick, while R8/M4 and R8/M5 had worked in both assays. (A) Calibration curves fitted by using the original absorbance value and (B) calibration curves fitted by using normalised ELISA signal. The fitted curve (obtained using Origin 2018 32-bit and presented as value ± standard error) corresponds to a four parameter logistic equation (sigmoidal curve): y = start + (end – start) × x^n / (k^n + x^n). And the normalised signal was calculated by the equation of (OD value – start) / (end - start) and the normalised calibration curve was fitted by the same mode. All parameters of calibration curve equation are showed in Table S3. The k in the equation corresponds to the EC50. Nonetheless, it can be used to study the affinity of the antibody couple for the antigen. The k values of three antibody couples, R8/M2, R8/M4 and R8/M5, for detection of nucleoprotein are 219.54 ± 4.20, 127.53 ± 4.85 and 107.77 ± 11.12 ng/mL, respectively (Table 3.4). The k of R8/M5 is the smallest and also showed the best affinity with the nucleoprotein.

Table 3.4. The equation parameters of ELISA calibration curves (original OD a.u.) for detection of nucleoprotein based on three different pairs of antibodies (R8 as the capture antibody, and M2, M4 and M5 as detection antibodies, respectively).

	M2	M4	M5
START	0.2 ± 0.0	0.2 ± 0.0	0.2 ± 0.0
END	1.2 ± 0.0	2.4 ± 0.0	2.4 ± 0.1
k	219.5 ± 4.2	127.5 ± 4.8	107.8 ± 11.1
n	3.1 ± 0.1	3.5 ± 0.5	2.5 ± 0.2

RSS	0.4	43.0	13.0
Adj. R^2	0.9998	0.9990	0.9992

3.4. Conclusions

Despite the successful implementation of the LFA development protocol[18], the significant amount of invested economic resources (~25,000 €), personnel, and time (over 10 months) to identify working antibodies is alarming. I understand that the majority of the antibodies are validated for a few specific applications, generally traditional laboratory-bound techniques (e.g. ELISA, Western Blot). However, the COVID-19 pandemic has demonstrated that I cannot rely exclusively on long (hours) and cumbersome (multistep) diagnostic techniques to effectively diagnose infectious diseases because I need sensing platform able to support massive (or high-frequency) testing. Therefore, I urge antibody producers and distributors to consider the implementation of more extensive characterization of their products, which would allow researchers to make better-informed purchases. At the same time, the integration of new antibodies into point-of-care devices would also be faster. The availability of information such as the binding kinetics of bioreceptors could lead researchers towards purchasing antibodies that better suit their platform's needs, e.g. antibodies with fast binding kinetics for a LFA, which features a short receptor analyte interaction time. I realize that a longer bioreceptor characterization implies higher costs for the company (e.g. new instrumentation, delayed commercial availability), nonetheless I truly believe that researchers would rather buy more expensive, but well characterized antibodies than cheaper but poorly characterized ones. This in turn would optimize the time and economic resources required for the development of a point-of-care diagnostic device, speeding up its placement in the market.

3.5. References

1. Wu, F. *et al.* A new coronavirus associated with human respiratory disease in China. *Nature* **579**, 265–269 (2020).

2. Zhou, P. *et al.* A pneumonia outbreak associated with a new coronavirus of probable bat origin. *Nature* **579**, 270–273 (2020).

3. Lan, J. *et al.* Structure of the SARS-CoV-2 spike receptor-binding domain bound to the ACE2 receptor. *Nature* **581**, 215–220 (2020).

4. Nagura-Ikeda, M. *et al.* Clinical Evaluation of Self-Collected Saliva by Quantitative Rever Transcription-PCR (RT-qPCR), Direct RT-qPCR, Reverse Transcription-Loop-Mediated Isothermal Amplification, and a Rapid Antigen Test To Diagnose COVID-19. *J. Clin. Microbiol.* **58**, 1–9 (2020).

5. Wells, C. R. *et al.* Optimal COVID-19 quarantine and testing strategies. *Nat. Commun.* **12**, 1–9 (2021).

6. Guglielmi, G. Fast coronavirus tests are coming. *Nature* **585**, 496–498 (2020).

7. Mercer, T. R. & Salit, M. Testing at scale during the COVID-19 pandemic. *Nat. Rev. Genet.* **0123456789**, (2021).

8. Rosati, G. *et al.* Nanodiagnostics to face SARS-CoV-2 and future pandemics : From an idea to the market and beyond. *ACS Nano* **15**, 17137–17149 (2021).

9. Idili, A., Parolo, C., Alvarez-Diduk, R. & Merkoçi, A. Rapid and Efficient Detection of the SARS-CoV-2 Spike Protein Using an Electrochemical Aptamer-Based Sensor. *ACS Sensors* **6**, 3093–3101 (2021).

10. Larremore, D. B. *et al.* Test sensitivity is secondary to frequency and turnaround time for COVID-19 screening. *Sci. Adv.* **7**, eabd5393 (2021).

11. Carter, L. J. *et al.* Assay Techniques and Test Development for COVID-19 Diagnosis. *ACS Cent. Sci.* 591–605 (2020) doi:10.1021/acscentsci.0c00501.

12. Vandenberg, O., Martiny, D., Rochas, O., van Belkum, A. & Kozlakidis, Z. Considerations for diagnostic COVID-19 tests. *Nat. Rev. Microbiol.* **19**, 171–183 (2021).

13. Organization, W. H. *Antigen-detection in the diagnosis of SARS-CoV-2 infection using rapid immunoassays: interim guidance, 11 September 2020*. (2020).

14. Guglielmi, G. Rapid coronavirus tests: a guide for the perplexed. *Nature* **590**, 202–205 (2021).

15. Miller, B. S. B. S. *et al.* Spin-enhanced nanodiamond biosensing for ultrasensitive diagnostics. *Nature* **587**, 588–593 (2020).

16. Sena-Torralba, A. *et al.* Paper-Based Electrophoretic Bioassay: Biosensing in Whole Blood Operating via Smartphone. *Anal. Chem.* **93**, 3112–3212 (2021).

17. Sena‐Torralba, A. *et al.* A novel ratiometric fluorescent approach for the modulation of the dynamic range of lateral flow immunoassays. *Adv. Mater. Technol.* **7**, 2101450 (2022).

18. Parolo, C. *et al.* Tutorial: design and fabrication of nanoparticle-based lateral-flow immunoassays. *Nat. Protoc.* **15**, 3788–3816 (2020).

19. Haselmann, V. *et al.* Clinica Chimica Acta Comparison of test performance of commercial anti-SARS-CoV-2 immunoassays in serum and plasma samples. *Clin. Chim. Acta* **510**, 73–78 (2020).

20. Charlton, C. L. *et al.* Evaluation of Six Commercial Mid- to High-Volume Antibody and Six Point-of-Care Lateral Flow Assays for Detection of SARS-CoV-2 Antibodies. *J. Clin. Microbiol.* **58**, e01361-20 (2020).

21. Mahapatra, S. & Chandra, P. Clinically practiced and commercially viable nanobio engineered analytical methods for COVID-19 diagnosis. *Biosens. Bioelectron.* **165**, 112361 (2020).

22. Serrano, M. M. *et al.* Comparison of commercial lateral flow immunoassays and ELISA for SARS-CoV-2 antibody detection. *J. Clin. Virol.* **129**, 104529 (2020).

23. Schnurra, C. *et al.* Comparison of the diagnostic sensitivity of SARS-CoV-2 nucleoprotein and glycoprotein-based antibody tests. *J. Clin. Virol.* **129**, 104544 (2020).

24. Krüttgen, A. *et al.* Comparison of four new commercial serologic assays for determination of SARS-CoV-2 IgG. *J. Clin. Virol.* **128**, 104394 (2020).

25. Chua, K. Y. L. . *et al.* F O C U S O N S A R S - C OV- 2 Clinical evaluation of four commercial immunoassays for the detection of antibodies against established SARS-CoV-2 infection. *Pathology* **52**, 778–782 (2020).

26. Trabaud, M.-A. *et al.* Comparison of eight commercial , high-throughput , automated or ELISA assays detecting SARS-CoV-2 IgG or total antibody. *J. Clin. Virol.* **132**, 104613 (2020).

27. Cate, D. M. *et al.* Antibody Screening Results for Anti-Nucleocapsid Antibodies Toward the Development of a Lateral Flow Assay to Detect SARS-CoV-2 Nucleocapsid Protein. *ACS Omega* **6**, 25116–25123 (2021).

28. Baker, M. Blame it on the antibodies. *Nature* **521**, 274–276 (2015).

29. Bradbury, A. & Plückthun, A. Reproducibility: Standardize antibodies used in research. *Nature* **518**, 27–29 (2015).

30. Couchman, J. R. Commercial antibodies: The good, bad, and really ugly. *J. Histochem. Cytochem.* **57**, 7–8 (2009).

31. Saper, C. B. An open letter to our readers on the use of antibodies. *J. Comp. Neurol.* **493**, 477–478 (2005).

32. Cubuk, J. *et al.* The SARS-CoV-2 nucleocapsid protein is dynamic, disordered, and phase separates with RNA. *Nat. Commun.* **12**, 1–17 (2021).

33. Zeng, W. *et al.* Biochemical characterization of SARS-CoV-2 nucleocapsid protein. *Biochem. Biophys. Res. Commun.* **527**, 618–623 (2020).

34. Morales-Narváez, E., Montón, H., Fomicheva, A. & Merkoçi, A. Signal enhancement in antibody microarrays using quantum dots nanocrystals: Application to potential Alzheimer's disease biomarker screening. *Anal. Chem.* **84**, 6821–6827 (2012).

35. Bergua, J. F. *et al.* Low-Cost, User-Friendly, All-Integrated Smartphone-Based Microplate Reader for Optical-Based Biological and Chemical Analyses. *Anal. Chem.* **94**, 1271–1285 (2022).

36. Analytical Tools to Improve Optimization Procedures for Lateral Flow Assays. *Diagnostics* **7**, 29 (2017).

37. Shan, D. *et al.* N-protein presents early in blood, dried blood and saliva during

asymptomatic and symptomatic SARS-CoV-2 infection. *Nat. Commun. 2021 121* **12**, 1–8 (2021).

38. Grant, B. D. *et al.* SARS-CoV-2 coronavirus nucleocapsid antigen-detecting half-strip lateral flow assay toward the development of point of care tests using commercially available reagents. *Anal. Chem.* **92**, 11305–11309 (2020).

CHAPTER 4.

Au-IrO_2 NFs as novel colorimetric labels in LFAs

4.1. Introduction

The recent COVID-19 outbreak has highlighted again the clinical relevance of lateral flow assays (LFAs) as simple and rapid diagnostic tools with an ability to support mass-scale screening[1,2]. They consist of a series of connected paper-like pads that, by capillarity, move the liquid sample along the strip, allowing for the rapid, low-cost, and naked-eye detection of the target molecule in its clinical range[3]. Because the signal transduction mechanism is based on the detection of the target through the formation of an adsorbed immune complex on the test line, they can be designed to detect any arbitrary molecule by simply changing the antibody receptors. To date, LFAs have been widely exploited in real-world applications ranging from clinical (e.g., pregnancy test, antigen detection, serological application, etc.)[4,5] to environmental monitoring (e.g., detection of heavy metals, bacteria, and contaminants)[6–8]. Besides their versatility, the success and popularity of LFAs rely on their simple operation, fast response (approximately 15 min), low cost, and naked-eye-readable results. Despite the success and popularity of LFAs due to their simple operation and fast response, their sensitivity is lower than that of well-established laboratory-based detection methods [e.g., polymerase chain reaction (PCR) and enzyme-linked immunosorbent assay (ELISA)]. In consequence, LFA's potential cannot be fully exploited yet for applications requiring the detection and quantification of ultra-low-concentrated biomarkers (e.g., circulating tumor DNA, tumor proteins)[9,10]. Therefore, the development of novel approaches with an ability to improve the sensitivity of LFAs without compromising their ease of use could reduce the burden of expensive laboratory-based methods, allowing a more efficient early diagnosis to support the mass-scale screening of biomarkers at the point of care[11].

The sensitivity of an LFA depends on a wide range of physical–chemical and biological factors including, but not limited to, the type of label (e.g., colorimetric, fluorescent, electrochemical, etc.), the affinity of the selected bioreceptors toward the targets, and the flow rates of different pads[12,13]. Among them, the selection of the optical label plays a key role because it can affect important parameters of the LFAs, from the flow of the sample to the signal-to-noise ratio (which is defined as the optical contrast between the test/control line and the nitrocellulose background) and must guarantee the naked eye detection, which is crucial for their use at the point of care[14]. The development of nanotechnology has boosted the synthesis and the generation of new labels (i.e.,

nanomaterials) with exceptional optical properties (e.g., absorption, transmission, scattering, and light emission), creating a new set of ideal candidates for biosensing purposes[15–17]. However, other features of the selected nanomaterial must also be considered, such as their size, shape, surface chemistry, and stability, to fully adapt it on an LFA.

To improve the sensitivity and limit of detection of LFAs, several experimental strategies have been developed over the last 2 decades[18,19]. Generally, those strategies aimed at improving the different components of the LFAs, such as labels[20–24], strip design[25–27], readout (optical or electrochemical)[28–30], and microfluidics[31] with the final goal to enhance the overall analytical response of the LFAs. Among them, the development of new labels with the ability to generate a stronger optical signal has been a simple yet effective approach to improve the sensitivity of LFAs[19]. For example, nanodiamonds, upconverting nanoparticles, quantum dots, and magnetic nanoparticles have been used to develop LFAs for the detection of clinically relevant targets[23,32–35]. In particular, AuNPs are the most used colorimetric LFA labels that allow efficient naked eye detection due to their strong surface plasmon resonance, simple synthesis, and conjugation. Indeed, their surface plasmon resonance in the visible region produces a strong red color, which makes the iconic red lines that are ideal for the naked eye detection[34]. Other examples of metallic NPs used for the development of colorimetric LFAs include iridium oxide nanoparticles (IrO_2 NPs)[22], rhodium nanoparticles[36], copper oxide nanoparticles[37], and Prussian blue nanoparticles[38]. Each NPs display different colorimetric properties, which allow the generation of test lines with different colors and better performances than the classical AuNPs-based LFAs, albeit higher costs, more complex synthesis, and different morphology and size which affect the bioconjugations.

Besides the composition of the label, the morphology and the size of the nanoparticles also play important roles in the sensitivity of LFAs[39,40]. For example, increasing the surface area of a nanoparticle allows it to load more bioreceptors (e.g., antibodies, proteins, or aptamers), or the presence of spiked structures can provide different optical properties due to surface-enhanced plasmons. In this context, several research groups have demonstrated how the use of non-spherical nanoparticles with strong plasmonic behaviors (e.g., nanorods, nanocubes, and nanostars) generally produces an improvement in the LFA sensitivity when compared to the use

of classical quasi-spherical AuNPs[41–43]. Looking in particular at mono- and bimetallic non-spherical nanoparticles, I found studies reporting up to 5-fold and 10-fold improvements in the sensitivity of LFAs when using gold and platinum nanoflowers, respectively[44–47]. Uniquely of bimetallic nanoparticles, they have ability to display both plasmonic and catalytic behavior (e.g., Au-based alloy nanoparticles)[48,49]. This feature has been recently harnessed by two works, where AuPt core–shell and AuPt nanoflowers have been described as dual labels for LFAs, increasing dramatically the sensitivity of the assay up to 2 orders of magnitude[50,51]. Thus, non-spherical and hierarchical nanoparticles appear as promising labels to enhance the analytical properties of LFAs.

Given the background, I were inspired by the plasmonic behavior of gold and iridium oxide (Au–IrO_2) nanoflowers that were recently reported by de Freitas and co-workers[52]. More specifically, harnessing their unique morphology and composition that provide excellent biocompatibility and plasmonic properties, I decided to use them as colorimetric labels in LFAs.

On the one hand, while the debate about the optimal size of a LFA's label remains open (depending on the type of nanoparticles, the porosity of the pads, the size of the bioreceptor, etc.), the ideal choice would be one that ensures optimal nanoparticle' stability and bioreceptor coverage without sacrificing the sensitivity of the assay. Bottom-up synthesis of mono- and bimetallic nanoparticles is a versatile tool to achieve this chemical and physical balance. Specifically, it is possible to tune their size and shape by simply changing the amount of reducing agent, pH, and solvent during their synthesis[53,54]. Therefore, the possibility to synthetically tune the size and shape of the NPs is an important parameter at the time of choosing the label to employ in a new LFA. On the other hand, the optical response of the nanoparticles is another crucial parameter to consider. In general, these nanoparticles should have large extinction coefficients (i.e., high optical intensities) that visually contrast with the white background of the LF membrane. For example, this explains why AuNPs that show bright red colors and absorb at wavelengths ca. 520–530 nm are sometimes preferred to bigger gold nanoparticles that allow a higher bioreceptor loading but absorb at higher wavelengths (e.g., 600 nm), reducing the visual contrast with the membrane.

Having this in mind, I selected as new optical labels for LFAs the Au–IrO_2 NFs whose synthesis was proposed by de Freitas et al[52]. The idea is to exploit their dark color to create a higher contrast with the white background of the LF strips, and therefore to improve the sensitivity of nanoparticle-based LFAs. These Au–IrO_2 NFs display strong optical properties, but due to their size (over 100 nm), they are not ideal for LFAs. Specifically, they would be more prone to precipitation and aggregation once dried on the LFA, limiting their flow through the membrane. Therefore, I rationally adapted their synthesis to decrease the NFs' size without compromising their stability. In particular, I achieved it by changing the reaction time and the reducing agent (citrate) concentration while keeping their optical properties. As a test bed, I successfully used the Au–IrO_2 NFs in a LFA for the detection of human immunoglobulin G (HIgG)[22,31].

4.2. Materials and methods

4.2.1. Reagents and apparatuses

$HAuCl_4 \cdot 3H_2O$ 99%, $IrCl_3 \cdot xH_2O$ 99%, $Na_3C_6O_7H_5 \cdot 2H_2O$ 99%, boric acid (H_3BO_3, 99%), sodium tetraborate decahydrate ($B_4NaO_7 \cdot H_2O$, 99%), phosphate buffered saline tablet, Tween-20, sucrose (99.5%), and bovine serum albumin (BSA, 96%) were supplied by Sigma-Aldrich. Human IgG from human serum (I2511), anti-human IgG (produced in goat; I1886), and anti-human IgG γ chain-specific HRP-modified (produced in goat; A6029) were also supplied by Sigma-Aldrich (Spain), while anti-goat IgG (produced in chicken, ab86245) and anti-mouse IgG H&L (produced in goat, ab6708) were supplied by Abcam. Human IgG-depleted serum was purchased from Celprogen. Chicken IgG (ab6829) and goat IgG 2 (ab6702) were bought from Abcam. Human IgG antibodies (1A6) were supplied by Thermo Fisher. Mouse IgG (40588-T62) and rabbit IgG (40143-R019) were supplied by Sino Biological. 20, 40, 60, and 80 nm of AuNPs were supplied by nanoComposix.

Nitrocellulose membrane CN150 was purchased from Sartorius Stediem (Göttingen, Germany). Cellulose membrane (CFSP001700) and glass fiber were purchased from Merck Millipore (Billerica, MA, USA), and supporting adhesive cards were purchased from Kenosha (Amstelveen, The Netherlands).

The stirrer used for conjugating antibodies to nanoflowers was a PCMT ThermoShaker (Grant Instruments, UK). A lateral flow dispenser was used to distribute the reagents over the nitrocellulose (IsoFlow Bioreagent, Imagene Technology, Germany). Nanoparticles were centrifuged in a Centrifuge Allegra 64 R from Beckman Coulter (USA). Lateral flow strips were cut using a cutter from Shanghai Kinbio Tech (China). A spectrophotometer SpectraMax ID3 (Molecular Devices, USA) was used to measure the UV–vis spectra of nanoflower suspensions. LFA scanner SkanMulti from Skannex (Oslo, Norway) was used to scan the LFs strips.

4.2.2. Preparation of AuNPs and Au–IrO_2 NFs

Both AuNPs and Au–IrO_2 NFs were synthesized as previously reported in the literature. The former were synthesized by the Turkevich method[55], while the latter were prepared using a modified version of the protocol reported by de Freitas et al[52].

4.2.2.1. Synthesis of AuNPs

For preparing AuNPs, a 50 mL of aqueous solution of 0.1% $HAuCl_4 \cdot 3H_2O$ was heated to boiling and vigorously stirred in a 250 mL Erlenmeyer flask. Then, 1.25 mL of 1% sodium citrate was added quickly to the boiling solution. Boiling was continued for an additional 10 min upon the color change from pale yellow to bright red. Finally, the suspension was cooled to room temperature under continuous stirring and stored at 4 °C until use.

4.2.2.2. Synthesis of Au–IrO_2 NFs

In order to evaluate the colorimetric properties of the Au–IrO_2 NFs, I prepared two nanoflowers with different compositions. Specifically, I used two different molar ratios of Au and Ir (i.e., Au/Ir [1:0.25] and [1:1.5]). In addition, I modified the protocol reported by de Freitas et al. by changing the citrate concentration and reaction time. These modifications in the protocol were necessary for the fabrication of particles with diameters suitable to run through the nitrocellulose pores.

Briefly, 5 mL of sodium citrate (2.5 mM) was heated until boiling. Meanwhile, 354 µL of $HAuCl_4 \cdot 3H_2O$, 12 mM, were mixed with 88.5 or 531 µL of $IrCl_3 \cdot xH_2O$, 12 mM (for [1:0.25] and [1:1.5] ratios, respectively), and then reached up to 1 mL with milliQ water. This solution was added in one shot to the boiling solution of citrate. Boiling was continued for an additional 5 min

upon the color change from pale green to petrol-blue. Finally, the suspension was cooled to room temperature under continuous stirring and then stored at 4 °C until use.

4.2.3. Characterization of Au–IrO_2 NFs

ICP–OES was used as a technique to determine the metal content (i.e., gold and iridium percentage) of the nanoflowers and was performed at the Servei d'Anàlisi Química of the Universitat Autónoma de Barcelona by using an inductively coupled plasma–optical emission spectrometer (PerkinElmer, model Optima 4300DV).

All the size measurements and morphological observations of nanoflowers were conducted in a field emission gun transmission electronic microscope (model TecnaiTM G2F20, FEI, USA) and a field emission scanning electron microscope (model Magellan 400L, FEI, USA).

XPS measurements were performed at room temperature with a SPECS PHOIBOS 150 hemispherical analyzer (SPECS GmbH, Berlin, Germany) at a base pressure of 5×10^{-10} mbar using monochromatic Al Kα radiation (1486.74 eV) as an excitation source operated at 300 W. The energy resolution, as measured by the full width at half-maximum of the Ag $3d_{5/2}$ peak for a sputtered silver foil, was 0.62 eV. Measurements were made using CasaXPS software. The hydrodynamic particle diameters and zeta potential measurements were performed in a Zetasizer Nano ZS (Malvern Instruments, UK).

4.2.4. Extinction coefficient calculations

For simplifying the calculations, firstly the shape of the nanoflowers were considered as a perfect sphere made of Au and IrO_2. Thus, the number of Au atoms and IrO_2 per particle (N) were calculated according to the Eq. 1 and by using the density (ρ) of Au and IrO_2 asbulk material (19.32 g/cm^3 for Au and 11.68 g/cm^3 for IrO_2, respectively); both atomic and molecular weight (M): 196.97 g/mol and 224.22 g/mol for Au and IrO_2, respectively);the Avogadro number (NA) to be 6.02×10^{23}; diameter of the particles (D): 65 nm for the NFs [1:0.25], and 55 nm for the NFs [1:1.5]

$$N = \pi\rho D3\ NA/6M \quad \text{Equation S1}$$

Finally, the concentration of NFs stock solution was calculated to be about 0.122 nM and 0.527 nM for Au-IrO_2 NFs [1:0.25] and [1:1.5], respectively, by using the final concentration of the

precursor metals in the colloid dispersion divided by the number of atoms or compound per particle (*N*). Given the strong absorption of the NFs in the UV-vis range, the extinction coefficients were empirically calculated based on the Beer-Lambert law:

$$A = \varepsilon l c \qquad \text{Equation S2}$$

where *A* is the absorbance, *ε* is the extinction coefficient, *l* is le path length and *c* is the NFs concentration. Therefore, the absorbance of AuNPs and the Au-IrO_2 NFs synthesized in this work were plotted against the concentration of nanoparticles calculated as shown above, giving a linear trend where the slope of the curve corresponds to the extinction coefficient.

4.2.5. Conjugation of antibodies to AuNPs and Au–IrO_2 NFs

Anti-human IgG antibodies were conjugated to nanomaterials, as previously reported[12,31]. AuNPs were adjusted to pH 9 with borate buffer (BB), 0.1 M and Au–IrO_2 NFs were adjusted to pH 7 with BB 0.01 M, at pH 8 and 9 with BB 0,1 M. Then, 1.5 mL of both nanomaterials were mixed with 100 µL of 140 µg/mL of anti-human IgG γ-chain specific HRP modified and incubated for 20 min at 650 rpm at room temperature. Then, 100 µL of 1 mg/mL BSA solution was added, and stirring was continued for another 20 min at 650 rpm at room temperature. AuNPs were centrifuged at 14,000 rpm and 4 °C for 20 min, while Au–IrO_2 NFs were centrifuged at 7000 rpm at room temperature for 20 min. Supernatants were removed, and the pellets of the conjugated nanomaterials were resuspended in 500 µL PBS buffer containing 5% sucrose, 1% BSA, and 0.5% Tween-20 to obtain an optical density (OD) of 3. For this conjugation, the optimal pH was 9 and 7 for AuNPs and Au–IrO_2 NFs, respectively.

4.2.6. Lateral flow immunoassays: Preparation of the strips and procedure

4.2.6.1. Preparation and assembly of strips

For HIgG detection, test and control lines were spotted onto the nitrocellulose by printing 1 mg/mL of anti-human IgG and anti-goat IgG, respectively, at a dispensing rate of 0.5 µL/cm using an IsoFlow reagent dispensing system. Finally, the nitrocellulose was dried at 37 °C for 2 h. The sample pad (cellulose) was prepared by dipping it into 10 mM PBS, 5% BSA, and 0.05% Tween-20 and dried at 60 °C for 2 h. The conjugate pads were prepared by carefully dispensing the

previously prepared anti-human IgG (γ-chain specific)-HRP/nanoparticle conjugates (with an OD = 3) and dried under vacuum for 2 h. Therefore, the different pads were assembled as follows: detection pad (nitrocellulose membrane), conjugation, sample, and absorbent pad. Finally, the strips were cut 4 mm wide using a strip cutter. Under these conditions, the minimum number of nanoparticles per mm^2 able to discriminate the intensity line from the background were 8.4×10^5 and 1.6×10^6 particles/mm^2 for Au–IrO_2 [1:0.25] NFs (65 nm) and Au–IrO_2 [1:0.25] NFs (53 nm), respectively[56].

4.2.6.2. Lateral flow immunoassay procedure

Sample solutions of 80 µL containing different concentrations of HIgG in PBS 10 mM at pH 7.4 ranging from 1 to 3000 ng/mL, were dispensed onto the sample pad and allowed to flow through the strips during 15 min. Although a visual response was observed in that time, the same volume of buffer was again dispensed to wash away the excess of conjugate and were dried for another 15 min. Three replicates of each concentration were performed, including the blank (buffer only).

4.2.6.3. Calibration curves of HIgG detection based on Au–IrO2 NFs LFAs

Calibration curves, specificity, recovery, and stability tests were performed by using immunoglobulin-depleted human serum spiked with human IgG. Specifically, samples were spiked with 0, 1, 3, 10, 30, 100, 300, 1000, and 3000 ng/mL of HIgG and tested by Au–IrO_2 NFs LFAs to check the feasibility in real sample detection.

4.2.6.4. Specificity tests for Au–IrO_2 NFs LFAs

Immunoglobulin-depleted human serum was spiked with 1000 ng/mL of IgGs from chicken, goat, mouse, rabbit, and human. Human serum samples (0 and 1000 ng/mL HIgG spiked) and the above-mentioned samples were tested by using the Au–IrO_2 NFs [1:0.25] and Au–IrO_2 NFs [1:1.5] LF strips to evaluate their specificity and selectivity for detection of HIgG.

4.2.6.5. Recovery tests for Au–IrO_2 NFs LFAs

Immunoglobulin-depleted human serum was spiked with 0, 30, 100, and 300 ng/mL of HIgG. Samples were detected in 1 day (intra-assay) and in 3 consecutive days (inter-assay). Recoveries were calculated by the equation (spiked concentration of HIgG/calculated concentration of HIgG

× 100) to evaluate the accuracy and precision of the Au–IrO_2 NFs LFAs.

4.2.6.6. Stability tests for Au–IrO_2 NFs LFAs

Au–IrO_2 NFs LF strips were stored at room temperature (25 °C) for 0, 1, 2, and 4 weeks. Immunoglobulin-depleted human serum samples spiked with 0, 30, 100, and 300 ng/mL of HIgG were tested by using the LF strips per storage period to evaluate the stability of the Au–IrO_2 NF systems.

4.2.7. Data Analysis

Once dry, a flatbed SkanMulti LFA scanner was used to scan the strips for obtaining the respective calibration curves. The image analysis was performed using ImageJ software, following the procedure reported by Parolo et al.[12] Origin version 8.5 software was used to fit the data to a four-parameter logistic curve.

4.3. Results and discussions

4.3.1. Synthesis of Au-IrO_2 nanoflowers

The synthesis of Au–IrO_2 NFs is based on a two-step reaction, and the mechanism behind their formation agrees with the nucleation and growth theory, as previously reported[52,57,58]. In the first step, gold ($HAuCl_4$) and iridium salt ($IrCl_3{\cdot}xH_2O$) solutions were mixed to induce the formation of the Au nuclei/seeds through the reduction of $AuCl_4^-$ species to $AuCl_2^-$ by $IrCl_6^{2-}$ [52,57] (see Figure 4.1, nucleation). This first co-reduction produces a color change from yellow to yellow-greenish. Of note, the mixing time of the precursors must be no longer than 5 min because this will induce the agglomeration of nanoflowers. This is due to the formation of bigger seeds, which leads to observe a solution that is clearly green. In the second step, the previously generated seeds were added into a boiling citrate solution to induce the growth of the nanoflowers by the further reduction of the pre-formed seeds by the citrate ions[52] (which act as a reducing agent and stabilizer) (see Figure 4.1, growth). This second reduction process produces a second color change in the solution from yellow-greenish to blackish-blue. The different intermediates involved in the reaction (i.e., nucleation and growth) of the NFs display different colorimetric properties; therefore, the synthesis can be monitored by naked-eye and UV–visible spectroscopy.

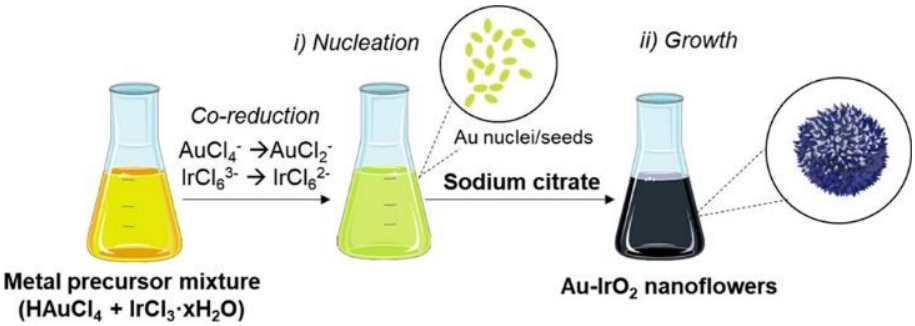

Figure 4.1. Mechanism of Au–IrO_2 NFs formation. (i) in the first step, the co-reduction of both metal precursors leads to the nanoflowers nuclei (nucleation); (ii) the next addition of sodium citrate allows their further reduction, growth, and stabilization, inducing a specific morphology of nanoflowers.

I tested two different metal ratios in order to evaluate how the metal content affects the plasmonic signal, and I selected [Au/Ir] ratios of [1:0.25] and [1:1.5]. The UV–visible spectra of the obtained Au–IrO_2 NFs suspension display a broad peak between 500 and 700 nm for both ratios, with maximum absorption around 600 nm (Figure 4.2). The presence of the single peak is indicative of the formation of an Au–IrO_2 bimetallic nanostructure, because two separated peaks indicate the formation of individual AuNPs and IrO_2 NPs (Figure 4.3)[59–61]. This preliminary data clearly demonstrates the efficacy of our synthetic approach to produce Au–IrO_2 NFs.

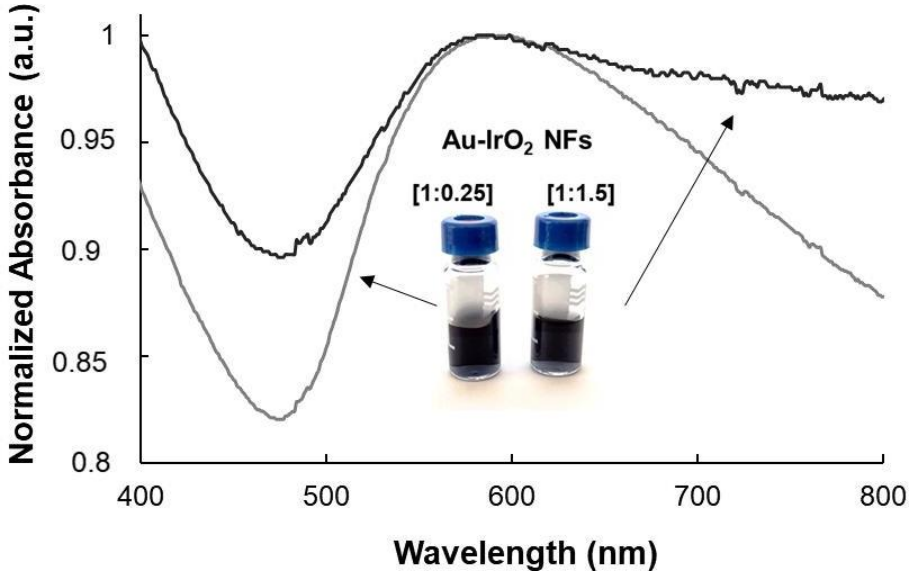

Figure 4.2. UV-visible spectra of Au-IrO_2 NFs. The presence of a single plasmonic peakindicates the formation of the Au-IrO_2 NFs, instead of individual AuNPs and IrO_2 NPs.

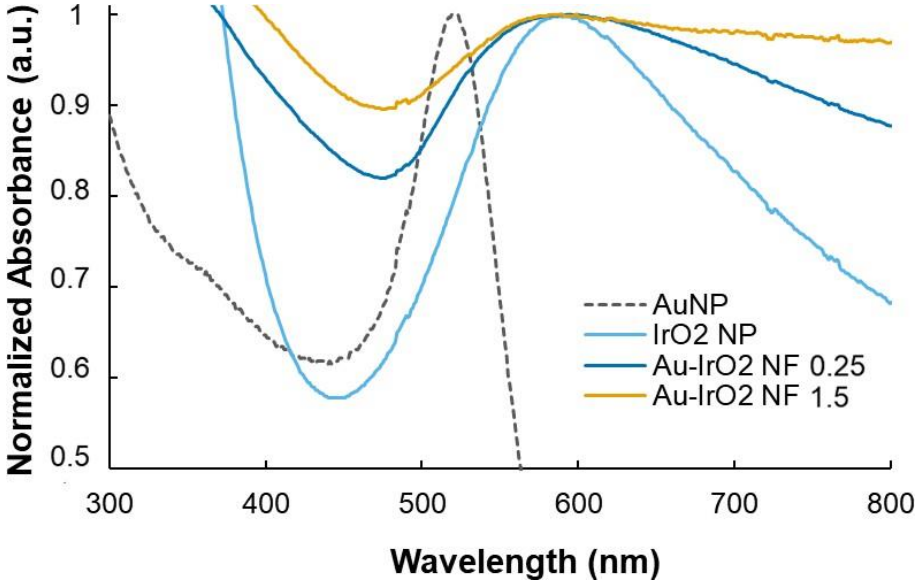

Figure 4.3. UV-vis spectra of AuNPs, IrO_2 NPs and Au-IrO_2 NFs. Syntheses of AuNPs and IrO_2 NPs were conducted as reported by Turkevich[55] and Harriman[62], respectively.

Our next goal is to synthetize smaller nanoflowers than those previously reported (i.e., <100 nm) to support the LFA platform. To achieve this, I decided to simultaneously work on two important parameters to tailor their synthesis: the [citrate]/[$AuCl_4^-$] ratio and the reaction time. Previous studies have reported that the [citrate]/[$AuCl_4^-$] ratio plays a key role in the synthesis and size of mono- or bimetallic nanoparticles in the presence of a reducing agent such as sodium citrate[53,63]. It has been reported that bigger ratios induce the formation of smaller nanoparticles[63]. Inspired by this observation, I decided to increase the citrate concentration from 1.7 to 2.5 mM to compensate an increment of [citrate]/[$AuCl_4^-$] ratio. Next, I also considered the reaction time as an important parameter because it is directly connected with the growth of the NFs. Therefore, I have also decreased the reaction time of the second step from 30 to 5 min to limit the NFs growth and size.

The rationale modification of both parameters of the reaction allowed us to obtain smaller nanoflowers with the expected stability and morphological features. I were able to decrease the diameter of Au–IrO_2 NFs [1:0.25] from 155 ± 6 to 65 ± 6 nm and the diameter of Au–IrO_2 NFs [1:1.5] from 93 ± 6 to 53 ± 4 nm, as shown by the TEM images in Figure 4.6. The results are in agreement with previous studies where the increase in the [citrate]/[AuCl4–] ratio provides smaller nanoparticles, while

the higher content of iridium induces the formation of nanoflowers with a lower size (due to the faster reduction kinetics of the AuCl4– species conducted by the IrCl62– ones)52. After optimizing the reaction, I scaled-up the initial volume of the NFs synthesis up to five times, obtaining a final volume of 30 mL and characterized the morphology and size distribution of Au–IrO2 NFs by using TEM measurements. The resulting scaled-up Au–IrO2 NFs were quite homogeneous with a narrow size distribution (Figure 4.4A and B), as well as showed the same morphology as those synthesized in the initial volume. The size distribution histograms show that the diameters of Au–IrO2 NFs [1:0.25] and [1:1.5] were 64 ± 3 nm (Figure 4.4A) and 55 ± 2 nm (Figure 4.4B), respectively. These results were consistent with the sizes of small-volume synthesis of Au–IrO2 NFs; thus, I demonstrate the feasibility of a scale-up synthesis for Au–IrO2 NFs.

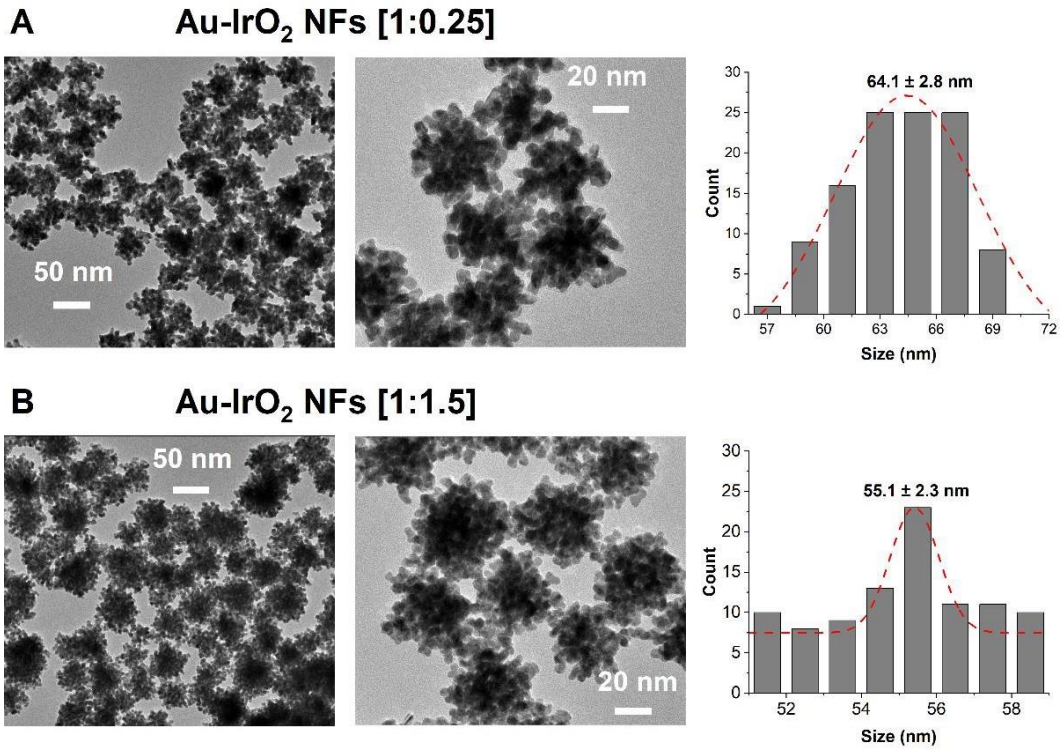

Figure 4.4. TEM images and histograms of Au-IrO2 NFs (synthesis 5 times scaled-up). (A) TEM images of Au-IrO2 NFs [1:0.25] at 50 nm scale (left), at 20 nm scale (middle) and its size distribution histogram (right); (B) TEM images of Au-IrO2 NFs [1:1.5] at 50 nm scale (left), at 20 nm scale (middle) and its distribution histogram.

4.3.2. Au–IrO_2 nanoflower characterization

Before applying the new Au–IrO_2 NFs as labels in LFAs, I proceeded with their full morphological and elemental characterization. Regarding the morphology of the particles, as shown by the TEM

images (Figure 4.6A,A′), both Au–IrO$_2$ NFs samples exhibited good mono-dispersity, homogeneous size, and branches on their surfaces (similar to those obtained by de Freitas et al.)[52], resembling a flower-like nanostructure. Interestingly, using the [Au/Ir] ratio of [1:0.25], the nanostructures showed a spikier surface when compared with the ones with ratio [1:1.5] (see Figure 4.6B,B′). Regarding the elemental analysis, the EDX results confirmed the presence of gold and iridium in the nanoflowers, while the EDX line-scan profile showed the distribution of both elements through the entire nanoparticle (Figure 4.5). Finally, the nanoflower compositions were directly determined by inductively coupled plasma–optical emission spectrometry (ICP–OES), showing the following percentages Au–IrO$_2$ NFs [1:0.25] with 85% Au and 5.9% Ir, while the ones with a [1:1.5] ratio showed 76% Au and 10% Ir.

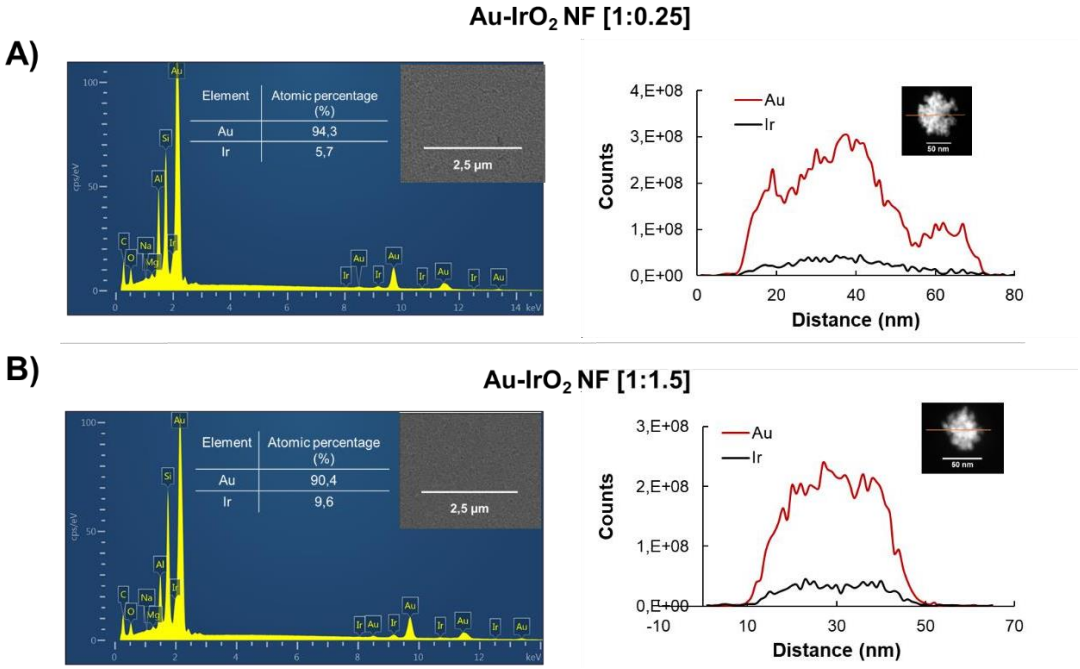

Figure 4.5. EDX spectra of Au-IrO2 nanoflowers and their EDX line-scan profile: (A)[1:0.25] and (B) [1:1.5] and EDX their line-scan profile.

I employed X-ray photoelectron spectroscopy (XPS) to study the surface chemistry of the Au–IrO$_2$ NFs. In this context, prior to element identification and their respective binding energies, both systems were calibrated to the C (1s) line at 284.8 eV, and the data were analyzed using specific software as mentioned above. For gold, two photoemission peaks associated with the Au 4f spin–orbit components were found between 84 and 88 eV and identified as Au 4f$_{7/2}$ and Au 4f$_{5/2}$ core level regions, respectively (see Figure 4.6C,C′). These peaks separated by ≈3.7 eV are

associated with Au^0, which is in agreement with the literature[64,65]. Regarding the iridium, two binding states around 62 and 65 eV were identified as Ir $4f_{7/2}$ and Ir $4f_{5/2}$ core-level regions, respectively. The values for this doublet, separated by ≈3 eV in binding energy, were very close with the ones reported for Ir^{4+} in IrO_2[66–68]. Detailed data about XPS spectra can be found in Table 4.1.

Table 4.1. XPS fitted data for Au-IrO2 NFs

	Au 4f (eV)		Ir 4f (eV)	
Sample	*4f7/2*	*4f5/2*	*4f7/2*	*4f5/2*
[1:0.25]	84.1	87.7	62.1	64.9
[1:1.5]	84.2	87.9	62.1	65.1

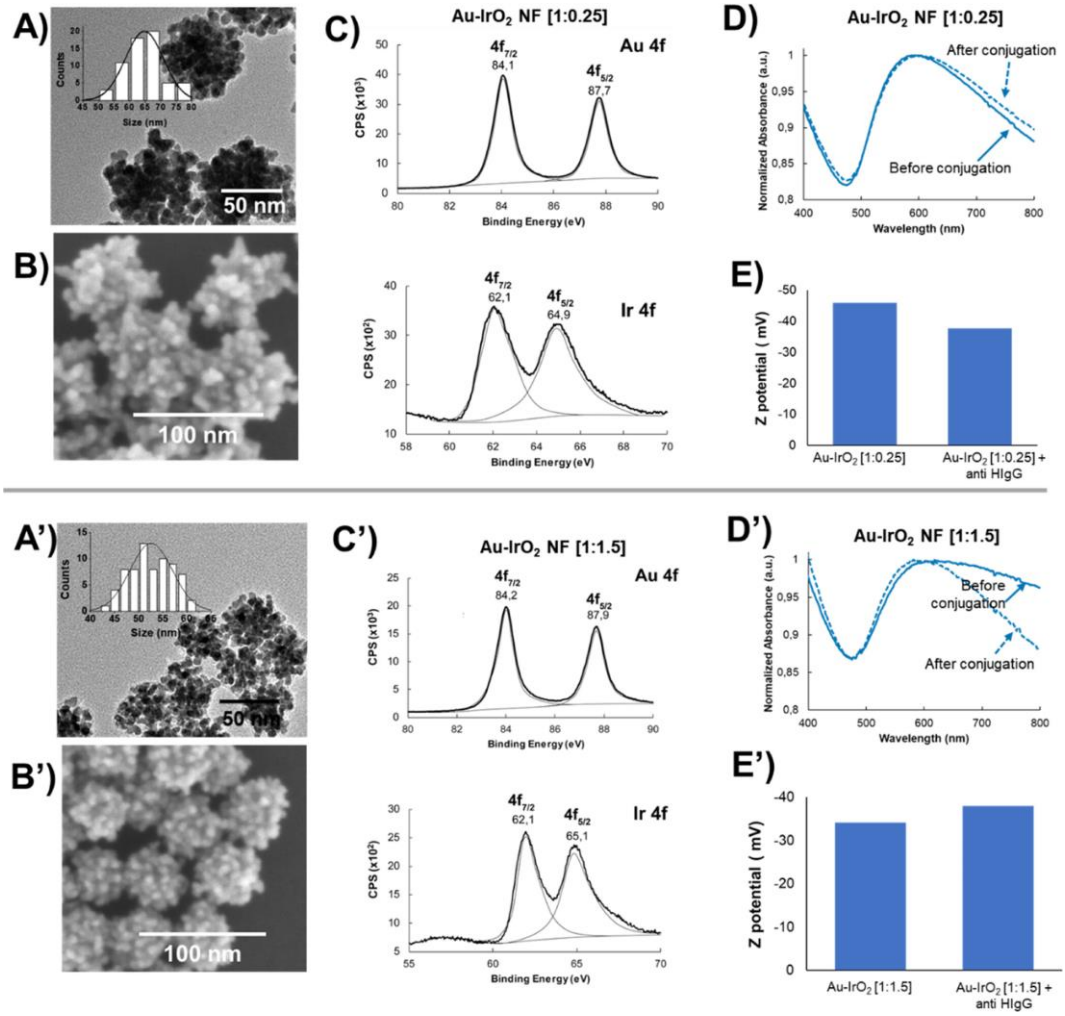

Figure 4.6. Characterization of Au–IrO$_2$ NFs and evaluation of the bioconjugation. The upper panel shows the characterization of the Au–IrO$_2$ NFs obtained with the [1:0.25] ratio using (A) the TEM, (B) the SEM, (C) the X-ray photoelectron spectra of Au 4f and Ir 4f, (D) UV–visible spectra before and after bioconjugation, and (E) *Z*-potential measurements before and after conjugation. Instead, the bottom panel (A′–E′) shows the same characterizations but for the Au–IrO$_2$ NFs obtained with the [1:1.5] ratio. In both cases, the Au–IrO$_2$ NFs resulted monodispersed and made of both Au and IrO$_2$; at the same time, the UV–vis and *Z*-potential measurements indicate the successful biofunctionalization of both nanoflowers with the anti-HIgG antibodies.

4.3.3. Bioconjugation of the Au–IrO$_2$ nanoflowers

Bioconjugation of the synthesized particles was optimized using three different pH values and evaluated by UV–vis spectrophotometry. Using pH 9, I observed the aggregation of the Au–IrO$_2$ NF–antibody conjugate, making it not a suitable condition for the preparation of optical LFA's labels. Instead, pH 7 and 8 guaranteed the stability of the Au–IrO$_2$ solutions. Specifically, as shown in (Figure 4.6D,1D′), the maximum absorbance peak did not change for either of the two Au–IrO$_2$ NF compositions after the conjugation with antibodies, indicating that the monodispersity was maintained after the conjugation process. This behavior is similar to a previously reported study by our group in which IrO$_2$ NPs did not exhibit any measurable change after the bioconjugation at neutral pH[22,68].

Dynamic light scattering (DLS) and *Z*-potential measurements were performed to AuNPs and Au–IrO$_2$ NFs before and after conjugation with the antibodies to evaluate the changes on the hydrodynamic sizes, surface charge, and stability of the nanoparticles. In all cases, the hydrodynamic sizes increased upon the bioconjugation (Figure 4.6E,E′), which can be attributable to a coating layer of antibodies over the nanoparticles (see Table 4.2). It is worthy to note that while the TEM provides the actual size of the metallic particle, the DLS provides the hydrodynamic size of the particle, which also takes into account the size of the antibodies on the particle surface. Finally, I estimated the stability of the Au–IrO$_2$ NFs using *Z*-potentials. Specifically, when absolute *Z*-potential values are within the range of ±30 mV, nanoparticles are likely to aggregate or sediment, instead if the absolute *Z*-potential values are above/below the ±30 mV range, nanoparticles remain stable in colloidal suspensions[69]. Before the conjugation, the *Z*-potential

values (in mV) were −41, −45.9, and −34.9 for AuNPs, Au–IrO_2 [1:0.25], and Au–IrO_2 [1:1.5], respectively. These values indicated that they were stable in colloidal solutions and negatively charged because of the citrate present on their surface, acting as a stabilizer. The physisorption of antibodies onto the nanoparticle surface led to an increase in the *Z*-potential from negative values to fewer negative values (in mV) up to −35.6, −37.7, and −38 mV for AuNPs, Au–IrO_2 [1:0.25], and Au–IrO_2 [1:1.5], respectively. These values indicated both the presence of antibodies on the NF's surface and their stability (see Table 4.2).

Table 4.2. DLS and Z-potential measurements

Nanoparticle	D*H* (nm)	PdI	Z potential (mV)
AuNP	27.4	0.355	-41.8
AuNP + anti HIgG	32.2	0.215	-35.6
Au-IrO_2 [1:0.25]	117.9	0.028	-45.9
Au-IrO_2 [1:0.25] + anti HIgG	140.0	0.085	-37.7
Au-IrO_2 [1:1.5]	122.3	0.118	-34.1
Au-IrO_2 [1:1.5] + anti HIgG	173.9	0.164	-38.0

DH: hydrodynamic size; PdI: polydispersity index

4.3.4. Lateral flow immunoassay

4.3.4.1. Calibration Curves of Au–IrO_2 NFs LFAs for detecting HIgG in PBS buffer and spiked human serum

To demonstrate the ability of Au–IrO_2 NFs to work as labels in LFAs, I compared their analytical performance against standard AuNPs for the detection of HIgG, a clinically relevant biomarker used in serological assays. Specifically, I fabricated LFA strips using a protocol previously reported[31], and I exploited three different NPs: AuNPs (40 nm in diameter) as a control, Au–IrO_2 NFs [1:0.25] and Au–IrO_2 NFs [1:1.5] to assess their performance on LFA strips. The effect of the AuNP's size on the LF sensitivity can be found in Figure 4.7. Then, I challenged AuNP- and Au–IrO_2 NFs-based LFAs at their optimal conditions with different concentrations of HIgG in immunoglobulin-depleted human serum samples ranging from 0 to 3000 ng/mL (Figure 4.8).

Quantitative analyses of the LFA strips were performed according to Parolo et al.[12], and the peak intensities of test lines were plotted versus HIgG concentration to obtain analytical parameters. Data were fitted using a four-parameter logistic curve as summarized in Table 4.3.

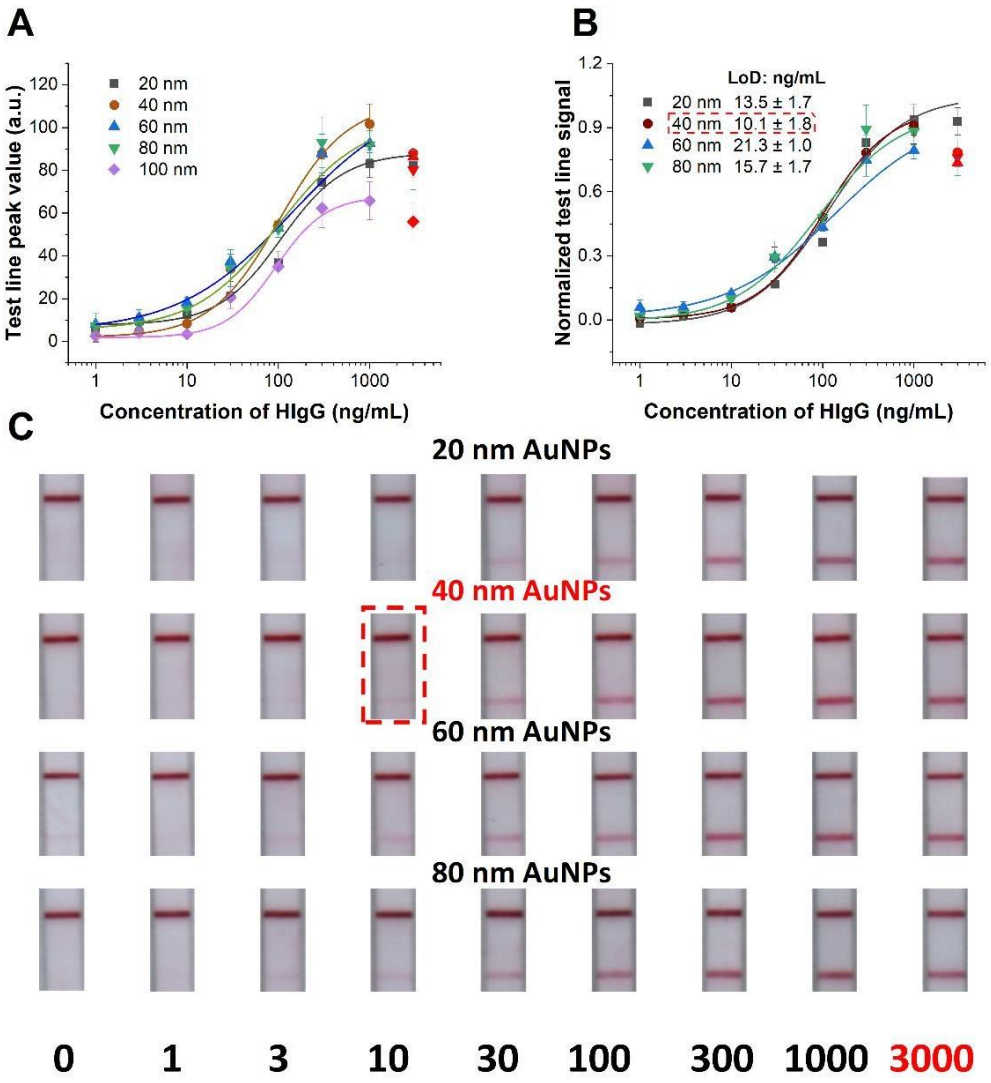

Figure 4.7. AuNPs size effect on sensitivity of LFAs. Calibration curves of 20, 40, 60 and 80 nm AuNPs-LFAs for detection of HIgG in immunoglobulins depleted human serum samples ranging from 0 to 3000 ng/mL. (A) Calibration curves of four AuNPs LFAs: test line peak signal as the y-axe and the log value of HIgG concentrations as the x-axe. (B) Calibration curves of four AuNPs LFAs: normalized test line signal (obtained from (A) equations) as the y-axe and the log value of HIgG concentrations as the x-axe. Equation parameters are summarized in Table S3. (C) The images of four AuNPs lateral flow test strips for detection human IgG ranging from 0 to 3000 ng/mL. 3000 ng/mL was excluded for the calibration curves of 40, 60 and 80 nm AuNPs LFAs.

Table 4.3. Equation parameters of all LFs systems for detection of HIgG inimmunoglobulins depleted human serum samples

	Au-IrO_2 NFs		AuNPs			
	[1:0.25]	**[1:1.5]**	**20 nm**	**40 nm**	**60 nm**	**80 nm**
(Start ± error)	3.96±0.80	-0.15±1.15	7.76±1.83	1.96±2.94	4.67±4.00	5.50±4.40
(End ± error)	110.91±1.80	148.01±12.54	88.13±6.79	111.70±12.94	115.65±20.32	103.53±11.14
(*k* ± error)	41.37±2.72	114.68±29.58	106.96±25.70	102.29±25.72	140.57±71.65	100.18±29.64
(n ± error)	1.02±0.05	0.70±0.06	1.27±0.22	1.16±0.23	0.70±0.19	0.96±0.20
Reduced ^{2}	0.44	0.06	6.68	4.14	4.66	2.33
R^2	0.99	0.99	0.99	0.99	0.99	0.99
Adjusted R^2	0.99	0.99	0.98	0.99	0.98	0.98

The fitted curves correspond to a four-parameter logistic curve (4PL, sigmoidal curve) following the equation: y = START + (END - START) * x^n / (k^n + x^n).

I found that AuNPs-based LFA strips exhibited an estimated visual limit of detection (LoD) of 10 ng/mL, while the use of nanoflowers allowed us to obtain lower visual LoDs of 3 ng/mL for both systems (i.e., Au–IrO2 NFs [1:0.25] and [1:1.5]) (see Figure 4.8). The quantitative analysis of the LFAs using a previously reported procedure[12] also highlights the superior analytical properties of Au–IrO_2 NFs in comparison to the standard AuNPs. Specifically, the calculated LoDs were 10.1, 1.3, and 1.2 ng/mL for AuNPs, Au–IrO_2 NFs [1:0.25], and Au–IrO_2 NFs [1:1.5], respectively. Meaning that about 7-fold and almost 8.5-fold improvements were achieved using Au–IrO_2 NFs [1:0.25] and Au–IrO_2 NFs [1:1.5] with respect to the classical AuNPs-LFAs. The LoDs obtained in real samples were similar to those obtained with the human IgG in PBS buffer (Figure 4.9), showing that the matrix did not affect substantially the signal, thus proving their potential for real sample applications. As I mentioned before, the sensitivity can be improved by different factors such as size, shape, and optical properties of the nanoparticles used as labels. In this work, the main contributor to this improvement is definitely the high optical intensity of the Au–IrO_2 NFs, especially the Au–IrO_2 NFs [1:0.25] which molar extinction coefficient (ε) is twofold the $\varepsilon_{AuNPs(40nm)}$ used in this work, i.e., 5×10^9 vs 2.5×10^9 M^{-1} cm^{-1}. Calculations of these values can be found in the Table 4.4. Based on

these results, the highest extinction coefficient corresponds to the Au-IrO2 NFs [1: 0.25] that agrees with the color intensity of the test lines and therefore, it is correlatedwith the signal to noise ratio. Despite these particles have been recently characterized[52], the molar extinction coefficients have been not reported yet, and the obtained values represent an approximate calculation to explain the strong absorption when compared with AuNPs.

Table 4.4. Extinction coefficients of nanoparticles

Nanoparticle	(ε± error) M^{-1} cm^{-1}
AuNP 20 nm	2.08±0.03 x 10^8
AuNP 40 nm	2.54±0.03 x 10^9
Au-IrO2 [1:0.25] NFs	5.04±0.01 x 10^9
Au-IrO2 [1:1.5] NFs	1.09±0.06 x 10^9

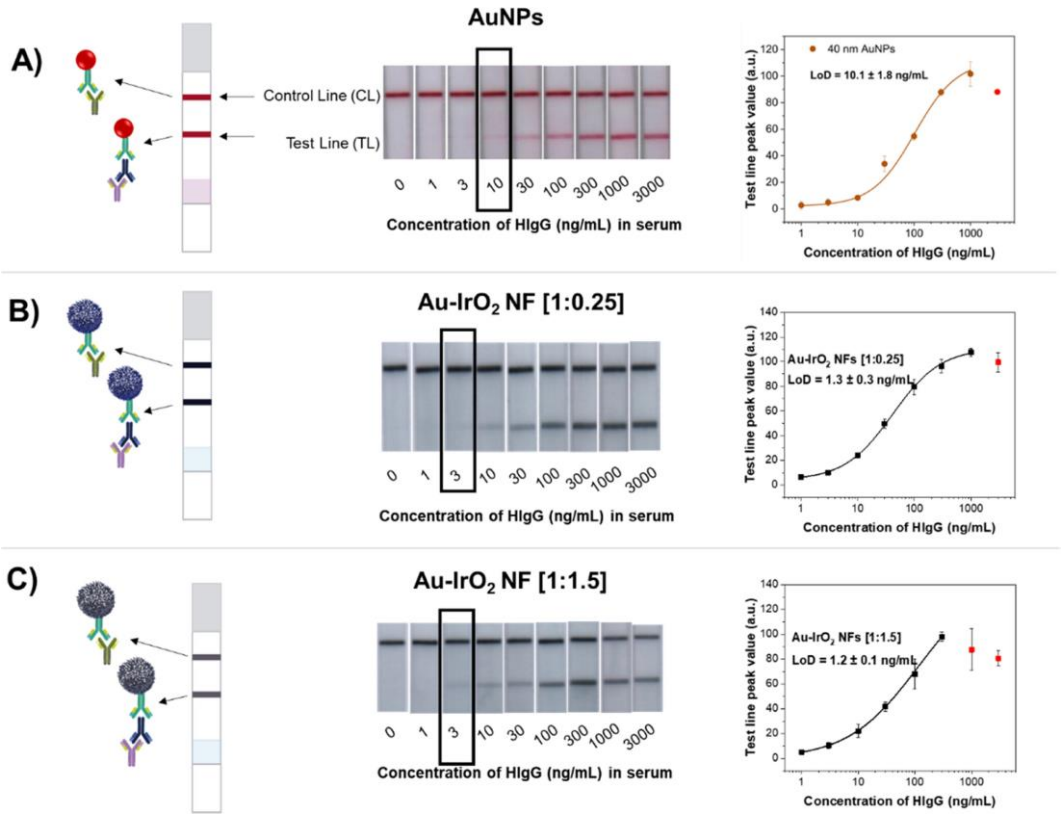

Figure 4.8. Quantification of HIgG in immunoglobulin-depleted human serum by LF strips with: (A) AuNPs, (B) Au–IrO$_2$ NFs [1:0.25], and (C) Au–IrO$_2$ NFs [1:1.5] as colorimetric labels, ranging from 1 to 3000 ng/mL

and their corresponding calibration curves at their optimal pH. Black rectangle over the LF strips indicates the visual limit of detection.

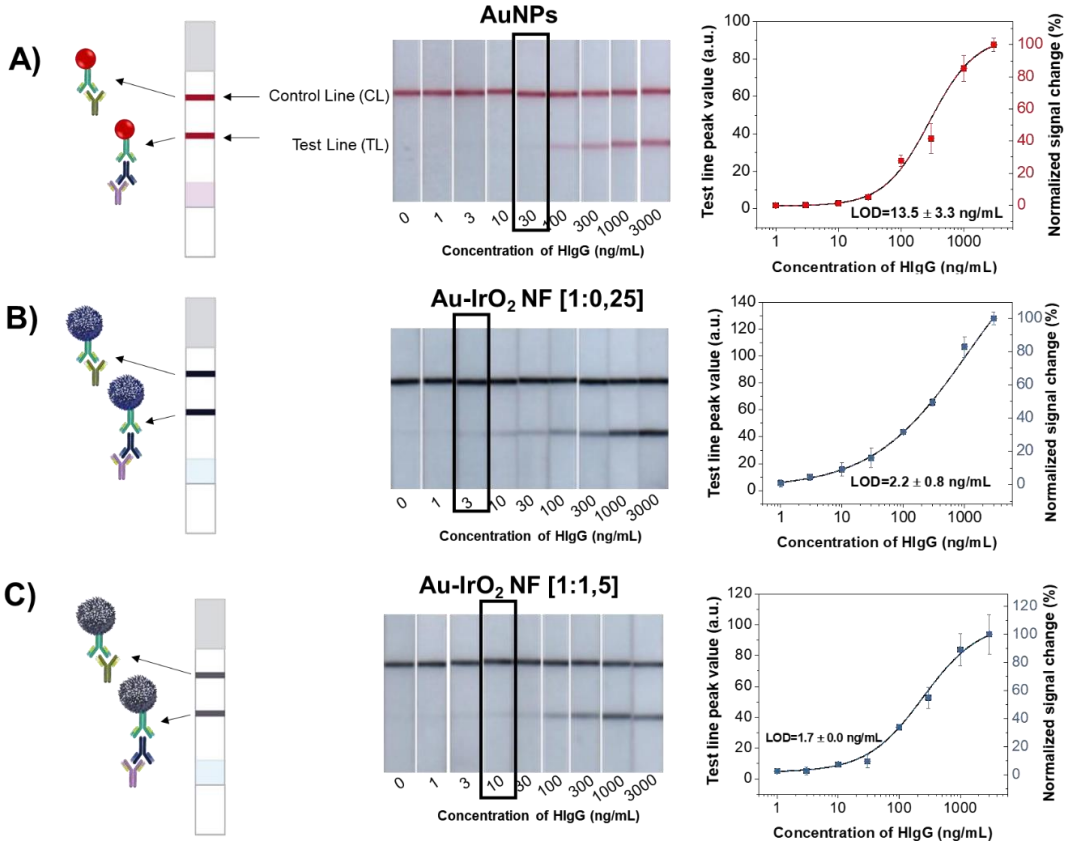

Figure 4.9. Quantification of HIgG (in PBS buffer) by LF strips with: (A) AuNPs (B) Au- IrO_2 NFs [1:0,25] and (C) Au-IrO2 NFs [1:1,5] as colorimetric labels, ranging from 0 to 3000 ng/mL and their corresponding calibration curves at their optimal pH. Blackrectangle over the LF strips indicates the visual limit of detection.

Specifically, the Au–IrO_2 NFs-based LFA strips employing a ratio of Au–IrO_2 NFs [1:0.25] display an intense blackish line, producing a bigger contrast with the nitrocellulose. On the contrary, using Au–IrO_2 NFs with higher iridium content [1:1.5] allow us to obtain a more grayish line at the same concentration of target (Figure 4.10). This difference can be attributable to the suppression of the localized surface plasmon resonance (LSPR) of the plasmonic component (Au) caused by a higher content of iridium in the Au–IrO_2 NFs [1:1.5], which leads to a decrease in the absorbance intensity of the nanoflowers[52]. These results are also supported by the better defined plasmonic peak of Au–IrO_2 NFs [1:0.25] observed in the UV–vis measurement.

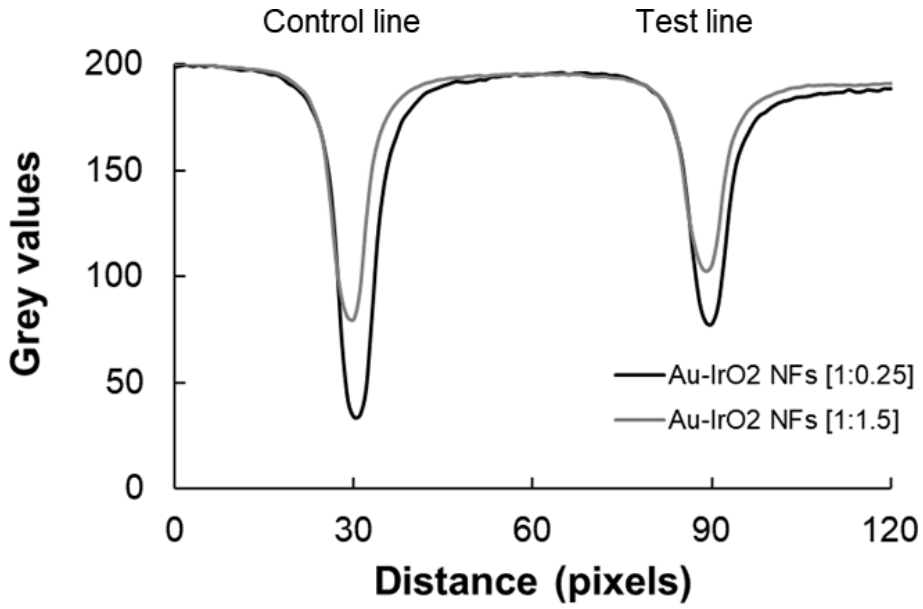

Figure 4.10. Plot profile of Au-IrO$_2$ NFs-LF strips at 1000 ng/mL (in PBS buffer).

An overview of different nanoparticle-based LFAs for the detection of immunoglobulin G is presented in Table 4.5. From the listed nanoparticles, besides the ones used in this work, the nanoparticles that exhibit the lowest LODs correspond to the gold nanocages[70] and Au–Pt nanoflowers[71] because of their unique shapes that allow a higher amount of immobilized antibodies on their surfaces. Spherical AuNPs (17 nm) were used as labels for the detection of HIgG, leading to LODs of 35 and 73 ng/mL in nitrocellulose membranes with different pore sizes, which also have an impact on the sensitivity of the assay[26]. A previous work from our group employed IrO_2 NPs as labels in LFAs due to their bioconjugation capabilities and their vivid blue color, enabling a better contrast with the nitrocellulose, improving the LOD by twofold compared with AuNP-based LFAs for HIgG detection[22]. Despite this, their synthesis is lengthy (ca. 3–4 h) and requires a high amount of blocking proteins upon bioconjugation to avoid the unspecific adsorptions onto the detection membrane. This blocking condition diminish the optical signal on the LFA strip and may detract from their colorimetric advantage with the AuNPs. Here instead, I achieved an 8.5-fold improvement using Au–IrO_2 NFs [1:1.5] (when compared with the optimized AuNP-based LFA) that are easy to synthesize and modify. Additionally, the Au–IrO_2 NFs have a tremendous potential to be used as electrocatalytic labels.

Table 4.5. Comparison of the nanoparticle-based LFAs for detection of IgG

Label	Target	range (ng/mL)	Lineal range (ng/mL)	LOD (ng/mL)	Ref.
Au nanocages	rabbit IgG	0–50	0.5–50	0.1	[70]
IrO_2 NPs	human IgG	0–1000	250–750	70	[22]
AuNPs-17 nm	human IgG	0–1000	10–1000	35	[26]
				73	
Au–Pt NFs	rabbit IgG	0–20	0.5–20	0.047	[71]
Au–IrO_2 NFs [1:0.25]	human IgG	0–3000	10–300	1.3	this work
Au–IrO_2 NFs [1:1.5]				1.2	

4.3.4.2. Specificity and selectivity of Au-IrO_2 NFs-based LFAs

Our LFA strips are sensitive and selective. To demonstrate the specificity of the Au–IrO_2 NFs-based LFAs, I challenged them against immunoglobulin-depleted human serum samples spiked with 1000 ng/mL of IgG from different hosts, such as chicken, goat, mouse, rabbit, and human. This ensures to change the chemistry of the biomolecule without changing the properties of the biological fluid. As demonstrated by the collected data, IgGs from chicken, goat, mouse, and rabbit produced very weak colorimetric signals, similar to their blank (obtained in PBS) (see Figure 4.11). As a positive control experiment, I spiked the serum sample with antibodies from human and, as expected, I observed a 62.3 and 67.7% cross-reaction rate with human IgG antigen (100%). Given the results, both Au–IrO_2 NFs-based LF systems showed good specificity and selectivity, as well as they could discriminate between human IgG from other IgG interfering biomolecules.

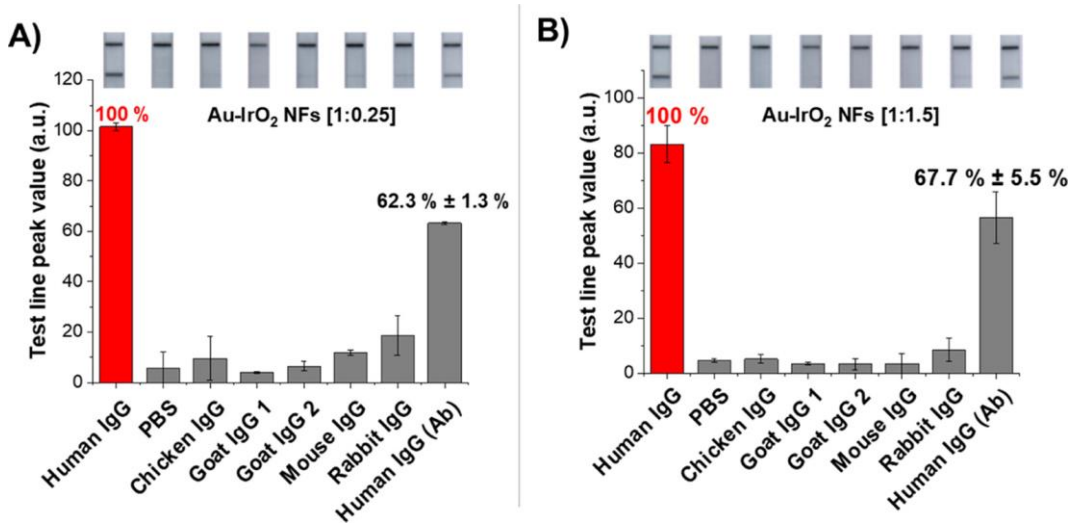

Figure 4.11. Specificity and selectivity tests of (A) Au–IrO$_2$ [1:0.25] and (B) Au–IrO$_2$ NFs [1:1.5] LFA for detection of human IgG. Immunoglobulin-depleted serum was spiked with 1000 ng/mL of IgG from chicken, goat, mouse, and rabbit hosts as the interferences.

4.3.4.3. Recovery of Au-IrO$_2$ NFs-based LFAs for detection of HIgG

The performance of the proposed LFAs was also evaluated by recovery experiments. Immunoglobulin-depleted human serum samples were spiked with 30, 100, and 300 ng/mL of human IgG in the same day (intra-assay) and in 3 consecutive days (inter-assay). The recoveries of Au–IrO$_2$ NFs [1:0.25] LFA ranged between 91.9 and 99.3% for intra-assay experiments and varied between 95.5 and 103.1% for inter-assay experiments. Similarly, the intra- and inter-assay recoveries of Au–IrO$_2$ NFs [1:1.5] LFA were from 92.2 to 109.7% and from 86.0 to 103.2%, respectively (see Table 4.6). Summarizing, all the recovery values were between 86 and 109%, and the coefficients of variation (CV) were less than 15% (Table 4.6). These results demonstrate that both Au–IrO$_2$ NFs LFAs possess a good accuracy and can be considered as a promising alternative for the detection of HIgG in a real scenario.

Table 4.6. Recoveries from the Intra- and Inter-Assays for Detecting HIgG Immunoglobulin-Depleted Human Serum Samples by Au–IrO$_2$ NFs LFAs

		Intra-assay		Inter-assay	
Au–IrO$_2$ NFs	**[spiked HIgG] ng/mL**	**[calculated HIgG] ng/mL**	**recovery (%)**	**[calculated HIgG] ng/mL**	**recovery (%)**
[1:0.25]	30	27.6 ± 3.3	91.9 ± 11.1	30.9 ± 3.2	103.1 ± 10.5
	100	98.5 ± 4.8	98.5 ± 4.8	99.9 ± 12.5	99.9 ± 12.5
	300	298.0 ± 31.2	99.3 ± 10.4	286.5 ± 38.1	95.5 ± 12.7
[1:1.5]	30	32.7 ± 2.4	109.7 ± 7.2	31.5 ± 4.3	103.2 ± 13.3
	100	106.5 ± 6.3	106.5 ± 6.3	97.0 ± 14.4	97.0 ± 14.4
	300	276.6 ± 23.9	92.2 ± 8.0	258.0 ± 36.5	86.0 ± 12.2

4.3.4.4. Stability of Au-IrO$_2$ NFs-based LFAs for detection of HIgG

To assess the performance of the proposed LFAs in the long-term, the Au–IrO$_2$ NFs-based LF strips were stored at room temperature for 0, 1, 2, and 4 weeks, and the signal of immunoglobulin-

depleted human serum samples with 0, 30, 100, and 300 ng/mL HIgG was measured (Figure 4.12A). For all human IgG concentrations tested, the CV values over the time ranged between 0.5 and 7.1% for the Au–IrO_2 NFs [1:0.25] LFA (Figure 4.12B) and between 0.7 and 8.5% for the Au–IrO_2 NFs [1:1.5] LFA (Figure 4.12C). These values demonstrate that both Au–IrO_2 NFs-based LFAs were stable for at least 1 month.

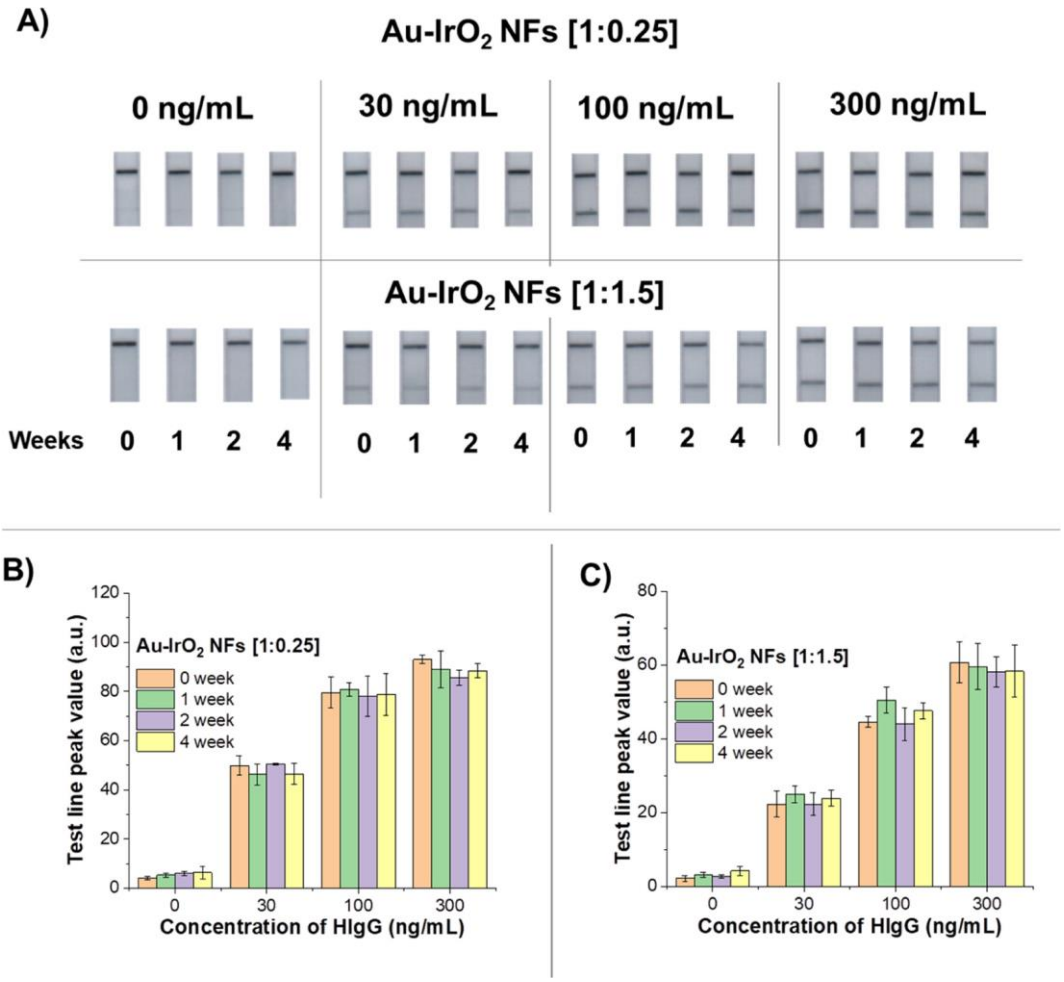

Figure 4.12. Stability performance of Au–IrO_2 NFs-based LFAs for detection of HIgG. (A) Optical intensity values for the detection of 0, 30, 100, and 3000 ng/mL of HIgG in immunoglobulin-depleted human serum, using LFA strips stored at room temperature for 0–4 weeks for (B) Au–IrO_2 NFs [1:0.25] and (C) Au–IrO_2 NFs [1:1.5] LFA, respectively.

4.4. Conclusions

To the best of our knowledge, I have demonstrated for the first time the use of tailored Au–IrO_2 NFs as colorimetric labels for LFAs for the detection of HIgG as a model biomarker. The

promising results obtained in this work indicate that Au–IrO_2 NFs can be used as superior colorimetric labels (compared to the standard AuNPs) in LFAs for the detection of protein biomarkers. Specifically, I managed to decrease the Au–IrO_2 NFs diameter to make them better suited to flow through the LFA strips, while at the same time I preserved their strong plasmonic behavior and stability. Particularly relevant for point-of-care applications, the synthesis and functionalization of Au–IrO_2 NFs are simple and straightforward, potentially supporting their mass production. Employing them as colorimetric labels in LFAs, I achieved an improvement in the LoD of up to 8.5-fold when compared to classical 40 nm AuNPs. Despite I demonstrate the ability of the Au–IrO_2 NFs-based LFA strips to detect the target in a commercial biological fluid, the selected artificially treated sample does not have the same complexity of a pooled human serum sample. This represents a limitation of this work; therefore, further studies need to be performed to optimize the LFAs to support samples from real patients. Looking ahead, I believe that due to the presence of IrO_2 on the nanoflower, they could also act as dual optical/electrochemical labels in paper-based electrochemical systems[68], thanks to their plasmonic peak and electrocatalytic behavior[52].

4.5. References

1. Kevadiya, B. D. *et al.* Diagnostics for SARS-CoV-2 infections. *Nat. Mater.* **20**, 593–605 (2021).

2. Rosati, G. *et al.* Nanodiagnostics to face SARS-CoV-2 and future pandemics : From an idea to the market and beyond. *ACS Nano* **15**, 17137–17149 (2021).

3. Mak, W. C., Beni, V. & Turner, A. P. F. Lateral-flow technology: From visual to instrumental. *TrAC - Trends Anal. Chem.* **79**, 297–305 (2016).

4. Banerjee, R. & Jaiswal, A. Recent advances in nanoparticle-based lateral flow immunoassay as a point-of-care diagnostic tool for infectious agents and diseases. *Analyst* **143**, 1970–1996 (2018).

5. Calabretta, M. M. *et al.* Precision medicine, bioanalytics and nanomaterials: toward a new generation of personalized portable diagnostics. *Analyst* **145**, 2841–2853 (2020).

6. Rodriguez, R. S. *et al.* Sensing food contaminants: advances in analytical methods and techniques. *Anal. Chem.* **93**, 23–40 (2020).

7. Xing, C., Liu, L., Zhang, X., Kuang, H. & Xu, C. Colorimetric detection of mercury based on a strip sensor. *Anal. Methods* **6**, 6247–6253 (2014).

8. Bergua, J. F. *et al.* Lateral flow device for water fecal pollution assessment: from troubleshooting of its microfluidics using bioluminescence to colorimetric monitoring of generic Escherichia coli. *Lab Chip* **21**, 2417–2426 (2021).

9. Shandilya, R. *et al.* Nanobiosensors: Point-of-care approaches for cancer diagnostics. *Biosens. Bioelectron.* **130**, 147–165 (2019).

10. Wang, X., Li, F. & Guo, Y. Recent trends in nanomaterial-based biosensors for point-of-care testing. *Front. Chem.* **8**, 586702 (2020).

11. Zhou, Y., Wu, Y., Ding, L., Huang, X. & Xiong, Y. Point-of-care COVID-19 diagnostics powered by lateral flow assay. *TrAC Trends Anal. Chem.* **145**, 116452 (2021).

12. Parolo, C. *et al.* Tutorial: design and fabrication of nanoparticle-based lateral-flow immunoassays. *Nat. Protoc.* **15**, 3788–3816 (2020).

13. Gasperino, D., Baughman, T., Hsieh, H. V, Bell, D. & Weigl, B. H. Improving lateral flow assay performance using computational modeling. *Annu. Rev. Anal. Chem.* **11**, 219–244 (2018).

14. Mahmoudi, T. *et al.* (Nano) tag–antibody conjugates in rapid tests. *J. Mater. Chem. B* **9**, 5414–5438 (2021).

15. Pirzada, M. & Altintas, Z. Nanomaterials for healthcare biosensing applications. *Sensors* **19**, 5311 (2019).

16. Song, L., Chen, J., Xu, B. Bin & Huang, Y. Flexible plasmonic biosensors for healthcare monitoring: Progress and prospects. *ACS Nano* **15**, 18822–18847 (2021).

17. Liu, H. *et al.* Etched-spiky Au@ Ag plasmonic-superstructure monolayer films for triple amplification of surface-enhanced Raman scattering signals. *Nanoscale Horizons* **7**, 554–

561 (2022).

18. Liu, Y., Zhan, L., Qin, Z., Sackrison, J. & Bischof, J. C. Ultrasensitive and Highly Specific Lateral Flow Assays for Point-of-Care Diagnosis. *ACS Nano* **15**, 3593–3611 (2021).

19. Nguyen, V.-T., Song, S., Park, S. & Joo, C. Recent advances in high-sensitivity detection methods for paper-based lateral-flow assay. *Biosens. Bioelectron.* **152**, 112015 (2020).

20. Bishop, J. D., Hsieh, H. V., Gasperino, D. J. & Weigl, B. H. Sensitivity enhancement in lateral flow assays: A systems perspective. *Lab Chip* **19**, 2486–2499 (2019).

21. Loynachan, C. N. *et al.* Platinum nanocatalyst amplification: redefining the gold standard for lateral flow immunoassays with ultrabroad dynamic range. *ACS Nano* **12**, 279–288 (2018).

22. Quesada-González, D. *et al.* Iridium oxide (IV) nanoparticle-based lateral flow immunoassay. *Biosens. Bioelectron.* **132**, 132–135 (2019).

23. Miller, B. S. B. S. *et al.* Spin-enhanced nanodiamond biosensing for ultrasensitive diagnostics. *Nature* **587**, 588–593 (2020).

24. Ruiz-Sanchez, A. J. *et al.* Tuneable plasmonic gold dendrimer nanochains for sensitive disease detection. *J. Mater. Chem. B* **5**, 7262–7266 (2017).

25. Parolo, C., Medina-Sánchez, M., de la Escosura-Muñiz, A. & Merkoçi, A. Simple paper architecture modifications lead to enhanced sensitivity in nanoparticle based lateral flow immunoassays. *Lab Chip* **13**, 386–390 (2013).

26. Sena-Torralba, A. *et al.* Lateral flow assay modified with time-delay wax barriers as a sensitivity and signal enhancement strategy. *Biosens. Bioelectron.* **168**, 112559 (2020).

27. Sena-Torralba, A. *et al.* A novel ratiometric fluorescent approach for the modulation of the dynamic range of lateral flow immunoassays. *Adv. Mater. Technol.* **7**, 2101450 (2022).

28. Rivas, L. *et al.* Triple lines gold nanoparticle-based lateral flow assay for enhanced and simultaneous detection of Leishmania DNA and endogenous control. *Nano Res.* **8**, 3704–

3714 (2015).

29. Miller, B. S. *et al.* Quantifying biomolecular binding constants using video paper analytical devices. *Chem. Eur. J.* **24**, 9783–9787 (2018).

30. Sena-Torralba, A. *et al.* Paper-Based Electrophoretic Bioassay: Biosensing in Whole Blood Operating via Smartphone. *Anal. Chem.* **93**, 3112–3212 (2021).

31. Rivas, L., Medina-Sánchez, M., de la Escosura-Muñiz, A. & Merkoçi, A. Improving sensitivity of gold nanoparticle-based lateral flow assays by using wax-printed pillars as delay barriers of microfluidics. *Lab Chip* **14**, 4406–4414 (2014).

32. He, H. *et al.* Quantitative lateral flow strip sensor using highly doped upconversion nanoparticles. *Anal. Chem.* **90**, 12356–12360 (2018).

33. Moyano, A. *et al.* Magnetic lateral flow immunoassays. *Diagnostics* **10**, 288 (2020).

34. Peng, L. *et al.* “Naked-eye” recognition: Emerging gold nano-family for visual sensing. *Appl. Mater. Today* **11**, 166–188 (2018).

35. Zhou, Y. *et al.* Emerging strategies to develop sensitive AuNP-based ICTS nanosensors. *TrAC Trends Anal. Chem.* **112**, 147–160 (2019).

36. He, Q. *et al.* Lateral flow immunosensor for ferritin based on dual signal-amplified strategy by rhodium nanoparticles. *ACS Appl. Bio Mater.* **3**, 8849–8856 (2020).

37. Yang, Z. *et al.* Development of a lateral flow strip biosensor based on copper oxide nanoparticles for rapid and sensitive detection of HPV16 DNA. *Sensors Actuators B Chem.* **285**, 326–332 (2019).

38. Tian, M. *et al.* A sensitive lateral flow immunochromatographic strip with prussian blue nanoparticles mediated signal generation and cascade amplification. *Sensors Actuators B Chem.* **309**, 127728 (2020).

39. Lou, S., Ye, J., Li, K. & Wu, A. A gold nanoparticle-based immunochromatographic assay: the influence of nanoparticulate size. *Analyst* **137**, 1174–1181 (2012).

40. Zhan, L. *et al.* The role of nanoparticle design in determining analytical performance of lateral flow immunoassays. *Nano Lett.* **17**, 7207–7212 (2017).

41. Lin, L., Huang, P., Dutta, S., Rochet, J. & Stanciu, L. A. Tuning a Bisphenol A Lateral Flow Assay Using Multiple Gold Nanosystems. *Part. Part. Syst. Charact.* **36**, 1900133 (2019).

42. Petrakova, A. V, Urusov, A. E., Zherdev, A. V & Dzantiev, B. B. Gold nanoparticles of different shape for bicolor lateral flow test. *Anal. Biochem.* **568**, 7–13 (2019).

43. Zhang, W. *et al.* Effect of different-sized gold nanoflowers on the detection performance of immunochromatographic assay for human chorionic gonadotropin detection. *Talanta* **194**, 604–610 (2019).

44. Serebrennikova, K., Samsonova, J. & Osipov, A. Hierarchical nanogold labels to improve the sensitivity of lateral flow immunoassay. *Nano-micro Lett.* **10**, 1–8 (2018).

45. Serebrennikova, K. V, Samsonova, J. V, Osipov, A. P., Senapati, D. & Kuznetsov, D. V. Gold nanoflowers and gold nanospheres as labels in lateral flow immunoassay of procalcitonin. *Nano Hybrids Compos.* **13**, 47–53 (2017).

46. Xu, P. *et al.* Effect of the tip length of multi-branched AuNFs on the detection performance of immunochromatographic assays. *Anal. Methods* **8**, 3316–3324 (2016).

47. Yang, H. *et al.* Platinum nanoflowers with peroxidase-like property in a dual immunoassay for dehydroepiandrosterone. *Microchim. Acta* **187**, 1–12 (2020).

48. Srinoi, P., Chen, Y.-T., Vittur, V., Marquez, M. D. & Lee, T. R. Bimetallic nanoparticles: enhanced magnetic and optical properties for emerging biological applications. *Appl. Sci.* **8**, 1106 (2018).

49. Sytwu, K., Vadai, M. & Dionne, J. A. Bimetallic nanostructures: combining plasmonic and catalytic metals for photocatalysis. *Adv. Phys. X* **4**, 1619480 (2019).

50. Gao, Z. *et al.* Platinum-decorated gold nanoparticles with dual functionalities for ultrasensitive colorimetric in vitro diagnostics. *Nano Lett.* **17**, 5572–5579 (2017).

51. Panferov, V. G., Safenkova, I. V, Zherdev, A. V & Dzantiev, B. B. Urchin peroxidase-

mimicking Au@ Pt nanoparticles as a label in lateral flow immunoassay: impact of nanoparticle composition on detection limit of Clavibacter michiganensis. *Microchim. Acta* **187**, 268 (2020).

52. De Freitas, I. C. *et al.* Design-controlled synthesis of IrO2 sub-monolayers on Au nanoflowers: Marrying plasmonic and electrocatalytic properties. *Nanoscale* **12**, 12281–12291 (2020).

53. FRENS, G. Controlled Nucleation for the Regulation of the Particle Size in Monodisperse Gold Suspensions. *Nat. Phys. Sci.* **241**, 20–22 (1973).

54. Kimling, J. *et al.* Turkevich method for gold nanoparticle synthesis revisited. *J. Phys. Chem. B* **110**, 15700–15707 (2006).

55. Turkevich, J., Stevenson, P. C. & Hillier, J. A study of the nucleation and growth processes in the synthesis of colloidal gold. *Discussions of the Faraday Society* vol. 11 55–75 (1951).

56. Khlebtsov, B. N., Tumskiy, R. S., Burov, A. M., Pylaev, T. E. & Khlebtsov, N. G. Quantifying the numbers of gold nanoparticles in the test zone of lateral flow immunoassay strips. *ACS Appl. Nano Mater.* **2**, 5020–5028 (2019).

57. Zhao, C., E, Y. & Fan, L. Enhanced electrochemical evolution of oxygen by using nanoflowers made from a gold and iridium oxide composite. *Microchim. Acta* **178**, 107–114 (2012).

58. You, H. & Fang, J. Particle-mediated nucleation and growth of solution-synthesized metal nanocrystals: A new story beyond the LaMer curve. *Nano Today* **11**, 145–167 (2016).

59. Devarajan, S., Bera, P. & Sampath, S. Bimetallic nanoparticles: A single step synthesis, stabilization, and characterization of Au–Ag, Au–Pd, and Au–Pt in sol–gel derived silicates. *J. Colloid Interface Sci.* **290**, 117–129 (2005).

60. Radziuk, D. V, Zhang, W., Shchukin, D. & Möhwald, H. Ultrasonic alloying of preformed gold and silver nanoparticles. *Small* **6**, 545–553 (2010).

61. Kariuki, N. N. *et al.* Composition-controlled synthesis of bimetallic gold− silver

nanoparticles. *Langmuir* **20**, 11240–11246 (2004).

62. Harriman, A., Thomas, J. M. & Milward, G. R. Catalytic and structural properties of iridium-iridium dioxide colloids. *New J. Chem.* **11**, 757–762 (1987).

63. Tran, M., DePenning, R., Turner, M. & Padalkar, S. Effect of citrate ratio and temperature on gold nanoparticle size and morphology. *Mater. Res. Express* **3**, 105027 (2016).

64. Naumkin, A. V, Kraut-Vass, A. & Powell, C. J. *NIST X-ray photoelectron spectroscopy database*. (Measurement Services Division of the National Institute of Standards and …, 2008).

65. Sahoo, S. R. & Ke, S.-C. Spin-orbit coupling effects in Au 4f core-level electronic structures in supported low-dimensional gold nanoparticles. *Nanomaterials* **11**, 554 (2021).

66. Freakley, S. J., Ruiz-Esquius, J. & Morgan, D. J. The X-ray photoelectron spectra of Ir, IrO2 and IrCl3 revisited. *Surf. Interface Anal.* **49**, 794–799 (2017).

67. Pfeifer, V. *et al.* The electronic structure of iridium and its oxides. *Surf. Interface Anal.* **48**, 261–273 (2016).

68. Rivas, L., de la Escosura-Muñiz, A., Pons, J. & Merkoçi, A. Alzheimer disease biomarker detection through electrocatalytic water oxidation induced by iridium oxide nanoparticles. *Electroanalysis* **26**, 1287–1294 (2014).

69. Clogston, J. D., Patri, A. K. & McNeil, S. Characterization of Nanoparticles Intended for Drug Delivery. Methods in Molecular Biology (Methods and Protocols). (2011).

70. Yang, Y., Ozsoz, M. & Liu, G. Gold nanocage-based lateral flow immunoassay for immunoglobulin G. *Microchim. Acta* **184**, 2023–2029 (2017).

71. Zhang, J. *et al.* Gold-platinum nanoflowers as a label and as an enzyme mimic for use in highly sensitive lateral flow immunoassays: application to detection of rabbit IgG. *Microchim. Acta* **186**, 1–9 (2019).

CHAPTER 5

AuNPs and Au-IrO_2 NFs as bioluminescence absorbers in bioanalytical platform based on inner filter effect

5.1. Introduction

Since its invention by Engvall and Perlmann in 1971[1], the enzyme-linked immunosorbent assay (ELISA) has become one of the most widely used bioanalytical techniques[1]. Its success relies on its ability to detect with high sensitivity almost any biomolecular target (e.g., peptides[2], proteins[3], antibodies[4,5], hormones[6], vitamins[7], and drugs[8,9]) directly from biological fluids (e.g., serum, plasma, cell, and tissue extracts, etc.) and within a few hours (between 2 and 8 hours)[10]. This provided an unprecedent analytical tool to monitor and assess clinically relevant targets involved, for example, in the progression of a disease (improving our understanding of pathophysiological events[11]) or in the development and testing of novel pharmaceutical treatments[12]. As a result, ELISA has become the cornerstone of clinical[13], pharmaceutical[14], and environmental analysis[15]. Despite its success, ELISA still has limitations, such as time-consuming procedures based on multi-step "batch" processes (i.e., separations, washing, or incubation), the use of large sample volumes, the need for trained personnel and expensive, bulky, and fragile equipment[16]. These drawbacks still hinder the widespread use of ELISA in low-income countries and rural areas[13,17], where fully equipped laboratories, specialized personnel, and significant economic resources may not be available[18,19]. Therefore, the development of new ELISA platforms with lower cost, easier to perform protocols, enzyme-free, high sensitivity and accuracy would allow the widespread use of this technique in low-resource settings[13] and promote the democratization of the healthcare system[20].

Over the past four decades, many research groups have attempted to address these technical challenges by proposing novel detection strategies and bioengineering approaches[13]. Regarding the former, most efforts have focused on making the assays more sensitive, accurate, and high throughput by improving one (or more) component of the ELISA assay (e.g., adsorbent substrate, recognition elements, signaling molecules, and staining reactants). For example, the introduction of nanomaterials and their use as new signaling molecules (e.g., gold nanoparticles[21], nanorods, nanostars, nanoflowers[22] and silver nanoparticles[23], etc.) has allowed the classical colorimetric signal to be converted to a fluorescent or chemiluminescent readout (e.g., plasmonic ELISA, bead-based ELISA called Luminex[24] and ELISpot[25]) achieving higher sensitivity and accuracy. At

the same time, the development of new bioengineering approaches has made ELISA easier-to-perform, for example, by reducing the number of steps, the time required to perform the assay, or the volume required for the analysis (e.g., using paper[26], sliding strips[27] and microfluidic platform[28]). Despite these achievements, less effort has been made to develop more sustainable, low-cost, and enzyme-free ELISA assays that could make the overall platform more robust and potentially applicable in resource-limited settings[13]. For example, most of the aforementioned studies still rely on the catalytic activity of enzymes[29], metal complexes/nanoparticles[30] or oligonucleotides (e.g., DNAzymes[31]), which require specific facilities for their production, synthesis, and storage[10].

Motivated by the above arguments, I propose here an alternative ELISA platform based on the inner filter effect (IFE)[32–35] between the bioluminescent bacteria of *Allivibrio fischeri* (*A. fischeri*)[36] and metallic nanoparticles. I named this new assay: Bioluminescent-Bacteria-Linked Immunosorbent Assay (BBLISA). IFE is a radiative energy transfer phenomenon observed in fluorescence measurements that results from the absorption of the excitation and/or emission energy of the fluorophore by the absorber, when the absorption spectrum of the absorber overlaps with the fluorescence excitation or emission spectrum of the fluorophore (Figure 5.1a)[34,37]. In the BBLISA, *A. fischeri* is the species that emits light (i.e., the bioluminescent signal) and the metallic nanoparticles are the species that absorb the emitted light (Figure 5.1b). More specifically, the presence of the biomolecular target induces the accumulation of the antibody-modified metallic nanoparticles in the well through the formation of the classic immune-sandwich complex (Figure 1c). The subsequent addition of the bioluminescent bacteria to the well allows the generation of a bioluminescent signal whose intensity is inversely-related to the number of metallic nanoparticles and thus to the selected target (Figure 5.1c). To demonstrate the bioanalytical properties of the proposed platform, I used BBLISA for the detection of two biomarkers (the human IgG (HIgG) and the SARS-CoV-2 nucleoprotein (Np)) in their clinically relevant ranges and directly in human serum. By using different metallic nanoparticles (with different light absorption properties) as molecular absorbers, I can modulate the sensitivity of the BBLISA to achieve the same analytical performance as a conventional ELISA.

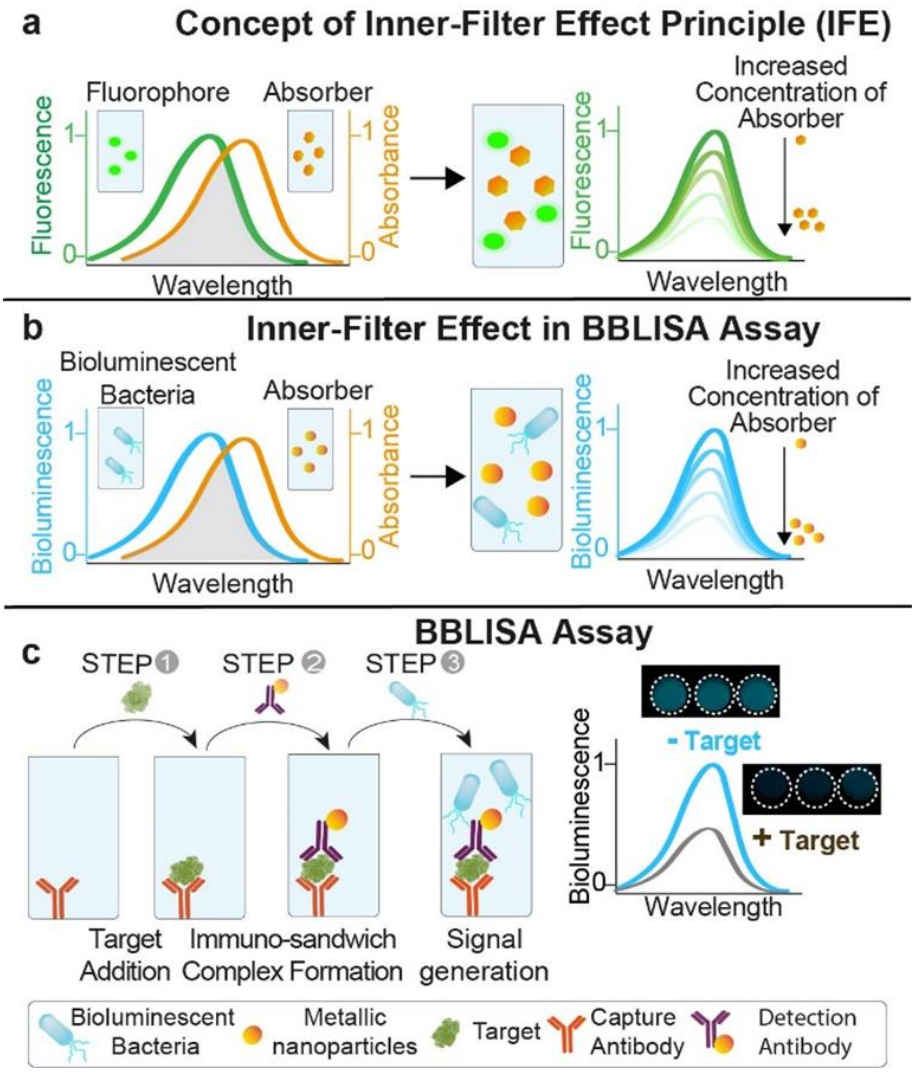

Figure 5.1. (a) Schematic illustration of the Inner Filter Effect (IFE) concept. To observe this optical effect, the absorption spectrum of the absorber must overlap with the emission spectrum of the fluorophore. As a result, when a fixed concentration of fluorophore is titrated into the well with an increasing concentration of absorber, a decrease in fluorescence emission is observed. (b) Schematic representation of IFE in the BBLISA assay. The absorber (i.e., metallic nanoparticles) was selected based on its absorption spectrum which must overlap the bioluminescence emission spectrum of the bioluminescent bacterium (i.e., *A. fischeri*). Therefore, when a fixed concentration of bioluminescent bacteria is titrated into the well with an increasing concentration of nanoparticles, a decrease in bioluminescence emission is observed. (c) Schematic of the BBLISA assay for the detection of clinically relevant targets. The BBLISA assay is based on the classic immunosandwich format and the protocol consists of the following steps: 1) the target is added to the well and captured by the capture antibody; 2) the detection antibody attached to the surface of a metallic nanoparticle recognizes the target inducing the formation of the immunosandwich complex; 3) the

solution containing *A. fischeri* is added to the well and the bioluminescence signal is immediately recorded. Using the immunosandwich format in the BBLISA assay, the optical signal is inversely-related to the concentration of the target.

5.2. Materials and methods

5.2.1. Reagents and buffers preparation

5.2.1.1 Chemicals and biomaterials

Tetrachloroauric acid trihydrate ($HAuCl_4 \cdot 3H_2O$ 99.9%), Iridium(III) chloride hydrate ($IrCl_3 \cdot xH_2O$ 99.9%), sodium citrate, phosphate buffer saline (PBS) tablets, disodium hydrogen phosphate heptahydrate, monosodium phosphate, sodium bicarbonate, sodium carbonate anhydrous, boric acid, sodium tetraborate decahydrate, sodium chloride, hydrochloric acid, sodium hydroxide, bovine serum albumin (BSA), Tween-20, 3,3′,5,5′-Tetramethylbenzidine (TMB, T0440 & T4444), sulfuric acid, human IgG from human serum (I2511), anti-human IgG (produced in goat; I1886), and biotinylated anti-human IgG (γ-chain specific) (produced in goat; B1140) were purchased from Sigma-Aldrich (St. Luis, MO, USA). Human immunoglobulin depleted serum was purchased from Celprogen (Torrance, CA, USA). SARS-CoV-2 nucleocapsid-his recombinant protein (40588-V08B), monoclonal mouse anti-nucleoprotein antibody (40143-MM08) and polyclonal rabbit anti-nucleoprotein antibody (40588-T30) was supplied by Sino Biological. Normal human serum (S1-100ML) was purchased from Sigma-Aldrich (St. Luis, MO, USA). Tributyltin (TBT), tryptone, yeast extract, glycerol for molecular biology, agar, sucrose and casein hydrolysate were purchased from Sigma-Aldrich (St. Luis, MO, USA).

5.2.1.2. Preparation of marine broth medium

Marine broth medium was prepared by dissolving 5 g of tryptone, 20 g of sodium chloride, 3 g of yeast extract, 3 mL of glyceol in 1000 mL of MilliQ H_2O and then autoclaved for 30 min at 121 °C.

5.2.1.3. Preparation of various buffers for BBLISA and ELISA

One PBS tablet (Sigma, P4417-100TAB) was dissolved into 200 mL of MilliQ H_2O to get the 0.01 M, pH 7.4 of PBS buffer. The washing buffer of 0.05% PBST was prepared by adding 0.5 mL Tween-20 to 999.5 mL of 0.01 M, pH 7.4 of PBS buffer. The 0.05 M, pH 9.6 of Carbonate-

Bicarbonate Buffer (CBS) was prepared by dissolving 2.88 g of sodium bicarbonate and 1.666 g of sodium carbonate (anhydrous) to 800 mL of MilliQ H_2O and then using MilliQ H_2O adjusting total volume to 1000 mL.

5.2.2. Production of bioluminescent bacteria

Aliivibrio fischeri (ATCC® 700601™) was purchased from the ATCC collection (Manassas, VA, USA) and stored at -80°C. To culture *Allivibrio fischeri* (*A. fischeri*) I followed a previously established protocol[36] using as medium marine broth (MB). Initially, 25 µL of a stock of *A. fischeri* was taken from -80°C storage and thawed at room temperature for a minimum of 10 minutes. This 2.5 µL of aliquot was then added to 25 mL of MB medium in an Erlenmeyer flask and the solution was cultured at room temperature for 18-24h with continuous orbital shaking at 135 rpm using a SSM1 Stuart mini-orbital shaker (Staffordshire, United Kingdom). If the culture needed to be renewed, 2.5 µL of a 24-hour-old bacterial culture was added to 25 mL of MB medium, and the process was repeated. The concentrations of bacterial suspensions were estimated by analyzing the optical density value at 600 nm (OD_{600}) using the Fisherbrand™ Cell Density Meter, and the software provided by Agilent Genomics (https://www.chem.agilent.com/store/biocalculators/calcODBacterial.jsp) was used for this purpose.

5.2.3. Synthesis of metallic nanoparticles

To characterize the BBLISA sensing mechanism (Figure 5.2), I used commercial AuNPs of different sizes (20, 40, 60, 80 and 100 nm) that were purchased from nanoComposix (Czech Republic). For the BBLISA experiments (Figure 5.9), I synthetized AuNPs of 20 nm using a revised Turkevich synthesis method[38]. Specifically, I added 8 mL of a 1% $HAuCl_4$ solution (25 mM) to an Aqua Regia- cleaned Erlenmeyer flask and adjusted the volume to 400 mL using milli-Q water. The solution was heated to boiling point, and 10 mL of 1% (w/v) sodium citrate was added with vigorous stirring using an IKA Magnetic Stirrers (Spain). The solution was kept at the same condition for 10 minutes until the color changed from light yellow ($HAuCl_4$ color) to deep blue and eventually to wine red. The solution was left to cool down to room temperature with only light stirring, and then stored at 4°C for later usage.

For the BBLISA experiments (Figures 5.10 and 5.14), gold-iridium oxide nanoflowers (Au-IrO_2 NFs) was synthesized following a synthesis method I recently developed[22]. Initially, I heated 25 mL of a solution of sodium citrate (2.5 mM) until it reached the boiling point. Next, I mixed 1770 µL of $HAuCl_4 \cdot 3H_2O$ (12 mM) with 442.5 µL of $IrCl_3 \cdot xH_2O$ (12 mM) and adjusted the solution to 5 mL using milli-Q water. This solution was added in a single step to the boiling sodium citrate solution. Boiling was continued for additional 2 minutes, during which time the solution's color changed from pale green to petrol blue. I then cooled the suspension to room temperature under continuous stirring and stored it at 4°C until further usage.

5.2.4. Optical characterization of *A. fischeri* and metallic nanoparticles

SpectraMax iD3 from Molecular Devices (San José, CA, USA) was used to obtain the bioluminescence and absorption spectra of bacteria and metallic nanoparticles, and to collect the colorimetric and bioluminescence signal during BBLISA experiments. Microplates were purchased from Thermo Fisher (Spain), including transparent 96-well microplates (10078850), transparent and white immuno nonsterile 96-well microplates (10777621 & 10396181), and white sterilized cell culture 96-well microplates (10072151).

To collect the bioluminescence spectra of *A. fischeri* bacteria (Figure 5.2a), 100 µL of a bacterial suspension with a concentration of 10^9 CFU/mL was added to white 96-well microplates. Bioluminescence was detected every 2 nm from 400 nm to 700 nm. To collect the absorption spectra of metallic nanoparticles (Figures 5.2a and 5.10a), 100 µL of different sizes of AuNPs (20 nm, 40 nm, 60 nm, 80 nm and 100 nm) and Au-IrO_2 NFs were pipetted into transparent 96-well microplates. Absorbance was detected every 2 nm from 400 nm to 700 nm.

5.2.5. Bioluminescence of bacteria in the presence of metallic nanoparticles

To characterize the inner filter effect between *A. fischeri* and metallic nanoparticles (Figures 5.2 and 5.10), the naked nanoparticles were first coated with BSA. Specifically, 1 mL of synthesized nanoparticles was mixed with 100 µL of 10% (w/v) BSA in H_2O and incubated for 30 min at room temperature under shaking at 550 rpm. The resulting conjugates were then centrifuged at room temperature using different speeds depending on the size of the AuNPs and Au-IrO2 NFs. More specifically, 14000 rpm (20 min, 20 nm AuNPs), 10000 rpm (20 min, 40 nm AuNPs), 8000 rpm

(15 min, 60 nm AuNPs), 5000 rpm (10 min, 80 nm AuNPs), 3500 rpm (10 min, 100 nm AuNPs), and 6000 rpm (10 min, Au-IrO_2 NFs). The supernatant was removed, and the pellets were resuspended using 500 µL of marine broth media. For the bioluminescence measurements, 50 µL of BSA coated nanoparticles were mixed with 50 µL of *A. fischeri* (10^9 CFU/mL) in 96-well microplates.

To obtain bioluminescence inhibition titration curves of *A. fischeri* ($1 \cdot 10^9$ CFU/mL) (Figures 5.2f and 5.10f), I coated metallic nanoparticles with BSA using the previous procedure. Specifically, I prepared 20 nm coated AuNPs at different concentrations (7.5 pM, 25 pM, 75 pM, 0.25 nM, 0.75 nM, 2.5 nM and 7.5 nM) in marine broth. Additionally, I prepared different concentrations of coated Au-IrO_2 NFs (0. 73 pM, 2.4 pM, 7.3 pM, 24 pM, 73 pM, 0.24 nM and 0.73 nM) in MB. I then mixed 50 µL of each nanoparticle concentration with 50 µL of *A. fischeri* (about 10^9 CFU/mL) in the 96-well microplates. Bioluminescence signals were collected from three different wells for each nanoparticle concentration.

5.2.6. Growth curves of *A. fischeri* in presence of AuNPs or Au-IrO_2 NFs

In order to obtain bacterial growth curves (Figures 5.2c and 5.10d), 40 µL of 20 nm AuNPs (2.5 nM) or Au-IrO_2 NFs (0.24 nM) coated with BSA were mixed with 160 µL of *A. fischeri* (10^3 CFU/mL) in the transparent 96-well microplate with a lid. Additionally, 40 µL of pesticide tributyltin (at a concentration of 100 ng/mL) was mixed with 160 µL of *A. fischeri* (about 10^3 CFU/mL) as positive-toxic control. The microplate was then placed on the support of SpectraMax iD3 and absorbance at 600 nm was detected every 10 min for 48 hours under orbital shaking. For the bacterial growth curves obtained collecting the bioluminescence signal, I repeated the previous procedure but I used white 96-well microplates with lids. All the measurements were performed using three replicates.

5.2.7. Characterization of *A. fischeri* and metallic nanoparticles

To characterize the internal structure, external morphology, dispersion, diameter, and size uniformity of AuNPs and Au-IrO_2 NFs, high-resolution transmission electron microscopy (HR-TEM) measurements were carried out using a Tecnic G2-F20 (Figure 5.6a and 5.10b). TEM grids (carbon film 300 MESH Copper grids CF300-CU) were obtained from Electron Microscopy

Sciences. For TEM imaging, metallic nanoparticles coated with BSA (AuNPs and Au-IrO_2 NFs) were first centrifuged and then diluted with milli-Q water until transparent color was achieved. The diameters of the nanoparticles and their size distribution were analyzed using Image J software and represented as a histogram (Figure 5.6b and 5.11a). SEM images of *Allivibrio fischeri* were obtained using a SEM Zeiss EVO MA10. A 20 mL aliquot of 10^9 CFU/mL fresh *A. fischeri* was processed according to SEM testing protocol[39], which enabled the clear visualization of the bacteria's morphology and structure (Figure 5.2d). Cryogenic Electron Microscopy (Cryo-EM) was used to visualize *Allivibrio fischeri* with metallic nanoparticles (AuNPs and Au-IrO_2 NFs) using TEM JEOL 2011 200 KV (Figure 5.2e and 5.10e). For the measurement, 10^9 CFU/mL of *A. fischeri* and metal nanoparticles coated with BSA (1.25 nM of AuNPs and 0.03 nM of Au-IrO_2 NFs) were mixed in equal volumes and processed for Cryo-TEM testing. A 3.9 µL aliquot of the resuspended was added to a carbon TEM grid, held with a pair of forceps, and loaded onto a preparation chamber containing a liquid ethane bath cooled to a temperature between -178°C and -180°C using an automated liquid nitrogen flow[40]. The resulting images were acquired by a Gatan Ultrascan US1000 CCD camera and analyzed with a Digital Micrograph 1.8.

5.2.8. Conjugation of metallic nanoparticles with antibodies

To conjugate anti-human IgG antibodies (anti-HIgG) and anti-nucleoprotein of SARS-CoV-2 antibodies (anti-Np) to metallic nanoparticles, I followed a previously established protocol[22,41]. I adjusted AuNPs solution to pH 8 and Au-IrO_2 NFs solution to pH 7 using 0.1 M of borate buffer (BB, pH 9.2) for conjugation with anti-HIgG and anti-Np, respectively. I then mixed 1.5 mL of AuNPs or Au-IrO_2 NFs with 100 µL of 30 µg/mL of biotinylated anti-HIgG (or 100 µL of 10 µg/mL of anti-Np) and incubated the mixture for 30 min with 550 rpm shaking at room temperature. Next, I added 100 µL of 1% BSA (w/v) solution and continued the incubation for another 30 min with 550 rpm shaking at RT. I centrifuged the AuNPs conjugates at 14000 rpm and RT for 20 min, while I centrifuged Au-IrO_2 NFs at 6000 rpm at RT for 10 min. I removed supernatants and washed the pellets of the conjugated nanomaterials one time using equal volume of PBST (0.01M PBS, 0.05% Tween-20, pH 7.4). I then centrifuged the pellets again using the same parameter and resuspended them in 0.75 mL (AuNPs conjugates) or 1.5 mL (Au-IrO_2 NFs) of PBS (0.01 M, pH 7.4) and stored at 4°C for further use. For the dynamic light scattering (DLS) and particle surface

charge measurement (Z-potential) (Figure 5.6c and 5.11b and Table 5.1), I used 1.25 nM of AuNPs and AuNPs conjugates aqueous solution (or 0.03 nM of Au-IrO_2 NFs and Au-IrO_2 NFs conjugates). These measurements allowed us to estimate the changes of size, distribution, and stability of metallic nanoparticles before and after conjugation with protein. For the incubation step I used a PCMT ThermoShaker (Grant Instruments, UK). Nanoparticles were centrifuged in a Centrifuge Allegra 64 R from Beckman Coulter (USA). DLS and Z-potential measurements were performed using ZetaSizer Nano ZS (Malvern, United Kingdom).

5.2.9. Detection of human IgG and SARS-CoV-2 nucleoprotein based on colorimetric ELISA

To coat the wells, 100 µL of 2 µg/mL of anti-HIgG or 5 µg/mL of anti-Np in Carbonate-Bicarbonate buffer (CBS, 0.05M, pH 9.6) was added to each well and incubated overnight at 4°C. The solution with the antibody was removed and the wells were washed three times with 250 µL of washing buffer PBST (0.01 M PBS, 0.05% Tween-20, pH 7.4). Next, 200 µL of 3% BSA (in 0.01 M PBS, pH 7.4) was added for blocking extra space and avoiding the non-specific interactions from detection antibody. The plate was incubated for 1 h at 37°C, followed by washing steps. For the assay, 100 µL of human IgG or nucleoprotein samples were added to the wells pre-coated with anti-HIgG or anti-Np, and the plate was incubated for 45 min at 37°C. Afterward, 100 µL of detection anti-HIgG or anti-Np antibody were added to each well and incubated for 30 min at 37°C. Next, 100 µL of streptavidin-HRP or secondary antibody modified by HRP was added to each well and incubated for another 30 min at 37°C. After each incubation step, the plate was washed three to five times with PBST. Finally, 100 µL of TMB (substrate solution) was added to each well and incubated for 20 min at 37°C, followed by the addition of 50 µL of 1M H_2SO_4 (stop solution). The plate was immediately read using a spectrophotometer at 450 nm and 620 nm.

5.2.10. Detection of human IgG or nucleoprotein based on BBLISA

The first three steps of the BBLISA protocol, which involve capture antibodies pre-coating, blocking with BSA, and analyte incubation, are identical to those in the colorimetric ELISA method. However, in BBLISA, the analyte-bound wells are incubated with AuNPs (2.5 nM) or Au-IrO_2 NFs (0.12 nM) conjugates for 30 min at 37°C, followed by washing five times. Finally, 100 µL of pre-cultured bioluminescent bacteria (*Allivibrio fischeri,* 10^9 CFU/mL) were added to the wells, and

bioluminescence is immediately collected using a spectrophotometer at 495 nm.

5.2.11. Data analysis

Colorimetric or bioluminescence signal were acquired with SpectraMax iD3. Fiji Image J-windows 64 bit was used to measure the diameter of nanoparticles from TEM images. Origin 2019-64 bit software was used for fitting curves using four parameter logistic equation[42].

To obtain the relative signal change (%) in BBLISA (Figures 5.2, 5.5b, 5.9, 5.10, 5.13b and 5.14) at a given absorber or target concentration I measured the bioluminescence signal and relates this to the initial signal of the *A. fischeri* in the absence of absorber or target, using the following formula:

$$Signal\ \ change\ \ (\%) = \frac{BL(absorber\ \ or\ \ target) - BL_0}{BL_0} \times 100$$

where BL (Absorber or target) is the bioluminescence in the presence of the absorber or the target; BL_0 is the bioluminescence of *A. fischeri* in the absence of absorber or target.

I fit the calibration curves for BBLISA with the following four parameter logistic equation:

$$Signal\ \ change\ \ (\%) = BL_{max} + \frac{(BL_{max} - BL_{min})}{\left(1 + \left(\frac{X}{IC_{50}}\right)^{h}\right)}$$

where X is the concentration of the target, BL_{max} is the maximum value of the signal change (%) in the absence of target, BL_{min} is the minimum value of the signal change (%) in the presence of the target, IC_{50} is the concentration of target where is located the inflection point, and h is the Hill coefficient which describes the slope of the curve.

To improve the comparison between BBLISA and ELISA, I normalized the signal change (%) (Figures 5.9 and 5.10) using the following equation:

$$Norm.Sign.Change = \frac{Signal\ \ change\ \ (\%)}{(BL_{max} - BL_{min})}$$

Additionally, I normalized absorbance (Figures 3 and 5) and bioluminescence signals using the following formulas:

$Norm.Bioluminescence = \frac{BL - BL_0}{BL_{max} - BL_0}$,

$$Norm.Absorbance = \frac{A - A_0}{A_{max} - A_0}$$

where A is the absorbance in the presence of the target, A_{max} represents the maximum absorbance value at saturating concentration of target, A_0 is the absorbance in the absence of target.

The limit of detection (LOD) was estimated measuring ten replicates of a blank sample, determining the mean value and standard deviation (SD), and calculating LOD as the mean ± 3 SD. The limit of quantification (LOQ), instead, was calculating as the mean of the blank ±10 SD (for ELISA (blank + 3 * SD; blank + 10 * SD and for BBLISA (blank - 3 * SD; blank - 10 * SD)). The dynamic range was calculated as the concentration range that induces a signal change of 10% to 90%. All of the performance parameters are summarized in Tables S2 and S3.

5.3. Results and discussions

5.3.1. BBLISA design and inner filter effect characterization

To develop the BBLISA, the first step is to select a molecular absorber that can efficiently absorb the light emitted by the bacteria (i.e., *A. fischeri*) (Figure 5.2a, blue spectrum). This molecular component must have an absorption spectrum that overlaps with the emission spectra of the *A. fischeri* (Figure 5.1b). In addition, it must be non-toxic to the bacteria, easy to functionalize with common bioreceptors (e.g., antibodies and aptamers), and must be stable over time. With this in mind, I chose the well-known and widely used gold nanoparticles (AuNPs) as a test bed[43]. More specifically, they exhibit plasmonic (absorption) peaks in the range of approximately from 515 nm to 575 nm (depending on the AuNP diameter)[44] (Figure 5.2a, colored spectra). Their synthesis is inexpensive and can be performed using different methods[38,45–48] with a small and low-cost laboratory equipment. Finally, they are non-toxic to both bacteria and humans[49,50], and can be easily functionalized with bioreceptors (both via non-covalent adsorption or using covalent strategies)[46,51,52]. Of note, the non-toxicity of AuNPs is crucial because it guarantees that the decrease in bioluminescence signal is due to the IFE and not to the death of bacteria due to the presence of the nanomaterial.

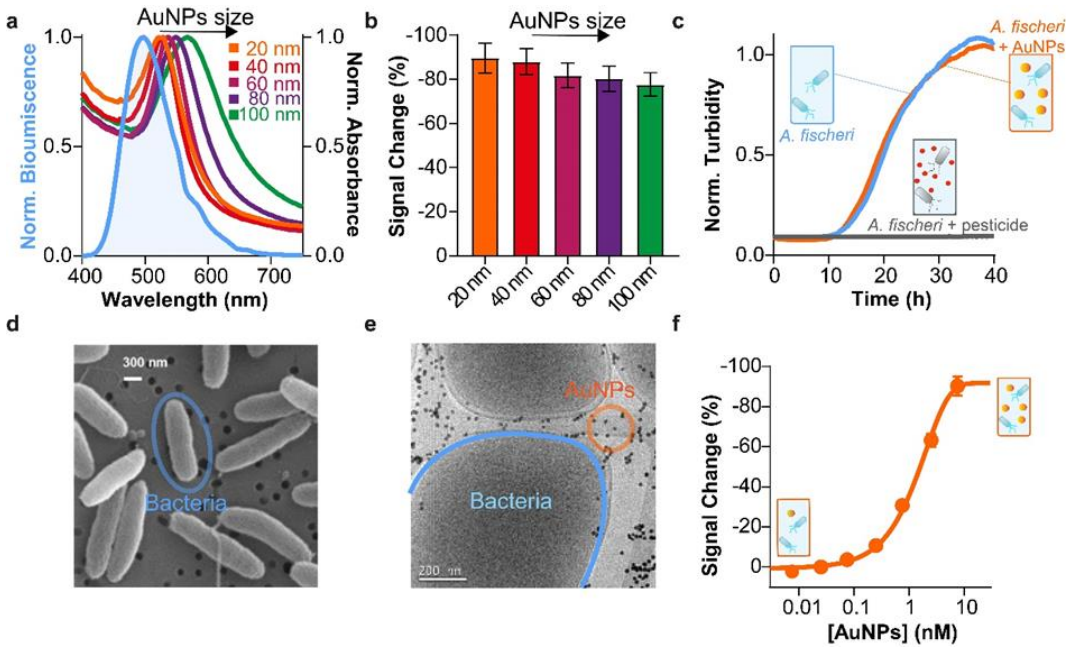

Figure 5.2. Characterization of the inner filter effect between *A. fischeri* and AuNPs. (a) Normalized emission spectrum of *A. fischeri* (blue) and the absorption spectra of different sizes of AuNPs (20, 40, 60, 80 and 100 nm; from orange to green) are shown. The overlapping capability between *A. fischeri* and AuNPs decreases as the size of AuNPs increases, as indicated by the plasmonic peak red shift associated with larger AuNPs. (b) Bioluminescence signal change of *A. fischeri* is plotted as a function of AuNPs with different sizes (i.e. 20, 40, 60, 80 and 100 nm). (c) Normalized absorbance at 600 nm of *A. fischeri* in the presence and absence of 20 nm AuNPs (2.5 nM, orange and blue curves) or pesticide tributyltin (100 ng/mL, grey curve) over a time period from 0 h to 40 h. The inset shows a cryo-TEM image indicating that AuNPs are distributed in the culture medium and some even adhere to the wall of *A. fischeri* without affecting their growth. (d) SEM image of *A. Fischeri* rod-shaped and terminal flagellated. (e) A cryo-TEM image of A. fischeri in the presence of AuNPs. (f) Bioluminescence signal change of *A. fischeri* ($1 \cdot 10^9$ CFU/mL) is plotted as a function of different concentrations of 20 nm AuNPs. All values reported are the average of three measurements and error bars reflect standard deviation.

Because AuNPs can efficiently absorb the light emitted by bacteria, they are an ideal molecular light absorber to demonstrate the bioanalytical properties of BBLISA. First, I characterized the optical properties of AuNPs to demonstrate their ability to support IFE[53]. To do this, I tested AuNPs with different diameters (20, 40, 60, 80 and 100 nm) since their absorption spectra vary with their size (Figure 5.2a, colored spectra)[54]. This allows us to create a set of molecular absorbers that

share the same chemical composition but have different absorption peaks and thus different light absorption capabilities. As expected, the AuNPs exhibit their respective absorption peaks at wavelengths of 520, 530, 538, 550 and 568 nm (Figure 5.2a, colored spectra). I then tested them in the presence of the bioluminescent bacteria in order to characterize their ability to adsorb the bioluminescent signal. AuNPs with smaller size progressively induce higher suppression of the signal change (relative change in signal upon the addition of the saturating AuNP or target) (Figure 5.2b). For example, I found that 20, 40, 60, 80, and 100 nm AuNPs decreased the bioluminescence signal by -90±7%, -88±6%, -82±6%, 80±6%, and -78±5%, respectively (Figure 2b). The slight difference reflects the ability of AuNPs to overlap the emission spectra of bacteria, however, their overlapping progressively decreases due to their size which induces the peak shift toward higher wavelengths. It should be noted that for better comparison, I used concentrations of AuNPs that produced the same absorbance of 0.32 ± 0.01 abs at the respective plasmonic peak (Figure 5.3). As expected, the 20 nm AuNPs perform best as light absorbers because their plasmonic peak better overlaps the light emitted by *A. fischeri* at 495 nm (Figure 5.2a, orange spectra), and I select them for the next development of BBLISA.

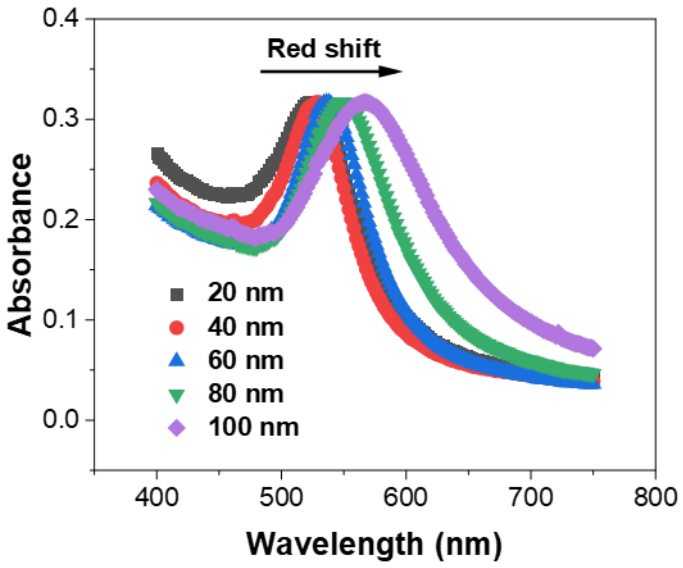

Figure 5.3. Raw absorption spectra of AuNPs of different size (20, 40, 60, 80, and 100 nm) shown in Figure 5.2a exhibit identical absorbance values at their maximum absorption wavelengths.

I sought to demonstrate that the decreased bioluminescence signal was due to the inner filter effect and not to a potential toxicity of AuNPs to the bacteria. To this end, I cultured the bacteria in the presence and in the absence of 20 nm AuNPs (concentration of 0.5 nM) and I used the pesticide tributyltin (concentration of 100 ng/mL) as a positive toxic control[36,55]. Turbidity measurements (using the correlation between absorbance at 600 nm and the number of microorganisms[56]) were firstly used to determine the number of microorganisms growing in the culture media. *A. fischeri* shows the same growth trend with and without AuNPs demonstrating their non-toxicity (Figure 5.2c, blue and orange curves). On the contrary, the presence of the tributyltin inhibited the bacterial growth due to its toxicity (Figure 5.2c, gray curve) and the same result was observed for the negative control (only culture media without *A. fischeri*) (Figure 5.2c, black and red curves). I then used the bioluminescence measurements to monitor bacterial growth kinetics (Figure 5.4). I found again that *A. fischeri* shows the same growth trend, however, the bioluminescence signal was lower in the presence of AuNPs for IFE than in the absence of AuNPs for the same concentration of bacteria. This result supports the previous turbidity measurements. To further demonstrate the IFE effect, I used SEM and Cryo-TEM images to visualize the interactions between the bacteria and AuNPs (Figure 5.2d and Figure 5.2e). For both images, the metal nanoparticles are dispersed in the culture medium and are not absorbed into the bacterial cells. This shows that the decrease in bioluminescence signal is not related to the distance between the bacteria and the AuNPs (as observed for the quenching[57]), but is due to the inner filter effect[32] that occurs between the AuNPs and the *A. fischeri*.

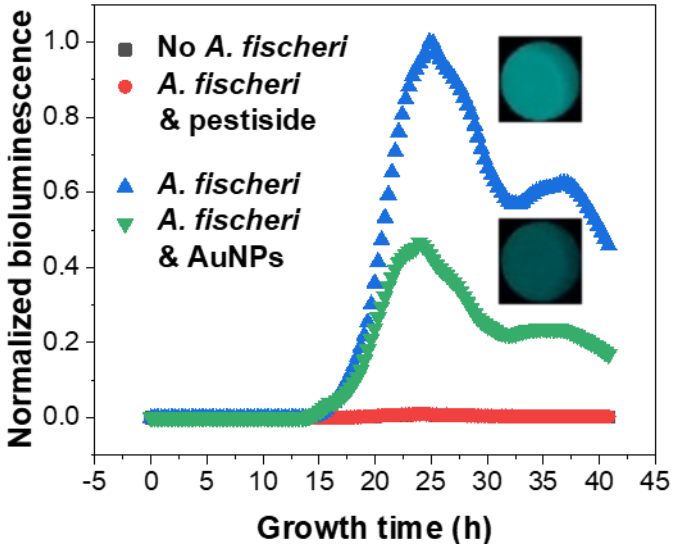

Figure 5.4. Normalized bioluminescence signal of *A. fischeri* in the presence and absence of 20 nm AuNPs was collected from 0 h to 42 h. Of note, the curves of No *A. fischeri* (black rectangle) is hidden by *A. fischeri* & pestiside (red circle) because they are completely overlapped and consistent with baseline. The embedded images were captured by a smartphone in a dark environment and represent the bioluminescence capability of *A. fischeri* in the presence (image above, weak BL intensity) and absence (image below, strong BL intensity) of 20 nm AuNPs. The normalized bioluminescence values are estimated as the ratio B/B_{max}, where B_{max} represents the maximum bioluminescence signal during the growth period (0-40h), and B is the bioluminescence signal at each detection time (growth time).

Finally, I characterized the correlation between the concentration of AuNPs and the suppression of the bioluminescence signal. I collected the light emitted by the bacteria ($1 \cdot 10^9$ CFU/mL) in the presence of increasing concentrations of 20 nm AuNPs (from 0.0075 nM to 7.5 nM) (Figure 5.2f). The optical data indicate that concentrations of AuNPs below 0.075 nM do not cause a relevant decrease in the bioluminescence signal (compared to the bioluminescence intensity in the absence of AuNPs). Conversely, AuNPs concentrations higher than 0.25 nM cause a progressive decrease in the bioluminescent signal. Specifically, 0.25 nM of AuNPs leads to an 11% decrease in bioluminescence intensity, while 7.5 nM concentration allows to reach 90% of bioluminescence suppression (Figure 5.2d). I then characterized the effect of different concentrations of *A. fischeri* have on the bioluminescence signal. As expected, an increase in bacterial concentration results in a higher background bioluminescence signal (Figure 5.5a). I tested four different concentrations of bacteria ($5 \cdot 10^7$, $1 \cdot 10^8$, $5 \cdot 10^8$ and $1 \cdot 10^9$ CFU/mL) in the presence of three concentrations of AuNPs (0.25, 0.75 and 2.5 nM). The addition of the AuNPs induces a decrease of the bioluminescence signal in all suspensions showing a raw signal change function of the bacteria concentrations. However, if the raw bioluminescent signal is converted into signal change (see Materials and Methods for more details), I obtain the same value of ~25%, ~50% and ~73% regardless of the bacterial concentration used (Figure 5.5b). This simply conversion of the raw signal allows to make the signal change independent from the initial bacterial concentration and is only related to the amount of AuNPs present in the solution. This is critical for the development of a diagnostic device because the final signal change can be directly related to the target concentration even if the illumination (in this case the bioluminescence generated by the bacteria)

varies from test to test.

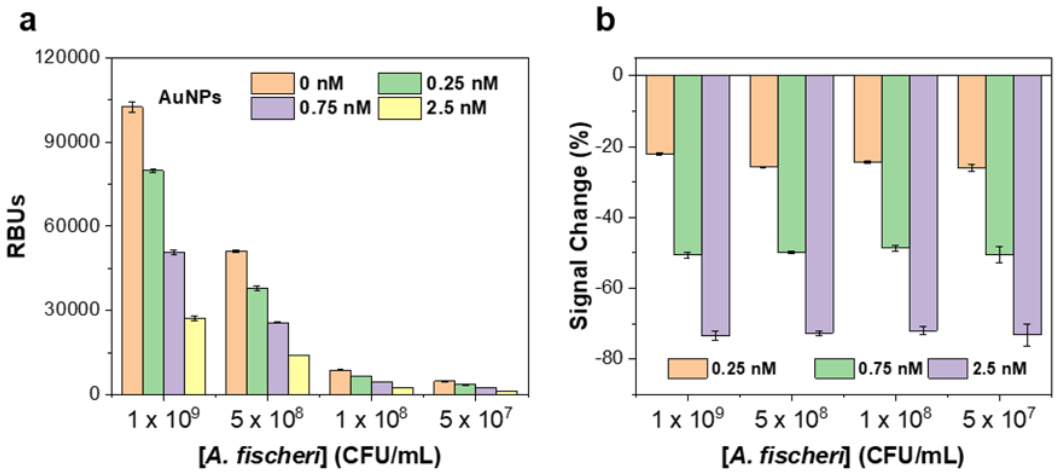

Figure 5.5. (a) Raw bioluminescence signals were collected from different solutions of *A. fischeri* (5 x 10^7, 1 x 10^8, 5 x 10^8 and 1 x 10^9 CFU/mL) in the absence and presence of 20 nm AuNPs (0.25, 0.75 and 2.5 nM). (b) The raw bioluminescence signals were then converted to signal change (%) (see Materials and Methods) for the different solutions of *A. fischeri* in the absence and presence of 20 nm AuNPs.

5.3.2. BBLISA based on AuNPs

BBLISA can detect the presence of the selected target in its clinically relevant range. After demonstrating the IFE between AuNPs and *A. fischeri* in solution, I decided to use it for the development of the BBLISA platform. Firstly, I synthesized AuNPs using the Turkevich method[38] and I characterized them using TEM images[41,58] (Figure 5.6a). As expected, the AuNPs exhibited a spherical morphology, homogenous size, an overall average diameter corresponding to 19.6 ± 0.9 nm, and a monodisperse size distribution (Figure 5.6a and b, Table 5.1). I then functionalized them with a primary antibody (i.e., anti-human IgG antibody) capable of detecting human immunoglobulin antibody (IgG), a common serologic biomarker associated with infection and inflammation[59]. I used DLS and Z-potential to confirm that the AuNPs were functionalized and fully covered with the anti-HIgG after the conjugation process (Figure 5.6c). Next, I characterized the analytical performance of the BBLISA (Figure 5.9) by collecting the bioluminescent signal from each well in the presence of increasing concentrations of the target (Figure 5.9a, orange curve; and Figure 5.7a). As expected, the presence of IgG induces the formation of the immune-sandwich complex which suppresses the bioluminescent signal (up to -23.2 ± 0.3 %). Fitting the

data with a four-parameter logistic equation I estimated an inflection point (IC_{50}) of 320 ± 40 ng/mL, a dynamic range of 25 ng/mL to 2500 ng/mL (i.e., the concentration range that induces a signal change of 10% to 90%[42]), and a limit of detection (LOD) of 2.0 ± 0.4 ng/mL (Figure 5.9a, Figure 5.7a and Table 5.2). These analytical parameters fall within the broad clinically relevant IgG range (from 7.0 mg/mL to 16.0 mg/mL)[60].

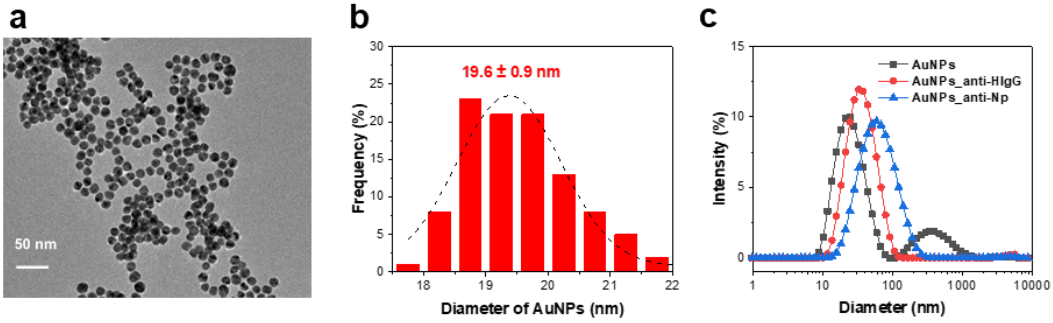

Figure 5.6. Characterization of AuNPs. (a) TEM image showing 20 nm AuNPs with spherical morphology and a homogeneous size and shape distribution. (b) Histogram graph of AuNPs with a size of 19.6 ± 0.9 nm (measured using ImageJ software on 100 particles from the TEM image). The black dashed line represents the Gaussian fitting used to present the size distribution. (c) DLS (Dynamic Light Scattering) analysis of AuNPs before and after conjugation with antibodies.

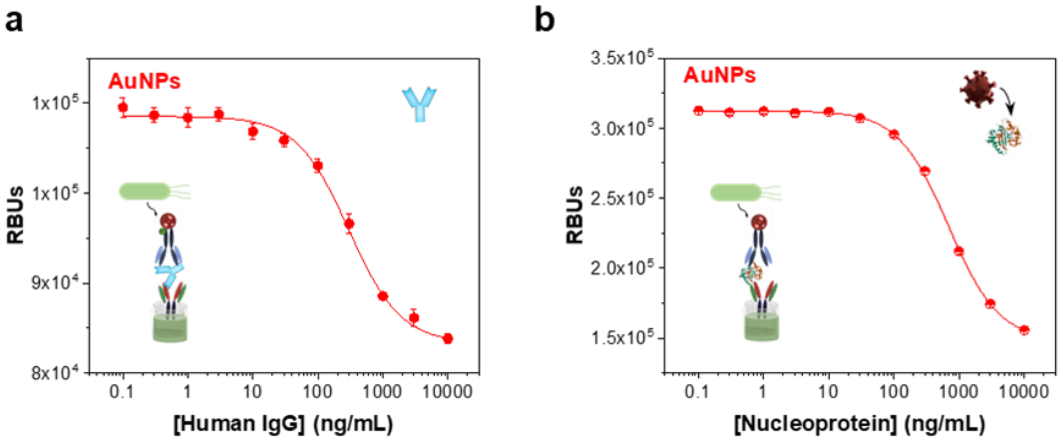

Figure 5.7. (a) Calibration curve for detection of human IgG based on BBLISA_AuNPs platform. (b) Calibration curve for detection of SARS-CoV-2 nucleoprotein based on BBLISA_AuNPs platform. Error bars reported reflect standard deviations derived from three independent wells.

Table 5.1. Z-Average, PDI (polydispersity index) and zeta potential of AuNPs and Au-IrO_2 NFs before and after conjugation with anti-HIgG and anti-Np antibodies.

	Z-Ave (nm)	PDI	Zeta Potential (mV)
AuNPs	27.0 ± 0.5	0.351 ± 0.012	− 41.9 ± 0.3
AuNPs_anti-HIgG	31.6 ± 0.7	0.210 ± 0.007	− 35.4 ± 0.4
AuNPs_anti-Np	50.2 ± 0.6	0.267 ± 0.004	− 34.5 ± 0.5
Au-IrO_2 NFs	120.7 ± 1.6	0.122 ± 0.004	− 33.9 ± 0.3
Au-IrO_2 NFs_anti-HIgG	171.2 ± 2.7	0.159 ± 0.005	− 38.2 ± 0.3
Au-IrO_2 NFs_anti-Np	168.9 ± 5.7	0.163 ± 0.011	− 38.2 ± 0.6

Table 5.2. Analytical performance of ELISA, BBLISA_AuNPs and BBLISA_Au-IrO_2 NFs for detection of human IgG and nucleoprotein in human serum.

Analyte	Parameters	ELISA (ng/mL)	BBLISA_AuNPs (ng/mL)	BBLISA_Au-IrO_2 NFs (ng/mL)
Human IgG	LOD	0.6 ± 0.1	2.0 ± 0.4	0.4 ± 0.1
	LOQ	1.3 ± 0.1	32 ± 5	1.7 ± 0.2
	IC_{50}	33 ± 4	320 ± 40	24 ± 5
	Linear range	8.0 - 100	25 - 2500	2 - 250
Nucleo-protein	LOD	0.6 ± 0.1	25 ± 6	0.6 ± 0.2
	LOQ	1.4 ± 0.1	66 ± 6	0.8 ± 0.1
	IC_{50}	37 ± 1	690 ± 20	28 ± 2
	Linear range	6 - 190	100 - 3700	3 - 255

BBLISA demonstrates clinically relevant accuracy when challenged with a real biological fluid. To evaluate the accuracy of the method in a clinical scenario, I used serum samples spiked with known concentrations of IgG target. Specifically, I spiked seven different concentrations of human IgG into HIgG-depleted human serum (i.e., a human serum that has been treated to remove naturally occurring IgG antibodies). Using the previously obtained calibration curve, I precisely calculated the concentration of spiked human IgG with a relevant error of ± 20% from 30 to 3000

ng/mL (Figure 5.9b and Table 5.3). Indeed, seven of spiked concentrations are perfectly positioned on the diagonal line of the graph indicating an excellent correlation between spiked and estimated concentrations. These data are further supported by the spiked recoveries ([estimated analyte] / [spiked analyte] * 100%), which values are between 80% and 120% (Table 5.3).

Table 5.3. The recoveries of human IgG and nucleoprotein based on BBLISA_AuNPs and BBLISA_Au-IrO_2 NFs.

Assays	Concentration of analyte (ng/mL)	Human IgG recovery (%)	Nucleoprotein recovery (%)
BBLISA_AuNPs	50	85.8 ± 10.7	N
	100	112.8 ± 5.5	104.1 ± 6.8
	200	85.8 ± 10.7	102.7 ± 6.8
	300	92.9 ± 7.2	100.7 ± 5.8
	600	N	103.9 ± 0.3
BBLISA_Au-IrO_2NFs	6	112.3 ± 9.7	94.1 ± 2.9
	20	113.3 ± 8.1	N
	30	N	82.3 ± 6.9
	60	110.3 ± 5.2	83.3 ± 1.0
	200	115.3 ± 2.0	81.0 ± 3.9
	300	N	96.1 ± 6.0

To better characterize the analytical performance of the BBLISA, I compared it with a classical colorimetric ELISA that relies on the enzyme horse-radish peroxidase to generate the optical signal. To obtain a direct comparison between the two assays, I used the same bioreceptors (i.e., immune-sandwich), reagents, and incubation times involved in the various steps of functionalization of the 96-well plates (e.g., coating, target incubation, washing; Figure 5.1c). I found that the ELISA has a higher sensitivity than the BBLISA (Figure 5.9a, green curve). For example, the IC_{50} is one order of magnitude lower (33 ± 4 ng/mL) and the LOD is 0.6 ± 0.1 ng/mL (Figure 5.8a and Table 5.2). I believe that the observed lower analytical performance of the

BBLISA is due to the reduced ability of the IFE to generate a change in the optical signal with respect to enzymatic amplification. However, the enzymatic amplification requires longer incubation times, more steps, and the use of toxic reagents.

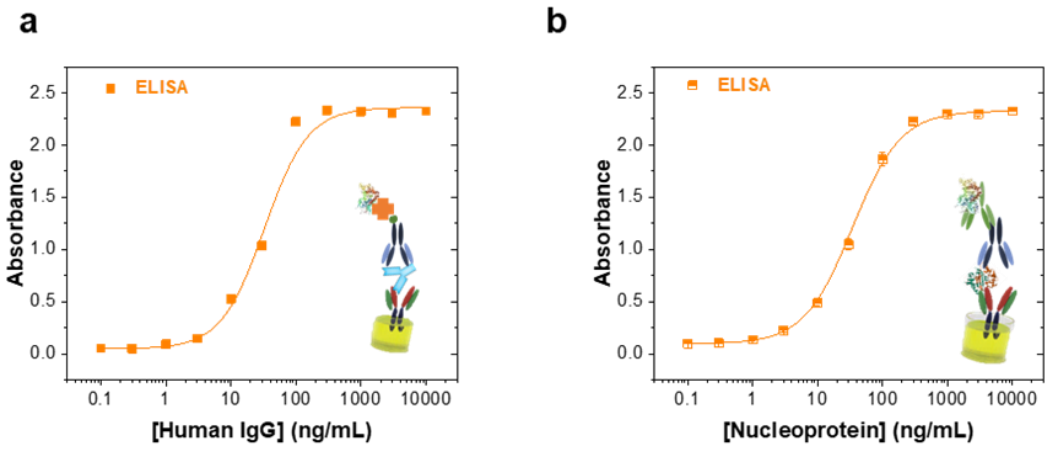

Figure 5.8. (a) Calibration curves for detection of human IgG based on classic ELISA platform. (b) Calibration curves for detection of nucleoprotein based on classic ELISA platform. Error bars reported reflect standard deviations derived from three independent wells.

To demonstrate the generalizability of our bioluminescent platform, I used BBLISA to detect a second different clinical target: the nucleoprotein of SARS-CoV-2[61] . I selected a new pair of antibodies that I have recently characterized that are able to specifically recognize the target by forming an immune-sandwich complex[41]. The BBLISA can efficiently detect the nucleoprotein with a higher signal change (up to -50.20 ± 0.05 %), and I estimated an IC_{50} and LOD of 690 ± 20 ng/mL and 25 ± 6 ng/mL, respectively (Figure 5.9c, orange curve; Figure 5.7b and Table 5.2). Our assay can precisely estimate nucleoprotein concentrations with good precision and accuracy (±20%) in its clinical range[61]. To demonstrate this, I challenged BBLISA with serum samples spiked with four different concentrations of nucleoprotein (Figure 5.9d and Table 5.3). Finally, I compared the analytical performance of the BBLISA with the ELISA (Figure 5.9c, green curve). As observed for IgG, the ELISA displays higher sensitivity, and I estimated an IC_{50} and LOD of 37 ± 1 ng/mL and 0.6 ± 0.1 ng/mL, respectively (Figure 5.8b and Table 5.2).

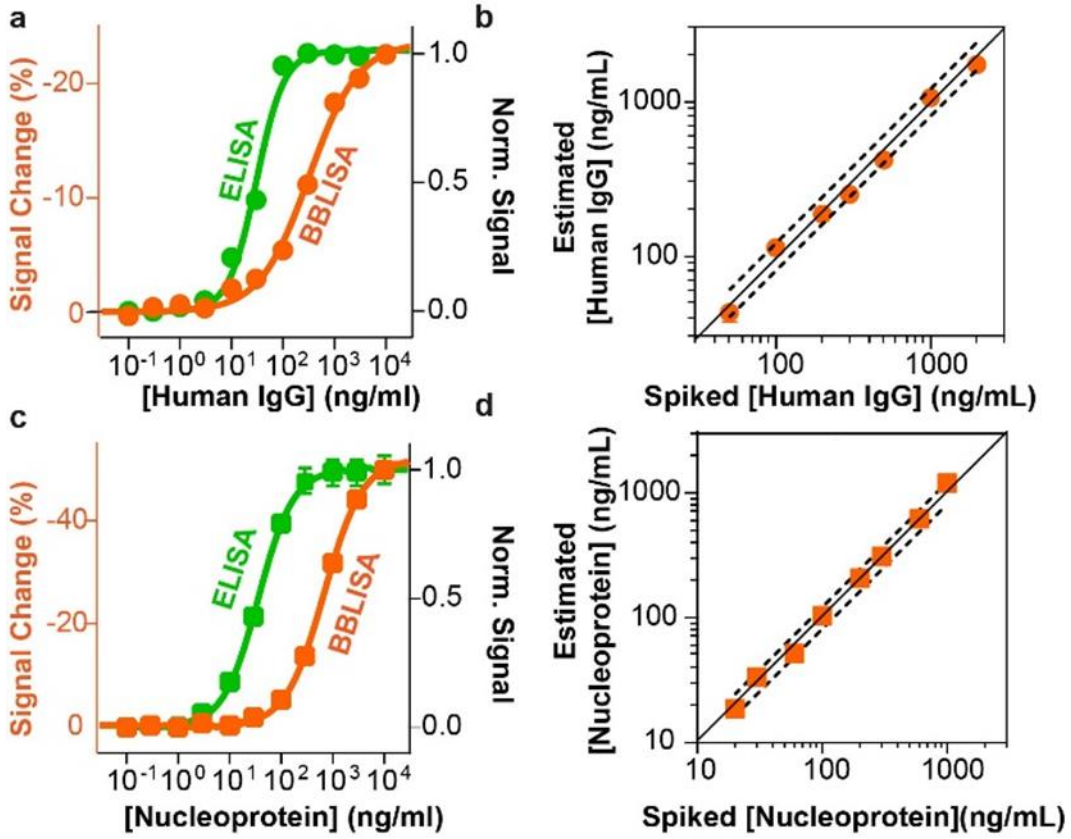

Figure 5.9. Detection of human IgG and nucleoprotein of SARS-CoV-2 in human serum based on ELISA and BBLISA_AuNPs. (a) Calibration curves for the detection of human IgG (from 0.1 to 3000 ng/mL) based on BBLISA_AuNPs (orange curve) and ELISA (green curve). (b) Accuracy of BBLISA_AuNPs for detection of human IgG from serum samples. (c) Calibration curves for the detection of SARS-CoV-2 nucleoprotein (from 0.1 to 3000 ng/mL) based on BBLISA_AuNPs (orange curve) and ELISA (green curve). (d) Accuracy of BBLISA_AuNPs for the detection of SARS-CoV-2 nucleoprotein from serum samples. Error bars reported for BBLISA and ELISA measurements reflect standard deviations derived from three independent wells.

5.3.3. BBLISA based on Au-IrO_2 NFs

To demonstrate the versatility of BBLISA and to improve its analytical performance, I have investigated new molecular absorbers with superior optical properties and an absorption spectrum that better overlaps the bioluminescence spectra of the *A. fischeri*. The goal is to improve the absorption of the light emitted by the bacteria to generate a stronger IFE effect and thus increase the sensitivity of the BBLISA. For this purpose, I decided to use gold-iridium oxide nanoflowers (Au-IrO_2 NFs), since they have a higher extinction coefficient and surface area than those of AuNPs[22] (Figure 5.10a), and I have recently optimized their synthesis to adapt them to a

colorimetric lateral flow assay (LFA)[22]. Following the same characterization protocol adopted for AuNPs, I demonstrate the ability of Au-IrO_2 NFs to be easily functionalized with bioreceptors[22], to support target biorecognition, and to be stable over time. First, I synthesized Au-IrO_2 NFs and I characterized them using TEM images (Figure 5.10b). The nanoflowers exhibit a spherical morphology with a highly tortuous branched structure (Figure 5.10b) and an overall average diameter of 62.3 ± 5.3 nm resulting in a monodisperse size distribution (Figure 5.11a). Next, I demonstrate their superior optical properties by comparing the absorbance spectrum of Au-IrO_2 NFs and AuNPs performed with the same nanoparticle concentrations (Figure 5.10a). As reported in previous studies[22], nanoflowers display approximately 25 times higher of molar extinction coefficient than 20 nm of AuNPs due to their surface flower-like branching morphology and the hybrid composition of gold and iridium[62], and their spectrum fully overlap with the emission spectra of bacteria ensuring higher absorption of bioluminescence (Figure 5.10c).

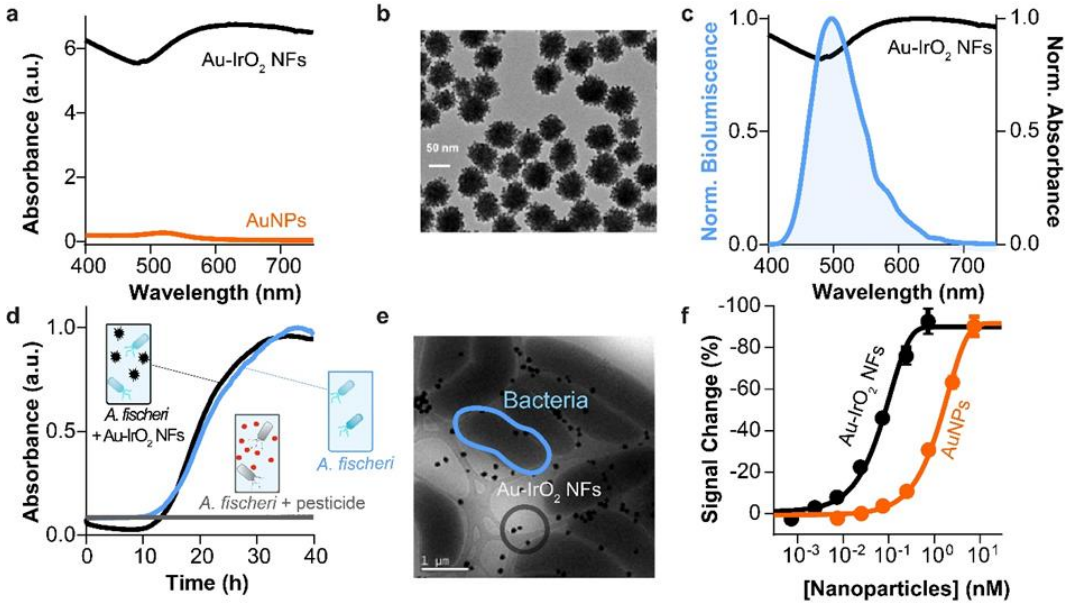

Figure 5.10. Optical characterization of inner filter effect between *A. fischeri* and Au-IrO_2 NFs. (a) Absorbance spectrum of AuNPs (orange) and Au-IrO_2 NFs (black) performed at same concentration (1.25 nM, 10 times concentrated). (b) TEM of Au-IrO_2 NFs displaying overall spherical morphology and a surface presenting highly tortuous branched structure. (c) Normalized bioluminescence emission spectrum of *A. fischeri* (10^9 CFU/mL, blue line) and absorbance spectrum of Au-IrO_2 NFs (black line). (d) Normalized turbidity signal (absorbance at 600 nm) of *A. fischeri* in the presence and absence of Au-IrO_2 NFs (0.24 nM, black and blue curves) or pesticide tributyltin (100 ng/mL, grey curve) from 0 h to 40 (e) Cryo TEM image of

A. fischeri with Au-IrO2 NFs. (f) Bioluminescence signal change of *A. fischeri* ($1 \cdot 10^9$ CFU/mL) as function of different concentrations of nanoparticles (i.e. AuNPs in orange, Au-IrO_2 NFs in black). All values reported are the average of three measurements and error bars reflect standard deviations.

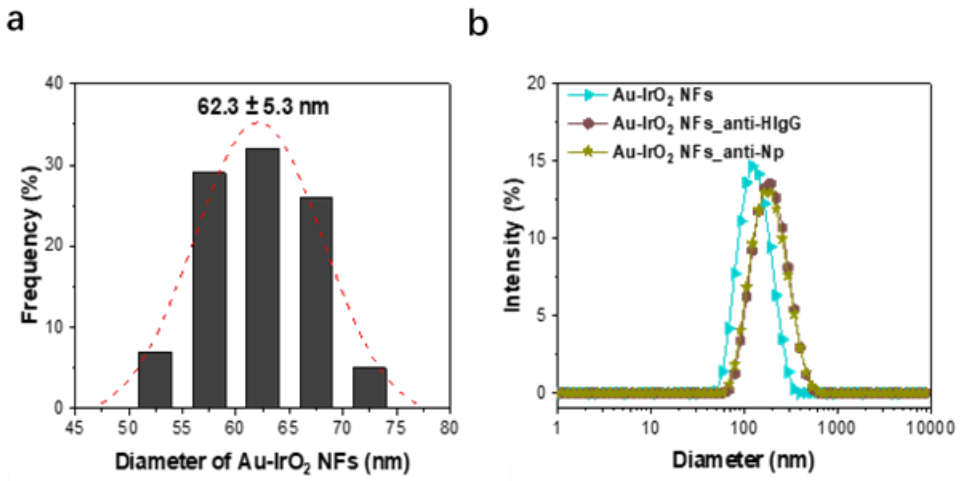

Figure 5.11. Characterization of Au-IrO_2 NFs. (a) Histogram graph of Au-IrO_2 NFs with a size of 62.3 ± 5.3 nm (measured using ImageJ software on 100 particles from the TEM image). The red dashed line represents the Gaussian fitting used to present the size distribution. (b) DLS (Dynamic Light Scattering) analysis of Au-IrO2 NFs before and after conjugation with antibodies.

Au-IrO_2 NFs have no toxic effect on bacteria and may even increase the IFE. I used turbidity measurements to investigate the toxicity of these nanoparticles by monitoring the growth of *A. fischeri* in the presence and in the absence of Au-IrO_2 NFs. Similar to what was observed for AuNPs (Figure 5.2c), the bimetallic nanoparticles exhibit the same behavior, affecting only the bioluminescent signal (Figure 5.10d and Figure 5.12). Cryo-TEM images of *A. fischeri* in the presence of Au-IrO_2 NFs clearly showed that the nanoparticles are distributed around the bacteria or in the culture medium, and are not absorbed into the bacterial cells (Figure 5.10e). This observation further supports our proposed mechanism, which is based on the inner filter effect and is not dependent on the distance between the light source and the filter particles[32]. Finally, I characterized the IFE by measuring the bioluminescent signal produced by the bacteria ($1 \cdot 10^9$ CFU/mL of *A. fischeri*) in the presence of increasing concentrations of Au-IrO_2 NFs (Figure 5.10f, black curve). The optical data demonstrate that NFs can suppress the bioluminescence signal more efficiently, requiring lower concentrations compared to AuNPs. For example, a six-fold

concentration of initially synthesized Au-IrO_2 NFs (0.73 nM) induces a signal change of -92.7% which would require a concentration of AuNPs at least ten times higher to obtain. Similar to the previous system, the signal change results reproducible and is not affected by the relative concentration of *A. fischeri* (Figure 5.13).

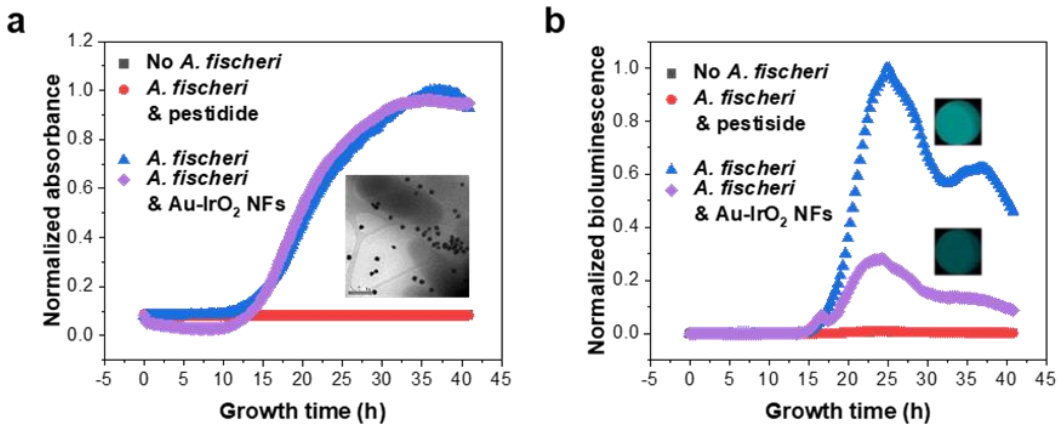

Figure 5.12. (a) The normalized absorbance at 600 nm of *A. fischeri* in the presence and absence of Au-IrO_2 NFs (2.5 nM, blue and purple curves) or the pesticide tributyltin (100 ng/mL, red curve) was measured 0 h to 40 h. Of note, the curves of No *A. fischeri* (black rectangle) is hidden by *A. fischeri* & pestiside (red circle) because they are completely overlapped and consistent with baseline. The inset shows a cryo-TEM image, indicating that Au-IrO_2 NFs are evenly distributed in the culture medium and some even adhere to the wall of *A. fischeri* without affecting their growth. (b) Normalized bioluminescence signal of *A. fischeri* in the presence and absence of Au-IrO_2 NFs was collected from 0 h to 42 h. Of note, the curves of No *A. fischeri* (black rectangle) is hidden by *A. fischeri* & pestiside (red circle) because they are completely overlapped and consistent with baseline. The embedded images were captured by a smartphone in a dark environment and represent the bioluminescence capability of *A. fischeri* in the presence (image above, weak BL intensity) and absence (image below, strong BL intensity) of Au-IrO_2 NFs. The normalized bioluminescence values are estimated as the ratio B/B_{max}, where B_{max} represents the maximum bioluminescence signal during the growth period (0-40h), and B is the bioluminescence signal at each detection time (growth time).

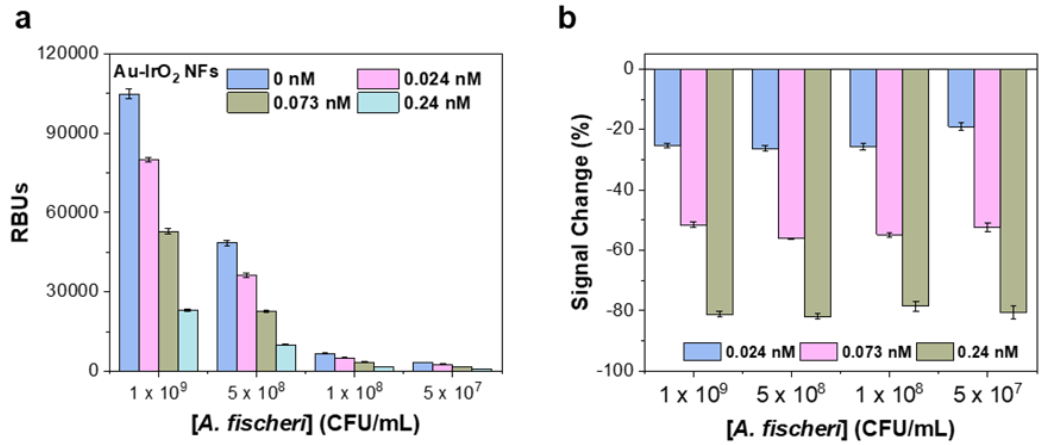

Figure 5.13. (a) Raw bioluminescence signals were collected from different solutions of *A. fischeri* (5 x 10^7, 1 x 10^8, 5 x 10^8 and 1 x 10^9 CFU/mL) in the absence and presence of Au-IrO_2 NFs (0.024, 0.073 and 0.24 nM). (b) The raw bioluminescence signals were then converted to signal change (%) (see Materials and methods) for the different solutions of *A. fischeri* in the absence and presence of of Au-IrO_2 NFs.

The high light absorption capacity of Au-IrO_2 NFs and their ability to induce a stronger IFE can be utilized to improve the BBLISA platform. I performed BBLISA experiments for the detection of human IgG and SARS-CoV-2 nucleoprotein (Figure 5.14). First, I used DLS and Z-potential to demonstrate that the Au-IrO_2 NFs are functionalized and coated with the corresponding primary antibody after the conjugation process (Figure 5.11b and Table 5.1). I then evaluated the analytical performance of the Au-IrO_2 NFs-based BBLISA against increasing concentration of IgG (Figure 5.14a and Figure 5.15a). By fitting the curve of signal change versus IgG concentration, I estimated IC_{50} and LOD values of 24 ± 5 ng/mL and 0.4 ± 0.1 ng/mL, respectively, which are lower than those obtained with the AuNPs- based BBLISA (LOD=2.0 ± 0.4 ng/mL). This indicates that I have significantly improved the sensitivity of our platform by achieving a five-fold lower detection limit. In addition, I used BBLISA to accurately estimate spiked HIgG concentrations in HIgG-depleted human serum (Figure 5.14b and Table 5.3). The recoveries of different spiked concentrations are between 80% and 120%, and the relative standard deviations are always less than 20% (Table 5.3). The improvement of the analytical performance can be further demonstrated by comparing the Au-IrO_2 NFs-based BBLISA with the classical ELISA (Figure 5.14a, green curve), where they show the higher IC_{50} and LOD values (Figure 5.14a, and Table 5.2). Finally, I performed a BBLISA to detect the nucleoprotein of SARS-CoV-2. As observed for the previous target, the Au-IrO_2 NFs-based BBLISA could detect SARS-CoV-2 nucleoprotein with

a lower LOD (0.6 ± 0.2 ng/mL) and IC_{50} (28 ± 2 ng/mL) (Figure 5.14c and Figure 5.15b) with respect to the AuNPs-based BBLISA. The recoveries of five different spiked concentrations are between 80% and 120% and the relative standard deviations are always below 10% (Figure 5.14d and Table 5.3). The overall analytical performance results are again comparable even better than those obtained with the standard ELISA (EC_{50}=37 ± 1 ng/mL, LOD=0.6 ± 0.1 ng/mL and dynamic range from 6 ng/mL to 190 ng/mL, ~ 32-fold), and also show a wider dynamic range (from 3 ng/mL to 255 ng/mL, ~ 85-fold) (Table 5.2).

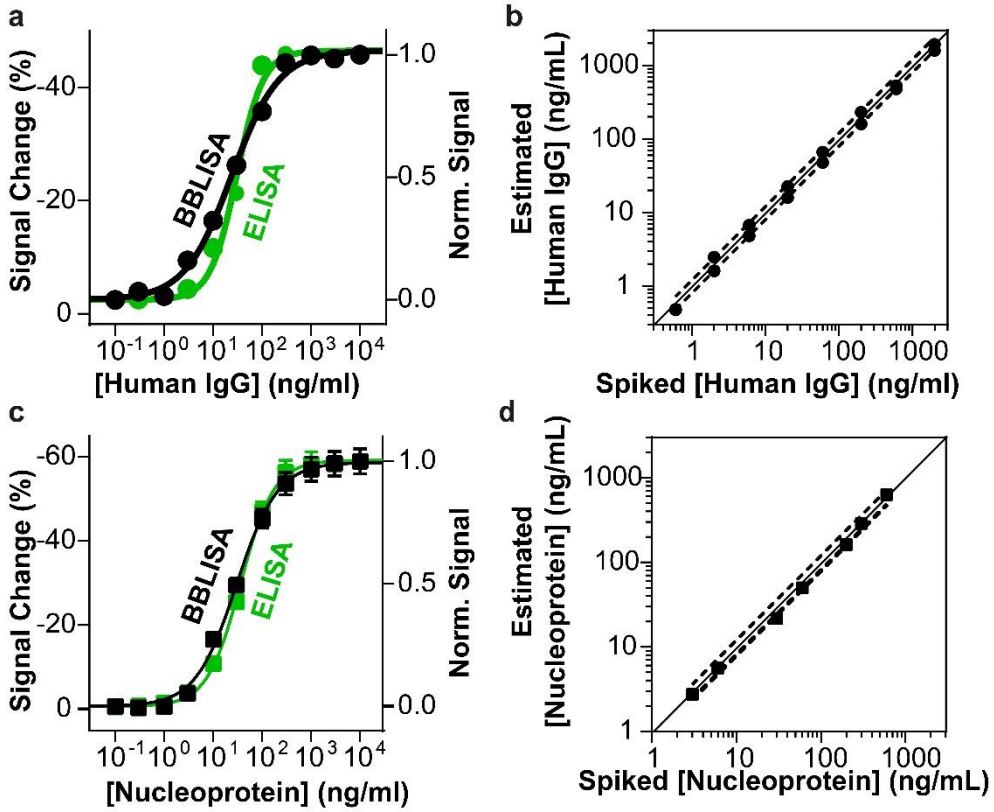

Figure 5.14. Detection of human IgG and nucleoprotein of SARS-CoV-2 in human serum based on ELISA and BBLISA_Au-IrO_2 NFs platform. (a) Calibration curves for the detection of human IgG (from 0.1 to 3000 ng/mL) based on ELISA (green curve) and BBLISA_Au-IrO2 NFs (black curve). (b) Accuracy of BBLISA_Au-IrO2 NFs for detection of human IgG from serum samples. (c) Calibration curves for the detection of SARS-CoV-2 nucleoprotein (from 0.1 to 3000 ng/mL) based on ELISA (green curve) and BBLISA_AuNPs (black curve). (d) Accuracy of BBLISA_Au-IrO2 NFs for detection of SARS-CoV-2 nucleoprotein from serum samples. Error bars reported for BBLISA and ELISA measurements reflect standard deviations derived from three independent wells.

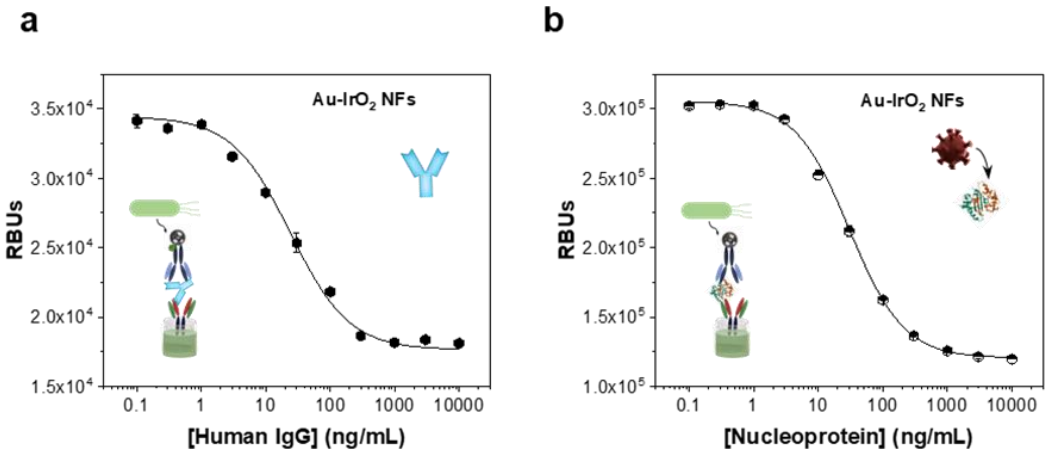

Figure 5.15. (a) Calibration curve for detection of human IgG based on BBLISA_ Au-IrO_2 NFs platform. (b) Calibration curve for detection of SARS-CoV-2 nucleoprotein based on BBLISA_ Au-IrO_2 NFs platform. Error bars reported reflect standard deviations derived from three independent wells.

5.4. Conclusions

In summary, I have developed a novel bioluminescence, enzyme-free, immunoassay based on the inner filter effect (IFE) between bioluminescent bacteria and metallic nanoparticles. I have named this newly developed assay BBLISA. By using AuNPs as molecular absorbers, I were able to demonstrate the sensing mechanism of BBLISA. Specifically, a set of AuNPs of different size were selected as test bed because their absorption spectra overlap with the emission spectra of the bioluminescent bacteria, they are non-toxic for the bacteria, they are stable, and easy to functionalize with bioreceptors. Our study showed that AuNPs can efficiently suppress the bioluminescence signal and I selected 20 nm AuNPs being able to generate the highest signal change. To demonstrate the clinical potential of this platform, I successfully applied BBLISA to detect human IgG and SARS-CoV-2 nucleoprotein in serum samples and I demonstrate the sensitive and selective detection of the selected clinically relevant biomarkers. I compared our platform against a classical colorimetric ELISA and I observed a lower sensitivity of the BBLISA. To improve the analytical performance, I exploited the inherent modularity and versatility of BBLISA which makes the platform readily adaptable for the use of new molecular absorbers with superior optical properties. I used bimetallic nanoparticles Au-IrO_2 NFs as new molecular absorbers to enhance the sensitivity of BBLISA. As AuNPs they are non-toxic for the bacteria, they are stable, and easy to functionalize with bioreceptors but unlike from them Au-IrO_2 NFs

showed higher absorption properties. Using these nanoparticles, I achieved higher sensitivity for the detection of the selected biomarkers, demonstrating the clinical potential of BBLISA as an alternative to the current ELISA.

The reported data demonstrate the ability of our proposed platform to detect clinically relevant biomarkers providing the same or even better sensitivity than conventional ELISA. BBLISA does not only display high analytical performance, but its versatility and modularity offer more advantages. For example, it is less expensive because it does not require enzyme-labelled antibody/streptavidin and/or chromogenic substrates for the generation of the signal. The use of bioluminescent signal eliminates the need for expensive microplate readers with sophisticated light sources to generate and collect a high optical signal. Because the bacteria can emit light with high yields, the bioluminescence signal can be easily collected by a commercial smartphone making the device able to support low-cost, optical devices[63]. In addition, the BBLISA platform is also faster because it requires fewer steps, for example, because the generation of the signal is not based on an enzymatic reaction, I do not need to stop the reaction at a specific time. Finally, the platform is more environmentally friendly because it does not require toxic reagents (such as the sulfuric acid that is commonly used as a stop solution for enzymatic reactions), and the growth of the bacteria in microbiological culture media allows for a continuous in-house regeneration of the "optical substrate" without the need of expensive equipment. Beside these advantages, a possible limitation of BBLISA is the nature of generation of the signal which is signal-off[64,65]. This could be compensated using new nanomaterials and bacteria with higher absorbance and bioluminescence properties, which could increase the magnitude of the IFE and the relative signal change. If achieved, this could lead to a synergistic integration of nanomaterials with living organisms improving our understanding of their biological properties to develop enhanced bioanalytical platforms.

5.5. References

1. Lequin, R. M. Enzyme immunoassay (EIA)/enzyme-linked immunosorbent assay (ELISA). *Clin. Chem.* **51**, 2415–2418 (2005).

2. Aydin, S. A short history, principles, and types of ELISA, and our laboratory experience

with peptide/protein analyses using ELISA. *Peptides* **72**, 4–15 (2015).

3. Lee, K. H. & Zeng, H. Aptamer-Based ELISA Assay for Highly Specific and Sensitive Detection of Zika NS1 Protein. *Anal. Chem.* **89**, 12743–12748 (2017).

4. Nithichanon, A. *et al.* Diagnosis of NTM active infection in lymphadenopathy patients with anti-interferon-gamma auto-antibody using inhibitory ELISA vs. indirect ELISA. *Sci. Rep.* **10**, 8968 (2020).

5. Tarasov, A. *et al.* A potentiometric biosensor for rapid on-site disease diagnostics. *Biosens. Bioelectron.* **79**, 669–678 (2016).

6. Zhdanov, A., Keefe, J., Franco-Waite, L., Konnaiyan, K. R. & Pyayt, A. Mobile phone based ELISA (MELISA). *Biosens. Bioelectron.* **103**, 138–142 (2018).

7. Bouillon, R. Free or Total 25OHD as Marker for Vitamin D Status? *J. Bone Miner. Res.* **31**, 1124–1127 (2016).

8. Xiao, X., Hu, S., Lai, X., Peng, J. & Lai, W. Developmental trend of immunoassays for monitoring hazards in food samples: A review. *Trends Food Sci. Technol.* **111**, 68–88 (2021).

9. Klumpp-Thomas, C. *et al.* Standardization of ELISA protocols for serosurveys of the SARS-CoV-2 pandemic using clinical and at-home blood sampling. *Nat. Commun.* **12**, 113 (2021).

10. Alhajj, M. & Farhana, A. Enzyme Linked Immunosorbent Assay. in (2023).

11. Tian, M. *et al.* Transpathology : molecular imaging-based pathology. 2338–2350 (2021).

12. Vargas, A. J. & Harris, C. C. Biomarker development in the precision medicine era: Lung cancer as a case study. *Nat. Rev. Cancer* **16**, 525–537 (2016).

13. Peng, P. *et al.* Emerging ELISA derived technologies for in vitro diagnostics. *TrAC - Trends Anal. Chem.* **152**, 116605 (2022).

14. Li, N. *et al.* Recent advances in sample preparation techniques for quantitative detection

of pharmaceuticals in biological samples. *TrAC - Trends Anal. Chem.* **142**, 116318 (2021).

15. Liu, B., Zhuang, J. & Wei, G. Recent advances in the design of colorimetric sensors for environmental monitoring. *Environ. Sci. Nano* **7**, 2195–2213 (2020).

16. Shafiee, H. *et al.* Emerging Technologies for Point-of-Care Management of HIV Infection. *Annu. Rev. Med.* **66**, 387–405 (2015).

17. Kai, J. *et al.* A novel microfluidic microplate as the next generation assay platform for enzyme linked immunoassays (ELISA). *Lab Chip* **12**, 4257–4262 (2012).

18. Shen, J. *et al.* Sensitive detection of a bacterial pathogen using allosteric probe-initiated catalysis and CRISPR-Cas13a amplification reaction. *Nat. Commun.* **11**, 267 (2020).

19. Eftekhari, A. *et al.* Bioassay of saliva proteins: The best alternative for conventional methods in non-invasive diagnosis of cancer. *Int. J. Biol. Macromol.* **124**, 1246–1255 (2019).

20. Hernández-Neuta, I. *et al.* Smartphone-based clinical diagnostics: towards democratization of evidence-based health care. *J. Intern. Med.* **285**, 19–39 (2019).

21. De La Rica, R. & Stevens, M. M. Plasmonic ELISA for the ultrasensitive detection of disease biomarkers with the naked eye. *Nat. Nanotechnol. 2012 712* **7**, 821–824 (2012).

22. Rivas, L., Hu, L., Parolo, C., Idili, A. & Merkoçi, A. Rational Approach to Tailor Au–IrO2 Nanoflowers as Colorimetric Labels for Lateral Flow Assays. *ACS Appl. Nano Mater.* **6**, 4151–4161 (2023).

23. Liu, Y. *et al.* Plasmonic and Photothermal Immunoassay via Enzyme-Triggered Crystal Growth on Gold Nanostars. *Anal. Chem.* **91**, 2086–2092 (2019).

24. Keene, C. D. *et al.* Luminex-based quantification of Alzheimer's disease neuropathologic change in formalin-fixed post-mortem human brain tissue. *Lab. Investig.* **99**, 1056–1067 (2019).

25. Janetzki, S. *et al.* Guidelines for the automated evaluation of Elispot assays. *Nat. Protoc.* **10**, 1098–1115 (2015).

26. Cheng, C. M. *et al.* Paper-based elisa. *Angew. Chemie - Int. Ed.* **49**, 4771–4774 (2010).

27. Verma, M. S. *et al.* Sliding-strip microfluidic device enables ELISA on paper. *Biosens. Bioelectron.* **99**, 77–84 (2018).

28. Zhang, P., He, M. & Zeng, Y. Ultrasensitive microfluidic analysis of circulating exosomes using a nanostructured graphene oxide/polydopamine coating. *Lab Chip* **16**, 3033–3042 (2016).

29. Sakamoto, S. *et al.* Enzyme-linked immunosorbent assay for the quantitative/qualitative analysis of plant secondary metabolites. *J. Nat. Med.* **72**, 32–42 (2018).

30. Yu, R.-J. *et al.* Metal-linked Immunosorbent Assay (MeLISA): the Enzyme-Free Alternative to ELISA for Biomarker Detection in Serum. *Theranostics* **6**, 1732–1739 (2016).

31. Hu, R. *et al.* DLISA: A DNAzyme-Based ELISA for Protein Enzyme-Free Immunoassay of Multiple Analytes. *Anal. Chem.* **87**, 7746–7753 (2015).

32. Zu, F. *et al.* The quenching of the fluorescence of carbon dots: A review on mechanisms and applications. *Microchimica Acta* vol. 184 1899–1914 (2017).

33. Chen, S., Yu, Y. L. & Wang, J. H. Inner filter effect-based fluorescent sensing systems: A review. *Analytica Chimica Acta* vol. 999 13–26 (2018).

34. Kumar Panigrahi, S. & Kumar Mishra, A. Inner filter effect in fluorescence spectroscopy: As a problem and as a solution. *J. Photochem. Photobiol. C Photochem. Rev.* **41**, 100318 (2019).

35. Zhang, J., Zhou, R., Tang, D., Hou, X. & Wu, P. Optically-active nanocrystals for inner filter effect-based fluorescence sensing: Achieving better spectral overlap. *TrAC Trends Anal. Chem.* **110**, 183–190 (2019).

36. Bergua, J. F., Álvarez-Diduk, R., Hu, L., Hassan, A. H. A. & Merkoçi, A. Improved Aliivibrio fischeri based-toxicity assay: Graphene-oxide as a sensitivity booster with a mobile-phone application. *J. Hazard. Mater.* **406**, 124434 (2021).

37. Yuan, P. & Walt, D. R. Calculation for fluorescence modulation by absorbing species and

its application to measurements using optical fibers. *Anal. Chem.* **59**, 2391–2394 (1987).

38. Turkevich, J., Stevenson, P. C. & Hillier, J. A study of the nucleation and growth processes in the synthesis of colloidal gold. *Discussions of the Faraday Society* vol. 11 55–75 (1951).

39. Serna, N. *et al.* Developing Protein–Antitumoral Drug Nanoconjugates as Bifunctional Antimicrobial Agents. *ACS Appl. Mater. Interfaces* **12**, 57746–57756 (2020).

40. Thompson, R. F., Walker, M., Siebert, C. A., Muench, S. P. & Ranson, N. A. An introduction to sample preparation and imaging by cryo-electron microscopy for structural biology. *Methods* **100**, 3–15 (2016).

41. Hu, L. *et al.* Selection and characterisation of bioreceptors to develop nanoparticle-based lateral-flow immunoassays in the context of the SARS-CoV-2 outbreak. *Lab Chip* **22**, 2938–2943 (2022).

42. Parolo, C. *et al.* Tutorial: design and fabrication of nanoparticle-based lateral-flow immunoassays. *Nat. Protoc.* **15**, 3788–3816 (2020).

43. Jeong, H.-H., Choi, E., Ellis, E. & Lee, T.-C. Recent advances in gold nanoparticles for biomedical applications: from hybrid structures to multi-functionality. *J. Mater. Chem. B* **7**, 3480–3496 (2019).

44. De La Escosura-Muñiz, A., Parolo, C., Maran, F. & Mekoi, A. Size-dependent direct electrochemical detection of gold nanoparticles: Application in magnetoimmunoassays. *Nanoscale* **3**, 3350–3356 (2011).

45. FRENS, G. Controlled Nucleation for the Regulation of the Particle Size in Monodisperse Gold Suspensions. *Nat. Phys. Sci.* **241**, 20–22 (1973).

46. Brust, M., Walker, M., Bethell, D., Schiffrin, D. J. & Whyman, R. Synthesis of Thiol-derivatised Gold Nanoparticles in. 801–802 (2000).

47. Reetz, M. T. & Helbig, W. Met ^. 7401–7402 (1994).

48. Siti, R. M., Khairunisak, A. R., Abdul Aziz, A. & Noordin, R. Green synthesis of 10 nm gold nanoparticles via seeded-growth method and its conjugation properties on lateral flow

immunoassay. *Adv. Mater. Res.* **686**, 8–12 (2013).

49. Burygin, G. L. *et al.* On the Enhanced Antibacterial Activity of Antibiotics Mixed with Gold Nanoparticles. *Nanoscale Res. Lett.* **4**, 794 (2009).

50. Jakhmola, A., Hornsby, T., Rod, K. & Tavakkoli, J. A Novel Gold Nanoparticles Drug Delivery System: Design and Ex Vivo Tissue Testing. in *2020 IEEE International Ultrasonics Symposium (IUS)* 1–3 (2020). doi:10.1109/IUS46767.2020.9251430.

51. Parolo, C. *et al.* Design, preparation, and evaluation of a fixed-orientation antibody/gold-nanoparticle conjugate as an immunosensing label. *ACS Appl. Mater. Interfaces* **5**, 10753–9 (2013).

52. Zong, J., Cobb, S. L. & Cameron, N. R. Peptide-functionalized gold nanoparticles: versatile biomaterials for diagnostic and therapeutic applications. *Biomater. Sci.* **5**, 872–886 (2017).

53. Chen, H., Zhou, K. & Zhao, G. Gold nanoparticles: From synthesis, properties to their potential application as colorimetric sensors in food safety screening. *Trends Food Sci. Technol.* **78**, 83–94 (2018).

54. Haiss, W., Thanh, N. T. K., Aveyard, J. & Fernig, D. G. Determination of Size and Concentration of Gold Nanoparticles from UV−Vis Spectra. *Anal. Chem.* **79**, 4215–4221 (2007).

55. Liu, J. *et al.* Bioluminescent nanopaper for rapid screening of toxic substances. *Nano Res.* **11**, 114–125 (2018).

56. Buss da Silva, N., Mattar Carciofi, B. A., Ellouze, M. & Baranyi, J. Optimization of turbidity experiments to estimate the probability of growth for individual bacterial cells. *Food Microbiol.* **83**, 109–112 (2019).

57. Quenching of Fluorescence BT - Principles of Fluorescence Spectroscopy. in (ed. Lakowicz, J. R.) 277–330 (Springer US, 2006). doi:10.1007/978-0-387-46312-4_8.

58. Sena-Torralba, A. *et al.* Lateral flow assay modified with time-delay wax barriers as a sensitivity and signal enhancement strategy. *Biosens. Bioelectron.* **168**, 112559 (2020).

59. Guo, Z. *et al.* Hyperboloid-Drum Microdisk Laser Biosensors for Ultrasensitive Detection of Human IgG. *Small* **16**, 2000239 (2020).

60. Gonzalez-Quintela, A. *et al.* Serum levels of immunoglobulins (IgG, IgA, IgM) in a general adult population and their relationship with alcohol consumption, smoking and common metabolic abnormalities. *Clin. Exp. Immunol.* **151**, 42–50 (2008).

61. Zhang, Y. *et al.* Diagnostic Value of Nucleocapsid Protein in Blood for SARS-CoV-2 Infection. *Clin. Chem.* **68**, 240–248 (2022).

62. De Freitas, I. C. *et al.* Design-controlled synthesis of IrO2 sub-monolayers on Au nanoflowers: Marrying plasmonic and electrocatalytic properties. *Nanoscale* **12**, 12281–12291 (2020).

63. Bergua, J. F. *et al.* Low-Cost, User-Friendly, All-Integrated Smartphone-Based Microplate Reader for Optical-Based Biological and Chemical Analyses. *Anal. Chem.* **94**, 1271–1285 (2022).

64. E. Wang, R., Zhang, Y., Cai, J., Cai, W. & Gao, T. Aptamer-Based Fluorescent Biosensors. *Curr. Med. Chem.* **18**, 4175–4184 (2011).

65. Oh, S. W., Hwang, D. W. & Lee, D. S. In vivo monitoring of microRNA biogenesis using reporter gene imaging. *Theranostics* **3**, 1004–1011 (2013).

GENERAL CONCLUSIONS

Considering the exposed objectives in Chapter 2 and the specific conclusions give at the end of each chapter, the following conclusion remarks are given.

I have successfully developed a LFA using AuNPs as colorimetric labels for the sensitive detection of SARS-CoV-2 nucleoprotein. Key achievements include the successful implementation of a LFA that works in saliva samples, demonstrating its potential for rapid point-of-care diagnostics, and antibody screening, revealing the complexity of antibody selection and the need for a more efficient and cost-effective process.

- Only 3 antibody couples out of over 80 antibody pairs were screened by using ELISA and half-stick dot test, the best one with a LOD of 3.0 ± 1.2 ng/mL in artificial saliva, which is similar to the LOD reported in other point-of-care biosensors.
- Although a working lateral flow assay was developed, the antibody selection process required over 10 months and 24,422.6 €, not acceptable for COVID-19 pandemic. The bioreceptors (e.g., antibodies, aptamers) producers should provide a thorough characterization of the binding behavior before making them commercially available, e.g. antibodies with fast binding kinetics for a LFAs.

A second important project that built on my research was the development of LFAs using Au-IrO_2 nanoflowers for the detection of human IgG, which led to remarkable success. Indeed, Au-IrO_2 nanoflowers exhibit better light absorption and larger specific surface area compared to conventional AuNPs, resulting in a significantly lower limit of detection (LOD) for human IgG in serum samples compared to conventional AuNPs-based LFAs, indicating the development of next-generation optical LFAs.

- 53 nm of Au-IrO_2 NFs were synthesized in a 5-fold volume scale-up, showing stronger light absorption ability (with bigger extinction coefficient) and larger specific surface area (with branch-like surface) than 20 nm or 40 nm of AuNPs commonly used in LFAs.
- Au-IrO_2 NFs-based LFAs achieved an 8.5-fold lower LOD (down to 1.2 ng/mL) for human IgG detection than 40 nm of AuNPs-based LFAs (10.1 ng/mL) in human serum samples, showing potential for the next generation of optical LFAs.

- As future perspectives, I believe that due to the presence of IrO_2 on the nanoflowers, they could also act as dual optical/electrochemical labels in paper-based electrochemical systems, thanks to their plasmonic peak and electrocatalytic behavior.

To conclude, I have developed a breakthrough bioanalytical platform using AuNPs and Au-IrO_2 nanoflowers as absorbers in a Bioluminescent Bacteria-Linked Immunosorbent Assay (BBLISA), which is an example of innovation in bioanalytical platforms. The inner filter effect between bioluminescent bacteria and metallic nanoparticles was used to detect human IgG and SARS-CoV-2 nucleoprotein. The results show a sensitivity and precision comparable to or better than a conventional ELISA.

- The IFE between bioluminescent bacteria *Allivibrio fischeri* and metallic nanoparticles was first time exploited and confirmed by UV-vis and bioluminescence spectrum, Cyro TEM images, growth curves and bioluminescence curves of *Allivibrio fischeri*, and the reproducible signal suppress trends.

- Thanks to advantage of the modularity and versatility of the BBLISA, the BBLISA was applied to detect two clinically relevant biomarkers (human IgG and nucleoprotein of SARS-CoV-2) in serum with the same even better sensitivity and precision of the classic ELISA.

- The novel bioanalytical assay of BBLISA results faster, safer, cheaper, and more user-friendly respect to the current ELISA platform, demonstrating the clinical potential of BBLISA as an alternative to the current ELISA.

- As future work, it is worth the integration BBLISA with smartphone, and the exploration and application of new nanomaterials and bacteria with higher absorbance and bioluminescence properties.

All these projects and milestones represent significant progress in the field of optical biosensors for point-of-care diagnostics. The adaptability demonstrated in the use of gold nanomaterials opens up new avenues for exploration and refinement. The achievements reported here are a testament to the continuous progress in this field and the constant pursuit of knowledge and innovation in the development of biosensors.

ANNEXES

As annexes are attached the following published chapter and experimental works:

Hu, L., Idili, A., Parolo, C., Álvarez-Diduk, R., Calucho, E., & Merkoçi, A. (2022). Optical smartphone-based sensing: diagnostic of biomarkers. In *The Detection of Biomarkers* (pp. 277-302). Academic Press.

Hu, L., Calucho, E., Fuentes-Chust, C., Parolo, C., Idili, A., Álvarez-Diduk, R., Rivas, L. & Merkoçi, A. (2022). Selection and characterisation of bioreceptors to develop nanoparticle-based lateral-flow immunoassays in the context of the SARS-CoV-2 outbreak. *Lab on a Chip*, *22*(16), 2938-2943.

Rivas, L., **Hu, L.**, Parolo, C., Idili, A., & Merkoçi, A. (2023). Rational Approach to Tailor Au–IrO2 Nanoflowers as Colorimetric Labels for Lateral Flow Assays. *ACS Applied Nano Materials*, *6*(6), 4151-4161.

Also the following posters and abstracts for oral presentations at different conferences:

Bergua, J. F., **Hu, L.**, Fuentes-Chust, C., Álvarez-Diduk, R., Hassan, A. H., Parolo, C., & Merkoçi, A. Lateral flow biosensor for rapid detection of *Escherichia coli*. – Poster presented at: *XXIV Transfrontier Meeting on Sensors and Biosensors*, Perpignan (2019).

Hu, L., Calucho, E., Fuentes-Chust, C., Parolo, C., Idili, A., Álvarez-Diduk, R., & Merkoçi, A. AuNPs-based lateral flow assay for detection of SARS-CoV-2 nucleoprotein: implicit design challenges in a new pandemic. – Poster presented at: *Biosensors for Pandemics 2021*, 2nd edition of an Online conference (2021).

Hu, L., Bergua, J. F., Fuentes-Chust, C., Álvarez-Diduk, R., Hassan, A. H., Parolo, C., & Merkoçi, A. Monitoring generic *Escherichia coli* based on lateral flow biosensor for water fecal pollution assessment. – Oral presented at: *Environmental Monitoring and Remediation, First Severo Ochoa Workshop on Environment*, Barcelona (2021).

Hu, L., Calucho, E., Fuentes-Chust, C., Parolo, C., Idili, A., Álvarez-Diduk, R., Rivas, L. & Merkoçi, A. Selection and characterization of bioreceptors to develop nanoparticle-bsed lateral flow immunoassays under COVID-19 pandemic. – Poster presented at: *XXVI Transfrontier Meeting on Sensors and Biosensors*, Barcelona (2022).

Rivas, L., **Hu, L.**, Parolo, C., Idili, A., & Merkoçi, A. A rational approach to tailor Au–IrO_2 nanoflowers as colorimetric labels for lateral flow assays. – Oral presented at: *The 22nd edition of the Trends in Nanotechnology International Conference*, Albania (2022).

Hu, L., Rossetti, M., & Merkoçi, A. Gold nanoparticles-based optical biosensor for rapid and cost-efficient diagnosis. – Oral presented at: *XXVII Transfrontier Meeting on Sensors and Biosensors*, Banyuls-sur-Mer (2023).

Chapter 11

Optical smartphone-based sensing: diagnostic of biomarkers

Liming Hu[1], Andrea Idili[1,2], Claudio Parolo[1], Ruslán Álvarez-Diduk[1], Enric Calucho[1] and Arben Merkoçi[1,3]
[1]Catalan Institute of Nanoscience and Nanotechnology (ICN2), Barcelona, Spain, [2]CSIC and the Barcelona Institute of Science and Technology (BIST), Barcelona, Spain, [3]Catalan Institution for Research and Advanced Studies (ICREA), Barcelona, Spain

11.1 Introduction

Biomarkers are nucleic acids, peptides, proteins, lipids, metabolites, or other small molecules whose accurate identification and quantification can be associated with the presence of a disease and its status (Strimbu & Tavel, 2010). Having this in mind, over the last three decades, the goal to reach the sensitive and rapid detection of biomarkers has stimulated the scientific community to develop novel molecular diagnostic platforms that can be used by healthcare personnel to accurately diagnose medical conditions (Kelley et al., 2014). Despite the efforts, the majority of developed diagnostic methods rely on the use of fully automated laboratories and skilled personnel which have hampered their use in developing countries and low-resource scenarios (Katoba et al., 2019; Sharma et al., 2015). To overcome this, many diagnostic platforms have been reengineered and integrated into point-of-care (PoC) sensing platforms in order to move the field of diagnostics from the laboratory directly to the end-user (Heidt et al., 2020). The World Health Organization (WHO) introduced new guidelines to help the design of PoC devices which should comply with the REASSURED criteria (Land et al., 2019). This means that they should provide Real-time connectivity, Ease of specimen collection, Affordable prices, Sensitive and Specific analytical performance, User-friendliness, Rapid and they should support Robust responses, an Equipment-free and Deliverable platform.

A clever approach to design and develop diagnostic tests able to comply with the REASSURED criteria relies on the use of a smartphone as readout platform (Alawsi & Al-Bawi, 2019; Hernández-Neuta et al., 2019). Smartphones have already caused a dramatic impact on our social lives thanks to their advanced features and functionalities (Gowthami & Venkatakrishnakumar, 2016). Specifically, their software systems are low-cost and all the different sensors integrated in smartphones' hardware make them a portable lab with the processing power of a computer. Among their different components, we can find: a fully operating system, ability to support artificial intelligence, internal storage, high resolution camera, wireless transmission capabilities and motion sensors. Therefore, it is no surprise that a number of public and private research centers have started to work on harnessing the potential of smartphones for diagnostic applications (Alawsi & Al-Bawi, 2019; Hernández-Neuta et al., 2019). Among the different components, the smartphone camera is the most attractive due to its ever-growing performance (i.e., macro lens, high resolution, auto focus, manual mode, etc.) and simple use. Many optical-based diagnostic tests have been integrated and validated using smartphones as optical reader (McCracken & Yoon, 2016), and these include absorbance (Brangel et al., 2018; Miller et al., 2018), fluorescence (Álvarez-DIduk et al., 2017), microscopic bio-imaging (Koydemir et al., 2015; Zhu et al., 2013), surface plasmon resonance (SPR) (Dutta et al., 2016), chemiluminescence (CL) (Zangheri et al., 2015), bioluminescence (Calabretta et al., 2020), electrochemiluminescence (ECL) (Chen et al., 2016), and photoluminescence (Lian et al., 2017).

In this chapter, we describe how the most recent research (from 2015 to 2020) in smartphone-based biosensing platforms allow the specific and rapid detection of clinically relevant biomarkers. Specifically, we will explain the importance of biomarkers' discovery and their detection related to human diseases. Then, we will provide a brief description on how smartphone can be integrated into optical-based diagnostic tests to support PoC technologies.

The Detection of Biomarkers. DOI: https://doi.org/10.1016/B978-0-12-822859-3.00003-1

Finally, we will offer an overview of the smartphone-based PoC sensing devices demonstrating their potential and utility in diagnostic field.

11.1.1 Definition and clinical significance of biomarkers

"Biological marker" or "biomarker" is a specific sign that can be measured accurately and reproducibly, and indicates the presence of a medical condition (i.e., an objective indication of a physiological as well as a pathological process or pharmacological response) (Jain, 2010; Strimbu & Tavel, 2010). Due to the clinical impact of this concept and its multidisciplinary applications, literature presents more precise definitions which coincide with the previous one, and with those coined by official institutions. For example, the WHO defines a biomarker as "almost any measurement reflecting an interaction between a biological system and a potential hazard, which may be chemical, physical, or biological. The measured response may be functional and physiological, biochemical at the cellular level, or molecular interaction." (World Health Orgnization, 1993). The National Institutes of Health (NIH) came up with a broader definition of biomarker, which is "a defined characteristic that is measured as an indicator of normal biological processes, pathogenic processes or responses to an exposure or intervention." (Strimbu & Tavel, 2010). From these definitions, it is clear that this concept goes beyond the classical well-known clinical biomarkers (e.g., alterations in blood pressure, blood lactate levels following exercise, blood glucose in diabetes mellitus, antibodies levels) and it involves any other specific alteration at the molecular level, for example, of a tissue, a cell, genetic network, RNA expression, metabolite or protein level (Jain, 2010; Strimbu & Tavel, 2010).

Focusing more on the clinical practice, the study of biomarkers includes also the development of technologies and tools addressed to understand the diagnosis, cause, progression and regression of a disease and the relative prediction and outcome of treatment (Lippert & Goetze, 2010; Mamas et al., 2011; Schwarzenbach et al., 2011; Stephenson et al., 2017). For example, clinical research for cancer and infectious diseases exploits a wide range of techniques to gain information about the location of a solid tumor and its state (Kulasingam & Diamandis, 2008; Ludwig & Weinstein, 2005), or the progression of an infection and the affected body's immune system response (Gold et al., 2010; Verma et al., 2016; Walzl et al., 2018). These techniques or methods could perform the measurement directly in the biological fluid (e.g., blood, saliva, urine, serum, cerebrospinal or interstitial fluid, sweat) or tissues, or can avoid the direct sampling of biological media and they can track and visualize the solid tumor through the use of optical nanodevices (Cabral et al., 2011) or radio-labeled molecules (Kręcisz et al., 2021).

As previously described by Mayeux (2004), there are two major types of biomarkers: biomarkers of exposure and biomarkers of disease. The first class is used in risk prediction while the second is used in screening, diagnosis, and monitoring of disease status (Fig. 11.1). This chapter will focus on this latter class. Biomarkers of disease can be classified based on the sequence of events observed in the pathological pathway (Fig. 11.1). For each stage, a specific (or multi) biomarker can be associated and exploited to investigate the biological history and evolution of a disease. For example, monitoring a biomarker's concentration over time is convenient for providing insight into disease progression, prognosis, and response to therapy (Colburn & Lee, 2003; Hampel et al., 2018; Shaw et al., 2007). In addition, biomarkers can be exploited to identify the earliest events in the biological history of the disease which is crucial for infectious diseases (Gold et al., 2010; Verma et al., 2016; Walzl et al., 2018). Furthermore, the detection of biomarkers leads to the study of potential mechanisms involved in the disease pathogenesis which can be useful to account for some of the variability and effect modification of risk prediction (Devarajan et al., 2003; Thompson et al., 2016).

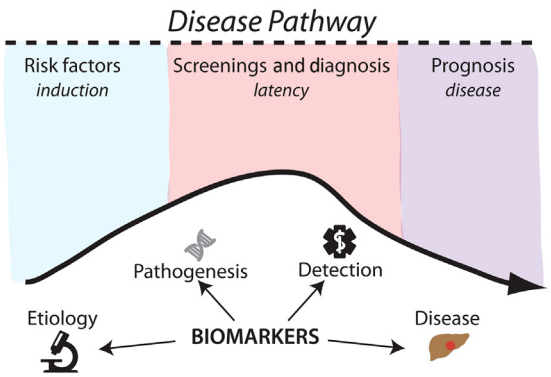

FIGURE 11.1 Disease pathway and potential impact of the biomarkers (Mayeux, 2004). *From Mayeux, R. (2004). Biomarkers: Potential uses and limitations.* NeuroRx, 1*(2), 182–188. https://doi.org/10.1602/neurorx.1.2.182.*

11.1.2 Discovery and validation of clinically relevant biomarkers

The ideal biomarker should directly reflect the stage of a disease at any time. This could be used, for example, for the early diagnosis or for the monitoring during clinical treatment. According to "The Handbook of Biomarkers" (Jain, 2010) an ideal biomarker should display the following features:

1. It must be specifically associated with a particular disease or disease state, and it must be able to differentiate between similar physiological conditions.
2. Standard biological fluids (i.e., serum, blood and urine) should be used for biomarker's identification.
3. Biomarker's detection should be rapid, simple, accurate and low-cost. Additionally, they should display a measurable and standard baseline as a reference point.

Therefore, as mentioned above, an ideal biomarker should demonstrate its association with a pathology or a specific disease state through the prediction of its expression level and its clinical ranges (i.e., its concentration).

Over the last five decades, the development of bioanalytical and biosensing technologies has opened new perspectives on understanding human health and disease processes (Kelley et al., 2014). The accuracy and precision of these technology platforms have allowed to target and discover many clinical targets directly in bodily fluids (i.e., saliva, blood, urine, interstitial fluids, serum, etc.) (Fig. 11.2). The identification and the next validation of these biomarkers have provided new tools to drive the clinical intervention and drug design (Kręcisz et al., 2021; Simon, 2014; Townsend & Arron, 2016). Currently, a single or a class of biomarkers can be associated with the diagnosis of many diseases, and their next monitoring to understand, for example, the efficiency of the clinical treatments. It is clear that the biomarker's quantification and the time required to achieve it play a key role in the majority of clinical decisions. Exploiting the use of laboratory test results, the past and the current clinical practice guidelines have improved as clinical decisions are more accurate. This has led to the refinement of the overall clinical outcomes, particularly in the interpretation of testing related to biological functions versus biomarkers.

11.1.3 Use of biomarkers to reach personalized medicine: from laboratory-based measurements to point-of-care technologies

Laboratory testing has strongly impacted the current clinical treatments improving the clinical management decisions process (e.g., selection of the treatment and its administration) and the final patients' outcomes (Lippi & Mattiuzzi, 2015). Despite the capability and affordability to provide valid and effective clinical data, such approach fails to solve the next new challenges of the real world: global health surveillance and personalized medicine. For example, the high cost, fragile instrumentations, and need of skilled personnel have hampered the use of laboratory testing in low-resources settings (Horvath, 2013). Furthermore, the low turnaround time (i.e., from a few hours to several days) provided by laboratory testing is still far from the time resolution required to achieve a full monitoring of the patient and,

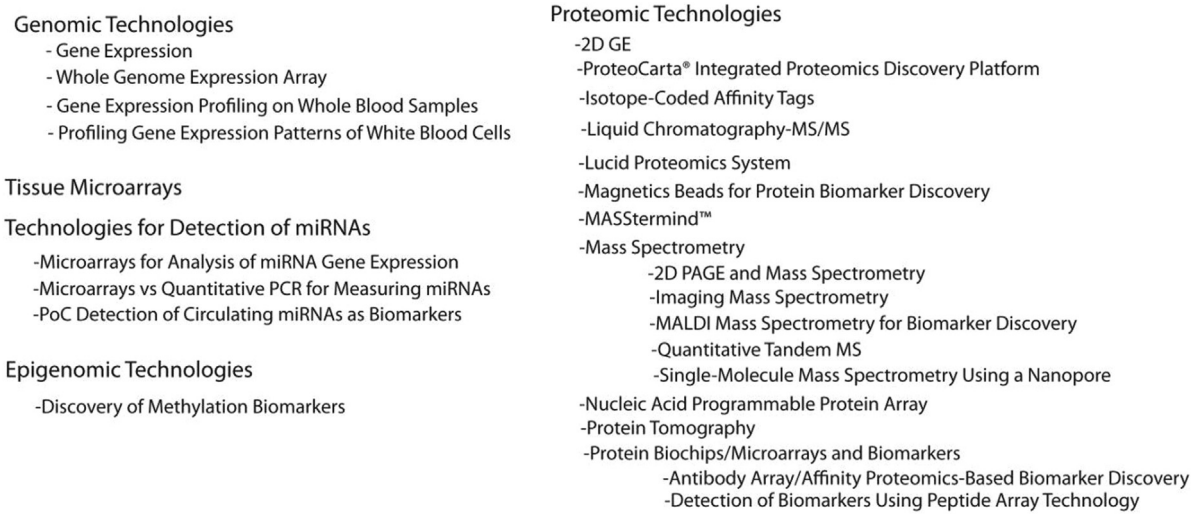

FIGURE 11.2 Overview of the technologies developed for the discovery of biomarkers.

then, a personalization of the clinical treatment (Lippi & Mattiuzzi, 2015). PoC testing technologies display all the required properties to overcome these challenges (Diagnosis et al., 2016). Specifically, PoC-based measurements can provide the rapid detection of biomarkers (i.e., within minutes) and often in a single-step process decreasing their overall cost (Purohit et al., 2020; Zhao et al., 2020). Their sensing platforms are designed to support their use by an untrained end-user directly on site. The success of glucose meters and pregnancy tests demonstrate the ability of PoC devices to solve real clinical problems through the patient's self-testing (Kwon et al., 2016; Purohit et al., 2020).

The constant improvement and ubiquity of smartphones make them ideal platforms for bringing the analytical features of laboratory testing at the point of care (Kwon et al., 2016; Li & Diamandis, 2016; Quesada-González & Merkoçi, 2017). The main goal is to exploit the advanced features and functionality of smartphones to fully integrate and automatize current commercial PoC technologies (Syedmoradi et al., 2017). For example, Martinez et al. have demonstrated how smartphones coupled with PoC devices can support telemedicine and off-site diagnosis (Martinez et al., 2008) offering the real-time connectivity required in the REASSURED criteria (Land et al., 2019). Among the different components integrated in the smartphone, the camera allows to convert the device into a high-performance optical reader. The growing evolution of smartphone cameras in terms of sensor size (12.8 mm × 9.6 mm), resolution (12−108 megapixels), lens quality and softwares have allowed to achieve an optical resolution which is comparable with common complementary metal oxide semiconductor/charge-coupled device (CMOS/CCD) cameras (Purohit et al., 2020). In addition, features such as manual mode [i.e., lens aperture, shutter speed, and sensitivity (ISO)] allow to control the most important parameters during the acquisition of the image which make these devices sensitive enough to support sensing applications. For example, the image acquisition can be easily integrated with optical-based biosensors. These sensing systems are designed to identify the presence of the selected biomarker through its interactions with recognition elements such as enzymes, antibodies, aptamers, dyes, etc. (McCracken & Yoon, 2016). The recognition event can be exploited and engineered in order to induce a change in the optical properties of the solution which can be collected by the camera. This has favored the use of smartphones as optical sensing device with colorimetric, fluorescent, spectroscopic, scattering, and microscopy-based sensing platforms (Aydindogan et al., 2018; Kanchi et al., 2018; Purohit et al., 2020; Zarei, 2017).

11.2 Optical smartphone-based biosensors for the detection of biomarkers

Generally, the main strategy exploited to integrate smartphones with optical biosensing platforms relies on the design of an enclosure device. This has to ensure a controlled environment for the lighting and it has to keep the device and the assay in close proximity. Using this setup, the smartphone's light-emitting diode (LED) can be used as an illumination source and the CMOS-based camera as a detector of the optical signal (Purohit et al., 2020; Yoon, 2019). At the same time, the signal can be processed through the use of software applications (app) which make the overall interface of the sensing device user-friendly and able to support artificial intelligence (e.g., machine learning) (Zhang et al., 2019). Moreover, depending on the selected biosensing platform the enclosure device can be modified with specific optical lenses, diffraction grating, filters, and secondary light or power sources in order to improve signal detection (Hernández-Neuta et al., 2019).

In the following sections, we describe the most exploited optical sensing modalities, such as colorimetry, fluorescence, luminescence, microscopy and SPR, and their applications for the detection of clinically relevant biomarkers. In order to help the reader, we have summarized all the previous studies cited in tables where we describe the name of biomarker detected and its related disease, technique, the biological fluid used for the measurement and analytical performance of the overall device [i.e., limit of detection (LOD) and time resolution].

11.2.1 Colorimetric point-of-care biosensors based on smartphone camera

Colorimetric bioassays exploit the change in the optical properties (e.g., absorbance or reflectance) of the analyte solution due to the binding between the target and the recognition element (Vilela et al., 2012). This optical change, for example, can be induced through the use of enzymes that catalyze the transformation of their substrate to a product, thus leading to a change or appearance of color. Since current smartphones rely on high-quality CMOS image sensors, the color change observed in the test solution can be easily collected and, then, converted into an RGB value by an image processing algorithm is allows the quantification of the biomarker without the need for stringent controls or the use of an optical filter to improve the signal. Therefore, colorimetric sensing platforms based on smartphone cameras have offered a novel approach for the development of PoC devices in healthcare applications (Quesada-González & Merkoçi, 2017; Zarei, 2017). In the last few years, several research groups have developed novel smartphone camera-based colorimetric sensors for the detection of biomarkers directly in body fluids (whole blood, serum, urine, sweat, saliva, etc.) that have improved disease diagnosis and early prevention (see Table 11.1).

TABLE 11.1 Smartphone-based colorimetric point-of-care biosensors for detection of biomarkers in different biological fluids (2015–2020).

Techniques	Biological fluids	Biomarker-LOD	Relate disease	Reference
Ag@Au colorimetric assay (CA), Immunoassay (IA)	Human blood (HB)	Hemoglobin-1.2 g dL^{-1}, HIV antibodies-N/A	HIV	Guo et al. (2015)
CA, Microfluidic	HB	Blood hematocrit-0.1%	Anemia	Kim et al. (2017)
CA, Paper-based microfluidic IA (μPIA)	HB	C-reactive protein (CRP)-54 ng mL^{-1}	Chronic heart and kidney disease	Dong et al. (2017)
CA, Disposable microfluidic device	HB	CD4-N/A	HIV/AIDS	Kanakasabapathy et al. (2017)
Self-propelled multifunctional Janus particles CA	HB	Procalcitonin (PCT)- <2 ng mL^{-1}	Sepsis	Russell et al. (2019)
CA, paper-based plasmonic IA	HB	IL-6–0.1 pg mL^{-1}	sepsis	Alba-Patiño et al. (2020)
CA (RGB and HSV)	Bloodstain	V value of HSV-8.5%	\	Shin et al. (2017)
Microplates CA, IA	Human serum (HS)	Human interleukin 6 (IL-6) -N/A	Autoimmune disease, Tumor, Nervous system disease etc.	Wang et al. (2016)
Microplates CA, IA	HS	IL-6–0.187 mg mL^{-1}	Autoimmune disease, Tumor, Nervous system disease etc.	Wang et al. (2017)
Au-Ag CA, PIA	HS	Cancer antigen 125 (CA125)-30 U mL^{-1}	Cancer	Hosu et al. (2017)
Mimicking peroxidase nanocomposite CA, μPIA	HS	Carcinoembryonic antigen (CEA)-0.51 pg mL^{-1}	Tumor	Alizadeh et al. (2018)
Porous silicon microcavities CA- ELISA,	HS	Antihistone H2 B antibodies and biomarkers of severe illnesses-10 fg mL^{-1}	Autoimmune disease	Ramakrishan et al. (2018)
Multiplexed CA, Paper-based microfluidic	HS	GPBB, CK-MB and cTnT-0.5, 0.5 and 0.05 ng mL^{-1}	Acute myocardial infarction (AMI)	Lim et al. (2019)
CA, sandwich ELISA, Smartphone video	HS	NS1 protein	Zika	Coleman et al. (2019)
Multiplexed CA, Paper-based microfluidic	HS	Glucose-0.3125 mM, lactate-0.2975 mM	Diabetes	Kim et al. (2019)
Enzyme@MOFs CA, μPAD	HS	Glucose-250 μM, uric acid-0.5 mM (naked eye)	Diabetes and gout	Kou et al. (2020)
CA (RGB), Diaper assay	Human urine (HU)	12 urinary biomarkers	Urinary system diseases	Karlsen et al. (2017)
CA (RGB), Wearable device (Diaper)	HU	Glucose, leukocytes, nitrite, blood and proteins	Urinary tract infection and kidney disease	Zhou & Dong (2018)
CA, AuNPs LFIA	HU	Urine 8-hydroxy-2′-deoxyguanosine (8-OHdG)-N/A	Diabetic retinopathy	Hainsworth et al. (2020)
Colorimetric, Wearable patch, Paper microfluidic, Wax printing	Sweat	pH, glucose (physiological range) and lactate-N/A	Diabetes	Zhang et al. (2019)
Confined multilayer paper reflectometry	Oral fluid (saliva)	L-lactate-0.01 mM	Severe sepsis, septic shock	Calabria et al. (2017)

(*Continued*)

TABLE 11.1 (Continued)

Techniques	Biological fluids	Biomarker-LOD	Relate disease	Reference
RGB colorimetric, Paper based strip coated with enzyme	Saliva	urea-10.4 mg dL^{-1}	kidney and liver disorders	Soni et al. (2018)
CA, On-chip RT-LAMP	Cell lines	Prostate cancer antigen 3 RNA-0.34 fg μL^{-1}	Prostate cancer	Wang et al. (2020)

Since blood can affect optical detection due to its intense red color by increasing background signal and decreasing the ratio of signal-to-noise, many efforts have been done to develop antiblood color interference sensors based on smartphone cameras for infectious disease screening and monitoring (Kim et al., 2017). For example, Guo et al. have developed a microfluidic-based smartphone device which can simultaneously detect concentrations of hemoglobin and HIV antibodies directly in whole blood (Guo et al., 2015) (Fig. 11.3A). The sensing mechanism is based on the measurement of the optical density of silver precipitation on gold colloids. Specifically, each test zone of microfluidic channel was modified with disease-specific antigen (Fig. 11.3A, bottom). When the blood sample flow through the channel, the target antibodies can be bound to the surface and next recognized by gold-labeled secondary antibodies. Then the excess of reactant was removed by washing buffer, and finally silver reagents was added onto gold particles to create an optically darkened zone which is dependent on the concentration of the target. Compared with a gold standard instrument (the Hemocue Hb 201 + analyzer) the smartphone-based device displays good accuracy within 1.2 g dL^{-1} for hemoglobin detection, and obtained 95% sensitivity and 95% specificity when analyzing the HIV antibodies. Kanakasabapathy et al. developed a smartphone-based sensor which allowed the rapid (30 min) counting of CD4 + T-cells, an important biomarker for the clinical disease management of HIV-positive patients (Kanakasabapathy et al., 2017). The system is composed of an inexpensive (<$5) cellphone accessory integrated into a disposable microfluidic immunoassay device. Using only a microvolume of whole blood (30 μL) it is possible to achieve CD4 + testing with analytical performance comparable with the manual analysis and fluorescence-activated cell sorting results. This device displays all the potential to dramatically impact HIV detection and management in low-resource setting scenarios.

Optical sensors based on smartphone camera also display high sensitivity for the detection of tumor markers in human serum. Alizadeh et al. showed a paper-based microfluidic colorimetric immunosensor for the detection of carcinoembryonic antigen (CEA) by using Co2(OH)2CO3-CeO2 nanocomposite, which mimics the peroxidase enzymatic activity, and the smartphone camera as an optical reader (i.e., collection of the photos and their analysis) (Alizadeh et al., 2018) (Fig. 11.3B). This device displays a very wide detection linear range (0.002−75.0 ng mL^{-1}) for CEA and good LOD (0.51 pg mL^{-1}). In another example, developers improved the detection efficiency and achieved high-throughput screening, by adapting the smartphone camera into an eight-channel spectrometer with nanometer resolution. The resulting device can simultaneously optically sense up to eight different samples by integrating optical accessories and a custom smartphone multiview app (Wang et al., 2017). The device shows high sensitivity (2 μg mL^{-1}) for detecting BSA protein and also had a good agreement ($R^2 = 0.9919$) and comparative LOD (10.6 pg mL^{-1}) with the lab instrument for detecting Human Interleukin-6 cancer biomarker.

Another interesting approach to carry out urine analysis, a common method in medical diagnostic with an important clinical value, was developed by Karlsen and Dong (2017). Specifically, an ambulatory prescreening PoC sensor compatible with commercially available diapers was developed to rapidly screen urine samples for incontinent or functionally impaired elderly. This portable and convenient sensor was integrated with a series of colorimetric reaction pads and accompanying reference colors, and the smartphone was used as reader and for data processing. The device can achieve semiquantitative analysis and detection of 12 different biomarkers (2−7 references/biomarker) in human urine. Moreover, the use of this sensing system is not affected by lighting intensity and color, device type (i.e., smartphone brand and model), device settings (e.g., ISO, shutter speed, aperture), and automatic camera preprocessing limitations.

A versatile, cost-effective, and wearable PoC patch sensor was developed for the rapid and quantitatively detection of biomarkers (glucose, pH, and lactate) directly in sweat (Fig. 11.3C). Unlike blood, which requires extraction from

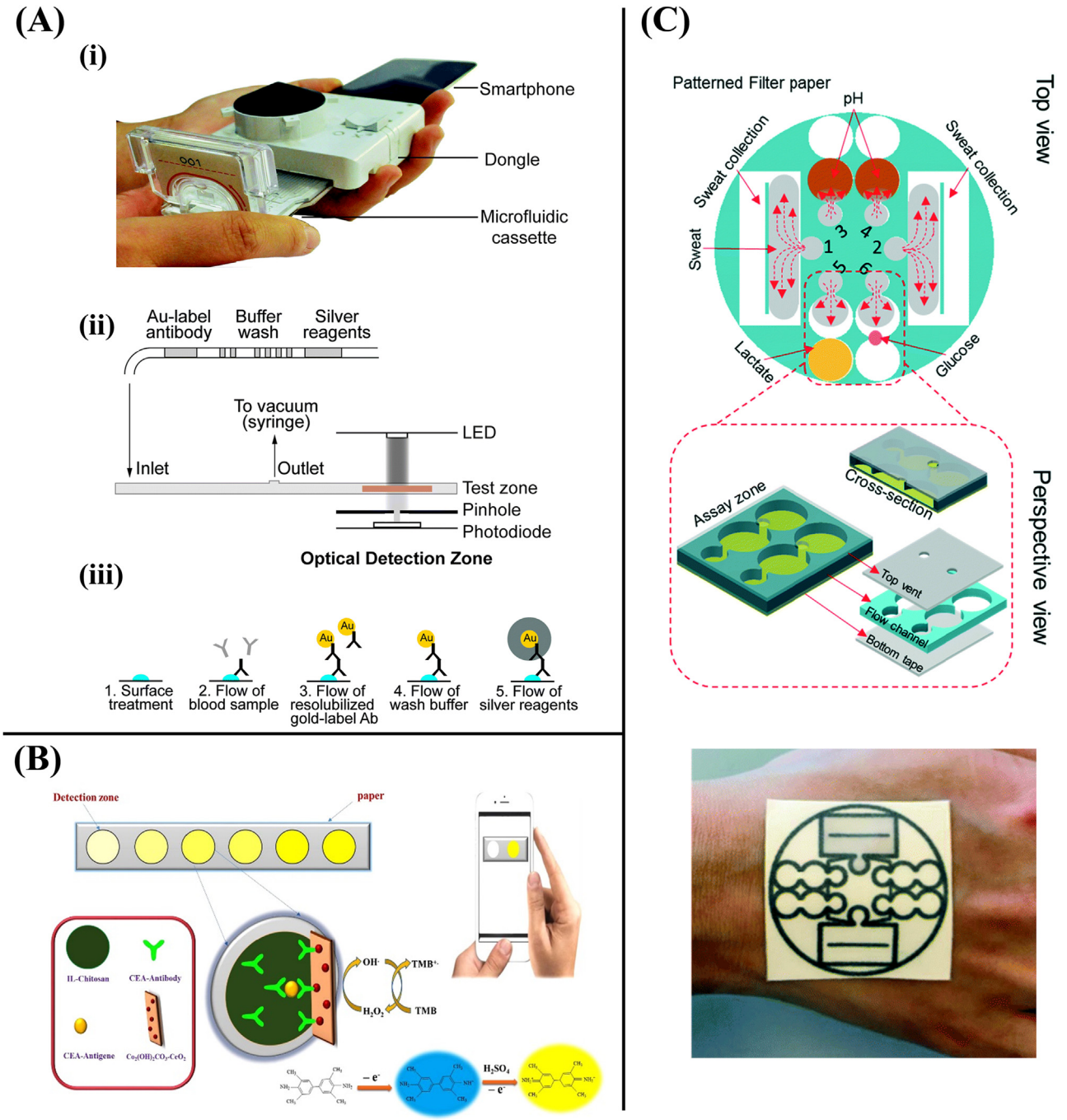

FIGURE 11.3 Smartphone-based colorimetric PoC biosensors for detection of the biomarkers in different samples (human blood, serum, and sweat). (A) Smartphone dongle for simultaneous detection of hemoglobin and detection of HIV antibodies in blood. (i) photograph of smartphone dongle; (ii) scheme of fluidic and optical experimental set-up; (iii) Scheme of immunoassay steps (Guo et al., 2015). (B) Scheme and assay procedure of CEA detection on the paper-based chip (Guo et al., 2015). (C) Schematic design of the wearable device for sweat collection and biosensing (Zhang et al., 2019). *From (A) (Guo et al., 2015); (B) (Guo et al., 2015); (C) (Zhang et al., 2019).*

the patient, sweat can be collected outside of the body, resulting in less invasive. The developed device combined a homemade wearable PoC patch with the imaging and computing functionalities of smartphones. By overcoming the issue of extremely low concentrations of glucose in the sweat samples, the device is engineered to concentrate the colorant (indicator) into a small detection zone in order to increase the sensitivity for the sweat glucose-sensing reactions, achieving accurate and rapid detection of the glucose in the physiological range (50−300 μM) (Zhang et al., 2019).

11.2.2 Fluorescence point-of-care biosensors based on smartphone camera

Smartphones can be fully integrated with biosensing platforms based on fluorescence readouts such as optofluidic (Ko et al., 2016), microfluidics (Kwon et al., 2016; Li & Diamandis, 2016; Quesada-González & Merkoçi, 2017), and lateral flow immunoassay (Gupta et al., 2019). Fluorescence is widely exploited as an optical signal for the detection of many clinically relevant biomarkers thanks to its high sensitivity and rapid detection. This technique relies on the detection of the emitted light from the target-fluorophore complex upon its radiative excitation through a light source. Since the majority of the available fluorophores display very close absorbance and emission peaks, and the current smartphone CMOS sensors are unable to distinguish such spectral difference, optical filters and lenses have to be integrated into the enclosure device (Kim et al., 2017). This ensures that only the light emitted by the fluorophore will be filtered and detected by the smartphone's camera. Another important parameter to take into account during the design is the optical excitation source. Indeed, the fluorescence signal is proportional to the intensity and spectral range of the excitation source. Therefore the correct excitation source has to be selected in accordance with the optical properties of the selected fluorophore (Yoon, 2019).

The need to achieve lower detection limits and to perform the measurement in spatially sensitive environments is pushing research efforts towards the improvement of the device design itself. Specifically, high-performance filters and nanomaterials have been integrated in mobile sensors to improve light rejection (i.e., light outside cannot enter into the device interfering with the detection), scattering, and diffraction of emitted light (Hernández-Neuta et al., 2019). All these efforts have produced smart fluorescence-based smartphone biosensors able to rapidly detect biomarkers in their clinical range through PoC platforms. This demonstrates all their potentials to solve real clinical problems, in particular for the ability of these devices to support multiplexed measurements (Guo et al., 2015).

Recently, a smartphone-enabled fluorescent optofluidic platform was developed by Issadore's group for detection of brain-derived exosomes (Ko et al., 2016) (Fig. 11.4A). These exosomes have shown great potential as a noninvasive biomarker of brain recovery. Because exosomes display small size (30−100 nm) and the sample preparation is extremely time-consuming (> 24 h), their detection is still limited in clinical settings. The developed device can detect exosome biomarkers exploiting an enzymatic reaction (GluR2 + exosomes) within 1 h, which is 10 times faster than conventional techniques, therefore, fully solving the challenge of traditional exosome detection. Li et al. have combined the complement fixation test (CFT) with a microfluidic platform, and a smartphone to develop a fast, simple and miniaturized device for the diagnosis of biomarkers (Li & Shi, Fang, et al., 2016). Compared with ELISA or other traditional immunoassays, this miniaturized device significantly shortened the detection time of CFT, reduced sample consumption and washing steps. The platform was able to sensitively and selectively detect CEA and recombinant avian influenza A (rH7N9) virus protein in human serum without complexed steps of protein immobilization, blocking, and washing steps (see Table 11.2).

In addition to single fluorescence detection device, researchers are committed to develop multimode smartphone-based optical sensors. For example, Barbosa et al. presented a novel, power-free and portable smartphone-based fluoropolymer microfluidic device for colorimetric and fluorescent quantitative detection of prostate specific antigen (PSA) in whole blood (Barbosa et al., 2015). The device consists of a smartphone integrated with a magnifying lens, a light source, and a microcapillary film coated with fluoropolymer probe. The proposed sensing platform was able to perform selective and accurate analysis of PSA in whole blood. The device displays a LOD of less than 0.9 ng mL^{-1} and a total assay time of 13−20 min, which proves a major progress in successful integration of portable, low-cost microfluidic devices with commercial immunological reagents and affordable smartphones. More recently, Long et al. developed a smartphone camera-based optical sensing platform able to collect colorimetric absorption spectra, fluorescence emission spectra, and resonance emission spectra (Long et al., 2017) (Fig. 11.4C). The platform was designed for the detection of phenylalanine in human serum, achieving a LOD of less than 0.5 nM.

Paper is attracting a lot of interest due to the unique advantages such as low cost, portability, and capillarity, which allow the pump-free movement of the sample (Parolo et al., 2020; Parolo & Merkoçi, 2013). For this reason, efforts have been made to integrate this substrate in smartphone-based fluorescent sensing platforms for clinical detection of biomarkers. For example, Rong et al. developed a smartphone-based fluorescent lateral flow immunoassay (F-LFIA) platform for the infectious diseases screening (Rong et al., 2019). The F-LFIA was exploited to detect Zika virus nonstructural protein 1 (ZIKV NS1) in human serum (Fig. 11.4B). This PoC device supports the quantitative detection (with a LOD of 0.15 ng mL^{-1}) and excellent selectivity within 20 min. The rapid, portable, and cost-effective smartphone-based F-LFIA platform is expected to be an excellent choice for infectious diseases screening in resources-limited regions. Semiconductor quantum dots (QDs) are an excellent fluorescent probe for optical detection platforms due to their ultra-high fluorescence intensity, quantum yield and great Stoke shifts (Hu et al., 2017). Gupta et al.

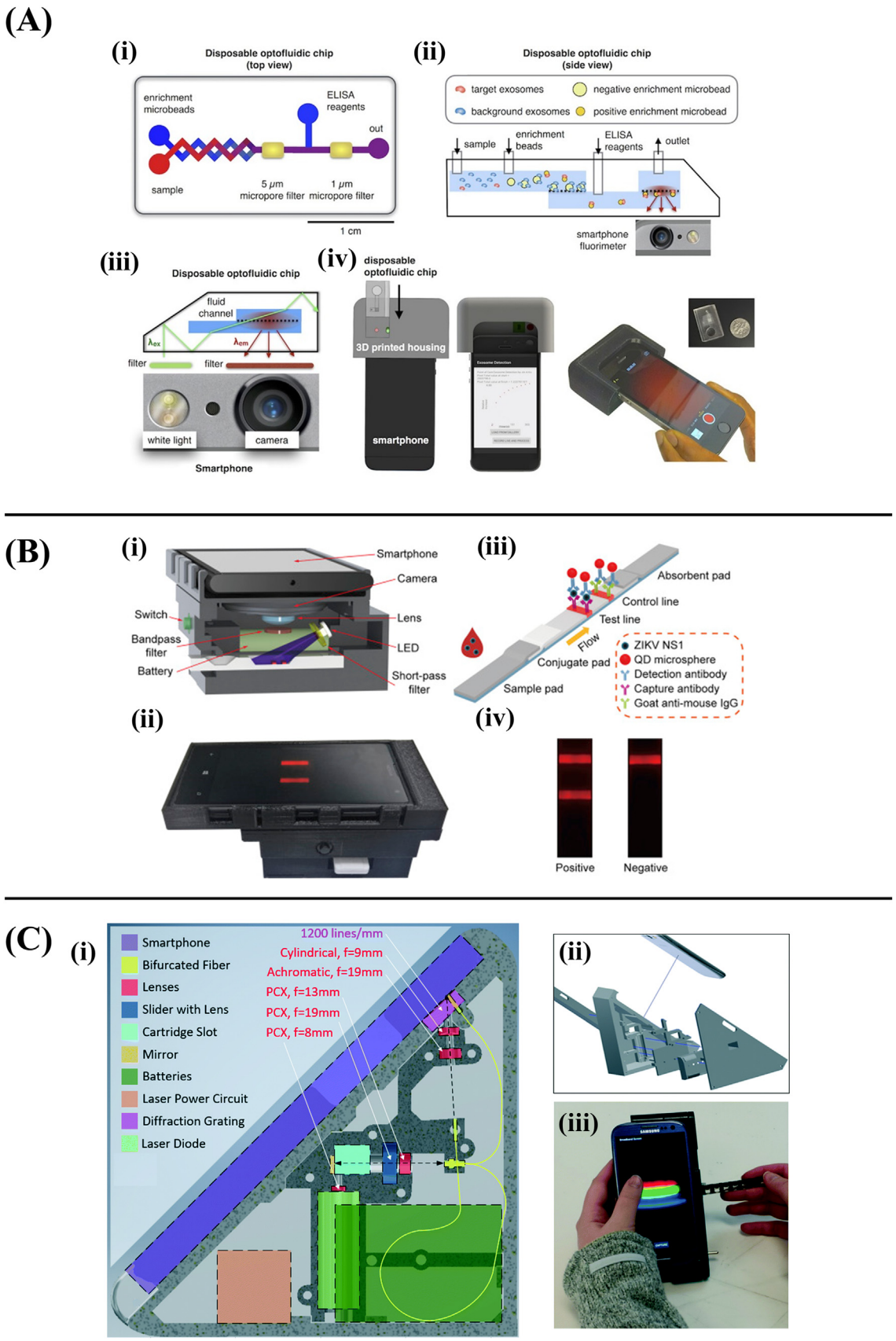

FIGURE 11.4 Smartphone-based fluorescence PoC biosensors integrated with microfluidic and lateral flow assay. (A) Design and implementation of microfluidic-based mobile exosome detector (μMED). (i) top view of μMED, showing sample inputs, chaotic mixers where reagents are rapidly mixed and incubated on-chip, and the integrated micropore filters that are used to trap beads; (ii) side view of μMED, showing the step-by-step assay carried out on our chip; (iii) optical setup for μMED's integrated fluorescence read out; (iv) a CAD scheme of the integrated device and a photograph of the μMED in action (Ko et al., 2016). (B) Overview of the design and application of the smartphone-based fluorescent LFIA platform. (i) 3D scheme of the smartphone-based fluorescence imaging device; (ii) photograph of the developed fluorescent LFIA reader; (iii) scheme of the fluorescent LFIA for the detection of ZIKV NS1; (iv) image of the test strips in the presence (left) and absence (right) of ZIKV NS1 (Rong et al., 2019). (C) Schematic design of a multimode smartphone analyzer. (i) scheme of internal layout for optical and electrical components; (ii) 3D CAD model was created, comprised of five plastic parts printed via stereolithography; (iii) photograph of final device in use with absorption cartridge (Long et al., 2017). *From (A) (Ko et al., 2016); (B) (Rong et al., 2019); (C) (Long et al., 2017).*

TABLE 11.2 Fluorescence PoC biosensors based on smartphone.

Techniques		Biomarkers-LOD	Related disease	Reference
CA, Fluoropolymer microfluidic assay	HB		PSA cancer	Barbosa et al. (2015)
Fluorescence assay (FA), Optofluidic	HS		Mild traumatic brain injury	Ko et al. (2016)
FA, Microfluidic, CFT	HS		Cancer and avian influenza A	Li, and Shi, Fang, et al. (2016)
FA, RT-LAMP	HB, HS and saliva		Infectious disease	Priye et al. (2017)
FA, TRI analyzer	HS		Phenylketonuria	Long et al. (2017)
RGB, Indicator displacement approach	HU		Acute poisoning or cancer	Merli et al. (2018)
Ratiometric multicolor FA, RGB analysis	HS		Diabetes, bone disease, prostatic cancer, and liver dysfunction	Hou et al. (2019)
FA, Smartphone spectrum apparatus	Synthetic urine		Alzheimer's and Parkinson's	Neill et al. (2019)
FA polarization assays	PBS		Infection, inflammation, or cancer	Zhao et al. (2019)
FA (Polymer dots and QDs), Lateral flow assay	Buffer		N/A	Gupta et al. (2019)
Fluorescent DNA microarray, Paper microfluidic	Buffer		Breast cancer	Prasad et al. (2019)
FA signal-enhanced (ZnO nanowires), Paper-based immunoassay	HB		AMI	Guo et al. (2019)
F-LFIA	HS		Congenital birth defects and Guillain-Barre syndrome in adults	Rong et al. (2019)

compared the optical properties of semiconductor polymer dots (Pdots) and semiconductor QDs applying these to lateral flow assay for analysis of human IgG in order to evaluate their sensing performance (Gupta et al., 2019). The greater per-particle brightness of Pdots provides orders of magnitude better imaging sensitivity vs QDs, which is supported very well by analysis results from the lateral flow assay. Additionally, the Pdots also can realize multicolor imaging on smartphone. This proves that Pdots has great potential to be applied to smartphone-controlled fluorescent sensors to obtain higher sensitivity and lower LOD.

Fluorescence analysis is widely used in nucleic acid detection (Fu et al., 2020), such as real-time fluorescence quantitative PCR (Zhou et al., 2019), real-time fluorescence isothermal amplification (Veigas et al., 2017), and hybrid capture immunofluorescence analysis (Wang et al., 2017). Although these classic methods are accurate, they are still not fast and not enough portable. Prasad et al. developed a portable fluorescent microarray based on smartphone imaging system for the detection of Cy3-target DNA for the diagnosis of breast cancer (Prasad et al., 2019). A paper-based microfluidic platform was used to demonstrate the DNA hybridization assay. By analyzing RGB value of the images captured by smartphone CCD camera, the device achieved a comparable LOD of 0.4 μM. The smartphone-based paper microfluidic platform can be used into clinical settings for performing PoC testing. In addition to the commonly used fluorescence intensity readout, Lu's group reported a smartphone-enabled system using fluorescence polarization (FP) assay for biomarkers sensing (Purohit et al., 2020; Zhao et al., 2020). The FP assay can rapidly detect the connection of ligand-target by monitoring the movement of molecules, so it is widely used in rapid clinical diagnosis. The developed platform was demonstrated to detect Prostaglandin E2 using a competitive FP immunoassay, with a LOD of 1.57 ng mL^{-1} (see Table 11.2).

11.2.3 Luminescence biosensors on smartphone camera

Luminescence is an optical phenomenon applied in biosensing platforms taking advantage of successfully integrated smartphones for the detection of biomarkers. By definition, luminescence includes all the processes involved in the emission of light from any molecule. This emission is mainly due to the returning of electrons from their excited states to their ground states through a relaxation process. Depending on the nature of the excited state (i.e., singlet or triplet states) the luminescence can be divided in fluorescence and phosphorescence (Azim et al., 2018; Mckeever & Chen, 1997). In these processes, the emission requires the use of an excitation light source to induce the formation of the electronically excited states. However, the definition of luminescence includes also all the light emission processes that do not require a light excitation source. For example, when the emission of light is triggered by a chemical reaction this process is called CL (Clough et al., 2016). The same process can occur inside the living organisms and take the name of bioluminescence (BL) (Roda & Guardigli, 2012). On the contrary, photoluminescence (PL) is produced using a light excitation in the spectral range of ultraviolet or X-ray (Bebb & Williams, 1972). Finally, electrochemical luminesence (ECL) is a luminescence process induced by an electrochemical reaction in solutions (Miao, 2008). Such spontaneous emission of light observed in these processes was exploited to develop new biosensing platforms achieving high sensitive detection. Therefore, such optical techniques can be fully combined with digital camera technology and mobile devices to produce PoC analytical devices able to achieve the rapid and easy diagnosis of clinically relevant biomarkers (Roda et al., 2016).

A chemiluminescent agent is a compound or species participating in the luminescence reaction where the formation of the product comes with the release of energy in the form of emitted photons. These agents can be divided in luminescent substrates for enzymatic reactions, direct chemiluminescent agents, and electrochemiluminescent agents. For example, the luminescent substrate produce light after the catalytic action of enzymes. The enzymes commonly used in chemiluminescent immunoassay (CLIA) are horseradish peroxidase (HRP) and alkaline phosphatase (AP) (Kricka, 1996). Luminol and its derivatives are the most commonly used substrates for HRP (Azim et al., 2018). Roda et al. developed a smartphone-based CL assay for detection of total cholesterol, an important biomarker for heart disease, exploiting a cholesterol esterase/oxidase integrated with luminol-H_2O_2-HRP system (Roda et al., 2014) (Fig. 11.5A). The developed device can rapidly perform the analysis (within 3 min) without additional processing of the sample, and it displays a LOD of 20 mg dL^{-1}, which is comparable to another reported ECL assay in serum sample (Zhang et al., 2019). Although the LOD is slightly higher than other amperometric assays (Ruecha et al., 2014), this method only requires a smartphone as a detector making it convenient and cost-effective. Subsequently, Zangheri et al. combined CL and lateral flow immunoassay (LFIA) to develop a portable device for quantitative detection of cortisol in saliva (Zangheri et al., 2015), which is a biomarker of stress, anxiety, and depression (Tlili et al., 2011). This system is based on the substrate (luminol/enhancer/H_2O_2) and peroxidase enzyme. The smartphone camera is used as detector through photo acquisition, and data processing is performed by a custom app. The overall assay is easy-to-use, rapid (within 30 min), sensitive (with a LOD of 0.3 ng mL^{-1}), and has a quantitative detection range (between 0.3 and 60 ng mL^{-1}) which covers cortisol's clinical relevant range.

The diagnosis or treatments of some diseases often require multibiomarker testing, therefore, the detection of a single biomarker cannot meet the diagnostic needs. In a newly reported study, Li et al. developed a smartphone-based assay for the multiplexed detection of biomarkers integrating CLIA into a microfluidic chip (Kwon et al., 2016; Li & Diamandis, 2016; Quesada-González & Merkoçi, 2017). The assay exploits the luminol-H_2O_2 system to initiate cobalt-based zeolitic imidazolate frameworks ZIF-67 in order to produce CL and resonance transfer reactions, and thus obtain multiresolution CL signal. This platform was designed to detect three different cancer biomarkers [CEA, α-fetoprotein (AFP), and PSA] using both video and image modes. The platform displays a detection range and a LOD which are better than previous CL microfluidic paper-based devices for the same biomarkers detection. The ECL method combined with CL and an electrochemical reaction can further improve the sensitivity and accuracy of PoC biosensing platforms. Chen et al. proposed a handheld paper-based bipolar electrode-ECL (BPE-ECL) device combined with a battery energy supply and a smartphone as detector (Chen et al., 2016). Common luminol-H_2O_2 based ECL reaction was applied in this platform. The BPE-ECL system can detect glucose in artificial urine with a LOD of 0.030 nM supporting high throughput-out data.

Bioluminescence (BL) has recently emerged as a promising tool for PoC diagnostics based on smartphones. BL-based sensors are mainly divided into two categories: the first one exploits natural bioluminescent proteins, and the second one exploits entire bioluminescent bacteria or cells. Generally, bioluminescence is produced by the chemical reaction between light-producing molecules such as luciferin and luciferase. Roda et al. firstly reported the use of integrating BL coupled with bio-specific enzymatic reactions with smartphone camera to quantify biomarkers in biological

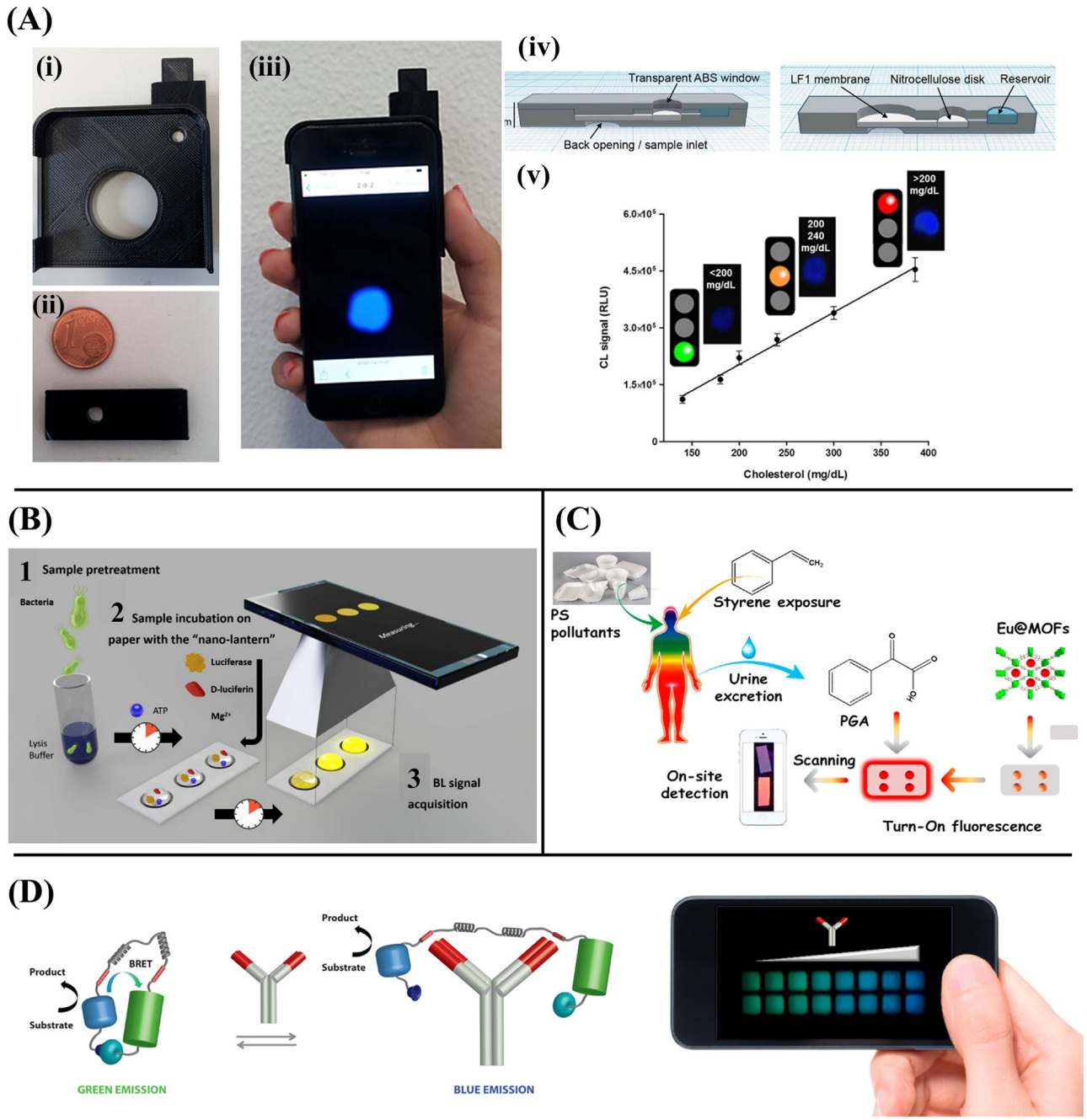

FIGURE 11.5 Different types of smartphone-based luminescence PoC biosensors. (A) Mobile chemistry PoC platform integrated biochemiluminescence detection on smartphones. (i) Photograph of the accessory; (ii) picture of minicartridge; (iii) picture of a representative CL acquisition with the smartphone; (iv) schematic drawings of the minicartridge showing the integration of the various components; (v) quantitative analysis of cholesterol in spiked human serum samples, along clinical detection index and corresponding CL images (Roda et al., 2014). (B) Schematic illustration of nano-lantern on paper for smartphone-based ATP detection (Calabretta et al., 2020). (C) Scheme of the turn-on fluorescence switch (photoluminescence) for on-site detecting urinary PGA (Lian et al., 2017). (D) Using bioluminescent sensor proteins and a smartphone for the detection of antibodies in human plasma. Scheme of the BRET sensor concept and image of bioluminescence acquisition with smartphone (Arts et al., 2016). *From (A) (Roda et al., 2014); (B) (Calabretta et al., 2020); (C) (Lian et al., 2017) and (D) Arts et al. (2016).*

fluids (Roda & Guardigli, 2012). The system is able to detect the total concentration of bile acids with high accuracy (LOD of 0.5 μM) and precision (using 3α-hydroxyl steroid dehydrogenase coimmobilized with bacterial luciferase system) in serum and oral fluids. Recently, Arts et al. presented a novel sensor called LUMABS which exploits the blue-light emitting luciferase NanoLuc as donor and the green fluorescent mNeonGreen as acceptor

(Arts et al., 2016) (Fig. 11.5D). The donor and acceptor are connected by a semiflexible linker which can be stretched by the presence of specific antibodies (i.e., antiHIV1-p17, hemagglutin (HA), and dengue virus type I). Therefore, the binding with the antibody increases the distance between the donor and the acceptor, so that, the optical readout based on bioluminescence resonance energy transfer (BRET) is related to the biomarker's concentration (Komatsu et al., 2018). The novel platform was used to detect three common antibodies using blood plasma displaying a LOD of 10 pM and without the need of washing steps. Compared with a sensor based on color change, the system based on BRET (i.e., based on two colors or two wavelengths) displays a more robust, stable and sensitive signal readout.

The combination of bioluminescence with magnetic separation technology can make the biomarker's detection more convenient and sensitive. Li et al. proposed a new approach based on modified magnetic beads and DNA-templated bioluminescent modules that allow the amplification of the signal readout (Li et al., 2018). Specifically, two DNA-based hairpin molecules are conjugated with a luciferase as donor and a green fluorescent protein as acceptor, respectively. The sequences of the two hairpins are designed to induce their self-assembling (into a long double-strand structure) only in presence of an initiator strand through a polymerization process called hybridization chain reaction (Dirks & Pierce, 2004; Idili et al., 2015). When the two hairpins are triggered forming the formation of the long DNA double strand structures, the donor and the acceptor will be in close proximity to allow energy transfer (in this case, BRET). This configuration permits the amplification of the bioluminescent signal read-out while coupling it with detection. To do so, aptamers and antibodies are used as receptors and designed to be initiators to trigger the DNA-based reaction in response to their biding with the targets. The platform displays a LOD of 18.3 and 7.7 pM for detection of α-thrombin and PSA in spiked human serum and an acceptable consistency with the gold standard technique ELISA.

Paper-based sensors are very popular in practical medical diagnosis due to their unique advantages (such as cost-effective, rapid, and simple). The group of A. Merkoçi reported a novel paper-based nano-lantern bioluminescence sensor combined with smartphone readout for detection of ATP (Calabretta et al., 2020) (Fig. 11.5B). The platform can rapidly (within 10 min) detect ATP in a small-volume of urine (just using 10 μL) with a LOD of 10^{-14} M which corresponds to 10^5 CFU mL^{-1} bacteria. The research of bioluminescent nucleic acid detection based on smartphone is also another hot topic (Zhou et al., 2019). Chang et al. introduced a smartphone bioluminescent genetic sensor coupled with semisynthetic luciferase for the detection of DNA/RNA biomarkers (Chang et al., 2020). This platform is based on a standard displacement reaction which allows the detection of two sequence simultaneously integrated acting as an AND gate on the sensor. Finally, the sensor was fully able to perform the analysis of three different of microRNA sequences (microRNA-21, -31, -141) in human serum using smartphone imaging with a LOD of 400 pM.

Lanthanides such as Europium (Eu) and Terbium (Tb) are widely used in photoluminescence sensors due to their high luminous intensity, long light lifetime and resistance to background interference (Lee et al., 2017; Yang et al., 2018). Lian et al. reported a paper-based photoluminescent sensor modified with Eu@MOFs for detection of phenylglyoxylic acid (PGA) in serum and urine (Lian et al., 2017) (Fig. 11.5C). The Eu@MOFs display distinct enhanced luminescence in presence of PGA exhibiting excellent selectivity. The PL device has several appealing advantages such as high sensitivity (LOD of 4.16 ng mL^{-1}), high speed (< 5 s), and a wide detection range (0.02−0.5 mg mL^{-1}). By combining photoluminescence, magnetic separation technology, multiplexed sensing, smartphone imaging and a multicolored luminescent nanoprobe, Xu and co-workers developed a new erasable and visible platform for PoC detection of dipicolinic acid (DPA) (Xu et al., 2019), which is an important biomarker for anthrax. The designed nanoprobe is composed of $CePO_4$:Tb-EDTA-Eu and Fe_3O_4 magnetic nanoparticles in which $CePO_4$:Tb was used as color supplier and the $CePO_4$:Tb-EDTA-Eu as the sensitive reactive signal for the detection of DPA. The device supports real-time analysis just using a color-scanning app on the smartphone. In addition, because the luminescence can be quenched by Cu^{2+} ions, they can be used to regenerate the sensor and allow the detection of cysteine (Cys) with high sensitivity (See Table 11.3).

11.2.4 Microscopy point-of-care biosensors based on smartphone camera

Over more than two centuries, optical microscopy has been a crucial and essential tool for life science and basic clinical research (Chen et al., 2016). For example, histological diagnosis is still used for the analysis of tissues in order to confirm the presence or absence of a disease, its grading and progression (Gurcan et al., 2009). The ability to provide quantitative images using microscopy has made this technique the "gold standard" for the final diagnosis of most clinical diseases (Rorke, 1997). Although the cost of microscope imaging has been greatly reduced in recent years, its overall cost still does not allow its wide use in limited resources settings (Mao & Huang, 2012). To overcome this, the combination of smartphone technology with microscope has allowed the integration of this optical technique into a PoC platform offering great potential for personalized medical diagnosis (Hernández-Neuta et al., 2019). Smartphones have

TABLE 11.3 Luminescence PoC biosensors based on smartphone.

Techniques	Sample	Analyte-LOD	Component of Smartphone and accessory	Reference
BL, CL	HS and oral fluid	total bile acids-0.5 μM, total cholesterol-20 mg/dL	Camera, Back-illuminated CMOS	Roda et al. (2014)
CL, Lateral flow immunoassay (LFIA)	Saliva	Cortisol-0.3 ng/mL	Camera, plano-convex lens and cartridge-insertion slot	Zangheri et al. (2015)
CL	Exhaled breath condensates	Hydrogen peroxide (H2O2)-264 nM	Camera, Photography software	(Quimbar et al., 2016)
BRET	Human plasma (HP)	Antibodies (against HIV1-p17, hemagglutinin (HA), and dengue virus type I)-10 pM	Camera, Photography software	Arts et al. (2016)
ECL	Artificial urine	Glucose-0.030 nM	Camera, Paper based bipolar electrode	Chen et al. (2016)
BL	Water	DMSO-IC50 8.9 ± 0.7% (v/v)	Camera, 3D printed minidarkbox and aligned optical interface	Cevenini et al. (2016)
PL	HS and HU	Phenylglyoxylic acid (PGA)-4.16 ng/mL	Camera, Color scanning APP	Lian et al. (2017)
PL, Magnetic seperation	HU	Dipicolinic acid (DPA)-10.3 nM, Cysteine-90 nM	Camera, Color scanning APP	J. Xu et al. (2019)
PL	Human plasma	Mucin-42.8 μg/mL	Camera	(Dutta et al., 2018)
BL, Loop-mediated isothermal amplification (LAMP)	Saliva, HS and HB	ZIKA virus(saliva and urine)- 5 PFU, HIV (blood)-N/A	Camera, Smat-connected cup, Custom Android app	Song et al. (2018)
PL, Colorimetry	HU	p-aminophenol (PAP)-5 μg/mL	Camera, Color scanning APP	Qin and Yan (2018)
PL, Ratiometric colorimetric	Bacillus subtilis spore solution	DPA-54 nM(PL) and 72 nM (Colorimetric)	Camera, Color scanning APP	M. Xu et al. (2019)
CL	HB and Bloodstain	Hemin-20 nM	Camera	Fereja et al. (2019)
BRET, Immunomagnetic seperation, Isothermal amplification	HS, human peripheral blood	α-thrombin-18.3 pM, Prostate specific antigen (PSA)-7.7 pM	Camera	Li et al. (2018)
PL, Absorbance energy-transfer emission effect (AETE effect)	Water	DPA-0.5 nM and 1.0 μM (UV lamp and smartphone), Bacillus subtilis spore-$1.95*10^6$ spores	Camera, UV lamp	Rong et al. (2019)
CL, ELISA	HS	Plasmodium falciparum Histidine Rich Protein 2 (PfHRP2)-8 ng/mL	USB-OTG port, Custom designed optical detector	Ghosh et al. (2020)
BL	HU	Bacterial ATP-3.8*10-14 M (One Plus 5 camera), Bacteria-105 CFU/mL	Camera	Calabretta et al. (2020)

(*Continued*)

TABLE 11.3 (Continued)

Techniques	Sample	Analyte-LOD	Component of Smartphone and accessory	Reference
BRET	HS	MicroRNA-400 pM	Camera	Chang et al. (2020)
CL, Chemiluminescence resonance energy transfer (CRET), Multiplexed immunoassay	HS	CEA, AFP and PSA-0.2 pg/mL, 3.2 pg/mL and 4.2 fg/mL (video mode); 2.1 pg/mL, 0.4 pg/mL and 3.9 pg/mL (image mode)	Camera	Li et al. (2020)
BRET, Microfluidic thread-based analytical devices (μTADs)	HB	anti-HIV/HA/ DEN-4.0 nM, 2.1 nM and 14.9 nM	Camera, 3D-printed lens adapter	Tomimuro et al. (2020)
Luminescence energy transfer (LRET), Paper-based sandwich immunoassay	HS	CEA-0.36 ng/mL	Camera	He et al. (2020)

displayed superb technical compatibility. Specifically, the detachable microscope lens is integrated into the smartphone camera in order to increase the magnification of the image (Dai et al., 2019). Using this method, it is possible to achieve an optical resolution comparable to traditional laboratory diagnostic microscopes, albeit with a lower price (Dai et al., 2019). In addition, image editing and processing applications and wireless components (Bluetooth and NFC) preinstalled on smartphones allow users to immediately process and transmit the images (Zarei, 2017; Zhang & Liu, 2016). Smartphones coupled with microscope lenses can become a very potential choice for microscopic imaging in developing countries (Koydemir & Ozcan, 2017). At date, several smartphone-based microscope sensors have been used for biomarker diagnosis and they can be divided into bright field microscope and fluorescence microscope (see Table 11.4).

For example, Cui et al. developed a portable smartphone-based brightfield microscope for the diagnosis of clinical biomarkers using a PoC platform based on an aggregation assay (Fig. 11.6C) (Cui et al., 2018). Polystirene (PS) microbeads were functionalized with antibodies and then integrated in a microfluidic device. In the absence of the target, the microbeads are free to flow through the microfluidic chamber as single particles. The presence of the target induced their aggregation and the formation of dimers. During their flow in the chamber the particles in the bound (dimers) and unbound (single) states are trapped inside designed wells, where they can be visualized through the smartphones. To perform the imaging process and counting of the particles specific algorithms and an app were developed. The device is able to detect PSA with a LOD of 0.125 ng mL^{-1} (3.67 pM) thus allowing its clinical quantification. The final platform is portable, cost-effective, high throughput and label-free displaying a great potential for diagnosis of other biomarkers (Cui et al., 2018). Wang's group proposed a brightfield smartphone imaging device for the detection of protein biomarkers using a simple microbubbling digital assay and magnetic enrichment technology (Chen et al., 2019) (Fig. 11.6D). The biosensor was designed for the detection of PSA and β-human chorionic gonadotropin (βhCG) two relevant biomarkers for postprostatectomy surveillance and early pregnancy detection. The sensing mechanism is based on the catalytic activity of platinum nanoparticles in presence of hydrogen peroxide which can produce microbubbles. Specifically, magnetic beads are functionalized with antibodies in order to detect the target and capture the platinum nanoparticles. Through the analysis and the detection of the microbubbles, the PoC device displays a LOD of 0.060 pg mL^{-1} (2.1 fM) and 2.84 pg mL^{-1} (0.034 mIU mL^{-1}) for PSA and βhCG, respectively, showing an overall sensitivity significantly higher than current central laboratory.

Goertz et al. reported a filter-less fluorescence microscopy platform combining an ultraviolet LED (light source), a smartphone (optical reader), and DNA single strands labeled with pyrene (recognition element) for the detection of oligonucleotide sequences (Goertz & White, 2015). Pyrene is a fluorescent molecule that displays a strong emission at 390 nm when it is free in solution (monomer state). Through $\pi-\pi$ interactions two pyrene molecules can interact and form a dimer complex (excimer) which shows a new visible emission peak at 490 nm and an associated larger Stoke shift. In order to exploit this effect for sensing applications, the pyrene molecules were coupled to specific DNA sequences designed as detection probes. Specifically, the presence of the target sequence induces the formation of a

TABLE 11.4 Microscope and surface plasmon

Methods	Biological fluids	Analyte-LOD	Reference
Fluorescence microscopy (FM)	N/A	TP3, TP3c, TT-N/A	Goertz et al. (2015)
Brightfield microcopy (BFM), Microbead aggregation	HS	PSA-0.125 ng/mL (3.67 pM)	Cui et al. (2018)
FM and BFM	Cell, tissue etc.	Cell and tissue observation, cell counting, plasmid transfection evaluations etc.	Dai et al. (2019)
FM, BFM and cross-polarized microscopy (CPM)	HB	DNA-a single nucleic acid binding fluorophore	Gordon et al. (2019)
Microbubbling digital assay, Brightfield smartphone imaging	HS	PSA-0.06 pg/mL (2.1 fM), bhCG-2.84 pg/mL (0.034 mIU/mL)	Chen et al. (2019)
FM, Microfluidic biochip	PBS	leukocytes-N/A	Sami et al. (2019)
FM, Autonomous capillary microfluidic chip (ACMC)	HS	cardiac Troponin I (cTnI)-94 pg/mL	Liang et al. (2019)
FM, Microfluidic biochip (μBiochip)	HB	CD64-N/A	Ozcan and Bashir (2019)
BFM	Semen	Sperm concentrarion and motility-N/A	Cheon et al. (2019)
FM, Paper-based μBiochip	Buffy coat blood	ROR1þ cancer cells-1 cell/μL (image)	Ulep et al. (2020)
FM, Nanoporous microneedles (nMNs)	Subcutaneous interstitial fluid from rats	estrogen (E2)- Sub nanogram/mL	Kang et al. (2020)
SPRi	N/A	Mouse IgG-nanomolar	Guner et al. (2017)
Grating-coupled SPR	Clinical injectable fluids	lipopolysaccharides-32.5 ng/mL(in water)	Zhang et al. (2018)
Spatially multiplexed SPR, Centrifugal Lab-on-a-Disc	HP	IgG-19.8 μg/mL	Miyazaki et al. (2018)
LSPR, Aptamer sensor	HB	Plasmodium falciparum Glutamate dehydrogenase (PfGDH)-264 pM	Sanjay et al. (2020)
SPR, Molecule imprinting	HS	Troponin I-7.1 ± 0.6 nM	Baldoneschi et al. (2020)
LSPR, μBiochip	HS	CA125-4.2 U/mL, CA15-3-0.87 U/mL	Fan et al. (2020)
SPR, Polymer multi-mode waveguide	HS	CRP-12.46 nM	Walter et al. (2020)

double-stranded structure where pyrene molecules are located in close proximity triggering the excimer signal. Dai et al. developed a handheld smartphone fluorescence microscope (HSFM) where a dual-functional polymer lens capable of imaging and filtering has been used for the first time (Fig. 11.6B) (Dai et al., 2019). The designed fluorescent module is so versatile that can be integrated with various brands and models of smartphones in order to support bright field and fluorescence imaging reaching a single-cell scale resolution (Dai et al., 2019). The HSFM system can successfully perform cell and tissue observations, cell counting, plasmid transfection evaluation, and superoxide production analysis. The collected clinical results are comparable with those obtained from a classic bulky optical microscope used in laboratory testing.

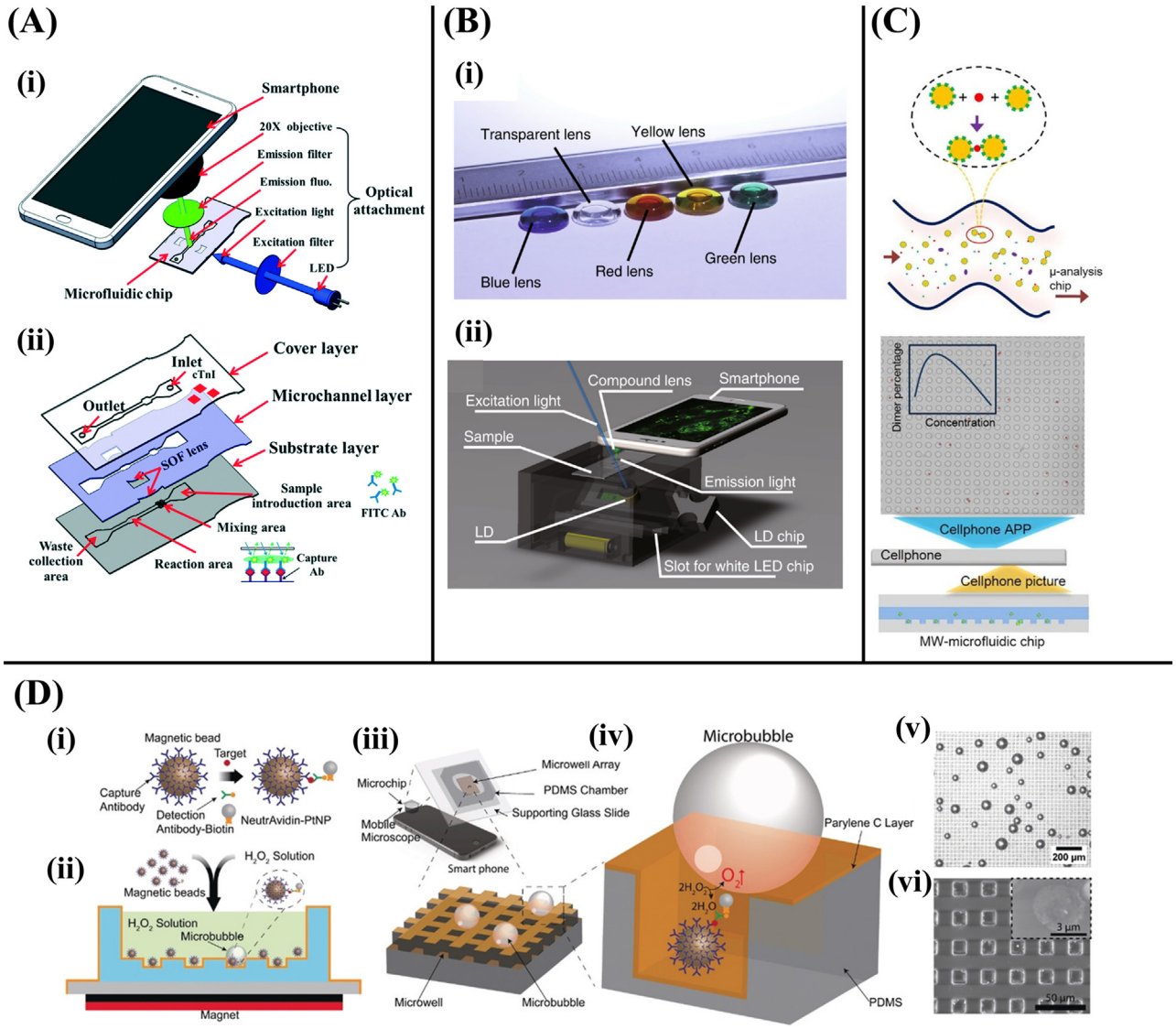

FIGURE 11.6 Different types of smartphone-based PoC microscopy biosensors. (A) (i) Scheme of the smartphone-app-ACMC platform (Fluo. indicates fluorescence. ACMC indicates autonomous capillary microfluidic chip); (ii) scheme of the ACMC (Liang et al., 2019). (B) Color compound lenses for a portable fluorescence microscope. (i) Different colors lenses were fabricated on glass disks to create various fluorescence filters; (ii) scheme of fluorescence imaging (Dai et al., 2019). (C) A portable smartphone PoC biosensor based on microwell-microfluidic chip and microbead aggregation assay. Scheme of the microbeads aggregation process (top); Statistics of the aggregated microbeads acquired by processing the photographs acquired by cellphone (Cui et al., 2018). (D) A smartphone-based bright-field microscopy biosensor for quantitation of femtomolar-level protein biomarkers detection integrating a simple microbubbling digital assay. (i) Magnetic beads functionalized with capture antibodies are used to capture PtNP-labeled target molecules; (ii) microbubbling signaling strategy; (iii) Microbubbling microchip with smart phone as readout device; (iv) oxygen microbubbles entrapped in the square microwell array serve as the visible digital signal; (v) Microscope image of the microbubbles on the microbubbling chip; (vi) scanning electron micrograph of a section of the microbubbling microchip (Chen et al., 2019). *From (A) (Liang et al., 2019); (B) (Dai et al., 2019); (C) (Cui et al., 2018); (D) (Chen et al., 2019).*

Recently, Ning's group proposed a portable smartphone-app-controlled fluorescence microscope for PoC diagnosis using a sandwich immunofluorescence assay (Liang et al., 2019) (Fig. 11.6A). This was combined and integrated into an autonomous capillary microfluidic chip (ACMC) and coupled with a smartphone. To avoid complex optical processing and bulky filters the smartphone-app-ACMC system was coupled with a self-aligned on-chip focusing (SOF) lenses. The platform was able to rapidly (within 12 min) monitor myocardial infarction biomarker cTnI with a LOD of 94 pg mL^{-1} in human serum. The portable palm-sized platform has good application prospects in the field of PoC devices, especially in resources-limited areas. Finally, Ulep et al. established a new fluorescence microscopy system

based on a smartphone and a capillary flow velocity assay which is integrated in a dual-layer paper-based microfluidic chip (Ulep et al., 2020). The optical device can simultaneously detect the ROR1 + cancer cells in complex buffy coat blood with a LOD of 1 cell μL^{-1} (fluorescence microscopy) and 0.1 cell μL^{-1} in the first 6 s assay (capillary flow velocity).

11.2.5 Surface plasmon resonance point-of-care biosensors based on smartphone camera

SPR is an important sensing platform widely used to study the interactions between bioreceptors and their targets. This is mainly due to its ability to support real-time and label-free measurements exploiting an optical readout (Homola, 2008; Pattnaik, 2005; Prabowo et al., 2018). For example, SPR biosensing platforms are very useful in pharmacological research to perform large-scale drug screening in order to characterize the binding between the drug and its target immobilized on the sensing surface (Rasooly & Herold, 2009). This biosensing platform exploits the different propagation of surface plasmons along the interface between a dielectric and a thin metal film (Mauriz et al., 2019). Specifically, these electromagnetic waves are produced by a light wave (excitation source) and they can propagate only in the proximity of a metal−water interface (Soler et al., 2019). Since their velocity is strongly affected by the refractive index of the interface, this parameter can be used to probe change on the surface monitoring the shift of the reflected light through a photodetector. For example, the binding between the selected bioreceptor and its specific target induces a change in the refractive index of the sensor surface allowing to track the formation of the biding complex. As a result of the advent of smartphones, SPR technology has been integrated into PoC platforms (Guner et al., 2017).

Guner et al. reported an SPRi system for in situ high-throughput detection using a smartphone readout (Guner et al., 2017). The grating coupled SPRi chip was fabricated by integrating an Au@Ag bimetallic Blu-ray disk and a disposable fluidic channel (Fig. 11.7A). The SPRi platform could detect mouse IgG with a nanomolar LOD. Instead, Miyazaki et al. developed a spatially multiplexed smartphone camera-based SPR biosensor with an integrated centrifugal lab-on-a-disk (LoaD) system (Miyazaki et al., 2018) (Fig. 11.7B). This innovative centrifugal LoaD platform can automatically realize plasma extraction and then distribute it evenly to five parallel channels for multiplexed sensing. The device can detect IgG with a LOD of 19.8 $\mu g\ mL^{-1}$ within 1 h. Fan et al. also proposed a multitesting unit smartphone biosensor based on LSPR integrated with microfluidic chip (Fan et al., 2020). This system can record 9 channels of signals at the same time, and it is easy to expand to more channels (up to a 72 units system). The device was successfully used to analyze CA125 and CA15−3 with a LOD of 4.2 and 0.87 U mL^{-1} in clinical serum samples. In addition to common immunoassays combined with SPR, the aptamer sensor is also easily integrated with SPR to improve sensitivity and stability. Sanjay and co-workers proposed a novel multichannel, optic fiber LSPR sensor for quantitative detection of *Plasmodium falciparum* Glutamate dehydrogenase (PfGDH) based on an inexpensive smartphone camera and flashlight (Sanjay et al., 2020) (Fig. 11.7C). The platform exhibited a LOD of 264 pM using 175 μL of blood samples, and the storage experiment under normal temperature shows that the sensor is quite stable within 20 days (see Table 11.4).

11.3 Summary and future perspectives

Here, we summarized the applications and progress in smartphone-based optical PoC devices for diagnostics of biomarkers during the past few years (2015−2020). We classified the smartphone-based PoC optical sensors according to the detection methods (colorimetry, fluorescence, luminescence, microscopy imaging, and SPR). It is clear how smartphones with their processing systems, high-resolution cameras, expandable storage capabilities, wireless transmission modules, and various apps can be used as excellent sensor signal detectors, processors, and data analysis tools. This allows smartphone-based optical PoC sensors to effectively overcome limitations of traditional laboratory-based devices and easily realize Real-time connectivity, Ease of specimen collection, Affordable prices, Sensitive and Specific analytical performance, User-friendliness, Rapid and Robust responses, an Equipment-free and Deliverable platform, that is REASSURED criteria stated by the WHO.

However, smartphone-based PoC optical biosensors still have some limitations and shortcomings that need to be solved. For the colorimetric PoC biosensors, the biggest problem is the image quality is easily affected by the ambient light, shooting angle, location, and built-in camera quality. It is thus necessary to develop smartphone accessories that guarantee always the same conditions for each photo, which in turn provide sensor-to-sensor reproducibility. For the smartphone-based fluorescence PoC biosensors, there are three main issues to solve: the auto-fluorescence of some substrates, the limitations of smartphone flash as excitation source, and the limitations of the smartphone camera to detect narrow-band fluorescence emission. Regarding the first issue, the use of pulse excitation, time-resolved fluorescent probes and near-infrared (NIR) or infrared probes can avoid the problem of substrate auto-fluorescence (Ulep et al., 2020).

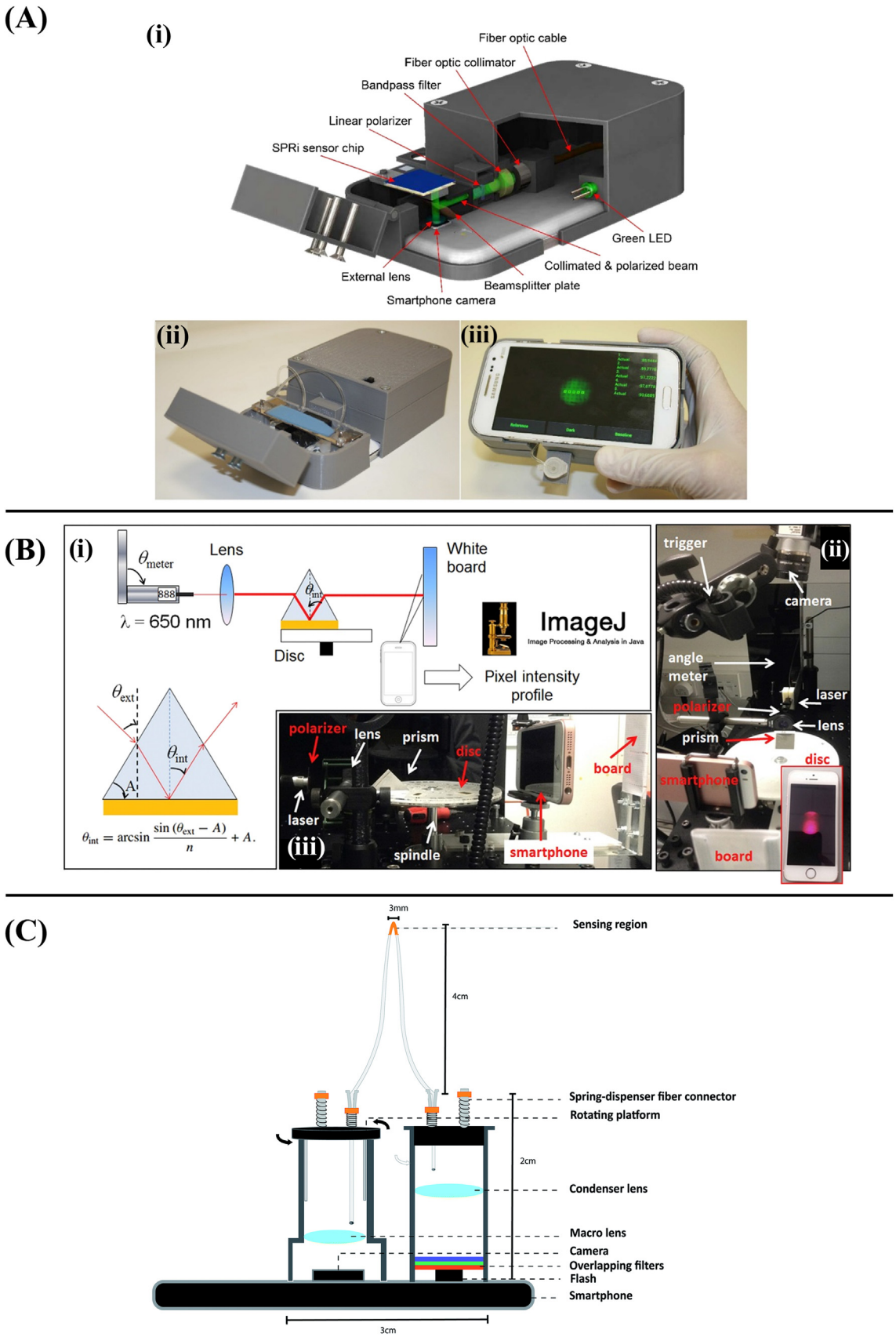

FIGURE 11.7 Smartphone-based SPR PoC biosensors. (A) Surface plasmon resonance imaging platform integrated with a smartphone. (i) and (ii) Scheme and photograph of the imaging apparatus; (iii) custom developed smartphone application for real-time and on-site monitoring of multiple sensing spots (Guner et al., 2017). (B) Label-free, spatially multiplexed SPR detection of immunoassays on a highly integrated centrifugal lab-on-a-disk platform. (i) Setup for disk-based SPR measurements. (ii) Frontal and (iii) lateral views of the centrifugal spin stand integrated to the surface plasmon generation optics. Inset: Magnified view of smartphone with camera (Miyazaki et al., 2018). (C) A smartphone-based fiber-optic aptasensor for label-free detection of plasmodium falciparum glutamate dehydrogenase. Cross-sectional view of the smartphone sensing platform (Sanjay et al., 2020). *From (A) (Guner et al., 2017), (B) (Miyazaki et al., 2018), (C) (Sanjay et al., 2020).*

Instead of the second two issues, connecting the smartphone (as a light source) with a contact CMOS fluorescence imager is a promising way to overcome those limitations (Ulep & Yoon, 2018).

In general, smartphone-based PoC sensors are promising solutions to bring advanced and sophisticated biomedical testing to resource-limited areas, doctors' offices, and even homes. We believe that with the development of 5G networks, artificial intelligence, edge computing, and other related technologies, smartphone-based PoC sensors will become widely spread.

Acknowledgments

A.M. acknowledge FEDER/Ministerio de Ciencia, Innovación y Universidades - Agencia Estatal de Investigación/_Project MAT2017-87202-P. A.M. also acknowledge ICN2 which is funded by the CERCA programme/Generalitat de Catalunya and supported by the Severo Ochoa Centres of Excellence programme that is funded by the Spanish Research Agency (AEI, grant no. SEV-2017-0706). A.M, L.H., A.I., C.P., R.A. and E.C. acknowledge Autonomous University of Barcelona (UAB) for their support. E.C. acknowledges Ministerio de Ciencia e Innovación of Spain and Fondo Social Europeo for the Fellowship PRE2018−084856 under the framework of "Plan Estatal de Investigación Científica y Técnica y de Innovación 2017−2020. L. H. acknowledges China Scholarship Council which is a non-profit institute affiliated with the Ministry of Education of the P. R. China. A.I. was supported by PROBIST postdoctoral fellowship funded by European Research Council (Marie Skłodowska-Curie grant agreement No. 754510).

References

Alawsi, T., & Al-Bawi, Z. (2019). *Engineering. Reports*, *1*, 1−30.

Alba-Patiño, A., Russell, S. M., Borges, M., Pazos-Pérez, N., Álvarez-Puebla, R. A., & De La Rica, R. (2020). Nanoparticle-based mobile biosensors for the rapid detection of sepsis biomarkers in whole blood. *Nanoscale Advances*, *2*, 1253−1260. Available from https://doi.org/10.1039/d0na00026d.

Alizadeh, N., Salimi, A., & Hallaj, R. (2018). Mimicking peroxidase activity of Co2(OH)2CO3-CeO2 nanocomposite for smartphone based detection of tumor marker using paper-based microfluidic immunodevice. *Talanta*, *189*, 100−110. Available from https://doi.org/10.1016/j.talanta.2018.06.034.

Álvarez-DIduk, R., Orozco, J., & Merkoçi, A. (2017). Paper strip-embedded graphene quantum dots: A screening device with a smartphone readout. *Scientific Reports*, *7*(1), 1−9. Available from https://doi.org/10.1038/s41598-017-01134-3.

Arts, R., Den Hartog, I., Zijlema, S. E., Thijssen, V., Van Der Beelen, S. H. E., & Merkx, M. (2016). Detection of antibodies in blood plasma using bioluminescent sensor proteins and a smartphone. *Analytical Chemistry*, *88*(8), 4525−4532. Available from https://doi.org/10.1021/acs.analchem.6b00534.

Aydindogan, E., Guler Celik, E., & Timur, S. (2018). Paper-based analytical methods for smartphone sensing with functional nanoparticles: Bridges from smart surfaces to global health. *Analytical Chemistry*, *90*(21), 12325−12333. Available from https://doi.org/10.1021/acs.analchem.8b03120.

Azim, M. A. U., Hasan, M., Ansari, I. H., & Nasreen, F. (2018). Chemiluminescence Immunoassay: Basic mechanism and applications. *Bangladesh Journal of Nuclear Medicine*, *18*(2), 171−178. Available from https://doi.org/10.3329/bjnm.v18i2.35240.

Baldoneschi, V., Palladino, P., Banchini, M., Minunni, M., & Scarano, S. (2020). Norepinephrine as new functional monomer for molecular imprinting: An applicative study for the optical sensing of cardiac biomarkers. *Biosensors and Bioelectronics*, *157*, 112161. Available from https://doi.org/10.1016/j.bios.2020.112161.

Barbosa, A. I., Gehlot, P., Sidapra, K., Edwards, A. D., & Reis, N. M. (2015). Portable smartphone quantitation of prostate specific antigen (PSA) in a fluoropolymer microfluidic device. *Biosensors and Bioelectronics*, *70*, 5−14. Available from https://doi.org/10.1016/j.bios.2015.03.006.

Bebb, H. B., & Williams, E. W. (1972). Photoluminescence I: Theory. *Semiconductors and Semimetals*, *8*, 181−320. Available from https://doi.org/10.1016/S0080-8784(08)62345-5.

Brangel, P., Sobarzo, A., Parolo, C., Miller, B. S., Howes, P. D., Gelkop, S., Lutwama, J. J., Dye, J. M., McKendry, R. A., Lobel, L., & Stevens, M. M. (2018). A serological point-of-care test for the detection of IgG antibodies against Ebola virus in human survivors. *ACS Nano*, *12*(1), 63−73. Available from https://doi.org/10.1021/acsnano.7b07021.

Cabral, H., Nishiyama, N., & Kataoka, K. (2011). Supramolecular nanodevices: From design validation to theranostic nanomedicine. *Accounts of Chemical Research*, *44*(10), 999−1008. Available from https://doi.org/10.1021/ar200094a.

Calabretta, M. M., Álvarez-Diduk, R., Michelini, E., Roda, A., & Merkoçi, A. (2020). *Biosensors & Bioelectronics*, *150*.

Calabria, D., Caliceti, C., Zangheri, M., Mirasoli, M., Simoni, P., & Roda, A. (2017). Smartphone−based enzymatic biosensor for oral fluid L-lactate detection in one minute using confined multilayer paper reflectometry. *Biosensors and Bioelectronics*, *94*, 124−130. Available from https://doi.org/10.1016/j.bios.2017.02.053.

Cevenini, L., Calabretta, M. M., Tarantino, G., Michelini, E., & Roda, A. (2016). Smartphone-interfaced 3D printed toxicity biosensor integrating bioluminescent "sentinel cells". *Sensors Actuators, B Chemical*, *225*, 249−257. Available from https://doi.org/10.1016/j.snb.2015.11.017.

Chang, D., Kim, K. T., Lindberg, E., & Winssinger, N. (2020). Smartphone DNA or RNA sensing using semisynthetic luciferase-based logic device. *ACS Sensors*, *5*(3), 807−813. Available from https://doi.org/10.1021/acssensors.9b02454.

Chen, H., Li, Z., Zhang, L., Sawaya, P., Shi, J., & Wang, P. (2019). Quantitation of Femtomolar-Level Protein Biomarkers Using a Simple Microbubbling Digital Assay and Bright-Field Smartphone Imaging. *Angewandte Chemie*, *131*, 14060−14066.

Chen, L., Zhang, C., & Xing, D. (2016). *Sensors Actuators*.

Cheon, W. H., Park, H. J., Park, M. J., Lim, M. Y., Park, J. H., Kang, B. J., & Park, N. C. (2019). Validation of a smartphone-based, computer-assisted sperm analysis system compared with laboratory-based manual microscopic semen analysis and computer-assisted semen analysis, pp. 380–387.

Clough, J. M., Balan, A., Van Daal, T. L. J., & Sijbesma, R. P. (2016). probing force with mechanobase-induced chemiluminescence. *Angewandte Chemie - International Edition*, *55*(4), 1445–1449. Available from https://doi.org/10.1002/anie.201508840.

Colburn, W. A., & Lee, J. W. (2003). Biomarkers, validation and pharmacokinetic-pharmacodynamic modelling. *Clinical Pharmacokinetics*, *42*(12), 997–1022. Available from https://doi.org/10.2165/00003088-200342120-00001.

Coleman, B., Coarsey, C., Kabir, M. A., & Asghar, W. (2019). Point-of-care colorimetric analysis through smartphone video. *Sensors Actuators, B Chemical*, *282*, 225–231. Available from https://doi.org/10.1016/j.snb.2018.11.036.

Cui, W., He, M., Mu, L., Lin, Z., Wang, Y., Pang, W., Reed, M., & Duan, X. (2018). Cellphone-enabled microwell-based microbead aggregation assay for portable biomarker detection. *ACS Sensors*, *3*(2), 432–440. Available from https://doi.org/10.1021/acssensors.7b00866.

Dai, B., Jiao, Z., Zheng, L., Bachman, H., Fu, Y., Wan, X., Zhang, Y., Huang, Y., Han, X., Zhao, C., Huang, T. J., Zhuang, S., & Zhang, D. (2019). Colour compound lenses for a portable fluorescence microscope. *Light: Science and Applications*, *8*(1), 1–13. Available from https://doi.org/10.1038/s41377-019-0187-1.

Devarajan, P., Mishra, J., Supavekin, S., Patterson, L. T., & Potter, S. S. (2003). Gene expression in early ischemic renal injury: Clues towards pathogenesis, biomarker discovery, and novel therapeutics. *Molecular Genetics and Metabolism*, *80*(4), 365–376. Available from https://doi.org/10.1016/j.ymgme.2003.09.012.

Diagnosis, P., Mahato, K., Prasad, A., Maurya, P. K., & Chandra, P. (2016). Nanobiosensors: Next generation point-of-care biomedical devices for personalized diagnosis. *Journal of Analytical & Bioanalytical Techniques*, *7*(2). Available from https://doi.org/10.4172/2155-9872.1000e125.

Dirks, R. M., & Pierce, N. A. (2004). Triggered amplification by hybridization chain reaction. *Proceedings of the National Academy of Sciences of the United States of America*, *101*(43), 15275–15278. Available from https://doi.org/10.1073/pnas.0407024101.

Dong, M., Wu, J., Ma, Z., Peretz-Soroka, H., Zhang, M., Komenda, P., … Lin, F. (2017). Rapid and low-cost CRP measurement by integrating a paper-based microfluidic immunoassay with smartphone (CRP-Chip). *Sensors (Switzerland)*, *17*, 1–13. Available from https://doi.org/10.3390/s17040684.

Dutta, S., Saikia, K., & Nath, P. (2016). Smartphone based LSPR sensing platform for bio-conjugation detection and quantification. *RSC Advances*, *6*(26), 21871–21880. Available from https://doi.org/10.1039/c6ra01113f.

Fan, Z., Geng, Z., Fang, W., Lv, X., Su, Y., Wang, S., & Chen, H. (2020). Smartphone biosensor system with multi-testing unit based on localized surface plasmon resonance integrated with microfluidics chip. *Sensors (Switzerland)*, *20*(2), 1–13. Available from https://doi.org/10.3390/s20020446.

Fereja, T. H., Kitte, S. A., Gao, W., Yuan, F., Snizhko, D., Qi, L., … Xu, G. (2019). Artesunate-luminol chemiluminescence system for the detection of hemin. *Talanta*, *204*, 379–385. Available from https://doi.org/10.1016/j.talanta.2019.06.007.

Fu, L., Qian, Y., Zhou, J., Zheng, L., & Wang, Y. (2020). Fluorescence-based quantitative platform for ultrasensitive food allergen detection: From immunoassays to DNA sensors. *Comprehensive Reviews in Food Science and Food Safety*, *19*(6), 3343–3364. Available from https://doi.org/10.1111/1541-4337.12641.

Ghosh, S., Aggarwal, K., Vinitha, T. U., Nguyen, T., Han, J., & Ahn, C. H. (2020). A new microchannel capillary flow assay (MCFA) platform with lyophilized chemiluminescence reagents for a smartphone-based POCT detecting malaria. *Microsystems & Nanoengineering*, *6*. Available from https://doi.org/10.1038/s41378-019-0108-8.

Goertz, J. P., & White, I. M. (2015). Smartphone-enabled filterless fluorescence assay utilizing the pyrene excimer. *Optics and Biophotonics in Low-Resource Settings*, *9314*. Available from https://doi.org/10.1117/12.2080225.

Gold, L., Ayers, D., Bertino, J., Bock, C., Bock, A., Brody., … Zichi, D. (2010). Aptamer-Based Multiplexed Proteomic Technology for Biomarker Discovery. *PLoS One*, 5.

Gordon, P., Venancio, V. P., Mertens-Talcott, S. U., & Coté, G. (2019). Portable bright-field, fluorescence, and cross-polarized microscope toward point-of-care imaging diagnostics. *Journal of Biomedical Optics*, *24*, 1. Available from https://doi.org/10.1117/1.jbo.24.9.096502.

Gowthami, S., & Venkatakrishnakumar, S. (2016). *International Journal of Scientific Engineering Applied. Science*, *3*, 2395–3470.

Guner, H., Ozgur, E., Kokturk, G., Celik, M., Esen, E., Topal, A. E., Ayas, S., Uludag, Y., Elbuken, C., & Dana, A. (2017). A smartphone based surface plasmon resonance imaging (SPRi) platform for on-site biodetection. *Sensors and Actuators, B: Chemical*, *239*, 571–577. Available from https://doi.org/10.1016/j.snb.2016.08.061.

Guo, T., Patnaik, R., Kuhlmann, K., Rai, A. J., & Sia, S. K. (2015). Smartphone dongle for simultaneous measurement of hemoglobin concentration and detection of HIV antibodies. *Lab on a Chip*, *15*(17), 3514–3520. Available from https://doi.org/10.1039/c5lc00609k.

Guo, X., Zong, L., Jiao, Y., Han, Y., Zhang, X., Xu, J., Li, L., Zhang, C. W., Liu, Z., Ju, Q., Liu, J., Xu, Z., Yu, H. D., & Huang, W. (2019). Signal-enhanced detection of multiplexed cardiac biomarkers by a paper-based fluorogenic immunodevice integrated with zinc oxide nanowires. *Analytical Chemistry*, *91*(14), 9300–9307. Available from https://doi.org/10.1021/acs.analchem.9b02557.

Gupta, R., Peveler, W. J., Lix, K., & Algar, W. R. (2019). Comparison of semiconducting polymer dots and semiconductor quantum dots for smartphone-based fluorescence assays. *Analytical Chemistry*, *91*(17), 10955–10960. Available from https://doi.org/10.1021/acs.analchem.9b02881.

Gurcan, M. N., Boucheron, L. E., Can, A., Madabhushi, A., Rajpoot, N. M., & Yener, B. (2009). Histopathological image analysis: A review. *IEEE Reviews in Biomedical Engineering*, *2*, 147–171. Available from https://doi.org/10.1109/RBME.2009.2034865.

Hainsworth, D. P., Gangula, A., Ghoshdastidar, S., Kannan, R., & Upendran, A. (2020). Diabetic retinopathy screening using a gold nanoparticle–based paper strip assay for the at-home detection of the urinary biomarker 8-hydroxy-2′-deoxyguanosine. *American Journal of Ophthalmology*. Available from https://doi.org/10.1016/j.ajo.2020.01.032.

Hampel, H., O'Bryant, S. E., Molinuevo, J. L., Zetterberg, H., Masters, C. L., Lista, S., Kiddle, S. J., Batrla, R., & Blennow, K. (2018). Blood-based biomarkers for Alzheimer disease: Mapping the road to the clinic. *Nature Reviews Neurology*, *14*(11), 639–652. Available from https://doi.org/10.1038/s41582-018-0079-7.

He, M., Shang, N., Shen, L., & Liu, Z. (2020). A paper-supported sandwich immunosensor based on upconversion luminescence resonance energy transfer for the visual and quantitative determination of a cancer biomarker in human serum. *Analyst*, *145*(12), 4181–4187.

Heidt, B., Siqueira, W. F., Eersels, K., Diliën, H., Grinsven., Fujiwara, R. T., & Cleij, T. J. (2020). *Biosensors*, *10*.

Hernández-Neuta, I., Neumann, F., Brightmeyer, J., Ba Tis, T., Madaboosi, N., Wei, Q., Ozcan, A., & Nilsson, M. (2019). Smartphone-based clinical diagnostics: towards democratization of evidence-based health care. *Journal of Internal Medicine*, *285*(1), 19–39. Available from https://doi.org/10.1111/joim.12820.

Homola, J. (2008). Surface plasmon resonance sensors for detection of chemical and biological species. *Chemical Reviews*, *108*(2), 462–493. Available from https://doi.org/10.1021/cr068107d.

Horvath, A. R. (2013). From evidence to best practice in laboratory medicine. *Clinical Biochemist Reviews*, *34*(2), 47–60. Available from http://www.aacb.asn.au/documents/item/1208.

Hosu, O., Ravalli, A., Lo Piccolo, G. M., Cristea, C., Sandulescu, R., & Marrazza, G. (2017). Smartphone-based immunosensor for CA125 detection. *Talanta*, *166*, 234–240. Available from https://doi.org/10.1016/j.talanta.2017.01.073.

Hou, L., Qin, Y., Li, J., Qin, S., Huang, Y., Lin, T., Guo, L., Ye, F., & Zhao, S. (2019). A ratiometric multicolor fluorescence biosensor for visual detection of alkaline phosphatase activity via a smartphone. *Biosensors and Bioelectronics*, *143*, 111605. Available from https://doi.org/10.1016/j.bios.2019.111605.

Hu, L. M., Luo, K., Xia, J., Xu, G. M., Wu, C. H., Han, J. J., Zhang, G. G., Liu, M., & Lai, W. H. (2017). Advantages of time-resolved fluorescent nanobeads compared with fluorescent submicrospheres, quantum dots, and colloidal gold as label in lateral flow assays for detection of ractopamine. *Biosensors and Bioelectronics*, *91*, 95–103. Available from https://doi.org/10.1016/j.bios.2016.12.030.

Idili, A., Porchetta, A., Amodio, A., Vallée-Bélisle, A., & Ricci, F. (2015). Controlling hybridization chain reactions with pH. *Nano Letters*, *15*(8), 5539–5544. Available from https://doi.org/10.1021/acs.nanolett.5b02123.

Jain, K. K. (2010). *The handbook of biomarkers*. Springer.

Kanakasabapathy, M. K., Pandya, H. J., Draz, M. S., Chug, M. K., Sadasivam, M., Kumar, S., Etemad, B., Yogesh, V., Safavieh, M., Asghar, W., Li, J. Z., Tsibris, A. M., Kuritzkes, D. R., & Shafiee, H. (2017). Rapid, label-free CD4 testing using a smartphone compatible device. *Lab on a Chip*, *17*(17), 2910–2919. Available from https://doi.org/10.1039/c7lc00273d.

Kanchi, S., Sabela, M. I., Mdluli, P. S., Inamuddin., & Bisetty, K. (2018). Smartphone based bioanalytical and diagnosis applications: A review. *Biosensors and Bioelectronics*, *102*, 136–149. Available from https://doi.org/10.1016/j.bios.2017.11.021.

Kang, Y. E., Seong, K. Y., Yim, S. G., Lee, Y., An, S. M., Kim, S. C., … Yang, S. Y. (2020). Nanochannel-driven rapid capture of sub-nanogram level biomarkers for painless preeclampsia diagnosis. *Biosensors and Bioelectronics*, *163*, 112281. Available from https://doi.org/10.1016/j.bios.2020.112281.

Karlsen, H., & Dong, T. (2017). Smartphone-based rapid screening of urinary biomarkers. *IEEE Transactions on Biomedical Circuits and Systems*, *11*(2), 455–463. Available from https://doi.org/10.1109/TBCAS.2016.2633508.

Katoba, J., Kuupiel, D., & Mashamba-Thompson, T. P. (2019). Toward improving accessibility of point-of-care diagnostic services for maternal and child health in low-and middle-income countries. *Point of Care*, *18*(1), 17–25. Available from https://doi.org/10.1097/POC.0000000000000180.

Kelley, S. O., Mirkin, C. A., Walt, D. R., Ismagilov, R. F., Toner, M., & Sargent, E. H. (2014). Advancing the speed, sensitivity and accuracy of biomolecular detection using multi-length-scale engineering. *Nature Nanotechnology*, *9*(12), 969–980. Available from https://doi.org/10.1038/nnano.2014.261.

Kim, D. W., Jeong, K. Y., & Yoon, H. C. (2019). *Smartphone-based medical diagnostics with microfluidic devices*. *Smartphone Based Medical Diagnostics* (pp. 103–128). Elsevier. Available from https://doi.org/10.1016/B978-0-12–817044-1.00007–7.

Kim, S. C., Jalal, U. M., Im, S. B., Ko, S., & Shim, J. S. (2017). A smartphone-based optical platform for colorimetric analysis of microfluidic device. *Sensors and Actuators, B: Chemical*, *239*, 52–59. Available from https://doi.org/10.1016/j.snb.2016.07.159.

Ko, J., Hemphill, M. A., Gabrieli, D., Wu, L., Yelleswarapu, V., Lawrence, G., Pennycooke, W., Singh, A., Meaney, D. F., & Issadore, D. (2016). Smartphone-enabled optofluidic exosome diagnostic for concussion recovery. *Scientific Reports*, *6*, 1–12. Available from https://doi.org/10.1038/srep31215.

Komatsu, N., Terai, K., Imanishi, A., Kamioka, Y., Sumiyama, K., Jin, T., Okada, Y., Nagai, T., & Matsuda, M. (2018). *Scientific Reports*, *8*, 1–14.

Kou, X., Tong, L., Shen, Y., Zhu, W., Yin, L., Huang, S., … Ouyang, G. (2020). Smartphone-assisted robust enzymes@ MOFs-based paper biosensor for point-of-care detection. *Biosensors and Bioelectronics*, *156*, 112095.

Koydemir, H. C., Gorocs, Z., Tseng, D., Cortazar, B., Feng, S., Chan, R. Y. L., Burbano, J., McLeod, E., & Ozcan, A. (2015). Rapid imaging, detection and quantification of *Giardia lamblia* cysts using mobile-phone based fluorescent microscopy and machine learning. *Lab on a Chip*, *15*(5), 1284–1293. Available from https://doi.org/10.1039/c4lc01358a.

Koydemir, H. C., & Ozcan, A. (2017). Mobile phones create new opportunities for microbiology research and clinical applications. *Future Microbiology*, *12*(8), 641–644. Available from https://doi.org/10.2217/fmb-2017-0046.

Kręcisz, P., Czarnecka, K., Królicki, L., Mikiciuk-Olasik, E., & Szymański, P. (2021). Radiolabeled peptides and antibodies in medicine. *Bioconjugate Chemistry*, *32*(1), 25–42. Available from https://doi.org/10.1021/acs.bioconjchem.0c00617.

Kricka, L. J. (1996). *Immunoassay* (pp. 337−353). Academic Press, Inc. Available from https://doi.org/10.1016/B978-0-12−214730-2.50016−9.

Kulasingam, V., & Diamandis, E. P. (2008). Strategies for discovering novel cancer biomarkers through utilization of emerging technologies. *Nature Clinical Practice. Oncology*, *5*(10), 588−599. Available from https://doi.org/10.1038/ncponc1187.

Kwon, L., Long, K. D., Wan, Y., Yu, H., & Cunningham, B. T. (2016). Medical diagnostics with mobile devices: Comparison of intrinsic and extrinsic sensing. *Biotechnology Advances*, *34*(3), 291−304. Available from https://doi.org/10.1016/j.biotechadv.2016.02.010.

Land, K. J., Boeras, D. I., Chen, X. S., Ramsay, A. R., & Peeling, R. W. (2019). REASSURED diagnostics to inform disease control strategies, strengthen health systems and improve patient outcomes. *Nature Microbiology*, *4*(1), 46−54. Available from https://doi.org/10.1038/s41564-018-0295-3.

Lee, S. Y., Lin, M., & Lee, A. (2017). *7*.

Li, F., Guo, L., Li, Z., He, J., & Cui, H. (2020). Temporal-spatial-color multiresolved chemiluminescence imaging for multiplex immunoassays using a smartphone coupled with microfluidic chip. *Analytical Chemistry*, *92*(10), 6827−6831. Available from https://doi.org/10.1021/acs.analchem.0c01405.

Li, M., & Diamandis, E. P. (2016). Technology-driven diagnostics: From smart doctor to smartphone. *Critical Reviews in Clinical Laboratory Sciences*, *53*(4), 268−276. Available from https://doi.org/10.3109/10408363.2016.1149689.

Li, M., Shi, Z. Z., Fang, C., Gao, A. X., Li, C. M., & Yu, L. (2016). *Analytica Chimica Acta*.

Li, Y., Yang, P., Lei, N., Ma, Y., Ji, Y., Zhu, C., & Wu, Y. (2018). Assembly of DNA-templated bioluminescent modules for amplified detection of protein biomarkers. *Analytical Chemistry*, *90*(19), 11495−11502. Available from https://doi.org/10.1021/acs.analchem.8b02734.

Lian, X., Miao, T., Xu, X., Zhang, C., & Yan, B. (2017). Eu3 + functionalized Sc-MOFs: Turn-on fluorescent switch for ppb-level biomarker of plastic pollutant polystyrene in serum and urine and on-site detection by smartphone. *Biosensors and Bioelectronics*, *97*, 299−304. Available from https://doi.org/10.1016/j.bios.2017.06.018.

Liang, C., Liu, Y., Niu, A., Liu, C., Li, J., & Ning, D. (2019). Smartphone-app based point-of-care testing for myocardial infarction biomarker cTnI using an autonomous capillary microfluidic chip with self-aligned on-chip focusing (SOF) lenses. *Lab on a Chip*, *19*(10), 1797−1807. Available from https://doi.org/10.1039/c9lc00259f.

Lim, W. Y., Thevarajah, T. M., Goh, B. T., & Khor, S. M. (2019). Paper microfluidic device for early diagnosis and prognosis of acute myocardial infarction via quantitative multiplex cardiac biomarker detection. *Biosensors and Bioelectronics*, *128*, 176−185. Available from https://doi.org/10.1016/j.bios.2018.12.049.

Lippert, S., & Goetze, J. P. (2010). C-type natriuretic-derived peptides as biomarkers in human disease. *Biomarkers in Medicine*, *4*(4), 631−639. Available from https://doi.org/10.2217/bmm.10.67.

Lippi, G., & Mattiuzzi, C. (2015). The biomarker paradigm: Between diagnostic efficiency and clinical efficacy. *Polskie Archiwum Medycyny Wewnetrznej*, *125*(4), 282−288. Available from https://doi.org/10.20452/pamw.2788.

Long, K. D., Woodburn, E. V., Le, H. M., Shah, U. K., Lumetta, S. S., & Cunningham, B. T. (2017). Multimode smartphone biosensing: The transmission, reflection, and intensity spectral (TRI)-analyzer. *Lab on a Chip*, *17*(19), 3246−3257. Available from https://doi.org/10.1039/c7lc00633k.

Ludwig, J. A., & Weinstein, J. N. (2005). Biomarkers in cancer staging, prognosis and treatment selection. *Nature Reviews. Cancer*, *5*(11), 845−856. Available from https://doi.org/10.1038/nrc1739.

Mamas, M., Dunn, W. B., Neyses, L., & Goodacre, R. (2011). The role of metabolites and metabolomics in clinically applicable biomarkers of disease. *Archives of Toxicology*, *85*(1), 5−17. Available from https://doi.org/10.1007/s00204-010-0609-6.

Mao, X., & Huang, T. J. (2012). Microfluidic diagnostics for the developing world. *Lab on a Chip*, *12*(8), 1412−1416. Available from https://doi.org/10.1039/c2lc90022j.

Martinez, A. W., Phillips, S. T., Carrilho, E., Thomas, S. W., Sindi, H., & Whitesides, G. M. (2008). Simple telemedicine for developing regions: Camera phones and paper-based microfluidic devices for real-time, off-site diagnosis. *Analytical Chemistry*, *80*(10), 3699−3707. Available from https://doi.org/10.1021/ac800112r.

Mauriz, E., Dey, P., & Lechuga, L. M. (2019). Advances in nanoplasmonic biosensors for clinical applications. *Analyst*, *144*(24), 7105−7129. Available from https://doi.org/10.1039/c9an00701f.

Mayeux, R. (2004). Biomarkers: Potential uses and limitations. *NeuroRx: The Journal of the American Society for Experimental NeuroTherapeutics*, *1*(2), 182−188. Available from https://doi.org/10.1602/neurorx.1.2.182.

McCracken, K. E., & Yoon, J. Y. (2016). Recent approaches for optical smartphone sensing in resource-limited settings: a brief review. *Analytical Methods*.

Mckeever, S. W. S., & Chen, R. (1997). Luminescence models. *Radiation Measurements*, *27*(5−6), 625−661. Available from https://doi.org/10.1016/S1350-4487(97)00203-5.

Merli, D., La Cognata, S., Balduzzi, F., Miljkovic, A., Toma, L., & Amendola, V. (2018). A smart supramolecular device for the detection of t,t-muconic acid in urine†. *New Journal of Chemistry*, *42*, 15460−15465. Available from https://doi.org/10.1039/c8nj02156b.

Miao, W. (2008). Electrogenerated chemiluminescence and its biorelated applications. *Chemical Reviews*, *108*(7), 2506−2553. Available from https://doi.org/10.1021/cr068083a.

Miller, B. S., Parolo, C., Turbé, V., Keane, C. E., Gray, E. R., & McKendry, R. A. (2018). Quantifying biomolecular binding constants using video paper analytical devices. *Chemistry - A European Journal*, *24*(39), 9783−9787. Available from https://doi.org/10.1002/chem.201802394.

Miyazaki, C. M., Kinahan, D. J., Mishra, R., Mangwanya, F., Kilcawley, N., Ferreira, M., & Ducrée, J. (2018). Label-free, spatially multiplexed SPR detection of immunoassays on a highly integrated centrifugal Lab-on-a-Disc platform. *Biosensors and Bioelectronics*, *119*, 86−93. Available from https://doi.org/10.1016/j.bios.2018.07.056.

Neill, D. L., Chang, Y. C., Chen, W., Li, L., & Xian, M. (2019). A smartphone based device for the detection of sulfane sulfurs in biological systems. *Sensors and Actuators B: Chemical*, *292*, 263−269. Available from https://doi.org/10.1016/j.snb.2019.04.099.

Ozcan, A., & Bashir, R. (2019). Smartphone-imaged microfluidic biochip for measuring CD64 expression from whole blood. *Analyst*, *144*, 3925−3935. Available from https://doi.org/10.1039/c9an00532c.

Parolo, C., & Merkoçi, A. (2013). Paper-based nanobiosensors for diagnostics. *Chemical Society Reviews*, *42*(2), 450−457. Available from https://doi.org/10.1039/c2cs35255a.

Parolo, C., Sena-Torralba, A., Bergua, J. F., Calucho, E., Fuentes-Chust, C., Hu, L., Rivas, L., Álvarez-Diduk, R., Nguyen, E. P., Cinti, S., Quesada-González, D., & Merkoçi, A. (2020). Tutorial: design and fabrication of nanoparticle-based lateral-flow immunoassays. *Nature Protocols*, *15*(12), 3788−3816. Available from https://doi.org/10.1038/s41596-020-0357-x.

Pattnaik, P. (2005). Surface plasmon resonance: Applications in understanding receptor-ligand interaction. *Applied Biochemistry and Biotechnology*, *126*(2), 79−92. Available from https://doi.org/10.1385/abab:126:2:079.

Prabowo, B. A., Purwidyantri, A., & Liu, K.-C. (2018). Surface Plasmon Resonance Optical Sensor: A Review on Light Source Technology. *Biosensors-Basel*, *8*(3), 80.

Prasad, A., Hasan, S. M. A., Grouchy, S., & Gartia, M. R. (2019). DNA microarray analysis using a smartphone to detect the BRCA-1 gene. *Analyst*, *144*(1), 197−205. Available from https://doi.org/10.1039/c8an01020j.

Priye, A., Bird, S. W., Light, Y. K., Ball, C. S., Negrete, O. A., & Meagher, R. J. (2017). A smartphone-based diagnostic platform for rapid detection of Zika, chikungunya, and dengue viruses. *Scientific Reports*, *7*, 1−11. Available from https://doi.org/10.1038/srep44778.

Purohit, B., Kumar, A., Mahato, K., & Chandra, P. (2020). Smartphone-assisted personalized diagnostic devices and wearable sensors. *Current Opinion in Biomedical Engineering*, *13*, 42−50. Available from https://doi.org/10.1016/j.cobme.2019.08.015.

Qin, S. J., & Yan, B. (2018). The point-of-care colorimetric detection of the biomarker of phenylamine in the human urine based on Tb3 + functionalized metal-organic framework. *Analytica Chimica Acta*, *1012*, 82−89. Available from https://doi.org/10.1016/j.aca.2018.01.041.

Quesada-González, D., & Merkoçi, A. (2017). Mobile phone-based biosensing: An emerging "diagnostic and communication" technology. *Biosensors and Bioelectronics*, *92*, 549−562. Available from https://doi.org/10.1016/j.bios.2016.10.062.

Quimbar, M. E., Krenek, K. M., & Lippert, A. R. (2016). A chemiluminescent platform for smartphone monitoring of H_2O_2 in human exhaled breath condensates. *Methods*, *109*, 123−130. Available from https://doi.org/10.1016/j.ymeth.2016.05.017.

Ramakrishan, S. K., Martin Fernandez, M., Cloitre, T., Agarwal, V., Cuisinier, F. J. G., & Gergely, C. (2018). Porous silicon microcavities redefine colorimetric ELISA sensitivity for ultrasensitive detection of autoimmune antibodies. *Sensors and Actuators B: Chemical*, *272*, 211−218. Available from https://doi.org/10.1016/j.snb.2018.05.154.

Rasooly, A., & Herold, K. E. (2009). Biosensors and biodetection: methods and protocols. *Methods in Molecular Biology*, 503.

Roda, A., & Guardigli, M. (2012). Analytical chemiluminescence and bioluminescence: Latest achievements and new horizons. *Analytical and Bioanalytical Chemistry*, *402*(1), 69−76. Available from https://doi.org/10.1007/s00216-011-5455-8.

Roda, A., Michelini, E., Cevenini, L., Calabria, D., Calabretta, M. M., & Simoni, P. (2014). Integrating biochemiluminescence detection on smartphones: Mobile chemistry platform for point-of-need analysis. *Analytical Chemistry*, *86*(15), 7299−7304. Available from https://doi.org/10.1021/ac502137s.

Roda, A., Michelini, E., Zangheri, M., Di Fusco, M., Calabria, D., & Simoni, P. (2016). Smartphone-based biosensors: A critical review and perspectives. *TrAC - Trends in Analytical Chemistry*, *79*, 317−325. Available from https://doi.org/10.1016/j.trac.2015.10.019.

Rong, Z., Wang, Q., Sun, N., Jia, X., Wang, K., Xiao, R., & Wang, S. (2019). Smartphone-based fluorescent lateral flow immunoassay platform for highly sensitive point-of-care detection of Zika virus nonstructural protein 1. *Analytica Chimica Acta*, *1055*, 140−147. Available from https://doi.org/10.1016/j.aca.2018.12.043.

Rorke, L. B. (1997). Pathologic diagnosis as the gold standard. *Cancer*, *79*(4), 665−667. Available from https://doi.org/10.1002/(SICI)1097-0142(19970215)79:4 < 665::AID-CNCR1 > 3.0.CO;2-D.

Ruecha, N., Rangkupan, R., Rodthongkum, N., & Chailapakul, O. (2014). Novel paper-based cholesterol biosensor using graphene/polyvinylpyrrolidone/polyaniline nanocomposite. *Biosensors and Bioelectronics*, *52*, 13−19. Available from https://doi.org/10.1016/j.bios.2013.08.018.

Russell, S. M., Alba-Patiño, A., Borges, M., & de la Rica, R. (2019). Multifunctional motion-to-color janus transducers for the rapid detection of sepsis biomarkers in whole blood. *Biosensors and Bioelectronics*, *140*, 111346. Available from https://doi.org/10.1016/j.bios.2019.111346.

Sanjay, M., Singh, N. K., Ngashangva, L., & Goswami, P. (2020). A smartphone-based fiber-optic aptasensor for label-free detection of: *Plasmodium falciparum* glutamate dehydrogenase. *Analytical Methods*, *12*(10), 1333−1341. Available from https://doi.org/10.1039/c9ay02406a.

Sami, M. A., Wagner, K., Parikh, P., & Hassan, U. (2019). Smartphone based microfluidic biosensor for leukocyte quantification at the point-of-care. *2019 IEEE Healthcare Innovation Point-of-Care Technologies. HI-POCT 2019*, 119−122. Available from https://doi.org/10.1109/HI-POCT45284.2019.8962697.

Schwarzenbach, H., Hoon, D. S. B., & Pantel, K. (2011). Cell-free nucleic acids as biomarkers in cancer patients. *Nature Reviews. Cancer*, *11*(6), 426−437. Available from https://doi.org/10.1038/nrc3066.

Sharma, S., Zapatero-Rodríguez, J., Estrela, P., & O'Kennedy, R. (2015). Point-of-Care diagnostics in low resource settings: Present status and future role of microfluidics. *Biosensors*, *5*(3), 577−601. Available from https://doi.org/10.3390/bios5030577.

Shaw, L. M., Korecka, M., Clark, C. M., Lee, V. M. Y., & Trojanowski, J. Q. (2007). Biomarkers of neurodegeneration for diagnosis and monitoring therapeutics. *Nature Reviews. Drug Discovery*, *6*(4), 295−303. Available from https://doi.org/10.1038/nrd2176.

Shin, J., Choi, S., Yang, J. S., Song, J., Choi, J. S., & Jung, H. I. (2017). Smart forensic phone: Colorimetric analysis of a bloodstain for age estimation using a smartphone. *Sensors and Actuators B: Chemical*, *243*, 221–225.

Simon, R. (2014). Biomarker based clinical trial design. *Chinese Clinical Oncology*, *3*(3), 1–8. Available from https://doi.org/10.3978/j.issn.2304-3865.2014.02.03.

Soler, M., Huertas, C. S., & Lechuga, L. M. (2019). Label-free plasmonic biosensors for point-of-care diagnostics: a review. *Expert Review of Molecular Diagnostics*, *19*(1), 71–81. Available from https://doi.org/10.1080/14737159.2019.1554435.

Song, J., Pandian, V., Mauk, M. G., Bau, H. H., Cherry, S., Tisi, L. C., & Liu, C. (2018). Smartphone-based mobile detection platform for molecular diagnostics and spatiotemporal disease mapping. *Analytical Chemistry*, *90*, 4823–4831. Available from https://doi.org/10.1021/acs.analchem.8b00283.

Soni, A., Surana, R. K., & Jha, S. K. (2018). Smartphone based optical biosensor for the detection of urea in saliva. *Sensors and Actuators B: Chemical*, *269*, 346–353. Available from https://doi.org/10.1016/j.snb.2018.04.108.

Stephenson, D. J., Hoeferlin, L. A., & Chalfant, C. E. (2017). Lipidomics in translational research and the clinical significance of lipid-based biomarkers. *Translational Research*, *189*, 13–29. Available from https://doi.org/10.1016/j.trsl.2017.06.006.

Strimbu, K., & Tavel, J. A. (2010). What are biomarkers? *Current Opinion in HIV and AIDS*, *5*(6), 463–466. Available from https://doi.org/10.1097/COH.0b013e32833ed177.

Syedmoradi, L., Daneshpour, M., Alvandipour, M., Gomez, F. A., Hajghassem, H., & Omidfar, K. (2017). Point of care testing: The impact of nanotechnology. *Biosensors and Bioelectronics*, *87*, 373–387. Available from https://doi.org/10.1016/j.bios.2016.08.084.

Thompson, A. G., Gray, E., Heman-Ackah, S. M., Mäger, I., Talbot, K., El Andaloussi, S., Wood, M. J., & Turner, M. R. (2016). Extracellular vesicles in neurodegenerative disease-pathogenesis to biomarkers. *Nature Reviews Neurology*, *12*(6), 346–357. Available from https://doi.org/10.1038/nrneurol.2016.68.

Tlili, C., Myung, N. V., Shetty, V., & Mulchandani, A. (2011). Label-free, chemiresistor immunosensor for stress biomarker cortisol in saliva. *Biosensors and Bioelectronics*, *26*(11), 4382–4386. Available from https://doi.org/10.1016/j.bios.2011.04.045.

Tomimuro, K., Tenda, K., Ni, Y., Hiruta, Y., Merkx, M., & Citterio, D. (2020). Thread-Based Bioluminescent Sensor for Detecting Multiple Antibodies in a Single Drop of Whole Blood. *ACS Sensors*, *5*, 1786–1794. Available from https://doi.org/10.1021/acssensors.0c00564.

Townsend, M. J., & Arron, J. R. (2016). Reducing the risk of failure: Biomarker-guided trial design. *Nature Reviews. Drug Discovery*, *15*(8), 517–518. Available from https://doi.org/10.1038/nrd.2016.124.

Ulep, T.-H., & Yoon, J.-Y. (2018). Challenges in paper-based fluorogenic optical sensing with smartphones. *NANO Convergence*, 5.

Ulep, T. H., Zenhausern, R., Gonzales, A., Knoff, D. S., Diaz, P. A., Castro, J. E., & Yoon, J. Y. (2020). Smartphone based on-chip fluorescence imaging and capillary flow velocity measurement for detecting ROR1 + cancer cells from buffy coat blood samples on dual-layer paper microfluidic chip. *Biosensors & Bioelectronics*, 153.

Veigas, B., Pinto, J., Vinhas, R., Calmeiro, T., Martins, R., Fortunato, E., & Baptista, P. V. (2017). Quantitative real-time monitoring of RCA amplification of cancer biomarkers mediated by a flexible ion sensitive platform. *Biosensors and Bioelectronics*, *91*, 788–795. Available from https://doi.org/10.1016/j.bios.2017.01.052.

Verma, P., Pandey, R. K., Prajapati, P., & Prajapati, V. K. (2016). Circulating microRNAs: Potential and emerging biomarkers for diagnosis of human infectious diseases. *Frontiers in Microbiology*, *7*(AUG), 1–7. Available from https://doi.org/10.3389/fmicb.2016.01274.

Vilela, D., González, M. C., & Escarpa, A. (2012). Sensing colorimetric approaches based on gold and silver nanoparticles aggregation: Chemical creativity behind the assay. A review. *Analytica Chimica Acta*, *751*, 24–43. Available from https://doi.org/10.1016/j.aca.2012.08.043.

Walter, J. G., Eilers, A., Alwis, L. S. M., Roth, B. W., & Bremer, K. (2020). SPR biosensor based on polymer multi-mode optical waveguide and nanoparticle signal enhancement. *Sensors*, *20*(10), 2889.

Walzl, G., McNerney, R., Plessis., Bates, M., McHugh, T. D., Chegou, N. N., & Zumla, A. (2018). Tuberculosis: advances and challenges in development of new diagnostics and biomarkers. *The Lancet Infectious Diseases*, *8*(7), e199–e210.

Wang, D., He, S., Wang, X., Yan, Y., Liu, J., Wu, S., ... Tang, Y. (2020). Rapid lateral flow immunoassay for the fluorescence detection of SARS-CoV-2 RNA. *Nat Biomed Eng* (12), 1150–1158.

Wang, L. J., Chang, Y. C., Sun, R., & Li, L. (2017). A multichannel smartphone optical biosensor for high-throughput point-of-care diagnostics. *Biosensors and Bioelectronics*, *87*, 686–692. Available from https://doi.org/10.1016/j.bios.2016.09.021.

Wang, L. J., Sun, R., Vasile, T., Chang, Y. C., & Li, L. (2016). High-throughput optical sensing immunoassays on smartphone. *Analytical Chemistry*, *88*, 8302–8308. Available from https://doi.org/10.1021/acs.analchem.6b02211.

World Health Orgnization. (1993).

Xu, M., Huang, W., Lu, D., Huang, C., Deng, J., & Zhou, T. (2019). Alizarin Red-Tb3 + complex as a ratiometric colorimetric and fluorescent dual probe for the smartphone-based detection of an anthrax biomarker. *Analytical Methods*, *11*(33), 4267–4273. Available from https://doi.org/10.1039/c9ay01235d.

Yang, Y., Su, P., & Tang, Y. (2018). Stimuli-responsive lanthanide-based smart luminescent materials for optical encoding and bio-applications. *ChemNanoMat*, *4*(11), 1097–1120. Available from https://doi.org/10.1002/cnma.201800212.

Yoon, J. Y. (2019).

Zangheri, M., Cevenini, L., Anfossi, L., Baggiani, C., Simoni, P., Di Nardo, F., & Roda, A. (2015). A simple and compact smartphone accessory for quantitative chemiluminescence-based lateral flow immunoassay for salivary cortisol detection. *Biosensors and Bioelectronics*, *64*, 63–68. Available from https://doi.org/10.1016/j.bios.2014.08.048.

Zarei, M. (2017). Portable biosensing devices for point-of-care diagnostics: Recent developments and applications. *TrAC - Trends in Analytical Chemistry*, *91*, 26–41. Available from https://doi.org/10.1016/j.trac.2017.04.001.

Zhang, D., & Liu, Q. (2016). Biosensors and bioelectronics on smartphone for portable biochemical detection. *Biosensors and Bioelectronics*, *75*, 273–284. Available from https://doi.org/10.1016/j.bios.2015.08.037.

Zhang, J., Khan, I., Zhang, Q., Liu, X., Dostalek, J., Liedberg, B., & Wang, Y. (2018). Lipopolysaccharides detection on a grating-coupled surface plasmon resonance smartphone biosensor. *Biosensors and Bioelectronics*, *99*, 312–317. Available from https://doi.org/10.1016/j.bios.2017.07.048.

Zhang, Z., Azizi, M., Lee, M., Davidowsky, P., Lawrence, P., & Abbaspourrad, A. (2019). A versatile, cost-effective, and flexible wearable biosensor for: In situ and ex situ sweat analysis, and personalized nutrition assessment. *Lab on a Chip*, *19*(20), 3448–3460. Available from https://doi.org/10.1039/c9lc00734b.

Zhao, W., Tian, S., Huang, L., Liu, K., Dong, L., & Guo, J. (2020). A smartphone-based biomedical sensory system. *Analyst*, *145*(8), 2873–2891. Available from https://doi.org/10.1039/c9an02294e.

Zhao, Z., Wei, L., Cao, M., & Lu, M. (2019). A smartphone-based system for fluorescence polarization assays. *Biosensors and Bioelectronics*, *128*, 91–96. Available from https://doi.org/10.1016/j.bios.2018.12.031.

Zhou, Jianyu, & Dong, Tao (2018). Design of a wearable device for real-time screening of urinary tract infection and kidney disease based on smartphone. *Analyst*, *143*(12), 2812–2818. Available from https://doi.org/10.1039/c8an00157j.

Zhou, S., Gou, T., Hu, J., Wu, W., Ding, X., Fang, W., Hu, Z., & Mu, Y. (2019). A highly integrated real-time digital PCR device for accurate DNA quantitative analysis. *Biosensors and Bioelectronics*, *128*, 151–158. Available from https://doi.org/10.1016/j.bios.2018.12.055.

Zhu, H., Sencan, I., Wong, J., Dimitrov, S., Tseng, D., Nagashima, K., & Ozcan, A. (2013). Cost-effective and rapid blood analysis on a cell-phone. *7*.

Lab on a Chip

COMMUNICATION

View Article Online
View Journal | View Issue

Cite this: *Lab Chip*, 2022, **22**, 2938

Received 27th May 2022,
Accepted 10th June 2022

DOI: 10.1039/d2lc00486k

rsc.li/loc

Selection and characterisation of bioreceptors to develop nanoparticle-based lateral-flow immunoassays in the context of the SARS-CoV-2 outbreak†

Liming Hu, ‡[a] Enric Calucho,‡[a] Celia Fuentes-Chust,[a] Claudio Parolo, [ab] Andrea Idili, [a] Ruslan Álvarez-Diduk, [a] Lourdes Rivas [a] and Arben Merkoçi *[ac]

This manuscript aims at raising the attention of the scientific community to the need for better characterised bioreceptors for fast development of point-of-care diagnostic devices able to support mass frequency testing. Particularly, we present the difficulties encountered in finding suitable antibodies for the development of a lateral flow assay for detecting the nucleoprotein of SARS-CoV-2.

Introduction

The COVID-19 pandemic[1–3] has shown the importance of developing reliable yet easy-to-use, cheap, fast, and portable diagnostic devices to support mass testing.[4–10] Diagnostic testing is fundamental for a rapid screening of the population, to identify and track positive cases (*i.e.* both symptomatic and asymptomatic individuals), and immunity assessment.[11,12] As suggested by the World Health Organization (WHO), in order to meet such a high demand of testing, countries have been relying on lateral flow assays (LFAs).[13] Indeed, such molecular sensing platforms allow achieving the rapid (<30 min), low-cost (5 USD), and single-step detection of the COVID-19 biomarkers.[14] Moreover, LFAs are an evolving platform with constantly improving sensitivity.[15–17] Our group recently provided a protocol describing the fabrication of a LFA to detect human IgG.[18] This is a generalisable protocol that can be easily adapted to other targets, such as the SARS-CoV-2 virus, only by changing the bioreceptors (*e.g.* antibodies or aptamers). However, the selection of suitable bioreceptors for the detection of SARS-CoV-2 unveiled several experimental hurdles, which we want to share with the community. More specifically, we want to raise attention towards the importance of comprehensive characterisation of bioreceptors (in this case, antibodies) before their implementation into LFAs. Many studies compare the performance of commercial SARS-CoV-2 diagnostic kits,[19–26] but to the best of our knowledge, only one recent work has focused on the technical challenges behind bioreceptor selection.[27]

The COVID-19 pandemic represents a unique situation due to the scarcity of antibodies against SARS-CoV-2 antigens at the beginning of the outbreak (from December 2019 to May 2020). During this period, the research community made an important effort in the characterisation process to select suitable antibodies to rapidly face the fast spread of the virus. The main goal of this characterisation is to understand whether the selected antibodies exhibit the required binding properties to work in a LFA platform. Specifically, antibodies have to display: (1) stability, in order to work under variable environmental conditions (temperature, humidity, pressure) and support long-term storage; (2) fast binding kinetics, due to the short time window for the bioreceptor–analyte interaction in the LFA assay (in the range of seconds to a few minutes); (3) strong binding affinity, as we want the signal to remain stable while and after the assay takes place.[18] Unfortunately, besides already identified technical problems associated with antibodies such as batch to batch differences,[28–31] suppliers do not provide enough characterisation of important binding parameters (*e.g.* binding and kinetic constants), and they test antibodies using only standard laboratory procedures (*e.g.*, ELISA, western blot). A parallel approach could be the estimation of these parameters through thermodynamics, binding, and kinetics studies, but this requires resources, time, and facilities that private companies may not be willing to

[a] *Nanobioelectronics & Biosensors Group, Catalan Institute of Nanoscience and Nanotechnology (ICN2), CSIC, BIST, Campus UAB, 08193, Bellaterra, Barcelona, Spain. E-mail: arben.merkoci@icn2.cat*
[b] *ISGlobal, Barcelona Centre for International Health Research (CRESIB), Hospital Clínic (Department of International Health), Universitat de Barcelona, Barcelona, Spain*
[c] *ICREA, Institució Catalana de Recerca i Estudis Avançats, Barcelona, Spain*

† Electronic supplementary information (ESI) available: Extended materials and methods, bioreceptor selection and characterisation data (PDF). See DOI: https://doi.org/10.1039/d2lc00486k

‡ These authors contributed equally.

implement.[18] This lack of experimental data does not allow developers to pursue a rational selection of antibodies forcing them into a trial-and-error approach. Since this can hide many technical challenges, here we present a study which describes how to proceed in such circumstances with experimental tools that are more available and can be performed by any laboratory, always keeping in mind that the final goal is the development of a colorimetric LFA to be implemented in COVID-19 diagnostics, and considering that similar scenarios can occur in the future.

Results and discussion

Following our fabrication protocol for LFA,[18] we characterised antibodies for their adaptation as bioreceptors in an AuNP-based LFA as they were released in the market. Specifically, among the antigens of SARS-CoV-2, we decided to target the nucleoprotein since it is highly abundant in the virion.[32,33] From April 2020 to February 2021, we purchased 17 commercial anti-nucleoprotein antibodies from different companies (see Table S1†). The criteria for the selection were: (1) cost, (2) antibody concentration (over 1 mg mL^{-1}), (3) delivery time, and (4) animal host used for its production. Since the recognition event in LFAs is based on the formation of the classic immune-sandwich complex (Fig. S3†), we screened antibodies through two phases: (1) ELISA, to quickly check antibody binding performance (Fig. 1) and (2) the half-stick format, to check their compatibility with the conditions encountered in a LFA (*i.e.*, under a constant flow in a nitrocellulose membrane) (Fig. 2). Firstly, we performed ELISA tests to identify the antibody combinations with the best binding performance (Fig. 1A). In order to carry out these measurements, we followed a previously reported ELISA protocol.[34,35] The experimental criteria to identify such antibodies were similar to the standard for evaluating antibody titre by the chessboard titration method, which allows assessing two variables simultaneously: antibody couples and the presence/absence of nucleoprotein.[36] Specifically, in the absence of the target (*i.e.* blank), the background signal has to display a value lower than 0.2 a.u. (OD Blank), while in the presence of a saturated concentration of nucleoprotein (100 ng mL^{-1}), the produced signal should be higher than 1.0 a.u. (OD Positive). Surprisingly, we found that out of 80 tested combinations, only 10 met these two criteria (Fig. 1B). Such a low success rate (12.5%) is a consequence of the high cross-reactivity between antibodies (in most cases, a blank signal as high as the positive can be observed (Fig. 1C)) and their low affinity for the target or slow kinetics (for antibody couples whose positive signals were lower than 1.0 a.u.) (Fig. 1D and E). It should be noted that all but one antibodies were publicised to work in ELISA and that none of them were part of a pre-validated matched pair.

Among the 10 working antibody combinations, we selected the 5 combinations of capture and detection

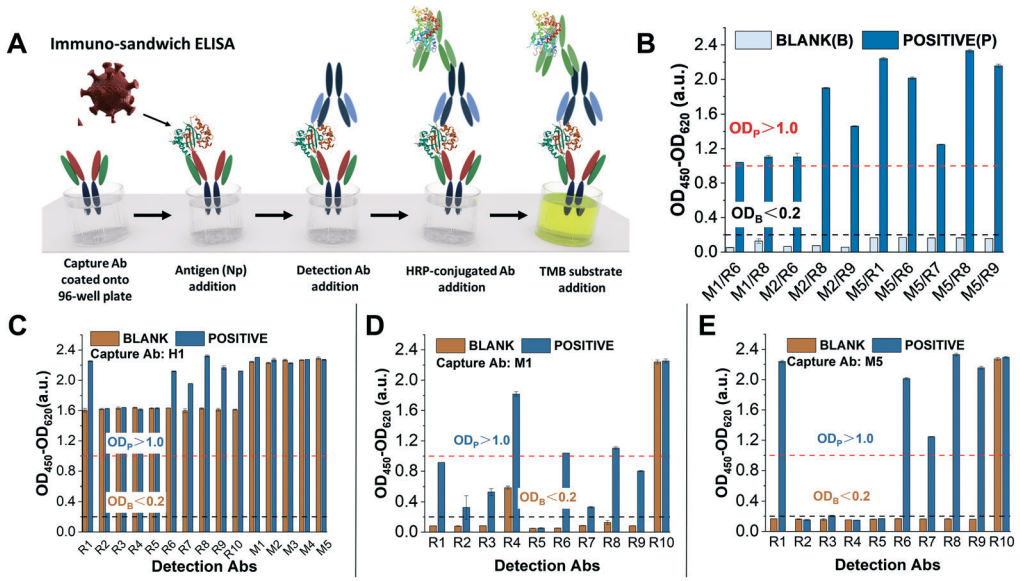

Fig. 1 ELISA tests were performed to screen antibody combinations with the best binding performance against the nucleoprotein (N protein) of SARS-CoV-2. (A) Schematic of the immune-sandwich ELISA procedure. (B) Antibody combinations with the best ELISA performance. The nucleoprotein concentrations of the blank and positive solutions are 0 ng mL^{-1} and 100 ng mL^{-1}, respectively. Antibody combinations that meet the performance requirements should have the following conditions: the OD value of the blank nucleoprotein solution is less than 0.2 a.u. and the OD value of the positive nucleoprotein solution is greater than 1.0 a.u.[27] (C–E) Each individual graph shows the ELISA test results of the same capture antibodies (coated on ELISA plate wells) combined with multiple detection antibodies. (C) Capture Abs H1 and detection Abs R1–R10 and M1/M5. None of the antibody combinations qualified because the OD value of the blanks was much greater than 0.2, which means high cross-reactivity and poor specificity; (D) capture Abs M1 and detection Abs R1–R1. Only M1/R6 and M1/R8 were qualified with OD blank <0.2 and OD positive >1.0 while the rest were not qualified due to OD blank >0.2 or OD positive <1.0; and (E) capture Abs M5 and detection Abs R1/R10. Couples M5/R1, M5/R6, M5/R7, M5/R8 and M5/R9 were satisfactory, especially M5/R1 and M5/R8, and the others were not qualified due to OD blank >0.2 (M5/R10) or OD positive <1.0.

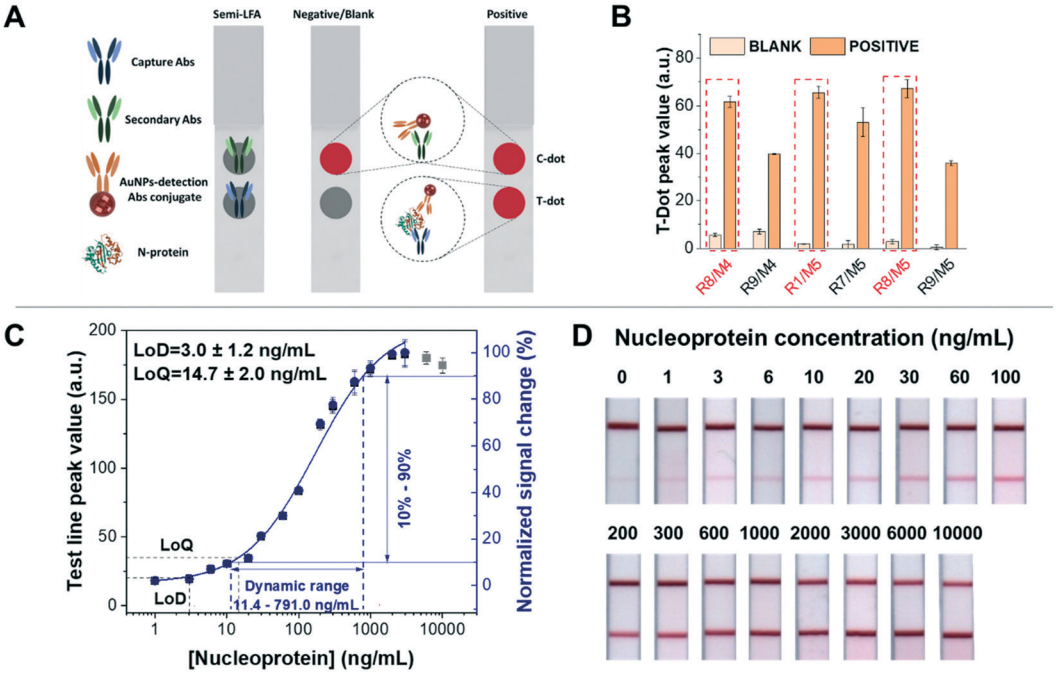

Fig. 2 Dot test for screening out antibody combinations and calibration curve of detection of nucleoprotein spiked in artificial saliva based on half-stick LFA. (A) Schematic representation of the dot test based on half-stick LFA: anti-nucleoprotein Abs (capture Abs) and secondary Abs were manually dropped on the nitrocellulose membrane as the test dot and control dot, respectively. When the half-stick is tested with a blank sample, only the control dot (or line) is visible, demonstrating that the assay functioned properly. If the sample contains nucleoproteins, both control and test dots (or lines) are visible, and the intensity of the latter will depend on the analyte concentration. (B) All antibody combinations with good performance in the dot test (easy to distinguish between blank and positive samples with the naked eye). R1/M5, R8/M4 and R8/M5 elicit the best response. (C) Calibration curve of the half-stick LFA with R8/M5 antibodies. The data were fitted to a four-parameter logistic curve (blue line). The fitted curve (obtained using Origin 2018 32-bit and presented as value ± standard error) corresponds to the following equation: y = start + (end − start) × x^n/(k^n + x^n), with start = 1.04 ± 1.09, end = 112.12 ± 10.21, k = 169.28 ± 44.06 and n = 0.90 ± 0.12. The reduced $\chi 2$ = 2.58, R2 = 1.00 and the adjusted R2 = 0.99 Grey points were beyond the curve range due to the saturation of bioreceptor binding sites. The dynamic range of the half-sticks is from 11.4 ng mL^{-1} to 791.0 ng mL^{-1}, calculated from the signal change from 10% to 90%, and the graph was obtained by analysing at least three (n = 3) independent LFAs for each target concentration. The fitting curve, LoD, LoQ, and dynamic range fully were acquired by the protocol from Parolo *et al.*[18] (D) Half-stick LFA for detection of nucleoprotein, responding to increasing concentrations of the nucleoprotein.

antibodies (M2/R8, M5/R1, M5/R6, M5/R8 and M5/R9) with the best performance in order to move on to the half-stick characterisation. To do this, we used dotted half-sticks rather than full LFA strips because they are faster to prepare (taking into account the number of antibody combinations) and smaller reagent amounts are required.[18,37] In order to identify the antibodies with the best binding performance in the nitrocellulose membrane, we established that the blank's signal should be <5.0 a.u. and the positive sample's signal >30.0 a.u. These values approximately correspond with the dynamic range obtained in a provided protocol for human IgG detection.[18] With these criteria, only 6 couples of antibodies showed a suitable binding performance in the half-stick format (Fig. 2B). We hypothesise that the shorter time of incubation/recognition and the absence of washing steps in half-stick dot tests compared to ELISAs are the causes of the decrease in the number of antibody couples compatible with a paper-based platform.

To demonstrate the feasibility of the half-stick assay for further experimentation with clinical samples, we tested it using artificial saliva, taking into account that COVID-19 diagnosis is possible using such a kind of sample.[4,38] The dot test results showed that three antibody couples (R1/M5, R8/M4 and R8/M5) had similar test line peak values for the detection of 100 ng mL^{-1} nucleoprotein (Fig. 2B). Then, preliminary calibration curves of R1/M5, R8/M4 and R8/M5 were obtained after testing the sensors with increasing concentrations of nucleoprotein (0, 3, 10, 30, 100, 300, 1000, and 3000 ng mL^{-1}) (Fig. S5†). Fitting the curves with a four-logistic parameter equation, we calculated the EC50, that is, the half maximal concentration of nucleoprotein that elicits a response halfway between the baseline and saturation signal. Given the immune-sandwich nature of the system, EC50 is a good indicator of affinity. The R8/M5 couple displays the lowest EC50 value (134.7 ng mL^{-1}), while the EC50 values for R8/M4 and R1/M5 are 197.9 ng mL^{-1} and 337.1 ng mL^{-1} respectively (Fig. S5 and Table S4†). Moreover, R8/M5 showed the best sensitivity for nucleoprotein detection, as observed from the steeper slope in the calibration curves (Fig. S5A and B†). Consequently, antibody couple R8/M5 was selected for the further development of a nucleoprotein LFA sensor. A half-stick was prepared by dispensing the R8 antibody on the test line (TL) and the secondary antibodies (anti-mouse IgG) on the control line (CL), while the antibody nucleoprotein M5

was conjugated to AuNPs. In order to characterise the sensor response, we challenged it using nucleoprotein-spiked artificial saliva samples covering a nucleoprotein concentration range between 1 ng mL^{-1} (21.2 pM) and 10 μg mL^{-1} (0.2 μM) (Fig. 2C). Through the analysis of the obtained half-sticks, we calculated a limit of detection (LoD) of 3.0 ± 1.2 ng mL^{-1}, limit of quantification (LoQ) of 14.7 ± 2.0 ng mL^{-1}, and a useful dynamic range of 11.4–791.0 ng mL^{-1} (Fig. 2C). The test line signals obtained using nucleoprotein concentrations higher than 10 ng mL^{-1} were clearly seen by the naked eye (Fig. 2D). In addition, the recovery of nucleoprotein samples ranged from 83.0 ± 2.0% to 116.7 ± 16.7%, demonstrating the accuracy of the test (Table S2†). The analytical performance of the described half-sticks is comparable to that of a full SARS-CoV-2 nucleoprotein LFA recently published for the detection of the nucleoprotein.[39] To further support our results, we found another recently published study by Cate *et al.*, in which 1021 anti-nucleoprotein antibodies were tested in LFA, taking advantage of an automatized, high-throughput robotic system,[27] and the couple of antibodies we independently selected has been found among the top performing couples.

Finally, to make stronger our message that knowing beforehand the binding behaviour of bioreceptors would speed up the development of diagnostic tests, we studied the binding constant of three couples of antibodies selected according to their performance in the preliminary steps, which goes as follows. One of them worked in ELISA but did not in half-stick (R8/M2), while the other two couples did work in both types of assays (R8/M4 and R8/M5). R8/M2 showed an EC50 at least 72% higher than those of the other two couples (R8/M4 and R8/M5) and also a higher working range, thus indicating a lower affinity, which is not suitable for LFAs (Table S3 and Fig. S4†).

Conclusions

Despite the successful implementation of the LFA development protocol,[18] the significant amount of invested economic resources (~25 000 €), personnel, and time (over 10 months) to identify working antibodies is alarming. We understand that the majority of the antibodies are validated for a few specific applications, generally traditional laboratory-bound techniques (*e.g.* ELISA, western blot). However, the COVID-19 pandemic has demonstrated that we cannot rely exclusively on long (hours) and cumbersome (multistep) diagnostic techniques to effectively diagnose infectious diseases because we need sensing platforms able to support massive (or high-frequency) testing. Therefore, we urge antibody producers and distributors to consider the implementation of more extensive characterisation of their products, which would allow researchers to make better-informed purchases. At the same time, the integration of new antibodies into point-of-care devices would also be faster. The availability of information such as the binding kinetics of bioreceptors could lead researchers towards purchasing antibodies that better suit their platform's needs, *e.g.* antibodies with fast binding kinetics for a LFA, which features a short receptor–analyte interaction time. We realise that longer bioreceptor characterisation implies higher costs for the company (*e.g.* new instrumentation, delayed commercial availability). Nonetheless, we truly believe that researchers would rather buy more expensive, but well characterised antibodies than cheaper but poorly characterised ones. This in turn would optimise the time and economic resources required for the development of a point-of-care diagnostic device, speeding up its placement in the market.

Author contributions

LH: conceptualisation, investigation, formal analysis, software, and writing – original draft. EC: conceptualisation, investigation, and writing – original draft. CFC: investigation and writing – review and editing. CP: methodology, data curation, supervision, and writing – review and editing. AI: supervision and writing – review and editing. RA: software, data curation, and supervision. LR: supervision and writing – review and editing. AM: project administration, funding acquisition, and supervision.

Conflicts of interest

There are no conflicts to declare.

Acknowledgements

We acknowledge Consejo Superior de Investigaciones Científicas (CSIC) for the project "COVID19-122" granted in the call "Nuevas ayudas extraordinarias a proyectos de investigación en el marco de las medidas urgentes extraordinarias para hacer frente al impacto económico y social del COVID-19 (Ayudas CSIC-COVID-19)". We acknowledge also the MICROB-PREDICT project that has received funding from the European Union's Horizon 2020 research and innovation programme under grant agreement No. 825694. Financial support from the EU Graphene Flagship Core 3 Project (No. 881603) is also acknowledged. This article reflects only the authors' view, and the European Commission is not responsible for any use that may be made of the information it contains. ICN2 is funded by the CERCA programme/Generalitat de Catalunya. ICN2 is supported by the Severo Ochoa Centres of Excellence programme, funded by the Spanish Research Agency (AEI, grant no. SEV-2017-0706). E. C. acknowledges Ministerio de Ciencia e Innovación of Spain and Fondo Social Europeo for the Fellowship PRE2018-084856 awarded under the call 'Ayudas para contratos predoctorales para la formación de doctores, Subprograma Estatal de Formación del Programa Estatal de Promoción del Talento y su Empleabilidad en I+D+i', under the framework of 'Plan Estatal de Investigación Científica y Técnica y de Innovación 2017–2020'. L. H. acknowledges the China Scholarship Council. L. H., E. C. and C. F.-C. acknowledge the Autonomous University of Barcelona (UAB) for their support. C. P. (ISGlobal) also acknowledges support

from the Spanish Ministry of Science and Innovation and State Research Agency through the "Centro de Excelencia Severo Ochoa 2019–2023" Program (CEX2018-000806-S), and support from the Generalitat de Catalunya through the CERCA Program. A. I. was supported by a PROBIST postdoctoral fellowship funded by the European Research Council (Marie Skłodowska-Curie grant agreement No. 754510).

Notes and references

1 F. Wu, S. Zhao, B. Yu, Y. M. Chen, W. Wang, Z. G. Song, Y. Hu, Z. W. Tao, J. H. Tian, Y. Y. Pei, M. L. Yuan, Y. L. Zhang, F. H. Dai, Y. Liu, Q. M. Wang, J. J. Zheng, L. Xu, E. C. Holmes and Y. Z. Zhang, *Nature*, 2020, **579**, 265–269.
2 P. Zhou, X. Yang, X. Wang, B. Hu, L. Zhang, W. Zhang, H. Guo, R. Jiang, M. Liu, Y. Chen, X. Shen, X. Wang, F. Zhan, Y. Wang, G. Xiao and Z. Shi, *Nature*, 2020, **579**, 270–273.
3 J. Lan, J. Ge, J. Yu, S. Shan, H. Zhou, S. Fan and Q. Zhang, *Nature*, 2020, **581**, 215–220.
4 M. Nagura-Ikeda, K. Imai, S. Tabata, K. Miyoshi, N. Murahara, T. Mizuno, M. Horiuchi, K. Kato, Y. Imoto, M. Iwata, S. Mimura, T. Ito, K. Tamura and Y. Kato, *J. Clin. Microbiol.*, 2020, **58**, 1–9.
5 C. R. Wells, J. P. Townsend, A. Pandey, S. M. Moghadas, G. Krieger, B. Singer, R. H. McDonald, M. C. Fitzpatrick and A. P. Galvani, *Nat. Commun.*, 2021, **12**, 1–9.
6 G. Guglielmi, *Nature*, 2020, **585**, 496.
7 T. R. Mercer and M. Salit, *Nat. Rev. Genet.*, 2021, **22**, 415–422.
8 G. Rosati, A. Idili, C. Parolo, C. Fuentes-Chust, E. Calucho, L. Hu, C. D. C. C. E. Silva, L. Rivas, E. P. Nguyen, J. F. Bergua, R. Alvárez-Diduk, J. Muñoz, C. Junot, O. Penon, D. Monferrer, E. Delamarche, A. Merkoçi, A. G. Rosati, A. Idili, C. Parolo, C. Fuentes, E. Calucho, L. Hu and C. D. C. Castro, *ACS Nano*, 2021, **15**, 17137–17149.
9 A. Idili, C. Parolo, R. Alvarez-Diduk and A. Merkoçi, *ACS Sens.*, 2021, **6**, 3093–3101.
10 D. B. Larremore, B. Wilder, E. Lester, S. Shehata, J. M. Burke, J. A. Hay, M. Tambe, M. J. Mina and R. Parker, *Sci. Adv.*, 2021, **7**, eabd5393.
11 L. J. Carter, L. V. Garner, J. W. Smoot, Y. Li, Q. Zhou, C. J. Saveson, J. M. Sasso, A. C. Gregg, D. J. Soares, T. R. Beskid, S. R. Jervey and C. Liu, *ACS Cent. Sci.*, 2020, 591–605.
12 O. Vandenberg, D. Martiny, O. Rochas, A. van Belkum and Z. Kozlakidis, *Nat. Rev. Microbiol.*, 2021, **19**, 171–183.
13 World Health Organization (WHO), Antigen-detection in the diagnosis of SARS-CoV-2 infection using rapid immunoassays Interim guidance, 11 September 2020, 2020.
14 G. Guglielmi, *Nature*, 2021, **590**, 202–205.
15 B. S. B. S. Miller, L. Bezinge, H. D. H. D. Gliddon, D. Da Huang, G. Dold, E. R. Gray, J. Heaney, P. J. Dobson, E. Nastouli, J. J. L. L. Morton and R. A. McKendry, *Nature*, 2020, **587**, 588–593.
16 A. Sena-Torralba, R. Alvarez-Diduk, C. Parolo, H. Torné-Morató, A. Müller and A. Merkoçi, *Anal. Chem.*, 2021, **93**, 3112–3212.
17 A. Sena-Torralba, H. Torné-Morató, C. Parolo, S. Ranjbar, M. A. Farahmand Nejad, R. Álvarez-Diduk, A. Idili, M. R. Hormozi-Nezhad and A. Merkoçi, *Adv. Mater. Technol.*, 2022, 2101450.
18 C. Parolo, A. Sena-Torralba, J. F. Bergua, E. Calucho, C. Fuentes-Chust, L. Hu, L. Rivas, R. Álvarez-Diduk, E. P. Nguyen, S. Cinti, D. Quesada-González and A. Merkoçi, *Nat. Protoc.*, 2020, **15**, 3788–3816.
19 V. Haselmann, M. Kittel, C. Gerhards, M. Thiaucourt, R. Eichner, V. Costina and M. Neumaier, *Clin. Chim. Acta*, 2020, **510**, 73–78.
20 S. Mahapatra and P. Chandra, *Biosens. Bioelectron.*, 2020, **165**, 112361.
21 C. L. Charlton, J. N. Kanji, K. Johal, A. Bailey, S. S. Plitt, C. Macdonald, A. Kunst, E. Buss, L. E. Burnes, K. Fonseca, B. M. Berenger, K. Schnabl and J. Hu, *J. Clin. Microbiol.*, 2020, **58**, e01361–20.
22 M. Martínez, D. Navalpotro, N. Tormo, R. Olmos, M. Moreno, M. Dolores, O. Mochón and C. Gimeno, *J. Clin. Virol.*, 2020, **129**, 104529.
23 C. Schnurra, N. Reiners, R. Biemann, T. Kaiser, H. Trawinski and C. Jassoy, *J. Clin. Virol.*, 2020, **129**, 104544.
24 A. Krüttgen, C. G. Cornelissen, M. Dreher, M. Hornef, M. Imöhl and M. Kleines, *J. Clin. Virol.*, 2020, **128**, 104394.
25 K. Y. L. Chua, S. Vogrin, I. Bittar, J. H. Horvath, H. Wimaleswaran, J. A. Trubiano, N. E. Holmes and Q. Lam, *Pathology*, 2020, **52**, 778–782.
26 M.-A. Trabaud, V. Icard, M.-P. Milon, A. Bal, B. Lina and V. Escuret, *J. Clin. Virol.*, 2020, **132**, 104613.
27 D. M. Cate, J. D. Bishop, H. V. Hsieh, V. A. Glukhova, L. F. Alonzo, H. G. Hermansky, B. Barrios-Lopez, B. D. Grant, C. E. Anderson, E. Spencer, S. Kuhn, R. Gallagher, R. Rivera, C. Bennett, S. A. Byrnes, J. T. Connelly, P. K. Dewan, D. S. Boyle, B. H. Weigl and K. P. Nichols, *ACS Omega*, 2021, **6**, 25116–25123.
28 M. Baker, *Nature*, 2015, **521**, 274–276.
29 A. Bradbury and A. Plückthun, *Nature*, 2015, **518**, 27–29.
30 J. R. Couchman, *J. Histochem. Cytochem.*, 2009, **57**, 7–8.
31 C. B. Saper, *J. Comp. Neurol.*, 2005, **493**, 477–478.
32 J. Cubuk, J. J. Alston, J. J. Incicco, S. Singh, M. D. Stuchell-Brereton, M. D. Ward, M. I. Zimmerman, N. Vithani, D. Griffith, J. A. Wagoner, G. R. Bowman, K. B. Hall, A. Soranno and A. S. Holehouse, *Nat. Commun.*, 2021, **12**, 1–17.
33 W. Zeng, G. Liu, H. Ma, D. Zhao, Y. Yang, M. Liu, A. Mohammed, C. Zhao, Y. Yang, J. Xie, C. Ding, X. Ma, J. Weng, Y. Gao, H. He and T. Jin, *Biochem. Biophys. Res. Commun.*, 2020, **527**, 618–623.
34 E. Morales-Narváez, H. Montón, A. Fomicheva and A. Merkoçi, *Anal. Chem.*, 2012, **84**, 6821–6827.
35 J. F. Bergua, R. Álvarez-Diduk, A. Idili, C. Parolo, M. Maymó, L. Hu and A. Merkoçi, *Anal. Chem.*, 2022, **94**, 1271–1285.
36 China National Intellectual Property Administration, CN102876634A, 2012, 1–21.
37 H. V. Hsieh, J. L. Dantzler and B. H. Weigl, *Diagnostics*, 2017, **7**, 29.

38 D. Shan, J. M. Johnson, S. C. Fernandes, H. Suib, S. Hwang, D. Wuel, M. Mendes, M. Holdridge, E. M. Burke, K. Beauregard, Y. Zhang, M. Cleary, S. Xu, X. Yao, P. P. Patel, T. Plavina, D. H. Wilson, L. Chang, K. M. Kaiser, J. Nattermann, S. V. Schmidt, E. Latz, K. Hrusovsky, D. Mattoon and A. J. Ball, *Nat. Commun.*, 2021, **12**, 1–8.
39 B. D. Grant, C. E. Anderson, J. R. Williford, L. F. Alonzo, V. A. Glukhova, D. S. Boyle, B. H. Weigl and K. P. Nichols, *Anal. Chem.*, 2020, **92**, 11305–11309.

ACS APPLIED NANO MATERIALS

www.acsanm.org Article

Rational Approach to Tailor Au−IrO_2 Nanoflowers as Colorimetric Labels for Lateral Flow Assays

Lourdes Rivas,* Liming Hu, Claudio Parolo, Andrea Idili, and Arben Merkoçi*

Cite This: *ACS Appl. Nano Mater.* 2023, 6, 4151−4161 Read Online

ACCESS | Metrics & More | Article Recommendations | Supporting Information

ABSTRACT: As the current pandemic has shown, lateral flow assays (LFAs) are a prime example of point-of-care devices enabling quick testing at an affordable price. However, their ease of use undeniably affects their sensitivity, making them less sensitive than other multi-step and time-consuming diagnostic assays, such as polymerase chain reactions and enzyme-linked immunosorbent assays. A possible solution to overcome this lack of sensitivity is the exploitation of bottom-up approaches to synthesize nanomaterials with outstanding properties for use as colorimetric labels in LFAs, that is, using nanoparticles with better optical capabilities to improve the generation of the colorimetric signal and the overall sensitivity of LFAs. Following this strategy, we rationally optimized the synthesis of gold and iridium oxide nanoflowers (Au−IrO_2 NFs) to enhance their physical−chemical properties as colorimetric labels in LFAs. Specifically, we were able to rationally control their size (from 155 to 53 nm in diameter) in order to guarantee an optimal flow along the different pads of a LFA. Moreover, thanks to their superior plasmonic behavior (compared to standard AuNPs), we could achieve an 8.5-fold lower limit of detection (down to 1.2 ng/mL) for human immunoglobulin G (HIgG) than standard LFAs (10.1 ng/mL). Therefore, due to their optical and redox properties, bioconjugation capabilities, and synergic combination of the individual components, Au−IrO_2 NFs appear as potential candidates for the next generation of optical LFAs.

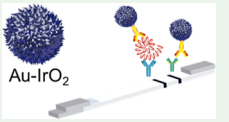

KEYWORDS: *lateral flow assay, gold nanoparticles, iridium oxide nanoparticles, paper-based biosensor, nanoflowers*

INTRODUCTION

The recent COVID-19 outbreak has highlighted again the clinical relevance of lateral flow assays (LFAs) as simple and rapid diagnostic tools with an ability to support mass-scale screening.[1,2] They consist of a series of connected paper-like pads that, by capillarity, move the liquid sample along the strip, allowing for the rapid, low-cost, and naked-eye detection of the target molecule in its clinical range.[3] Because the signal transduction mechanism is based on the detection of the target through the formation of an adsorbed immune complex on the test line, they can be designed to detect any arbitrary molecule by simply changing the antibody receptors. To date, LFAs have been widely exploited in real-world applications ranging from clinical (e.g., pregnancy test, antigen detection, serological application, etc.)[4,5] to environmental monitoring (e.g., detection of heavy metals, bacteria, and contaminants).[6−8] Besides their versatility, the success and popularity of LFAs rely on their simple operation, fast response (approximately 15 min), low cost, and naked-eye-readable results. Despite the success and popularity of LFAs due to their simple operation and fast response, their sensitivity is lower than that of well-established laboratory-based detection methods [e.g., polymerase chain reaction (PCR) and enzyme-linked immunosorbent assay (ELISA)]. In consequence, LFA's potential cannot be fully exploited yet for applications requiring the detection and quantification of ultra-low-concentrated biomarkers (e.g., circulating tumor DNA, tumor proteins).[9,10] Therefore, the development of novel approaches with an ability to improve the sensitivity of LFAs without compromising their ease of use could reduce the burden of expensive laboratory-based methods, allowing a more efficient early diagnosis to support the mass-scale screening of biomarkers at the point of care.[11]

The sensitivity of an LFA depends on a wide range of physical−chemical and biological factors including, but not limited to, the type of label (e.g., colorimetric, fluorescent, electrochemical, etc.), the affinity of the selected bioreceptors toward the targets, and the flow rates of different pads.[12,13] Among them, the selection of the optical label plays a key role because it can affect important parameters of the LFAs, from the flow of the sample to the signal-to-noise ratio (which is defined as the optical contrast between the test/control line and the nitrocellulose background) and must guarantee the naked eye detection, which is crucial for their use at the point of care.[14] The development of nanotechnology has boosted the synthesis and the generation of new labels (i.e., nanomaterials) with exceptional optical properties (e.g., absorption, transmission, scattering, and light emission), creating a new set of ideal candidates for biosensing purposes.[15−17] However, other features of the selected nanomaterial must also be considered, such as their size, shape, surface chemistry, and stability, to fully adapt it on an LFA.

Received: November 11, 2022
Accepted: March 2, 2023
Published: March 13, 2023

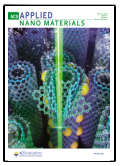

https://doi.org/10.1021/acsanm.2c04915
ACS Appl. Nano Mater. 2023, 6, 4151−4161

To improve the sensitivity and limit of detection of LFAs, several experimental strategies have been developed over the last 2 decades.[18,19] Generally, those strategies aimed at improving the different components of the LFAs, such as labels,[20−24] strip design,[25−27] readout (optical or electrochemical),[28−30] and microfluidics[31] with the final goal to enhance the overall analytical response of the LFAs. Among them, the development of new labels with the ability to generate a stronger optical signal has been a simple yet effective approach to improve the sensitivity of LFAs.[19] For example, nanodiamonds, upconverting nanoparticles, quantum dots, and magnetic nanoparticles have been used to develop LFAs for the detection of clinically relevant targets.[23,32−35] In particular, AuNPs are the most used colorimetric LFA labels that allow efficient naked eye detection due to their strong surface plasmon resonance, simple synthesis, and conjugation. Indeed, their surface plasmon resonance in the visible region produces a strong red color, which makes the iconic red lines that are ideal for the naked eye detection.[34] Other examples of metallic NPs used for the development of colorimetric LFAs include iridium oxide nanoparticles (IrO_2 NPs),[36] rhodium nanoparticles,[37] copper oxide nanoparticles,[38] and Prussian blue nanoparticles.[39] Each NPs display different colorimetric properties, which allow the generation of test lines with different colors and better performances than the classical AuNPs-based LFAs, albeit higher costs, more complex synthesis, and different morphology and size which affect the bioconjugations.

Besides the composition of the label, the morphology and the size of the nanoparticles also play important roles in the sensitivity of LFAs.[40,41] For example, increasing the surface area of a nanoparticle allows it to load more bioreceptors (e.g., antibodies, proteins, or aptamers), or the presence of spiked structures can provide different optical properties due to surface-enhanced plasmons. In this context, several research groups have demonstrated how the use of non-spherical nanoparticles with strong plasmonic behaviors (e.g., nanorods, nanocubes, and nanostars) generally produces an improvement in the LFA sensitivity when compared to the use of classical quasi-spherical AuNPs.[42−44] Looking in particular at mono- and bimetallic non-spherical nanoparticles, we found studies reporting up to 5-fold and 10-fold improvements in the sensitivity of LFAs when using gold and platinum nanoflowers, respectively.[45−48] Uniquely of bimetallic nanoparticles, they have ability to display both plasmonic and catalytic behavior (e.g., Au-based alloy nanoparticles).[49,50] This feature has been recently harnessed by two works, where AuPt core−shell and AuPt nanoflowers have been described as dual labels for LFAs, increasing dramatically the sensitivity of the assay up to 2 orders of magnitude.[51,52] Thus, non-spherical and hierarchical nanoparticles appear as promising labels to enhance the analytical properties of LFAs.

Given the background, we were inspired by the plasmonic behavior of gold and iridium oxide ($Au-IrO_2$) nanoflowers that were recently reported by de Freitas and co-workers.[53] More specifically, harnessing their unique morphology and composition that provide excellent biocompatibility and plasmonic properties, we decided to use them as colorimetric labels in LFAs.

Rationale. On the one hand, while the debate about the optimal size of a LFA's label remains open (depending on the type of nanoparticles, the porosity of the pads, the size of the bioreceptor, etc.), the ideal choice would be one that ensures optimal nanoparticle' stability and bioreceptor coverage without sacrificing the sensitivity of the assay. Bottom-up synthesis of mono- and bimetallic nanoparticles is a versatile tool to achieve this chemical and physical balance. Specifically, it is possible to tune their size and shape by simply changing the amount of reducing agent, pH, and solvent during their synthesis.[54,55] Therefore, the possibility to synthetically tune the size and shape of the NPs is an important parameter at the time of choosing the label to employ in a new LFA. On the other hand, the optical response of the nanoparticles is another crucial parameter to consider. In general, these nanoparticles should have large extinction coefficients (i.e., high optical intensities) that visually contrast with the white background of the LF membrane. For example, this explains why AuNPs that show bright red colors and absorb at wavelengths ca. 520−530 nm are sometimes preferred to bigger gold nanoparticles that allow a higher bioreceptor loading but absorb at higher wavelengths (e.g., 600 nm), reducing the visual contrast with the membrane.

Having this in mind, we selected as new optical labels for LFAs the $Au-IrO_2$ NFs whose synthesis was proposed by de Freitas et al.[53] The idea is to exploit their dark color to create a higher contrast with the white background of the LF strips, and therefore to improve the sensitivity of nanoparticle-based LFAs. These $Au-IrO_2$ NFs display strong optical properties, but due to their size (over 100 nm), they are not ideal for LFAs. Specifically, they would be more prone to precipitation and aggregation once dried on the LFA, limiting their flow through the membrane. Therefore, we rationally adapted their synthesis to decrease the NFs' size without compromising their stability. In particular, we achieved it by changing the reaction time and the reducing agent (citrate) concentration while keeping their optical properties. As a test bed, we successfully used the $Au-IrO_2$ NFs in a LFA for the detection of human immunoglobulin G (HIgG).[31,36]

RESULTS AND DISCUSSION

Synthesis of $Au-IrO_2$ Nanoflowers. The synthesis of $Au-IrO_2$ NFs is based on a two-step reaction, and the mechanism behind their formation agrees with the nucleation and growth theory, as previously reported.[53,56,57] In the first step, gold ($HAuCl_4$) and iridium salt ($IrCl_3{\cdot}xH_2O$) solutions were mixed to induce the formation of the Au nuclei/seeds through the reduction of $AuCl_4^-$ species to $AuCl_2^-$ by $IrCl_6^{2-}$[53,56] (see Scheme 1, nucleation). This first co-reduction produces a color change from yellow to yellow-greenish. Of

Scheme 1. Mechanism of $Au-IrO_2$ NFs Formation. (i) In the First Step, the Co-Reduction of Both Metal Precursors Leads to the Nanoflowers Nuclei (Nucleation); (ii) the Next Addition of Sodium Citrate Allows Their Further Reduction, Growth, and Stabilization, Inducing a Specific Morphology of Nanoflowers

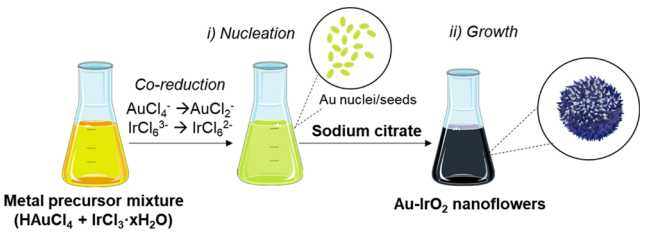

https://doi.org/10.1021/acsanm.2c04915
ACS Appl. Nano Mater. 2023, 6, 4151−4161

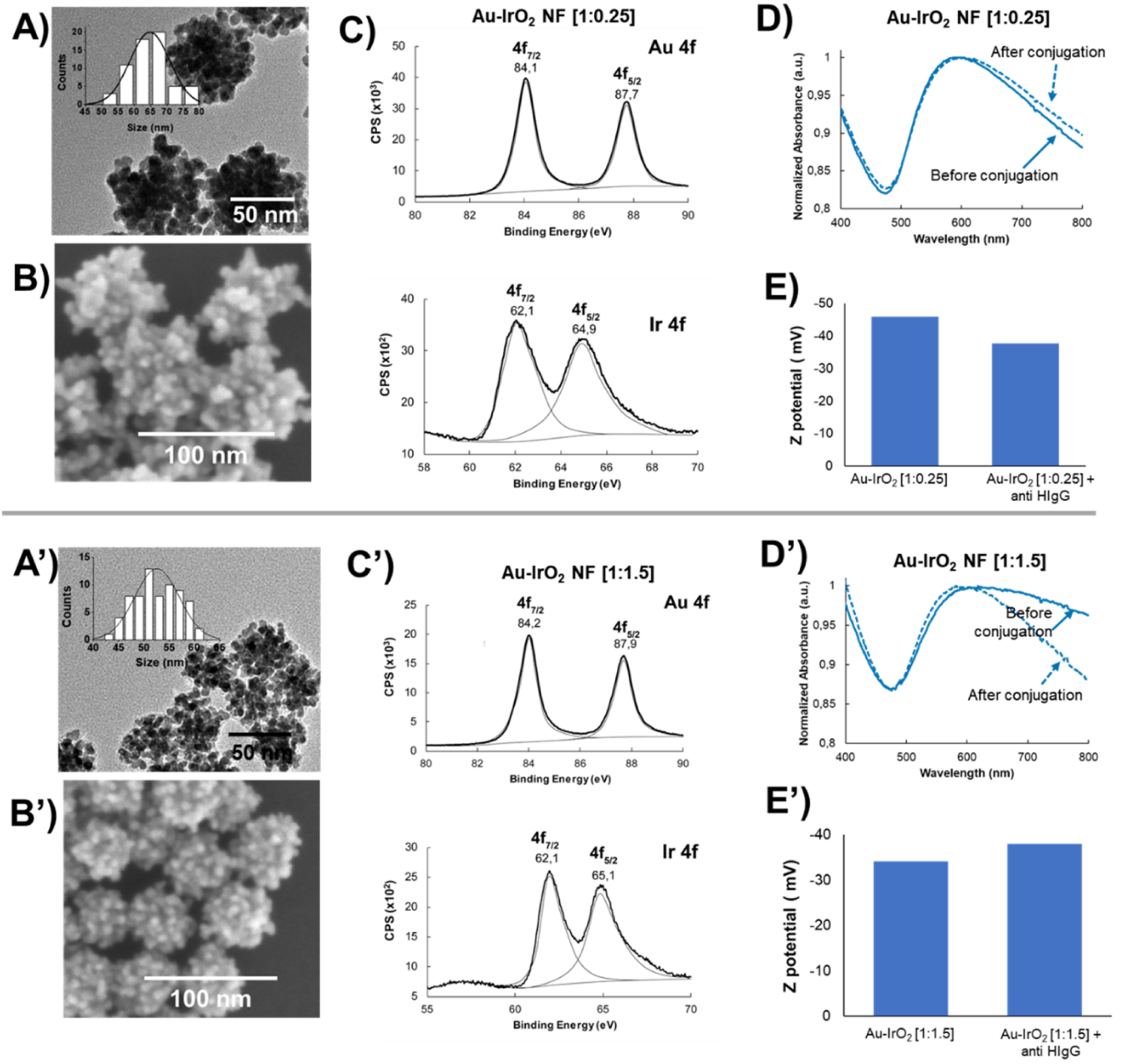

Figure 1. Characterization of Au−IrO_2 NFs and evaluation of the bioconjugation. The upper panel shows the characterization of the Au−IrO_2 NFs obtained with the [1:0.25] ratio using (A) the TEM, (B) the SEM, (C) the X-ray photoelectron spectra of Au 4f and Ir 4f, (D) UV−visible spectra before and after bioconjugation, and (E) *Z*-potential measurements before and after conjugation. Instead, the bottom panel (A′−E′) shows the same characterizations but for the Au−IrO_2 NFs obtained with the [1:1.5] ratio. In both cases, the Au−IrO_2 NFs resulted monodispersed and made of both Au and IrO_2; at the same time, the UV−vis and *Z*-potential measurements indicate the successful biofunctionalization of both nanoflowers with the anti-HIgG antibodies.

note, the mixing time of the precursors must be no longer than 5 min because this will induce the agglomeration of nanoflowers. This is due to the formation of bigger seeds, which leads to observe a solution that is clearly green. In the second step, the previously generated seeds were added into a boiling citrate solution to induce the growth of the nanoflowers by the further reduction of the pre-formed seeds by the citrate ions[53] (which act as a reducing agent and stabilizer) (see Scheme 1, growth). This second reduction process produces a second color change in the solution from yellow-greenish to blackish-blue. The different intermediates involved in the reaction (i.e., nucleation and growth) of the NFs display different colorimetric properties; therefore, the synthesis can be monitored by naked-eye and UV−visible spectroscopy. We tested two different metal ratios in order to evaluate how the metal content affects the plasmonic signal, and we selected [Au/Ir] ratios of [1:0.25] and [1:1.5]. The UV−visible spectra of the obtained Au−IrO_2 NFs suspension display a broad peak between 500 and 700 nm for both ratios, with maximum absorption around 600 nm (Figure S1). The presence of the single peak is indicative of the formation of an Au−IrO_2 bimetallic nanostructure, because two separated peaks indicate the formation of individual AuNPs and IrO_2 NPs (Figure

https://doi.org/10.1021/acsanm.2c04915
ACS Appl. Nano Mater. 2023, 6, 4151−4161

S2).[58−60] This preliminary data clearly demonstrates the efficacy of our synthetic approach to produce Au−IrO_2 NFs.

Our next goal is to synthetize smaller nanoflowers than those previously reported (i.e., <100 nm) to support the LFA platform. To achieve this, we decided to simultaneously work on two important parameters to tailor their synthesis: the [citrate]/[$AuCl_4^-$] ratio and the reaction time. Previous studies have reported that the [citrate]/[$AuCl_4^-$] ratio plays a key role in the synthesis and size of mono- or bimetallic nanoparticles in the presence of a reducing agent such as sodium citrate.[54,61] It has been reported that bigger ratios induce the formation of smaller nanoparticles.[61] Inspired by this observation, we decided to increase the citrate concentration from 1.7 to 2.5 mM to compensate an increment of [citrate]/[$AuCl_4^-$] ratio. Next, we also considered the reaction time as an important parameter because it is directly connected with the growth of the NFs. Therefore, we have also decreased the reaction time of the second step from 30 to 5 min to limit the NFs growth and size.

The rationale modification of both parameters of the reaction allowed us to obtain smaller nanoflowers with the expected stability and morphological features. We were able to decrease the diameter of Au−IrO_2 NFs [1:0.25] from 155 ± 6 to 65 ± 6 nm and the diameter of Au−IrO_2 NFs [1:1.5] from 93 ± 6 to 53 ± 4 nm, as shown by the TEM images in Figure 1. The results are in agreement with previous studies where the increase in the [citrate]/[$AuCl_4^-$] ratio provides smaller nanoparticles, while the higher content of iridium induces the formation of nanoflowers with a lower size (due to the faster reduction kinetics of the $AuCl_4^-$ species conducted by the $IrCl_6^{2-}$ ones).[53] After optimizing the reaction, we scaled-up the initial volume of the NFs synthesis up to five times, obtaining a final volume of 30 mL and characterized the morphology and size distribution of Au−IrO_2 NFs by using TEM measurements. The resulting scaled-up Au−IrO_2 NFs were quite homogeneous with a narrow size distribution (Figure S3A,B), as well as showed the same morphology as those synthesized in the initial volume. The size distribution histograms show that the diameters of Au−IrO_2 NFs [1:0.25] and [1:1.5] were 64 ± 3 nm (Figure S3A) and 55 ± 2 nm (Figure S3B), respectively. These results were consistent with the sizes of small-volume synthesis of Au−IrO_2 NFs; thus, we demonstrate the feasibility of a scale-up synthesis for Au−IrO_2 NFs.

Au−IrO_2 Nanoflower Characterization. Before applying the new Au−IrO_2 NFs as labels in LFAs, we proceeded with their full morphological and elemental characterization. Regarding the morphology of the particles, as shown by the TEM images (Figure 1A,A′), both Au−IrO_2 NFs samples exhibited good mono-dispersity, homogeneous size, and branches on their surfaces (similar to those obtained by de Freitas et al.),[53] resembling a flower-like nanostructure. Interestingly, using the [Au/Ir] ratio of [1:0.25], the nanostructures showed a spikier surface when compared with the ones with ratio [1:1.5] (see Figure 1B,B′). Regarding the elemental analysis, the EDX results confirmed the presence of gold and iridium in the nanoflowers, while the EDX line-scan profile showed the distribution of both elements through the entire nanoparticle (Figure S4). Finally, the nanoflower compositions were directly determined by inductively coupled plasma−optical emission spectrometry (ICP−OES), showing the following percentages Au−IrO_2 NFs [1:0.25] with 85% Au and 5.9% Ir, while the ones with a [1:1.5] ratio showed 76% Au and 10% Ir.

We employed X-ray photoelectron spectroscopy (XPS) to study the surface chemistry of the Au−IrO_2 NFs. In this context, prior to element identification and their respective binding energies, both systems were calibrated to the C (1s) line at 284.8 eV, and the data were analyzed using specific software as mentioned above. For gold, two photoemission peaks associated with the Au 4f spin−orbit components were found between 84 and 88 eV and identified as Au $4f_{7/2}$ and Au $4f_{5/2}$ core level regions, respectively (see Figure 1C,C′). These peaks separated by ≈3.7 eV are associated with Au^0, which is in agreement with the literature.[62,63] Regarding the iridium, two binding states around 62 and 65 eV were identified as Ir $4f_{7/2}$ and Ir $4f_{5/2}$ core-level regions, respectively. The values for this doublet, separated by ≈3 eV in binding energy, were very close with the ones reported for Ir^{4+} in IrO_2.[64−66] Detailed data about XPS spectra can be found in Table S1.

Bioconjugation of the Au−IrO_2 Nanoflowers. Bioconjugation of the synthesized particles was optimized using three different pH values and evaluated by UV−vis spectrophotometry. Using pH 9, we observed the aggregation of the Au−IrO_2 NF−antibody conjugate, making it not a suitable condition for the preparation of optical LFA's labels. Instead, pH 7 and 8 guaranteed the stability of the Au−IrO_2 solutions. Specifically, as shown in (Figure 1D,1D′), the maximum absorbance peak did not change for either of the two Au−IrO_2 NF compositions after the conjugation with antibodies, indicating that the monodispersity was maintained after the conjugation process. This behavior is similar to a previously reported study by our group in which IrO_2 NPs did not exhibit any measurable change after the bioconjugation at neutral pH.[22,66]

Dynamic light scattering (DLS) and *Z*-potential measurements were performed to AuNPs and Au−IrO_2 NFs before and after conjugation with the antibodies to evaluate the changes on the hydrodynamic sizes, surface charge, and stability of the nanoparticles. In all cases, the hydrodynamic sizes increased upon the bioconjugation (Figure 1E,E′), which can be attributable to a coating layer of antibodies over the nanoparticles (see Table S2). It is worthy to note that while the TEM provides the actual size of the metallic particle, the DLS provides the hydrodynamic size of the particle, which also takes into account the size of the antibodies on the particle surface. Finally, we estimated the stability of the Au−IrO_2 NFs using *Z*-potentials. Specifically, when absolute *Z*-potential values are within the range of ±30 mV, nanoparticles are likely to aggregate or sediment, instead if the absolute *Z*-potential values are above/below the ±30 mV range, nanoparticles remain stable in colloidal suspensions.[67] Before the conjugation, the *Z*-potential values (in mV) were −41, −45.9, and −34.9 for AuNPs, Au−IrO_2 [1:0.25], and Au−IrO_2 [1:1.5], respectively. These values indicated that they were stable in colloidal solutions and negatively charged because of the citrate present on their surface, acting as a stabilizer. The physisorption of antibodies onto the nanoparticle surface led to an increase in the *Z*-potential from negative values to fewer negative values (in mV) up to −35.6, −37.7, and −38 mV for AuNPs, Au−IrO_2 [1:0.25], and Au−IrO_2 [1:1.5], respectively. These values indicated both the presence of antibodies on the NF's surface and their stability (see Table S2).

Lateral Flow Immunoassay. To demonstrate the ability of Au−IrO_2 NFs to work as labels in LFAs, we compared their

https://doi.org/10.1021/acsanm.2c04915
ACS Appl. Nano Mater. 2023, 6, 4151−4161

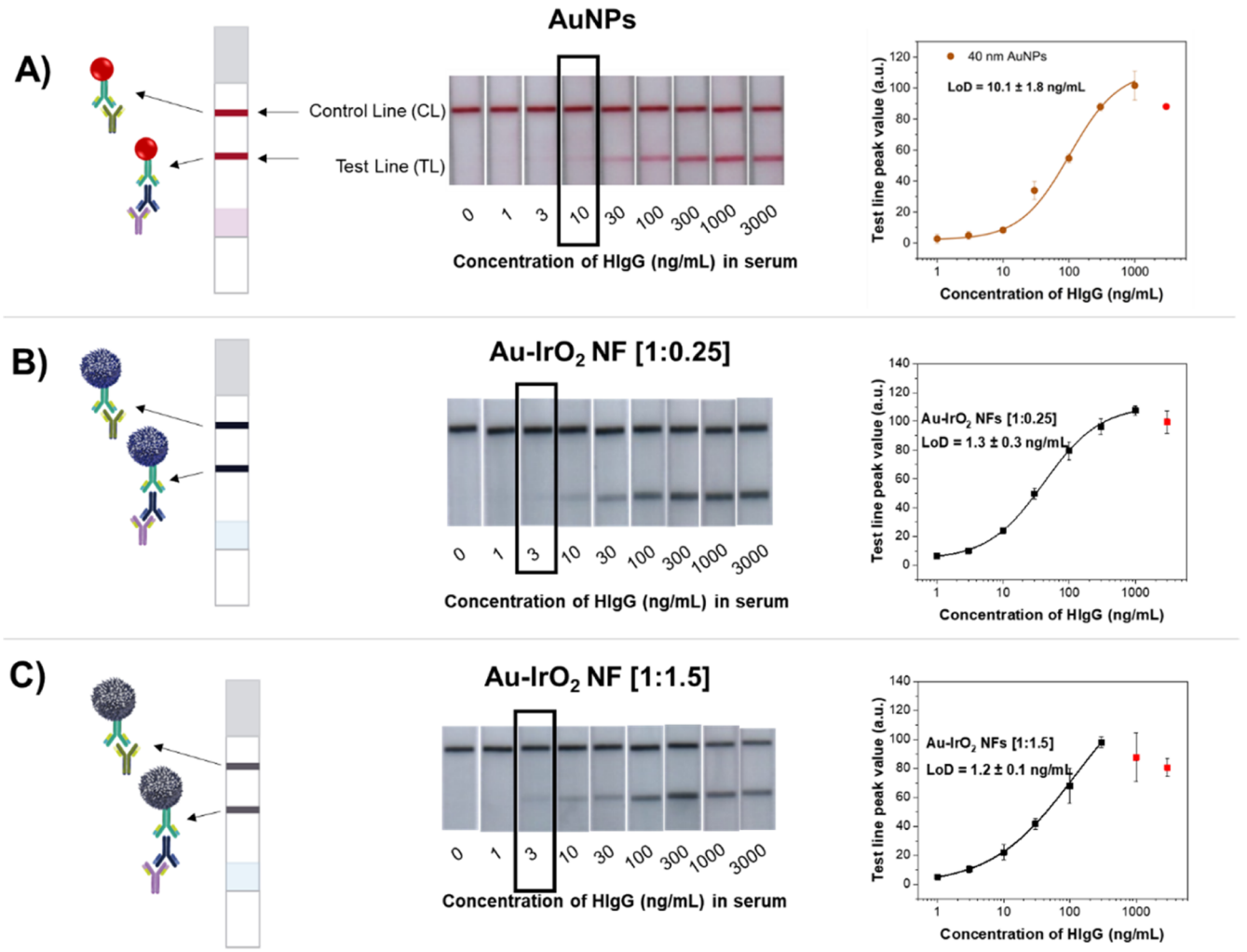

Figure 2. Quantification of HIgG in immunoglobulin-depleted human serum by LF strips with: (A) AuNPs, (B) Au−IrO_2 NFs [1:0.25], and (C) Au−IrO_2 NFs [1:1.5] as colorimetric labels, ranging from 1 to 3000 ng/mL and their corresponding calibration curves at their optimal pH. Black rectangle over the LF strips indicates the visual limit of detection.

analytical performance against standard AuNPs for the detection of HIgG, a clinically relevant biomarker used in serological assays. Specifically, we fabricated LFA strips using a protocol previously reported,[31] and we exploited three different NPs: AuNPs (40 nm in diameter) as a control, Au−IrO_2 NFs [1:0.25] and Au−IrO_2 NFs [1:1.5] to assess their performance on LFA strips. The effect of the AuNP's size on the LF sensitivity can be found in the Supporting Information (Figure S5). Then, we challenged AuNP- and Au−IrO_2 NFs-based LFAs at their optimal conditions with different concentrations of HIgG in immunoglobulin-depleted human serum samples ranging from 0 to 3000 ng/mL (Figure 2). Quantitative analyses of the LFA strips were performed according to Parolo et al.,[12] and the peak intensities of test lines were plotted versus HIgG concentration to obtain analytical parameters. Data were fitted using a four-parameter logistic curve as summarized in Table S3.

We found that AuNPs-based LFA strips exhibited an estimated visual limit of detection (LoD) of 10 ng/mL, while the use of nanoflowers allowed us to obtain lower visual LoDs of 3 ng/mL for both systems (i.e., Au−IrO_2 NFs [1:0.25] and [1:1.5]) (see Figure 2). The quantitative analysis of the LFAs using a previously reported procedure[12] also highlights the superior analytical properties of Au−IrO_2 NFs in comparison to the standard AuNPs. Specifically, the calculated LoDs were 10.1, 1.3, and 1.2 ng/mL for AuNPs, Au−IrO_2 NFs [1:0.25], and Au−IrO_2 NFs [1:1.5], respectively. Meaning that about 7-fold and almost 8.5-fold improvements were achieved using Au−IrO_2 NFs [1:0.25] and Au−IrO_2 NFs [1:1.5] with respect to the classical AuNPs-LFAs. The LoDs obtained in real samples were similar to those obtained with the human IgG in PBS buffer (Figure S6), showing that the matrix did not affect substantially the signal, thus proving their potential for real sample applications. As we mentioned before, the sensitivity can be improved by different factors such as size, shape, and optical properties of the nanoparticles used as labels. In this work, the main contributor to this improvement is definitely the high optical intensity of the Au−IrO_2 NFs, especially the Au−IrO_2 NFs [1:0.25] which molar extinction coefficient (ε) is twofold the $\varepsilon_{AuNPs(40nm)}$ used in this work, i.e., 5×10^9 vs 2.5×10^9 M^{-1} cm^{-1}. Calculations of these values can be found in the Supporting Information (see Table S4).

Specifically, the Au−IrO_2 NFs-based LFA strips employing a ratio of Au−IrO_2 NFs [1:0.25] display an intense blackish line, producing a bigger contrast with the nitrocellulose. On the contrary, using Au−IrO_2 NFs with higher iridium content [1:1.5] allow us to obtain a more grayish line at the same concentration of target (Figure S7). This difference can be

https://doi.org/10.1021/acsanm.2c04915
ACS Appl. Nano Mater. 2023, 6, 4151−4161

Table 1. Comparison of the Nanoparticle-Based LFAs for Detection of IgG

label	target	range (ng/mL)	lineal range (ng/mL)	LoD (ng/mL)	references
Au nanocages	rabbit IgG	0−50	0.5−50	0.1	68
IrO_2 NPs	human IgG	0−1000	250−750	70	22
AuNPs-17 nm	human IgG	0−1000	10−1000	35	26
				73	
Au−Pt NFs	rabbit IgG	0−20	0.5−20	0.047	69
Au−IrO_2 NFs [1:0.25]	human IgG	0−3000	10−300	1.3	this work
Au−IrO_2 NFs [1:1.5]				1.2	

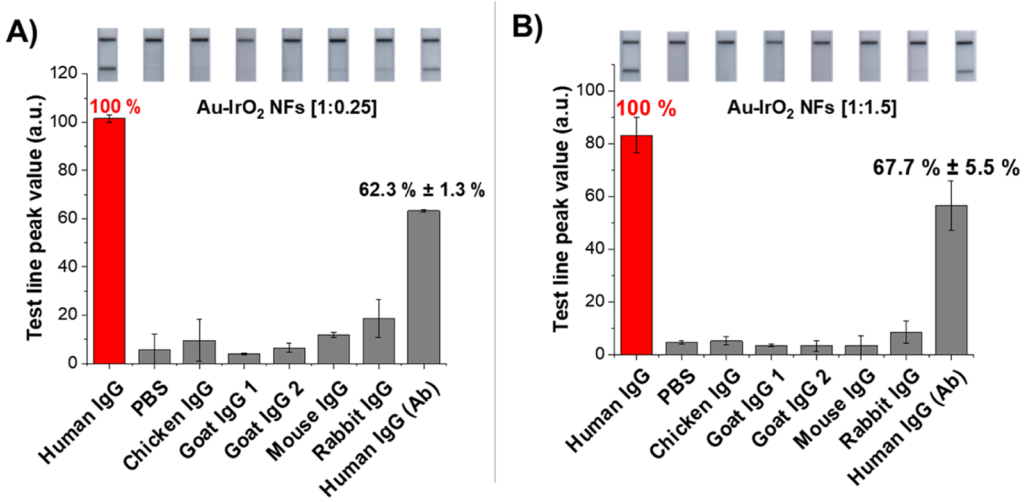

Figure 3. Specificity and selectivity tests of (A) Au−IrO_2 [1:0.25] and (B) Au−IrO_2 NFs [1:1.5] LFA for detection of human IgG. Immunoglobulin-depleted serum was spiked with 1000 ng/mL of IgG from chicken, goat, mouse, and rabbit hosts as the interferences.

Table 2. Recoveries from the Intra- and Inter-Assays for Detecting HIgG in Immunoglobulin-Depleted Human Serum Samples by Au−IrO_2 NFs LFAs

		intra-assay		inter-assay	
Au−IrO_2 NFs	[spiked HIgG] ng/mL	[calculated HIgG] ng/mL	recovery (%)	[calculated HIgG] ng/mL	recovery (%)
[1:0.25]	30	27.6 ± 3.3	91.9 ± 11.1	30.9 ± 3.2	103.1 ± 10.5
	100	98.5 ± 4.8	98.5 ± 4.8	99.9 ± 12.5	99.9 ± 12.5
	300	298.0 ± 31.2	99.3 ± 10.4	286.5 ± 38.1	95.5 ± 12.7
[1:1.5]	30	32.7 ± 2.4	109.7 ± 7.2	31.5 ± 4.3	103.2 ± 13.3
	100	106.5 ± 6.3	106.5 ± 6.3	97.0 ± 14.4	97.0 ± 14.4
	300	276.6 ± 23.9	92.2 ± 8.0	258.0 ± 36.5	86.0 ± 12.2

attributable to the suppression of the localized surface plasmon resonance (LSPR) of the plasmonic component (Au) caused by a higher content of iridium in the Au−IrO_2 NFs [1:1.5], which leads to a decrease in the absorbance intensity of the nanoflowers.[53] These results are also supported by the better defined plasmonic peak of Au−IrO_2 NFs [1:0.25] observed in the UV−vis measurement.

An overview of different nanoparticle-based LFAs for the detection of immunoglobulin G is presented in Table 1. From the listed nanoparticles, besides the ones used in this work, the nanoparticles that exhibit the lowest LoDs correspond to the gold nanocages[68] and Au−Pt nanoflowers[69] because of their unique shapes that allow a higher amount of immobilized antibodies on their surfaces. Spherical AuNPs (17 nm) were used as labels for the detection of HIgG, leading to LoDs of 35 and 73 ng/mL in nitrocellulose membranes with different pore sizes, which also have an impact on the sensitivity of the assay.[26] A previous work from our group employed IrO_2 NPs as labels in LFAs due to their bioconjugation capabilities and their vivid blue color, enabling a better contrast with the nitrocellulose, improving the LoD by twofold compared with AuNP-based LFAs for HIgG detection.[22] Despite this, their synthesis is lengthy (ca. 3−4 h) and requires a high amount of blocking proteins upon bioconjugation to avoid the unspecific adsorptions onto the detection membrane. This blocking condition diminish the optical signal on the LFA strip and may detract from their colorimetric advantage with the AuNPs. Here instead, we achieved an 8.5-fold improvement using Au−IrO_2 NFs [1:1.5] (when compared with the optimized AuNP-based LFA) that are easy to synthesize and modify. Additionally, the Au−IrO_2 NFs have a tremendous potential to be used as electrocatalytic labels.

Our LFA strips are sensitive and selective. To demonstrate the specificity of the Au−IrO_2 NFs-based LFAs, we challenged them against immunoglobulin-depleted human serum samples spiked with 1000 ng/mL of IgG from different hosts, such as chicken, goat, mouse, rabbit, and human. This ensures to change the chemistry of the biomolecule without changing the

https://doi.org/10.1021/acsanm.2c04915
ACS Appl. Nano Mater. 2023, 6, 4151−4161

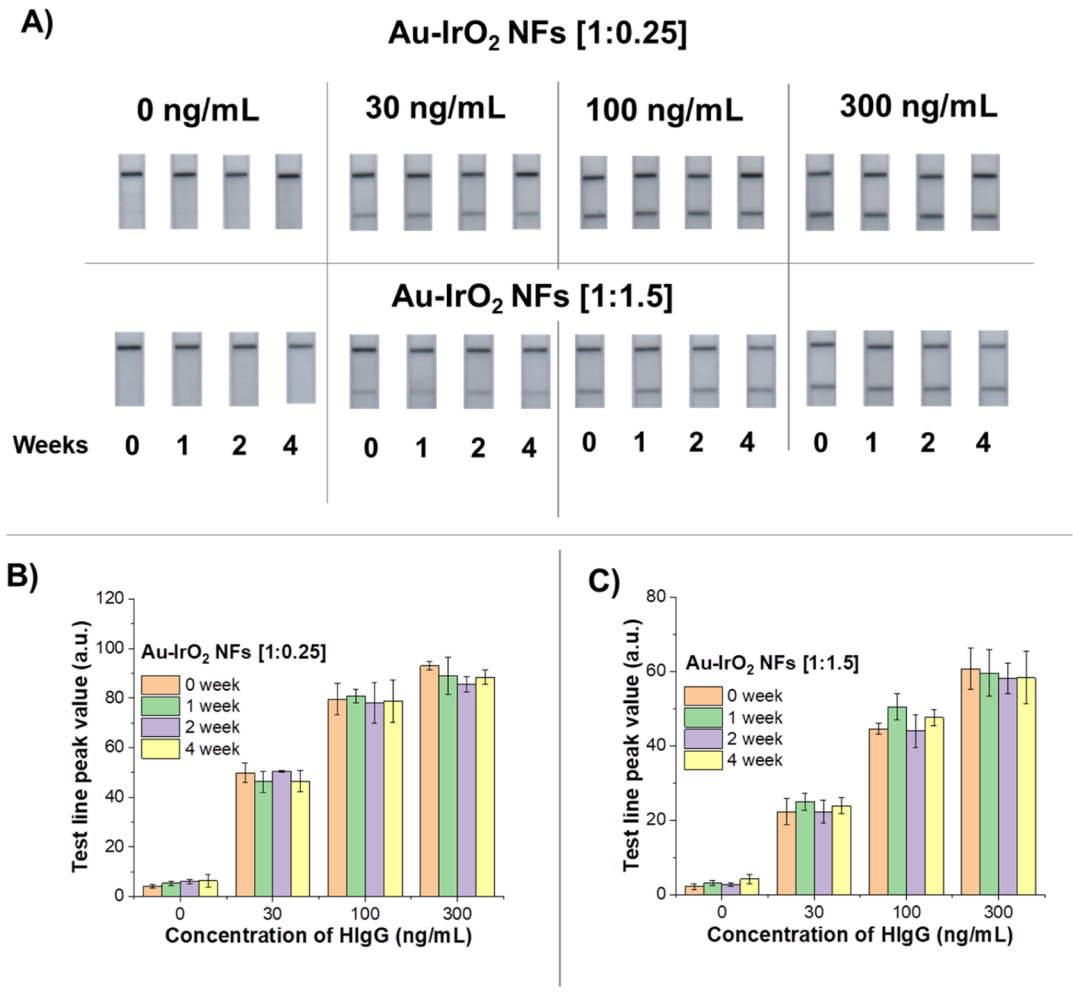

Figure 4. Stability assays. Au−IrO_2 NFs-based LFAs after performing the stability assay (A). Optical intensity values for the detection of 0, 30, 100, and 3000 ng/mL of HIgG in immunoglobulin-depleted human serum, using LFA strips stored at room temperature for 0−4 weeks for (B) Au−IrO_2 NFs [1:0.25] and (C) Au−IrO_2 NFs [1:1.5] LFA, respectively.

properties of the biological fluid. As demonstrated by the collected data, IgGs from chicken, goat, mouse, and rabbit produced very weak colorimetric signals, similar to their blank (obtained in PBS) (see Figure 3). As a positive control experiment, we spiked the serum sample with antibodies from human and, as expected, we observed a 62.3 and 67.7% cross-reaction rate with human IgG antigen (100%). Given the results, both Au−IrO_2 NFs-based LF systems showed good specificity and selectivity, as well as they could discriminate between human IgG from other IgG interfering biomolecules.

The performance of the proposed LFAs was also evaluated by recovery experiments. Immunoglobulin-depleted human serum samples were spiked with 30, 100, and 300 ng/mL of human IgG in the same day (intra-assay) and in 3 consecutive days (inter-assay). The recoveries of Au−IrO_2 NFs [1:0.25] LFA ranged between 91.9 and 99.3% for intra-assay experiments and varied between 95.5 and 103.1% for inter-assay experiments. Similarly, the intra- and inter-assay recoveries of Au−IrO_2 NFs [1:1.5] LFA were from 92.2 to 109.7% and from 86.0 to 103.2%, respectively (see Table 2). Summarizing, all the recovery values were between 86 and 109%, and the coefficients of variation (CV) were less than 15% (Table 2). These results demonstrate that both Au−IrO_2 NFs LFAs possess a good accuracy and can be considered as a promising alternative for the detection of HIgG in a real scenario.

To assess the performance of the proposed LFAs in the long-term, the Au−IrO_2 NFs-based LF strips were stored at room temperature for 0, 1, 2, and 4 weeks, and the signal of immunoglobulin-depleted human serum samples with 0, 30, 100, and 300 ng/mL HIgG was measured (Figure 4A). For all human IgG concentrations tested, the CV values over the time ranged between 0.5 and 7.1% for the Au−IrO_2 NFs [1:0.25] LFA (Figure 4B) and between 0.7 and 8.5% for the Au−IrO_2 NFs [1:1.5] LFA (Figure 4C). These values demonstrate that both Au−IrO_2 NFs-based LFAs were stable for at least 1 month.

■ CONCLUSIONS

To the best of our knowledge, we have demonstrated for the first time the use of tailored Au−IrO_2 NFs as colorimetric labels for LFAs for the detection of HIgG as a model biomarker. The promising results obtained in this work indicate that Au−IrO_2 NFs can be used as superior colorimetric labels (compared to the standard AuNPs) in LFAs for the detection of protein biomarkers. Specifically, we managed to decrease the Au−IrO_2 NFs diameter to make them better suited to flow through the LFA strips, while at the same time we preserved their strong plasmonic behavior and stability. Particularly relevant for point-of-care applications, the synthesis and functionalization of Au−IrO_2 NFs are simple

https://doi.org/10.1021/acsanm.2c04915
ACS Appl. Nano Mater. 2023, 6, 4151−4161

and straightforward, potentially supporting their mass production. Employing them as colorimetric labels in LFAs, we achieved an improvement in the LoD of up to 8.5-fold when compared to classical 40 nm AuNPs. Despite we demonstrate the ability of the Au−IrO_2 NFs-based LFA strips to detect the target in a commercial biological fluid, the selected artificially treated sample does not have the same complexity of a pooled human serum sample. This represents a limitation of this work; therefore, further studies need to be performed to optimize the LFAs to support samples from real patients. Looking ahead, we believe that due to the presence of IrO_2 on the nanoflower, they could also act as dual optical/electrochemical labels in paper-based electrochemical systems,[66] thanks to their plasmonic peak and electrocatalytic behavior.[53]

EXPERIMENTAL SECTION

Reagents and Apparatuses. $HAuCl_4{\cdot}3H_2O$ 99%, $IrCl_3{\cdot}xH_2O$ 99%, $Na_3C_6O_7H_5{\cdot}2H_2O$ 99%, boric acid (H_3BO_3, 99%), sodium tetraborate decahydrate ($B_4NaO_7{\cdot}H_2O$, 99%), phosphate buffered saline tablet, Tween-20, sucrose (99.5%), and bovine serum albumin (BSA, 96%) were supplied by Sigma-Aldrich. Human IgG from human serum (I2511), anti-human IgG (produced in goat; I1886), and anti-human IgG γ chain-specific HRP-modified (produced in goat; A6029) were also supplied by Sigma-Aldrich (Spain), while anti-goat IgG (produced in chicken, ab86245) and anti-mouse IgG H&L (produced in goat, ab6708) were supplied by Abcam. Human IgG-depleted serum was purchased from Celprogen. Chicken IgG (ab6829) and goat IgG 2 (ab6702) were bought from Abcam. Human IgG antibodies (1A6) were supplied by Thermo Fisher. Mouse IgG (40588-T62) and rabbit IgG (40143-R019) were supplied by Sino Biological. 20, 40, 60, and 80 nm of AuNPs were supplied by nanoComposix.

Nitrocellulose membrane CN150 was purchased from Sartorius Stedim (Göttingen, Germany). Cellulose membrane (CFSP001700) and glass fiber were purchased from Merck Millipore (Billerica, MA, USA), and supporting adhesive cards were purchased from Kenosha (Amstelveen, The Netherlands).

The stirrer used for conjugating antibodies to nanoflowers was a PCMT ThermoShaker (Grant Instruments, UK). A lateral flow dispenser was used to distribute the reagents over the nitrocellulose (IsoFlow Bioreagent, Imagene Technology, Germany). Nanoparticles were centrifuged in a Centrifuge Allegra 64 R from Beckman Coulter (USA). Lateral flow strips were cut using a cutter from Shanghai Kinbio Tech (China). A spectrophotometer SpectraMax ID3 (Molecular Devices, USA) was used to measure the UV−vis spectra of nanoflower suspensions. LFA scanner SkanMulti from Skannex (Oslo, Norway) was used to scan the LFs strips.

Preparation of Nanomaterials. Both AuNPs and Au−IrO_2 NFs were synthesized as previously reported in the literature. The former were synthesized by the Turkevich method,[70] while the latter were prepared using a modified version of the protocol reported by de Freitas et al.[53]

AuNPs. For preparing AuNPs, a 50 mL of aqueous solution of 0.1% $HAuCl_4{\cdot}3H_2O$ was heated to boiling and vigorously stirred in a 250 mL Erlenmeyer flask. Then, 1.25 mL of 1% sodium citrate was added quickly to the boiling solution. Boiling was continued for an additional 10 min upon the color change from pale yellow to bright red. Finally, the suspension was cooled to room temperature under continuous stirring and stored at 4 °C until use.

Au−IrO_2 NFs. In order to evaluate the colorimetric properties of the Au−IrO_2 NFs, we prepared two nanoflowers with different compositions. Specifically, we used two different molar ratios of Au and Ir (i.e., Au/Ir [1:0.25] and [1:1.5]). In addition, we modified the protocol reported by de Freitas et al. by changing the citrate concentration and reaction time. These modifications in the protocol were necessary for the fabrication of particles with diameters suitable to run through the nitrocellulose pores.

Briefly, 5 mL of sodium citrate (2.5 mM) was heated until boiling. Meanwhile, 354 μL of $HAuCl_4{\cdot}3H_2O$, 12 mM, were mixed with 88.5 or 531 μL of $IrCl_3{\cdot}xH_2O$, 12 mM (for [1:0.25] and [1:1.5] ratios, respectively), and then reached up to 1 mL with milliQ water. This solution was added in one shot to the boiling solution of citrate. Boiling was continued for an additional 5 min upon the color change from pale green to petrol-blue. Finally, the suspension was cooled to room temperature under continuous stirring and then stored at 4 °C until use.

Characterization of Au−IrO_2 NFs. ICP−OES was used as a technique to determine the metal content (i.e., gold and iridium percentage) of the nanoflowers and was performed at the Servei d'Anàlisi Química of the Universitat Autónoma de Barcelona by using an inductively coupled plasma−optical emission spectrometer (PerkinElmer, model Optima 4300DV).

All the size measurements and morphological observations of nanoflowers were conducted in a field emission gun transmission electronic microscope (model TecnaiTM G2F20, FEI, USA) and a field emission scanning electron microscope (model Magellan 400L, FEI, USA).

XPS measurements were performed at room temperature with a SPECS PHOIBOS 150 hemispherical analyzer (SPECS GmbH, Berlin, Germany) at a base pressure of 5×10^{-10} mbar using monochromatic Al Kα radiation (1486.74 eV) as an excitation source operated at 300 W. The energy resolution, as measured by the full width at half-maximum of the Ag $3d_{5/2}$ peak for a sputtered silver foil, was 0.62 eV. Measurements were made using CasaXPS software. The hydrodynamic particle diameters and zeta potential measurements were performed in a Zetasizer Nano ZS (Malvern Instruments, UK).

Conjugation of Antibodies to Nanomaterials. Anti-human IgG antibodies were conjugated to nanomaterials, as previously reported.[12,31] AuNPs were adjusted to pH 9 with borate buffer (BB), 0.1 M and Au−IrO_2 NFs were adjusted to pH 7 with BB 0.01 M, at pH 8 and 9 with BB 0,1 M. Then, 1.5 mL of both nanomaterials were mixed with 100 μL of 140 μg/mL of anti-human IgG γ-chain specific HRP modified and incubated for 20 min at 650 rpm at room temperature. Then, 100 μL of 1 mg/mL BSA solution was added, and stirring was continued for another 20 min at 650 rpm at room temperature. AuNPs were centrifuged at 14,000 rpm and 4 °C for 20 min, while Au−IrO_2 NFs were centrifuged at 7000 rpm at room temperature for 20 min. Supernatants were removed, and the pellets of the conjugated nanomaterials were resuspended in 500 μL PBS buffer containing 5% sucrose, 1% BSA, and 0.5% Tween-20 to obtain an optical density (OD) of 3. For this conjugation, the optimal pH was 9 and 7 for AuNPs and Au−IrO_2 NFs, respectively.

Lateral Flow Immunoassays: Preparation of the Strips and Procedure. Preparation and Assembly. For HIgG detection, test and control lines were spotted onto the nitrocellulose by printing 1 mg/mL of anti-human IgG and anti-goat IgG, respectively, at a dispensing rate of 0.5 μL/cm using an IsoFlow reagent dispensing system. Finally, the nitrocellulose was dried at 37 °C for 2 h. The sample pad (cellulose) was prepared by dipping it into 10 mM PBS, 5% BSA, and 0.05% Tween-20 and dried at 60 °C for 2 h. The conjugate pads were prepared by carefully dispensing the previously prepared anti-human IgG (γ-chain specific)-HRP/nanoparticle conjugates (with an OD = 3) and dried under vacuum for 2 h. Therefore, the different pads were assembled as follows: detection pad (nitrocellulose membrane), conjugation, sample, and absorbent pad. Finally, the strips were cut 4 mm wide using a strip cutter. Under these conditions, the minimum number of nanoparticles per mm^2 able to discriminate the intensity line from the background were 8.4×10^5 and 1.6×10^6 particles/mm^2 for Au−IrO_2 [1:0.25] NFs (65 nm) and Au−IrO_2 [1:0.25] NFs (53 nm), respectively.[71]

Lateral Flow Immunoassay Procedure. Sample solutions of 80 μL containing different concentrations of HIgG in PBS 10 mM at pH 7.4 ranging from 1 to 3000 ng/mL, were dispensed onto the sample pad and allowed to flow through the strips during 15 min. Although a visual response was observed in that time, the same volume of buffer was again dispensed to wash away the excess of conjugate and were

https://doi.org/10.1021/acsanm.2c04915
ACS Appl. Nano Mater. 2023, 6, 4151−4161

dried for another 15 min. Three replicates of each concentration were performed, including the blank (buffer only).

Calibration Curves of Au−IrO_2 NFs for Detecting HIgG in Spiked Human Serum (Immunoglobulins Depleted). Calibration curves, specificity, recovery, and stability tests were performed by using immunoglobulin-depleted human serum spiked with human IgG. Specifically, samples were spiked with 0, 1, 3, 10, 30, 100, 300, 1000, and 3000 ng/mL of HIgG and tested by Au−IrO_2 NFs LFAs to check the feasibility in real sample detection.

Specificity Tests for Au−IrO_2 NFs LFAs. Immunoglobulin-depleted human serum was spiked with 1000 ng/mL of IgGs from chicken, goat, mouse, rabbit, and human. Human serum samples (0 and 1000 ng/mL HIgG spiked) and the above-mentioned samples were tested by using the Au−IrO_2 NFs [1:0.25] and Au−IrO_2 NFs [1:1.5] LF strips to evaluate their specificity and selectivity for detection of HIgG.

Recovery Tests for Au−IrO_2 NFs LFAs. Immunoglobulin-depleted human serum was spiked with 0, 30, 100, and 300 ng/mL of HIgG. Samples were detected in 1 day (intra-assay) and in 3 consecutive days (inter-assay). Recoveries were calculated by the equation (spiked concentration of HIgG/calculated concentration of HIgG × 100) to evaluate the accuracy and precision of the Au−IrO_2 NFs LFAs.

Stability Tests for Au−IrO_2 NFs LFAs. Au−IrO_2 NFs LF strips were stored at room temperature (25 °C) for 0, 1, 2, and 4 weeks. Immunoglobulin-depleted human serum samples spiked with 0, 30, 100, and 300 ng/mL of HIgG were tested by using the LF strips per storage period to evaluate the stability of the Au−IrO_2 NF systems.

Data Analysis. Once dry, a flatbed SkanMulti LFA scanner was used to scan the strips for obtaining the respective calibration curves. The image analysis was performed using ImageJ software, following the procedure reported by Parolo et al.[12] Origin version 8.5 software was used to fit the data to a four-parameter logistic curve.

■ ASSOCIATED CONTENT

Supporting Information

The Supporting Information is available free of charge at https://pubs.acs.org/doi/10.1021/acsanm.2c04915.

Characterization results of Au−IrO_2 NFs, including UV−vis spectra, TEM images, EDX and line scale profiles, XPS spectra, DLS curves, and *Z*-potential measurements, and calibration curve data for Au−IrO_2 LFAs and AuNPs-LFAs (PDF)

■ AUTHOR INFORMATION

Corresponding Authors

Lourdes Rivas − *Nanobioelectronics & Biosensors Group, Institut Català de Nanociència i Nanotecnologia (ICN2), and the Barcelona Institute of Science and Technology (BIST), 08193 Barcelona, Spain;* orcid.org/0000-0002-1510-5927; Email: lourdes.rivas.t@gmail.com

Arben Merkoçi − *Nanobioelectronics & Biosensors Group, Institut Català de Nanociència i Nanotecnologia (ICN2), and the Barcelona Institute of Science and Technology (BIST), 08193 Barcelona, Spain; ICREA, Institució Catalana de Recerca i Estudis Avançats, 08010 Barcelona, Spain;* orcid.org/0000-0003-2486-8085; Email: arben.merkoci@icn2.cat

Authors

Liming Hu − *Nanobioelectronics & Biosensors Group, Institut Català de Nanociència i Nanotecnologia (ICN2), and the Barcelona Institute of Science and Technology (BIST), 08193 Barcelona, Spain;* orcid.org/0000-0002-8666-9287

Claudio Parolo − *Nanobioelectronics & Biosensors Group, Institut Català de Nanociència i Nanotecnologia (ICN2), and the Barcelona Institute of Science and Technology (BIST), 08193 Barcelona, Spain; Barcelona Institute for Global Health (ISGlobal), 08036 Barcelona, Spain;* orcid.org/0000-0001-9481-4408

Andrea Idili − *Nanobioelectronics & Biosensors Group, Institut Català de Nanociència i Nanotecnologia (ICN2), and the Barcelona Institute of Science and Technology (BIST), 08193 Barcelona, Spain; Chemistry Department, University of Rome, Tor Vergata, 00133 Rome, Italy;* orcid.org/0000-0002-6004-270X

Complete contact information is available at: https://pubs.acs.org/10.1021/acsanm.2c04915

Author Contributions

L.R. and L.H. contributed equally to this work. L.R. conceptualization, methodology, experimental, formal analysis, figures, writing-original draft, writing-review and editing. L.H. experimental, methodology, formal analysis, figures, writing-review and editing. C.P. methodology, writing-original draft, writing-review and editing. A.I. writing-original draft, writing-review and editing. A.M. funding acquisition, supervision.

Notes

The authors declare no competing financial interest.

■ ACKNOWLEDGMENTS

ICN2 is funded by the CERCA Programme/Generalitat de Catalunya. C.P. (ISGlobal) acknowledges support from the Spanish Ministry of Science and Innovation and the State Research Agency through the "Centro de Excelencia Severo Ochoa 2019-2023" Program (CEX2018-000806-S), and support from the Generalitat de Catalunya through the CERCA Program. L.H. acknowledges funding through the China Scholarship Council, as well as acknowledges Autonomous University of Barcelona (UAB) for their support. A.I. was supported by a PROBIST postdoctoral fellowship funded by the European Research Council (Marie Skłodowska-Curie grant agreement no. 754510). L.R. acknowledges Dr. L.K. for her valuable assistance.

■ REFERENCES

(1) Kevadiya, B. D.; Machhi, J.; Herskovitz, J.; Oleynikov, M. D.; Blomberg, W. R.; Bajwa, N.; Soni, D.; Das, S.; Hasan, M.; Patel, M.; Senan, A. M.; Gorantla, S.; McMillan, J. E.; Edagwa, B.; Eisenberg, R.; Gurumurthy, C. B.; Reid, S. P. M.; Punyadeera, C.; Chang, L.; Gendelman, H. E. Diagnostics for SARS-CoV-2 Infections. *Nat. Mater.* **2021**, *20*, 593−605.

(2) Rosati, G.; Idili, A.; Parolo, C.; Fuentes-Chust, C.; Calucho, E.; Hu, L.; Castro e Silva, C. D. C.; Rivas, L.; Nguyen, E. P.; Bergua, J. F.; Alvárez-Diduk, R.; Muñoz, J.; Junot, C.; Penon, O.; Monferrer, D.; Delamarche, E.; Merkoçi, A. Nanodiagnostics to Face SARS-CoV-2 and Future Pandemics: From an Idea to the Market and Beyond. *ACS Nano* **2021**, *15*, 17137−17149.

(3) Mak, W. C.; Beni, V.; Turner, A. P. F. Lateral-Flow Technology: From Visual to Instrumental. *TrAC, Trends Anal. Chem.* **2016**, *79*, 297−305.

(4) Banerjee, R.; Jaiswal, A. Recent Advances in Nanoparticle-Based Lateral Flow Immunoassay as a Point-of-Care Diagnostic Tool for Infectious Agents and Diseases. *Analyst* **2018**, *143*, 1970−1996.

(5) Calabretta, M. M.; Zangheri, M.; Lopreside, A.; Marchegiani, E.; Montali, L.; Simoni, P.; Roda, A. Precision Medicine, Bioanalytics and Nanomaterials: Toward a New Generation of Personalized Portable Diagnostics. *Analyst* **2020**, *145*, 2841−2853.

(6) Rodriguez, R. S.; O'Keefe, T. L.; Froehlich, C.; Lewis, R. E.; Sheldon, T. R.; Haynes, C. L. Sensing Food Contaminants: Advances in Analytical Methods and Techniques. *Anal. Chem.* **2021**, *93*, 23−40.

(7) Xing, C.; Liu, L.; Zhang, X.; Kuang, H.; Xu, C. Colorimetric Detection of Mercury Based on a Strip Sensor. *Anal. Methods* **2014**, *6*, 6247−6253.
(8) Bergua, J. F.; Hu, L.; Fuentes-Chust, C.; Álvarez-Diduk, R.; Hassan, A. H. A.; Parolo, C.; Merkoçi, A. Lateral Flow Device for Water Fecal Pollution Assessment: From Troubleshooting of Its Microfluidics Using Bioluminescence to Colorimetric Monitoring of GenericEscherichia Coli. *Lab Chip* **2021**, *21*, 2417−2426.
(9) Shandilya, R.; Bhargava, A.; Bunkar, N.; Tiwari, R.; Goryacheva, I. Y.; Mishra, P. K. Nanobiosensors: Point-of-Care Approaches for Cancer Diagnostics. *Biosens. Bioelectron.* **2019**, *130*, 147−165.
(10) Wang, X.; Li, F.; Guo, Y. Recent Trends in Nanomaterial-Based Biosensors for Point-of-Care Testing. *Front. Chem.* **2020**, *8*, 1−6.
(11) Zhou, Y.; Wu, Y.; Ding, L.; Huang, X.; Xiong, Y. Point-of-Care COVID-19 Diagnostics Powered by Lateral Flow Assay. *TrAC, Trends Anal. Chem.* **2021**, *145*, 116452.
(12) Parolo, C.; Sena-Torralba, A.; Bergua, J. F.; Calucho, E.; Fuentes-Chust, C.; Hu, L.; Rivas, L.; Álvarez-Diduk, R.; Nguyen, E. P.; Cinti, S.; Quesada-González, D.; Merkoçi, A. Tutorial: Design and Fabrication of Nanoparticle-Based Lateral-Flow Immunoassays. *Nat. Protoc.* **2020**, *15*, 3788−3816.
(13) Gasperino, D.; Baughman, T.; Hsieh, H. V.; Bell, D.; Weigl, B. H. Improving Lateral Flow Assay Performance Using Computational Modeling. *Annu. Rev. Anal. Chem.* **2018**, *11*, 219−244.
(14) Mahmoudi, T.; Pourhassan-Moghaddam, M.; Shirdel, B.; Baradaran, B.; Morales-Narváez, E.; Golmohammadi, H. (Nano)tag-antibody conjugates in rapid tests. *J. Mater. Chem. B* **2021**, *9*, 5414−5438.
(15) Pirzada, M.; Altintas, Z. Nanomaterials for Healthcare Biosensing Applications. *Sensors* **2019**, *19*, 5311.
(16) Song, L.; Chen, J.; Xu, B.; Huang, Y. Flexible Plasmonic Biosensors for Healthcare Monitoring: Progress and Prospects. *ACS Nano* **2021**, *15*, 18822−18847.
(17) Liu, H.; Zeng, H.; Song, L.; Zhang, H.; Chen, J.; Li, L.; Xiao, L.; Su, Z.; Huang, J.; Xiao, Z. Etched-Spiky Au@Ag Plasmonic-Superstructure Monolayer Films for Triple Amplification of Surface-Enhanced Raman Scattering Signals. *Nanoscale Horiz.* **2022**, *7*, 554−561.
(18) Liu, Y.; Zhan, L.; Qin, Z.; Sackrison, J.; Bischof, J. C. Ultrasensitive and Highly Specific Lateral Flow Assays for Point-of-Care Diagnosis. *ACS Nano* **2021**, *15*, 3593−3611.
(19) Nguyen, V.; Song, S.; Park, S.; Joo, C. Recent Advances in High-Sensitivity Detection Methods for Paper-Based Lateral-Flow Assay. *Biosens. Bioelectron.* **2020**, *152*, 112015.
(20) Bishop, J. D.; Hsieh, H. V.; Gasperino, D. J.; Weigl, B. H. Sensitivity Enhancement in Lateral Flow Assays: A Systems Perspective. *Lab Chip* **2019**, *19*, 2486−2499.
(21) Loynachan, C. N.; Thomas, M. R.; Gray, E. R.; Richards, D. A.; Kim, J.; Miller, B. S.; Brookes, J. C.; Agarwal, S.; Chudasama, V.; McKendry, R. A.; Stevens, M. M. Platinum Nanocatalyst Amplification: Redefining the Gold Standard for Lateral Flow Immunoassays with Ultrabroad Dynamic Range. *ACS Nano* **2018**, *12*, 279−288.
(22) Quesada-González, D.; Sena-Torralba, A.; Wicaksono, W. P.; de la Escosura-Muñiz, A.; Ivandini, T. A.; Merkoçi, A. Iridium oxide (IV) nanoparticle-based lateral flow immunoassay. *Biosens. Bioelectron.* **2019**, *132*, 132−135.
(23) Miller, B. S.; Bezinge, L.; Gliddon, H. D.; Huang, D.; Dold, G.; Gray, E. R.; Heaney, J.; Dobson, P. J.; Nastouli, E.; Morton, J. J. L.; McKendry, R. A. Spin-Enhanced Nanodiamond Biosensing for Ultrasensitive Diagnostics. *Nature* **2020**, *587*, 588−593.
(24) Ruiz-Sanchez, A.; Parolo, C.; Miller, B. S.; Gray, E. R.; Schlegel, K.; McKendry, R. A. Tuneable Plasmonic Gold Dendrimer Nanochains for Sensitive Disease Detection. *J. Mater. Chem. B* **2017**, *5*, 7262−7266.
(25) Parolo, C.; Medina-Sánchez, M.; de la Escosura-Muñiz, A.; Merkoçi, A. Simple Paper Architecture Modifications Lead to Enhanced Sensitivity in Nanoparticle Based Lateral Flow Immunoassays. *Lab Chip* **2013**, *13*, 386−390.
(26) Sena-Torralba, A.; Ngo, D. B.; Parolo, C.; Hu, L.; Álvarez-Diduk, R.; Bergua, J. F.; Rosati, G.; Surareungchai, W.; Merkoçi, A. Lateral Flow Assay Modified with Time-Delay Wax Barriers as a Sensitivity and Signal Enhancement Strategy. *Biosens. Bioelectron.* **2020**, *168*, 112559.
(27) Sena-Torralba, A.; Torné-Morató, H.; Parolo, C.; Ranjbar, S.; Farahmand Nejad, M. A.; Álvarez-Diduk, R.; Idili, A.; Hormozi-Nezhad, M. R.; Merkoçi, A. A Novel Ratiometric Fluorescent Approach for the Modulation of the Dynamic Range of Lateral Flow Immunoassays. *Adv. Mater. Technol.* **2022**, *7*, 2101450.
(28) Rivas, L.; de la Escosura-Muñiz, A.; Serrano, L.; Altet, L.; Francino, O.; Sánchez, A.; Merkoçi, A. Triple Lines Gold Nanoparticle-Based Lateral Flow Assay for Enhanced and Simultaneous Detection of Leishmania DNA and Endogenous Control. *Nano Res.* **2015**, *8*, 3704−3714.
(29) Miller, B. S.; Parolo, C.; Turbé, V.; Keane, C. E.; Gray, E. R.; McKendry, R. A. Quantifying Biomolecular Binding Constants Using Video Paper Analytical Devices. *Chem.—Eur. J.* **2018**, *24*, 9783−9787.
(30) Sena-Torralba, A.; Alvarez-Diduk, A.; Parolo, C.; Torné-Morató, H.; Müller, A.; Merkoçi, A. Paper-Based Electrophoretic Bioassay: Biosensing in Whole Blood Operating via Smartphone. *Anal. Chem.* **2021**, *93*, 3112−3121.
(31) Rivas, L.; Medina-Sánchez, M.; de la Escosura-Muñiz, A.; Merkoçi, A. Improving Sensitivity of Gold Nanoparticle-Based Lateral Flow Assays by Using Wax-Printed Pillars as Delay Barriers of Microfluidics. *Lab Chip* **2014**, *14*, 4406−4414.
(32) He, H.; Liu, B.; Wen, S.; Liao, J.; Lin, G.; Zhou, J.; Jin, D. Quantitative Lateral Flow Strip Sensor Using Highly Doped Upconversion Nanoparticles. *Anal. Chem.* **2018**, *90*, 12356−12360.
(33) Moyano, A.; Serrano-Pertierra, E.; Salvador, M.; Martínez-García, J. C.; Rivas, M.; Blanco-López, M. C. Magnetic Lateral Flow Immunoassays. *Diagnostics* **2020**, *10*, 288.
(34) Peng, L.; Li, B. L.; Zhou, C. W.; Li, N. B.; Setyawati, M. I.; Zou, H. L. Naked-Eye Recognition: Emerging Gold Nano-Family for Visual Sensing. *Appl. Mater. Today* **2018**, *11*, 166−188.
(35) Zhou, Y.; Ding, L.; Wu, Y.; Huang, X.; Lai, W.; Xiong, Y. Emerging Strategies to Develop Sensitive AuNP-Based ICTS Nanosensors. *TrAC, Trends Anal. Chem.* **2019**, *112*, 147−160.
(36) Quesada-González, D.; Sena-Torralba, A.; Wicaksono, W. P.; de la Escosura-Muñiz, A.; Ivandini, T. A.; Merkoçi, A. Iridium Oxide (IV) Nanoparticle-Based Lateral Flow Immunoassay. *Biosens. Bioelectron.* **2019**, *132*, 132.
(37) He, Q.; Yang, H.; Pan, J.; Cui, X.; Shen, D.; Eremin, S. A.; Fang, Y.; Zhao, S. Lateral Flow Immunosensor for Ferritin Based on Dual Signal-Amplified Strategy by Rhodium Nanoparticles. *ACS Appl. Bio Mater.* **2020**, *3*, 8849−8856.
(38) Yang, Z.; Yi, C.; Lv, S.; Sheng, Y.; Wen, W.; Zhang, X.; Wang, S. Development of a Lateral Fl Ow Strip Biosensor Based on Copper Oxide Nanoparticles for Rapid and Sensitive Detection of HPV16 DNA. *Sens. Actuators, B* **2019**, *285*, 326−332.
(39) Tian, M.; Xie, W.; Zhang, T.; Liu, Y.; Lu, Z.; Li, C. M.; Liu, Y. A Sensitive Lateral Flow Immunochromatographic Strip with Prussian Blue Nanoparticles Mediated Signal Generation and Cascade Amplification. *Sens. Actuators, B* **2020**, *309*, 127728.
(40) Lou, S.; Ye, J.; Li, K.; Wu, A. A Gold Nanoparticle-Based Immunochromatographic Assay: The Influence of Nanoparticulate Size. *Analyst* **2012**, *137*, 1174−1181.
(41) Zhan, L.; Guo, S. Z.; Song, F.; Gong, Y.; Xu, F.; Boulware, D. R.; McAlpine, M. C.; Chan, W. C. W.; Bischof, J. C. The Role of Nanoparticle Design in Determining Analytical Performance of Lateral Flow Immunoassays. *Nano Lett.* **2017**, *17*, 7207−7212.
(42) Lin, L. K.; Huang, P. Y.; Dutta, S.; Rochet, J. C.; Stanciu, L. A. Tuning a Bisphenol A Lateral Flow Assay Using Multiple Gold Nanosystems. *Part. Part. Syst. Charact.* **2019**, *36*, 1900133.
(43) Petrakova, A. V.; Urusov, A. E.; Zherdev, A. V.; Dzantiev, B. B. Gold Nanoparticles of Different Shape for Bicolor Lateral Flow Test. *Anal. Biochem.* **2019**, *568*, 7−13.
(44) Zhang, W.; Duan, H.; Chen, R.; Ma, T.; Zeng, L.; Leng, Y.; Xiong, Y. Effect of Different-Sized Gold Nanoflowers on the

https://doi.org/10.1021/acsanm.2c04915
ACS Appl. Nano Mater. 2023, 6, 4151−4161

Detection Performance of Immunochromatographic Assay for Human Chorionic Gonadotropin Detection. *Talanta* **2019**, *194*, 604−610.
(45) Serebrennikova, K.; Samsonova, J.; Osipov, A. Hierarchical Nanogold Labels to Improve the Sensitivity of Lateral Flow Immunoassay. *Nano-Micro Lett.* **2018**, *10*, 1−8.
(46) Serebrennikova, K. V.; Samsonova, J. V.; Osipov, A. P.; Senapati, D.; Kuznetsov, D. V. Gold Nanoflowers and Gold Nanospheres as Labels in Lateral Flow Immunoassay of Procalcitonin. *Nano Hybrids and Composites* **2017**, *13*, 47−53.
(47) Xu, P.; Li, J.; Huang, X.; Duan, H.; Ji, Y.; Xiong, Y. Effect of the Tip Length of Multi-Branched AuNFs on the Detection Performance of Immunochromatographic Assays. *Anal. Methods* **2016**, *8*, 3316−3324.
(48) Yang, H.; He, Q.; Chen, Y.; Shen, D.; Xiao, H.; Eremin, S. A.; Cui, X.; Zhao, S. Platinum Nanoflowers with Peroxidase-like Property in a Dual Immunoassay for Dehydroepiandrosterone. *Microchim. Acta* **2020**, *187*, 592.
(49) Srinoi, P.; Chen, Y. T.; Vittur, V.; Marquez, M. D.; Lee, T. R. Bimetallic Nanoparticles: Enhanced Magnetic and Optical Properties for Emerging Biological Applications. *Appl. Sci.* **2018**, *8*, 1106.
(50) Sytwu, K.; Vadai, M.; Dionne, J. A. Bimetallic Nanostructures: Combining Plasmonic and Catalytic Metals for Photocatalysis. *Adv. Phys.: X* **2019**, *4*, 1619480.
(51) Gao, Z.; Ye, H.; Tang, D.; Tao, J.; Habibi, S.; Minerick, A.; Tang, D.; Xia, X. Platinum-Decorated Gold Nanoparticles with Dual Functionalities for Ultrasensitive Colorimetric in Vitro Diagnostics. *Nano Lett.* **2017**, *17*, 5572−5579.
(52) Panferov, V. G.; Safenkova, I. V.; Zherdev, A. V.; Dzantiev, B. B. Urchin Peroxidase-Mimicking Au@Pt Nanoparticles as a Label in Lateral Flow Immunoassay: Impact of Nanoparticle Composition on Detection Limit of Clavibacter Michiganensis. *Microchim. Acta* **2020**, *187*, 268.
(53) de Freitas, I. C.; Parreira, L. S.; Barbosa, E. C. M.; Novaes, B. A.; Mou, T.; Alves, T. V.; Quiroz, J.; Wang, Y. C.; Slater, T. J.; Thomas, A.; Wang, B.; Haigh, S. J.; Camargo, P. H. C. Design-Controlled Synthesis of IrO2 Sub-Monolayers on Au Nanoflowers: Marrying Plasmonic and Electrocatalytic Properties. *Nanoscale* **2020**, *12*, 12281−12291.
(54) Frens, G. Controlled Nucleation for the Regulation of the Particle Size in Monodisperse Gold Suspensions. *Nat. Phys. Sci.* **1973**, *241*, 20−22.
(55) Kimling, J.; Maier, M.; Okenve, B.; Kotaidis, V.; Ballot, H.; Plech, A. Turkevich Method for Gold Nanoparticle Synthesis Revisited. *J. Phys. Chem. B* **2006**, *110*, 15700−15707.
(56) Zhao, C.; Fan, L. Enhanced Electrochemical Evolution of Oxygen by Using Nanoflowers Made from a Gold and Iridium Oxide Composite. *Microchim. Acta* **2012**, *178*, 107−114.
(57) You, H.; Fang, J. Particle-Mediated Nucleation and Growth of Solution-Synthesized Metal Nanocrystals: A New Story beyond the LaMer Curve. *Nano Today* **2016**, *11*, 145−167.
(58) Devarajan, S.; Bera, P.; Sampath, S. Bimetallic Nanoparticles: A Single Step Synthesis, Stabilization, and Characterization of Au-Ag, Au-Pd, and Au-Pt in Sol-Gel Derived Silicates. *J. Colloid Interface Sci.* **2005**, *290*, 117−129.
(59) Radziuk, D. V.; Zhang, W.; Shchukin, D.; Möhwald, H. Ultrasonic Alloying of Preformed Gold and Silver Nanoparticles. *Small* **2010**, *6*, 545−553.
(60) Kariuki, N. N.; Luo, J.; Maye, M. M.; Hassan, S. A.; Menard, T.; Naslund, H. R.; Lin, Y.; Wang, C.; Engelhard, M. H.; Zhong, C. Composition-Controlled Synthesis of Bimetallic Gold - Silver Nanoparticles. *Langmuir* **2004**, *20*, 11240.
(61) Tran, M.; DePenning, R.; Turner, M.; Padalkar, S. Effect of Citrate Ratio and Temperature on Gold Nanoparticle Size and Morphology. *Mater. Res. Express* **2016**, *3*, 105027.
(62) Naumkin, A. V.; Kraut-Vass, A.; Garrenstroom, S. W.; Powell, C. J. *NIST X-Ray Photoelectron Spectroscopy Database*. https://srdata.nist.gov/xps/, 2012.
(63) Sahoo, S. R.; Ke, S. C. Spin-Orbit Coupling Effects in Au 4f Core-Level Electronic Structures in Supported Low-Dimensional Gold Nanoparticles. *Nanomaterials* **2021**, *11*, 554.
(64) Freakley, S. J.; Ruiz-Esquius, J.; Morgan, D. J. The X-Ray Photoelectron Spectra of Ir , IrO2 and IrCl3 Revisited. *Surf. Interface Anal.* **2017**, *49*, 794−799.
(65) Pfeifer, V.; Jones, T. E.; Velasco Vélez, J. J.; Massué, C.; Arrigo, R.; Teschner, D.; Girgsdies, F.; Scherzer, M.; Greiner, M. T.; Allan, J.; Hashagen, M.; Weinberg, G.; Piccinin, S.; Hävecker, M.; Knop-Gericke, A.; Schlögl, R. The Electronic Structure of Iridium and Its Oxides. *Surf. Interface Anal.* **2016**, *48*, 261−273.
(66) Rivas, L.; de la Escosura-Muñiz, A.; Pons, J.; Merkoçi, A. Alzheimer Disease Biomarker Detection Through Electrocatalytic Water Oxidation Induced by Iridium Oxide Nanoparticles. *Electroanalysis* **2014**, *26*, 1287−1294.
(67) Clogston, J. D.; Patri, A. K. Zeta Potential Measurements. In *Methods in Molecular Biology (Methods and Protocols)*; Mc Neils, S., Ed.; Humana Press Inc., 2011; pp 63−70.
(68) Yang, Y.; Ozsoz, M.; Liu, G. Gold Nanocage-Based Lateral Flow Immunoassay for Immunoglobulin G. *Microchim. Acta* **2017**, *184*, 2023−2029.
(69) Zhang, J.; Yu, Q.; Qiu, W.; Li, K.; Qian, L.; Zhang, X.; Liu, G. Gold-Platinum Nanoflowers as a Label and as an Enzyme Mimic for Use in Highly Sensitive Lateral Flow Immunoassays: Application to Detection of Rabbit IgG. *Microchim. Acta* **2019**, *186*, 357.
(70) Turkevich, J.; Stevenson, P. C.; Hillier, J. A Study of the Nucleation and Growth Processes in the Synthesis of Colloidal Gold. *Discuss. Faraday Soc.* **1951**, *11*, 55−75.
(71) Khlebtsov, B. N.; Tumskiy, R. S.; Burov, A. M.; Pylaev, T. E.; Khlebtsov, N. G. Quantifying the Numbers of Gold Nanoparticles in the Test Zone of Lateral Flow Immunoassay Strips. *ACS Appl. Nano Mater.* **2019**, *2*, 5020−5028.

https://doi.org/10.1021/acsanm.2c04915
ACS Appl. Nano Mater. 2023, 6, 4151−4161

Lateral Flow Biosensor for Rapid Detection of *Escherichia coli*

José Fran Bergua[1], Liming Hu[1], Celia Fuentes[1], Ruslan Álvarez-Diduk[1], Abdel-Rahim Hassan[2], Claudio Parolo[1], Arben Merkoçi[1,3]

[1] *Catalan Institute of Nanoscience and Nanotechnology (ICN2), CSIC and BIST, Campus UAB, Bellaterra, 08193 Barcelona, Spain*

[2] *Department of Food Hygiene and Control, Faculty of Veterinary Medicine, Beni-Suef University, Beni-Suef 62511, Egypt*

[3] *ICREA, Institució Catalana de Recerca i Estudis Avançats, 08010 Barcelona, Spain*

[*] *e-mail: arben.merkoçi@icn2.cat*

INTRODUCTION

Microbiological pollution is one of the important threats for good water quality worldwide. ***Escherichia coli (E. coli)* is a good indicator for water microbiological pollution** because of two main reasons: first, *E. coli* is the most abundant bacteria in mammal digestive systems; and second, *E. coli* can be also more easily grown and detected than other water-borne pathogens (i.e. other bacteria and viruses)[1].

The traditional gold standard methods to detect *E. coli* (**filtration membrane and direct bacteria cultivation**) rely on long detection time **(› 24 h)** and complicated procedures, which hinder in-situ detection and in-the-field analysis[2,3]. Lateral flow assay offers several advantages over the aforementioned technologies, such as rapidity, simplicity, low-cost, easy interpretation, user friendly usage and in-situ detection[4]. In this work, we have developed a **polyclonal antibody-based** lateral flow biosensor (LFB) with an easily-interpretable colorimetric output to detect **"general" *E. coli***. Performance of LFB was tested and its **sensitivity, selectivity, accuracy, reproducibility and applicability with real samples** were studied. After optimization, a sensitivity of **10^4 CFU/mL** in river water samples was achieved by combining the LFB with a filtration system within a total time of 30 minutes.

Schematic of *E. coli* LFB

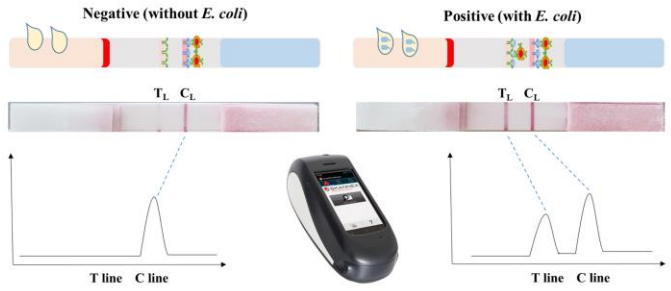

Selectivity and specificity of *E.coli* LFB

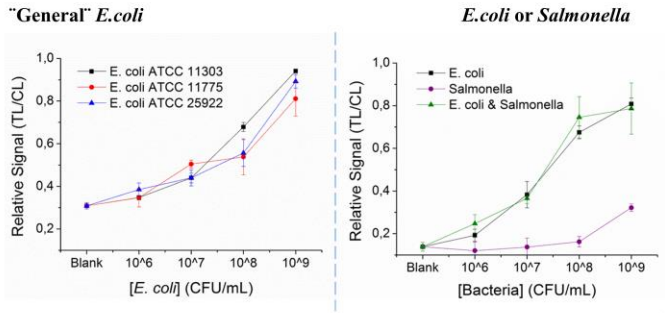

E. coli detection in real samples

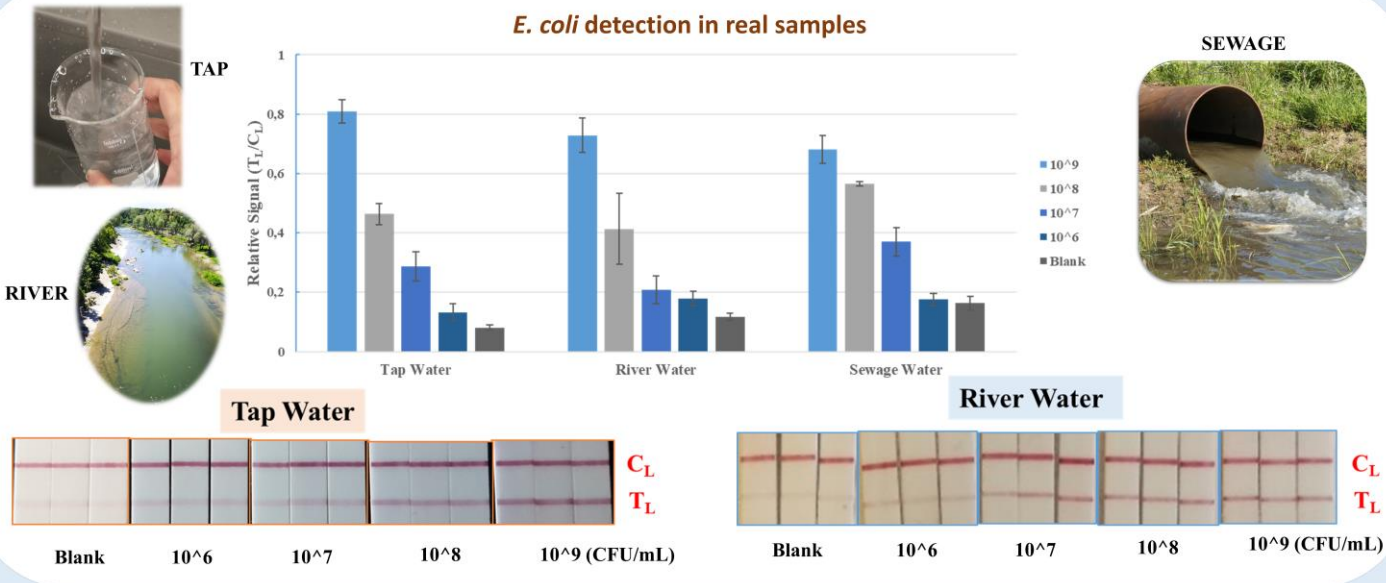

CONCLUSIONS

- In combination with a basic filtration system, this LFB showed two orders of magnitude improvement of sensitivity **(10^4 CFU/mL)**.
- The LFBs were stable with good reproducibility **(RSD: intra-assay ‹ 10%, inter-assay ‹ 15%).**
- These LFBs were able to detect several different strains of *E. coli* but distinguishing them from *Salmonella*, proving the potential application of detection of **"general" *E. coli*** in water samples.
- The LFBs were detected with the **tap, river and sewage waters**, providing good sensitivity and recoveries analyzing spiked samples.

REFERENCE

1. Garcia-Armisen, T., Prats, J. & Servais, P. *Can. J. Microbiol.* **53,** 798–801 (2007).
2. Yan, R. *et al. ACS Sustain. Chem. Eng.* **6,** 4504–4509 (2018).
3. Kumar Gunda, N. S. *et al. Anal. Methods* **6,** 6236–6246 (2014).
4. Quesada-González, D. & Merkoçi, A. *Biosens. Bioelectron.* **73,** 47–63 (2015).

ACKNOWLEDGEMENTS: This work was supported by the European Commission Program, H2020-WATER, INTCATCH 450 Project (689341). ICN2 acknowledges support from the Severo Ochoa Program (MINECO, 451 Grant SEV-2013-0295). The Nanobioelectronics and Biosensors Group acknowledges the 452 support from the Generalitat de Cataluña (Grant 2014 SGR 260).

FEB. 02-03, 2021
CONFERENCE ONLINE
BIOSENSORS FOR PANDEMICS

AuNP-based lateral flow assay for detection of SARS-CoV-2 nucleoprotein: implicit design challenges in a new pandemic

Liming Hu [a], Enric Calucho [a], Celia Fuentes-Chust [a], Ruslan Álvarez-Diduk [a], Andrea Idili [a], Claudio Parolo [a], Arben Merkoçi [a,b]
a Nanobioelectronics & Biosensors Group, Institut Català de Nanociència i Nanotecnologia (ICN2), Campus UAB, 08193 Bellaterra, Barcelona, Spain
b Institució Catalana de Recerca i Estudis Avançats (ICREA), 08010 Barcelona, Spain

ABSTRACT 2020 was marked by a SARS-CoV-2 outbreak that has claimed more than 2 million lives around the world [1], pushed healthcare systems to their limits, shaken the economy at all levels and greatly affected people's daily life. Roughly one year after the appearance of the first case of COVID-19, although there are vaccines available, the eradication of the pandemic is an enduring challenge due to the extremely rapid infectivity and the emergence of new strains of the virus. Therefore, there is the need of diagnostic devices dedicated to each situation: general screening, herd immunity, strain identification, etc.

Lateral flow assays make ideal point-of-care testing platforms due to their simplicity, low cost and user friendliness [2]. Moreover, paper can be easily functionalized with different kind of bioreceptors (e.g., antibodies, DNA, etc.). Herein, we present a AuNP-based lateral flow device for the detection of SARS-CoV-2 nucleoprotein, from the screening of antibodies to the preliminary testing of the device [3].

In the scenario of a new pandemic, the initial lack of bioreceptors for the development of diagnostic platforms creates the conditions for a race towards the launch of the first commercially available products. Therefore, the performance of these new bioreceptors is unbeknownst to researchers during the first stages of the pandemic. Here we will show and discuss the standardization procedures and previous validation of receptor as guidelines to be used for urgent design and application of LFA. ELISA tests were carried out to determine the most efficient set of antibodies for its later transfer to a paper-based format. However, changing the environment on which antibodies work doesn't always translate well, thus we take the opportunity to raise this issue in the context of a congress devoted to biosensors for pandemics.

Nucleoprotein LFA design

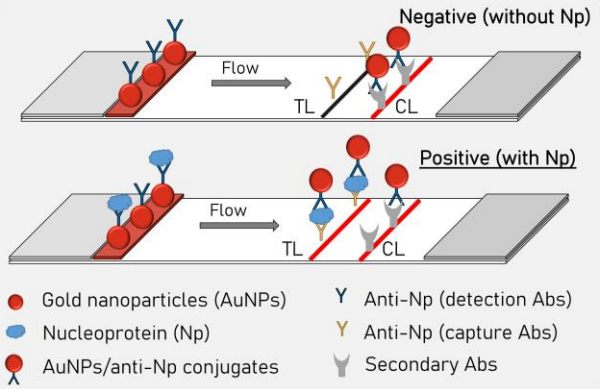

Figure 1. Scheme of LFA for detecting SARS-CoV-2 nucleoprotein.

LFA fabrication and measurement

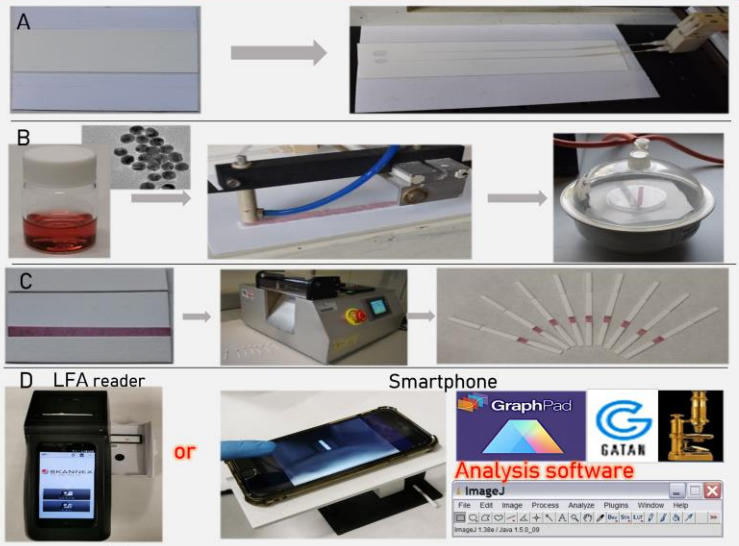

Figure 2. (A) antibodies are dispensed on nitrocellulose membrane to form the test line and control line; (B) Conjugation of AuNPs with antibodies are sprayed on glass fiber to form the conjugate pad; (C) Various pads are assembled and cut into lateral flow strips; (D) LFA reader or smartphone are used for detecting and analysis the lateral flow strips.

Nucleoprotein LFA results

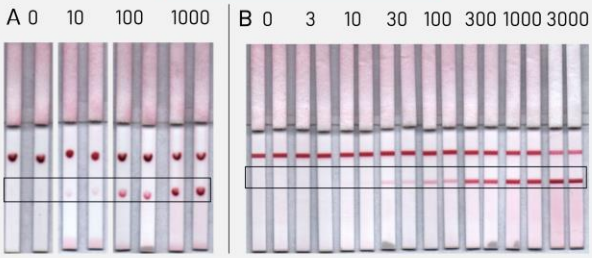

Figure 4. (A) Dot test for rapid evaluation of antibody performance; (B) LFA for detecting gradient concentration of Np (ng/mL) in PBS. Naked eye LOD: 10 ng/mL.

Nucleoprotein LFA development: antibodies selection

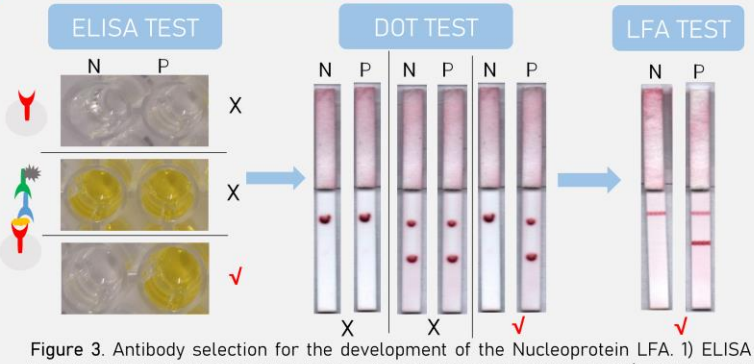

Figure 3. Antibody selection for the development of the Nucleoprotein LFA. 1) ELISA test for preliminary screening from a large number of antibodies; 2) Dot test for performance screening on nitrocellulose membrane of antibodies; 3) Antibodies with satisfactory performance on both ELISA and Dot tests are then used for developing a complete SARS-CoV-2 nucleoprotein LFA.
Note: N-negative, P-positive; 'X' means negative results and '√' indicates positive results

CONCLUSIONS Selection of high-quality antibodies is the most critical step to establish a specific and sensitive LFA. Compared with LFA, ELISA's various reaction conditions (long time, strict temperature control, shaking, free antibodies, and high enzyme sensitivity) are more likely to lead to immune reaction. Therefore, antibodies with good performance on ELISA tests are not necessarily fit for LFA, and antibodies with poor ELISA results are not tested on LFA. To develop a proper LFA diagnostic product as soon as possible in the context of a pandemic, high-throughput and rapid ELISA testing must be used to select antibodies with good sensitivity and specificity from a large number of commercial antibodies. Then dot test is used as a secondary screening, which is less time- and reagent-consuming than a full-fledged LFA, while still having strong conformity between them. Here, we formally adopted this process to develop a SARS-CoV-2 nucleoprotein LFA.

CONTACT PERSON

Arben Merkoçi
arben.merkoci@icn2.cat

REFERENCES

[1] WHO Coronavirus Disease (COVID-19) Dashboard; URL: https://covid19.who.int/
[2] K. J. Land, D. I. Boeras, X. S. Chen, A. R. Ramsay, R. W. Peeling, Nat. Microbiol. (2019), 4, 46.
[3] Parolo, C., Sena-Torralba, A., Bergua, J.F., Calucho, E., Fuentes-Chust, C., Hu, L., Rivas, L., Álvarez-Diduk, R., Nguyen, E.P., Cinti, S., Quesada-González, D., and Merkoçi, A. Nature Protocols, 15 (2020) 3788-3816.

We acknowledge FEDER/Ministerio de Ciencia, Innovación y Universidades – Agencia Estatal de Investigación/_Project MAT2017-87202-P. The ICN2 is funded by the CERCA programme / Generalitat de Catalunya. The ICN2 is supported by the Severo Ochoa Centres of Excellence programme, funded by the Spanish Research Agency (AEI, grant no. SEV-2017-0706). The authors acknowledge Consejo Superior de Investigaciones Científicas (CSIC) for the funded project COVID19-122.

BIOSENSORS FOR PANDEMICS
FEB. 02-03, 2021 CONFERENCE ONLINE

Monitoring generic *Escherichia coli* based on lateral flow biosensor for water fecal pollution assessment

Liming Hu[1,*] José Fran Bergua[1], Celia Fuentes[1], Ruslan Álvarez-Diduk[1], Abdel-Rahim Hassan[2], Claudio Parolo[1], Arben Merkoçi[1,3]

[1]Catalan Institute of Nanoscience and Nanotechnology (ICN2), CSIC and BIST, Campus UAB, Bellaterra, 08193 Barcelona, Spain

[2]Department of Food Hygiene and Control, Faculty of Veterinary Medicine, Beni-Suef University, Beni-Suef 62511, Egypt

[3]ICREA, Catalan Institution for Research and Advanced Studies, Passeig Lluís Companys 23, 08010 Barcelona, Spain

(*) liming.hu@icn2.cat

Microbiological pollution is one of the important threats for good water quality worldwide. *Escherichia coli (E. coli)* is a good indicator for monitoring water microbiological pollution due to two main reasons: first, *E. coli* is the most abundant bacteria in mammal digestive systems; and second, *E. coli* can be also more easily grown and detected than other water-borne pathogens (i.e. other bacteria and viruses)[1].

The traditional gold standard methods to detect *E. coli* (filtration membrane and direct bacteria cultivation) are time-consuming (>24 h), expensive, well-equipped and complicated, which hinder in-situ detection and in-the-field analysis[2]. Lateral flow assay offers several advantages over the aforementioned technologies, such as rapidity, simplicity, low-cost, easy interpretation, easy usage and mass screening on site[3]. In this work, we firstly utilized the bioluminescent bacteria (*Allivibrio fischeri*) to analogously characterize the fluidity of *E.coli* on different size of nitrocellulose membrane and rapidly choose the optimal membrane, and optimized the size of gold nanoparticles, the concentration of antibody conjugated on nanoparticles and concentration of capture antibody sprayed on membrane and then developed a polyclonal antibody-based lateral flow biosensor (LFB) with an easily-interpretable colorimetric output to detect "general" *E. coli.* Finally, under the optimal conditions, a sensitivity of 10^4 CFU/mL in river water samples was achieved by combining the LFB with a filtration system within a total time of 30 minutes with a good reproducibility (RSD: intra-assay< 10%, inter-assay< 15%)[4].

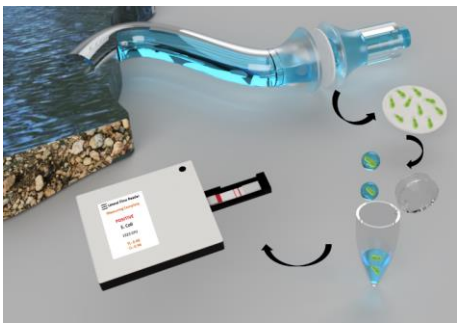

Figure 1 *E.coli* lateral flow biosensor for water monitoring

Keywords: Lateral flow, *Escherichia coli*, water quality monitoring

Funding

This work was supported by the European Commission Program, H2020-WATER, INTCATCH Project (689341). ICN2 is funded by CERCA programme, Generalitat de Catalunya, Grant SEV-2017-0706 funded by MCIN/AEI/ 10.13039/501100011033.

Reference(s)

[1] Garcia-Armisen, T., Prats, J. & Servais, P. Comparison of culturable fecal coliforms and *Escherichia coli* enumeration in freshwaters. Can. J. Microbiol. **53**, 798–801 (2007).

[2] Yan, R., Zhangxuan S., Jie C., et al. On–Off–On Gold Nanocluster-Based Fluorescent Probe for Rapid *Escherichia coli* Differentiation, Detection and Bactericide Screening. ACS Sustain. Chem. Eng. **6**, 4504–4509 (2018).

[3] Quesada-González, D. & Merkoçi, A. Nanoparticle-based lateral flow biosensors. Biosens. Bioelectron. **73**, 47–63 (2015).

[4] Bergua, J. F., Liming H., et al. Lateral flow device for water fecal pollution assessment: From troubleshooting of its microfluidics using bioluminescence to colorimetric monitoring of generic *Escherichia coli*. Lab Chip **21**, 2417–2426 (2021).

Selection and characterization of bioreceptors to develop nanoparticle-based lateral-flow immunoassays under COVID-19 pandemic

Liming Hu[1], Enric Calucho[1], Celia Fuentes-Chust[1], Claudio Parolo[1,2], Andrea Idili[1], Ruslan Álvarez-Diduk[1], Lourdes Rivas[1], and Arben Merkoçi[1,3*]

[1]Nanobioelectronics & Biosensors Group, Institut Català de Nanociència i Nanotecnologia (ICN2), Campus UAB, Barcelona, Spain.
[2]ISGlobal, Barcelona Institute for Global Health, Barcelona, Spain.
[3]ICREA, Institució Catalana de Recerca i Estudis Avançats, Barcelona, Spain.

INTRODUCTION The COVID-19 outbreak has imposed the urgent need for rapid and low-cost diagnostic tools able to support high-frequency testing[1,2]. Among the different diagnostic platforms, **lateral flow assay (LFA)** allows the rapid and specific measurement of biomarkers in their clinical relevant range. Due to their advantages (fast, simple, low cost, and user-friendly etc.) **WHO suggested their use to fight the COVID-19 outbreak and recognized people infected with SARS-CoV-2**[3]. **The selection of bioreceptors with strong affinity and high specificity is crucial** in the development of lateral flow assays, especially in the sandwich ELISA format. This work aims at raising the attention of the scientific community to the need for **better characterized bioreceptors for fast development of point-of-care diagnostic devices able to support mass frequency testing**. Particularly, we present the difficulties encountered in finding suitable antibodies for the development of a lateral flow assay for detecting the nucleoprotein of SARS-CoV-2.

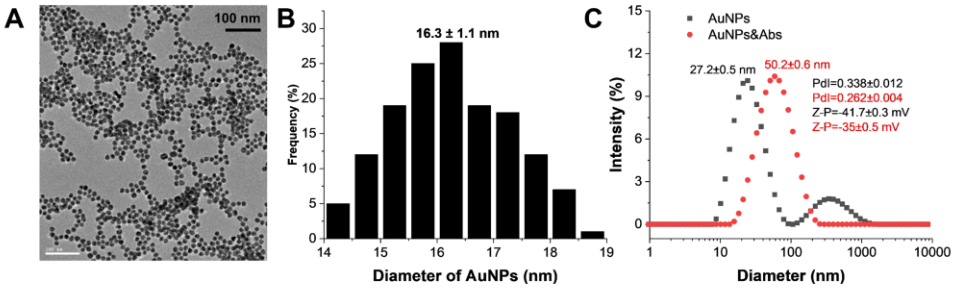

Figure 1. Characterization of AuNPs before and after conjugation with anti-nucleoprotein Abs. (A) TEM images of AuNPs with uniform shape distribution; (B) Histogram of AuNPs (Average size of AuNPs: 16.3 ± 1.1 nm, 150 particles); (C) The change of average hydrodynamic diameters, PDI and Z-potential of AuNPs before and after conjugation with anti-nucleoprotein Abs.

Figure 2. ELISA tests to screen antibody combinations against the nucleoprotein of the SARS-CoV-2. (A) Schematic representation of the immunosandwich ELISA. (B) Antibody combinations with best ELISA performance. (C-E) Each individual graph shows the ELISA test results of same capture antibodies (coated on ELISA plate wells) combined with multiple detection antibodies.

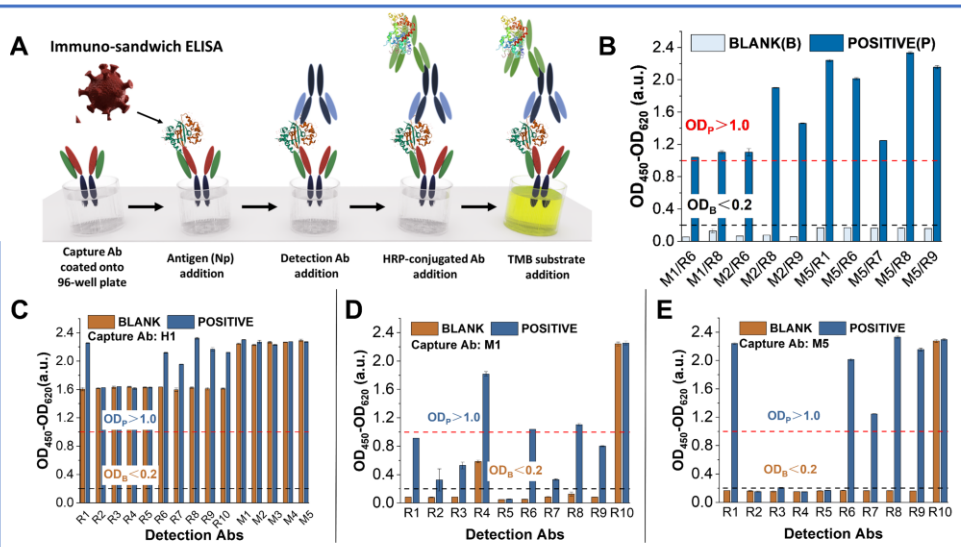

Figure 3. Dot test for screening out antibody combinations and calibration curve of detection of nucleoprotein spiked in artificial saliva based on half-stick LFA. (A) Schematic representation of the dot test on half-stick LFA. (B) All antibody combinations with good performance in the dot test (easy to distinguish between blank and positive samples with the naked eye). R1/M5, R8/M4 and R8/M5 elicit the best response. (C) Calibration curve of the half-stick LFA with R8/M5 antibodies. The data was fitted to a four-parameter logistic curve (blue line).

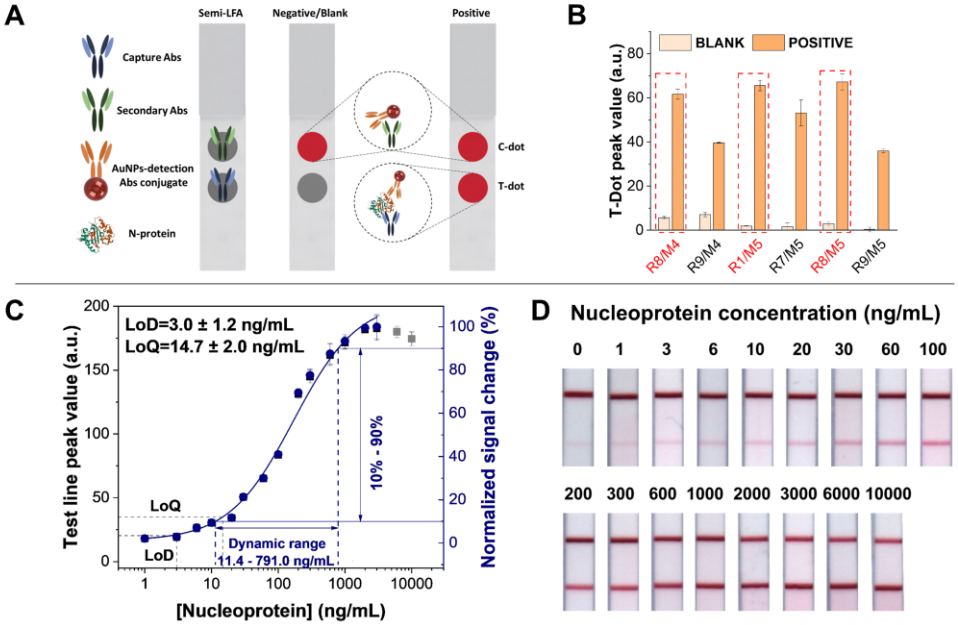

CONCLUSION

we developed **LFA to detect SARS-CoV-2 nucleoprotein in saliva** using two techniques of **ELISA and the half-stick dot format of LFA** to select only **2 couples of antibodies from 80 pairs** tested on ELISA. The whole antibody selection required **over 10 months and ~25,000 €**, making it **poorly effective** during an emergency situation as the current COVID-19 pandemic. Therefore, we urge antibody producers and distributors to consider the implementation of **more extensive characterization** of their products. We realize that a longer bioreceptor characterization implies higher costs for companies, nonetheless we truly believe that researchers would **rather buy more-expensive, but well-characterized antibodies than cheaper but poorly-characterized ones**.

REFERENCE

[1] Guglielmi, G., Nature, 2020, 585, 496.
[2] Wells, C. R. et al. Nat. Commun., 2021, 12, 1–9.
[3] World Health Organization. 2020.
Note: The work was published on Lab on a Chip as open access. https://doi.org/10.1039/D2LC00486K

CONTACT PERSON

Prof. Arben Merkoçi (arben.merkoci@icn2.cat)
Liming Hu (liming.hu@icn2.cat)
Enric Calucho (enric.calucho@icn2.cat)

Horizon 2020 European Union Funding for Research & Innovation

A rational approach to tailor Au-IrO_2 nanoflowers as colorimetric labels for lateral flow assays

Lourdes Rivas,[1] **Liming Hu**,[1] Claudio Parolo,[1,2] Andrea Idili,[1] Arben Merkoçi[1,3*]
[1]*Nanobioelectronics & Biosensors Group, Institut Català de Nanociència i Nanotecnologia (ICN2), Campus UAB, Barcelona, Spain.*
[2]*Barcelona Institute for Global Health (ISGlobal), Barcelona, Spain*
[3]*ICREA, Institució Catalana de Recerca i Estudis Avançats, Barcelona, Spain.*
arben.merkoci@icn2.cat

Lateral flow assay (LFA) is regarded as an ideal screening tool and is widely used in clinical diagnostics due to its simplicity, rapidity, user-friendliness and low cost[1,2]. In particular, during the COVID-19 pandemic, colorimetric lateral flow assay (especially gold nanoparticles based LFA) has demonstrated its convenience and superiority in personal home use[3]. However, lateral flow assay shows relatively low sensitivity due to short reaction time and insufficient sample processing (i.e. sample matrix colour interference). The application of nanoparticles with higher extinction coefficient (stronger light absorption capacity) is the most direct and simplest way to improve the sensitivity of lateral flow assay. Following this strategy, we rationally optimize the synthesis of gold and iridium oxide nanoflowers (Au-IrO_2 NFs) referring to De Freitas and co-workers' work[4] with modification by increasing the concentration of reduction reagent (2.5 mM sodium citrate) and decreasing reaction time. Specifically, we were able to rationally control their size (from 155 nm to 53 nm in diameter) in order to guarantee an optimal flow along the different pads of a LFA. Then, thanks to their superior plasmonic behavior (compared to standard AuNPs), we could achieve an 8-fold lower limit of detection (down to 1.7 ng/mL) for human immunoglobulin G (human IgG) than standard LFAs (13.5 ng/mL). And the Au-IrO_2 NFs based lateral flow assay can specifically identify the human IgG among various IgG from other hosts. Meanwhile, the Au-IrO_2 NFs based LFA showed acceptable recovery for detecting human IgG spiked in human serum (human IgG depleted). Therefore, due to their optical and redox properties, bioconjugation capabilities, and the synergic combination of the individual components, Au-IrO_2 NFs appear as potential candidates for the next generation of optical LFAs.

References

[1] Parolo, C., Sena-Torralba, A., Bergua, J. F., Calucho, E., Fuentes-Chust, C., Hu, L., Rivas, L., Álvarez Diduk, R., Nguyen, E. P., Cinti, S., Quesada González, & Merkoçi, A, Nature protocols, 15 (2020) 3788-3816.
[2] Brangel, P., Sobarzo, A., Parolo, C., Miller, B.S., Howes, P.D., Gelkop, S., Lutwama, J.J., Dye, J.M., McKendry, R.A., Lobel, L., Stevens, M.M., ACS Nano 12 (2018) 63-73.
[3] World Health Organization. 2020.
[4] De Freitas, I. C., Parreira, L. S., Barbosa, E. C. M., Novaes, B. A., Mou, T., Alves, T. V., Quiroz, J., Wang, Y. C., Slater, T. J., Thomas, A., Wang, B., Haigh, S. J., Camargo, P. H. C, Nanoscale 12 (2020) 12281-12291.

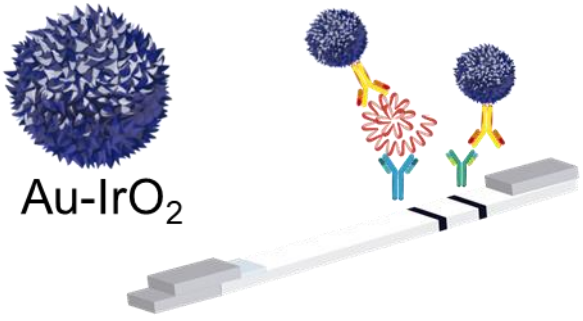

Figure 1: Scheme of Au-IrO2 nanoflowers based lateral flow assay

GOLD NANOPATICLES-BASED OPTICAL BIOSENSORS FOR RAPID AND COST-EFFICIENT DIAGNOSIS

L.M. Hu[1], M. Rossetti[1], A. Merkoçi[1,2,*]

[1] *Nanobioelectronics & Biosensors Group, Catalan Institute of Nanoscience and Nanotechnology (ICN2), CSIC and BIST, Campus UAB, Bellaterra, Barcelona, Spain.*
[2] *Institució Catalana de Recerca i Estudis Avançats (ICREA), Passeig Lluís Companys 23, 08010, Barcelona, Spain*
[*] *e-mail: arben.merkoci@icn2.cat*

In the last decades, with the rapid development of nanotechnology and nanoscience, nanomaterials have been introduced to enhance the sensitivities of bioassays. In particular, gold nanoparticles (AuNPs) have attracted considerable interest due to their unique optical properties and various advantages including strong localized surface plasmon resonance (LSPR[1]), signal amplification capabilities, biocompatibility, ease of functionalization, rapid response, stability, cost-effectiveness, multiplexing capabilities, miniaturization and portability potential and clinical versatility. These features make them highly valuable in point-of-care diagnosis, especially in lateral flow devices[2,3]. However, non-spherical nanoparticles with strong plasmonic behaviors can improve the sensitivity due to the stronger light absorption capacity, multibranched surface structure and bigger surface-area-to-volume ratio[4], when compared to the use of classical spherical AuNPs. Beyond their use in lateral flow, gold-based nanomaterial can be also employed as efficient absorbers in inner filter effect (IFE[5]) assays or as efficient quencher[6] in DNA-based sensors.
Here, I show the use of AuNPs and non-spherical nanoparticles, i.e. gold-iridium oxides nanoflowers (Au-IrO_2 NFs), for different applications, ranging from their use in lateral flow assays[4,7], to their use as strong and efficient absorbers in bioluminescent assays (BBLISA), and to their use as quencher in fluorescence DNA-based sensors. Detailed protocol and some preliminary results related to the detection of neutrophil gelatinase-associated lipocalin (NGAL) protein and miRNA-5100 for monitoring acute kidney injury will be shown.

[1] Hang, Y., Boryczka, J. & Wu, N. *Chem. Soc. Rev.*, 2022, **51**, 329–375.
[2] Liu, Y., Zhan, L., Qin, Z., Sackrison, J. & Bischof, J. C. *ACS Nano*, 2021, **15**, 3593–3611.
[3] Sena-Torralba, A. *et al. Biosens. Bioelectron.*, 2020, **168**, 112559.
[4] Rivas, L., Hu, L., Parolo, C., Idili, A. & Merkoçi, A. *ACS Appl. Nano Mater.*, 2023, **6**, 4151–4161.
[5] Chen, S., Yu, Y.-L. & Wang, J.-H. *Anal. Chim. Acta*, 2018, **999**, 13–26.
[6] Chen, C. & Hildebrandt, N. *TrAC Trends Anal. Chem.*, 2020, **123**, 115748.
[7] Hu, L. *et al. Lab Chip*, 2022, **22**, 2938–2943.

Acknowledgements: We acknowledge Consejo Superior de Investigaciones Científicas (CSIC) for the project "COVID19-122". The MICROB-PREDICT project has received funding from the European Union's Horizon 2020 research and innovation programme under grant agreement No 881603. ICN2 is funded by CERCA programme / Generalitat de Catalunya. The ICN2 is supported by the Severo Ochoa Centres of Excellence programme, Grant CEX2021-001214-S, funded by MCIN/AEI/10.13039.501100011033. Grant PID2021-124795NB-I00 funded by MCIN/AEI/ 10.13039/501100011033 and by "ERDF A way of making Europe".L.H. acknowledges China Scholarship Council (No. 201808360196) and acknowledges Universitat Autonoma de Barcelona (UAB) for the possibility of performing this work inside the framework of Biotechnology PhD Programme. Marianna Rossetti acknowledges the MSCA project funded the European Union's Horizon 2020 research and innovation programme under the Marie Sklodowska-Curie grant agreement No 101029884. CP acknowledges support from the grant CEX2018-000806-S funded by MCIN/AEI/ 10.13039/501100011033, support from the Generalitat de Catalunya through the CERCA Program and support from the Spanish Ministry of Science and Innovation through the program PID2020-116770RJ-I00 and CPP2021-008658.